BRNO UNIVERSITY OF TECHNOLOGY
VYSOKÉ UČENÍ TECHNICKÉ V BRNĚ

FACULTY OF CIVIL ENGINEERING
FAKULTA STAVEBNÍ

INSTITUTE OF STRUCTURAL MECHANICS
ÚSTAV STAVEBNÍ MECHANIKY

ALGORITHMS FOR DESIGN AND ANALYSIS OF MEMBRANE STRUCTURES
ALGORITMY PRO NÁVRH A ANALÝZU MEMBRÁNOVÝCH KONSTRUKCÍ

DOCTORAL THESIS
DISERTAČNÍ PRÁCE

AUTHOR
AUTOR PRÁCE
M.Eng. Ing. Rostislav Lang

SUPERVISOR
VEDOUCÍ PRÁCE
doc. Ing. IVAN NĚMEC, CSc.

BRNO 2019

VYSOKÉ UČENÍ TECHNICKÉ V BRNĚ
FAKULTA STAVEBNÍ

Studijní program	P3607 Stavební inženýrství
Typ studijního programu	Doktorský studijní program s kombinovanou formou studia
Studijní obor	3607V009 Konstrukce a dopravní stavby
Pracoviště	Ústav stavební mechaniky

ZADÁNÍ DISERTAČNÍ PRÁCE

Student	M.Eng. Ing. Rostislav Lang
Název	Algoritmy pro návrh a analýzu membránových konstrukcí
Vedoucí práce	doc. Ing. Ivan Němec, CSc.
Datum zadání	5. 2. 2013
Datum odevzdání	4. 10. 2019

V Brně dne 4. 10. 2019

prof. Ing. Drahomír Novák, DrSc.
Vedoucí ústavu

prof. Ing. Miroslav Bajer, CSc.
Děkan Fakulty stavební VUT

ZÁSADY PRO VYPRACOVÁNÍ

Cílem práce je popis vhodných algoritmů pro navrhování membránových konstrukcí. Tyto algoritmy se budou skládat jak z vybraných existujících obecných metod, tak z metod přímo navržených během doktorského studia. V rámci disertační práce tak budou popsány jednotlivé metody, které slouží k výpočtu počátečních rovnovážných tvarů membránových konstrukcí, dále k analýze jejich statické či dynamické odezvy a také postupy pro generování střihových vzorů.

STRUKTURA DISERTAČNÍ PRÁCE

VŠKP vypracujte a rozčleňte podle dále uvedené struktury:

1. Textová část VŠKP zpracovaná podle Směrnice rektora "Úprava, odevzdávání, zveřejňování a uchovávání vysokoškolských kvalifikačních prací" a Směrnice děkana "Úprava, odevzdávání, zveřejňování a uchovávání vysokoškolských kvalifikačních prací na FAST VUT" (povinná součást VŠKP).
2. Přílohy textové části VŠKP zpracované podle Směrnice rektora "Úprava, odevzdávání, zveřejňování a uchovávání vysokoškolských kvalifikačních prací" a Směrnice děkana "Úprava, odevzdávání, zveřejňování a uchovávání vysokoškolských kvalifikačních prací na FAST VUT" (nepovinná součást VŠKP v případě, že přílohy nejsou součástí textové části VŠKP, ale textovou část doplňují).

---

doc. Ing. Ivan Němec, CSc.
Vedoucí disertační práce

ABSTRACT

The present thesis deals with membrane structures, focusing on the description of both the inherent physical necessitates which has to be dealt and the algorithms used when developing the FEM software. After introducing physical basis of the individual design and analysis steps, the specific issues associated with these calculation procedures as well as the particular solution processes are described.

The first chapter deals with the form finding analysis, which is inherently associated with designing tensile structures. The equilibrium shape is derived from the requirement for the resulting prestress, given boundary conditions and applied external load. However, this process is also generally dealing with a complex task of searching for the equilibrium itself. Therefore, necessary stabilization techniques are an inherent part of the calculation procedures. The selected methods as well as the proposed technique specialized for the calculation of conical membranes are presented. In addition to the given thesis scope, the proposal of an algorithm for dealing with optimizing the shapes of arches and shells is described.

In the chapter about the structural analysis, the main focus is given to the phenomenon of membranes wrinkling. This sudden loss of stability, when the compression occurs, strongly affects the structural response. The proposed algorithm is presented, which is modularly applicable to both the elastic and inelastic materials as described in detail.

The chapter dealing with the cutting pattern generation process presents the proposal of the selected combination of two existing solution methods. This algorithms sequence focuses on reaching the optimum combination of the calculation speed, generality and precision.

The individual chapters are complemented by presenting of the examples analyzed by using the described algorithms, which demonstrate the individual physical or implementation issues and the associated solution procedures.

KEYWORDS

Membrane structures, tensile structures, form finding, wrinkling, structural analysis, generation of cutting patterns, FEA software

ABSTRAKT

Předkládaná práce se zabývá problematikou navrhování membránových konstrukcí, a to především s ohledem na vývoj potřebných výpočetních nástrojů v rámci MKP programů. Po uvedení základních fyzikálních požadavků jednotlivých kroků při navrhování těchto konstrukcí budou dále prezentovány vybrané či navržené algoritmy.

Kapitola form finding se zabývá analýzou tvaru membránových konstrukcí. Rovnovážný tvar je odvozen od požadavku na výsledné předpětí, specifikované okrajové podmínky a aplikované zatížení. Obecně se ale tento proces zabývá i samotným hledáním rovnovážné soustavy sil v prostoru. V důsledku této skutečnosti jsou součástí popisované analýzy také vhodné stabilizační metody. V této kapitole budou prezentovány jak zvolené postupy, tak i navržená stabilizační technika specializovaná na hledání tvarů kuželových membrán. Dále je také popsán navržený algoritmus pro řešení úloh optimalizujících tvary ohybově tuhých konstrukcí, které jsou spjaty s hledáním labilních rovnovážných konfigurací.

Kapitola structural analysis je zaměřená především na fenomén vrásnění membrán. Tato náhlá ztráta stability silně ovlivňuje statickou i dynamickou odezvu membránových konstrukcí. V rámci této kapitoly je představena a verifikována navržená výpočetní metoda, modulárně aplikovatelná na lineární, nelineárně elastické i plastické materiály používané pro uvedené konstrukce.

Kapitola cutting pattern generation se zabývá výpočtem střihových vzorů, nezbytných pro výrobní proces membránových konstrukcí. Pro tento proces je v rámci předkládané práce navržena kombinace dvou různých metod. Zvolená posloupnost algoritmů cílí na optimalizaci poměru rychlosti, obecnosti a přesnosti výpočtu.

Zmíněné kapitoly jsou doplněny jednotlivými příklady, analyzovanými pomocí popisovaných algoritmů, které demonstrují konkrétní fyzikální problémy či nezbytné implementační procesy.

KLÍČOVÁ SLOVA

Membránové konstrukce, tahové konstrukce, hledání tvaru, vrásnění, generování střihových vzorů, MKP program

BIBLIOGRAFIC CITATION

LANG, Rostislav. *Algorithms for design and analysis of membrane structures.* Brno, 2019. 139 p. Doctoral thesis. Brno University of Technology, Faculty Civil Engineering, Department of Structural Mechanics. Supervised by doc. Ing. Ivan Němec, CSc.

DECLARATION OF ORIGINALITY

I declare that I have written the Doctoral Thesis titled *Algorithms for design and analysis of membrane structures* independently, under the guidance of the supervisor and using exclusively the technical references and other sources of information cited in the thesis and listed in the comprehensive bibliography at the end of the thesis.

In Brno 4. 10. 2019

M.Eng. Ing. Rostislav Lang
author

ACKNOWLEDGEMENT

I would like to sincerely appreciate the supervision of my thesis by doc. Ing. Ivan Němec, CSc. I am really grateful that I was given such a freedom in the research and development works as well as for the advice whenever I asked for a help.

Further, I would like to express my gratitude to all the colleagues I had the opportunity and honour to cooperate with. There are really many of them, who spent a long time in cooperation on the development of the FEA software packages based on the algorithms introduced in this work.

Last, but certainly not least, I would like to appreciate the support provided by my beloved wife, who supported me all the time and encouraged me whenever I needed.

CONTENT

1 INTRODUCTION

The membrane structures are fascinating from many points of view. From an architectural aspect, they are light, beautiful and non-conventional. From civil engineer's point of view, membrane structures have the ability to overcome large spans and are really uncommon in their design and fabrication processes, both of them influenced by special requirements associated with these structures. From a point of view of a developer of computer FEM software, these structures represent a great challenge, as it is necessary to cope with their large nonlinearities in structural analysis, and develop special tools for form finding and cutting pattern generation. More than anywhere else, the cooperation of all these professions can be observed as the shapes of tensile structures are driven by the will of nature and its physical laws more than by the will of a man.

Fig. 1 Iconic Structure Tanzbrunnen Designed by Frei Otto, Cologne, Germany [I, II]

Fig. 2 Roof of Denver International Airport, USA [III]

Even though the tensile structures are one of the oldest types of structures, serving mostly in the past for covering both the permanent and temporary living places and for shading, their renaissance has started in the second half of the 20th century. The growth in their usage in

modern architecture and civil engineering, with respect to their size and variety, was strongly affected by the development in the field of available materials, the advent of computers, and the development in the field of computational mechanics of structures. Nowadays, these structures are able to take impressive shapes and to overcome large spans, so they are used for roofing of public spaces (Fig. 1), stadiums, stations, airports (Fig. 2) etc.

1.1 OUTLINE OF THE THESIS

This thesis is structured into the following chapters, covering the topics from the general theoretical introduction, following with the chapters focused on the particular membrane constructions design steps up to the chapter that presents a usage of described algorithms in practice.

Continuum Mechanics

This chapter includes a brief introduction into the essential principles of the continuum mechanics, which are the basis for further work. The Lagrangian continuum is described and the important quantities are depicted, namely the deformation gradient, different strain and stress measures. The principle of the virtual work and linearization of this general principle is further described and used in the following chapters.

Finite Element Procedure

The chapter is focused on the continuum discretization, the description of the basics of finite elements and the system of equations assemblage process in static and dynamic analyses, based on the usage of finite elements. The possible solution procedures used for the calculation of static and dynamic response are introduced.

Form Finding

The membrane structures are made of the material that only acts in tension and, as a consequence of this fact, the structural response of them is derived from their tension and curvature. For those structures, the statement 'Form follows force' is completely true, therefore the requirement of the forces is the main designing parameter. In contrast with conventional civil engineering design procedures, where the shape of the structure is predefined and the internal forces are calculated, the forces are predefined here and the shape is searched for. This implies that the structural analysis must be preceded by the form finding analysis to obtain the initial equilibrium position of the structure. The algorithms for this process as well as the proposals of two special stabilization techniques are presented. The numerical examples demonstrate solving of the individual physical or implementation issues.

Structural Analysis

The structural analysis, starting from this initial equilibrium position, is characterized by strong nonlinearities in both, the geometrical and the material response. The material lacks the bending stiffness as well as the compressive strength since the stability loss occurs due to local buckling immediately even at low compression stress, and exhibit itself as wrinkling of the membrane.

The proposed algorithm for dealing with this phenomenon as well as the examples verifying this method are presented.

Cutting Pattern Generation

The other characteristic designing step is the generation of cutting patterns, which is crucial for the manufacturing process. The double-curved shapes of the membrane structures need to be decomposed into pieces, for which the planar approximations are calculated in order to obtain the patterns that can be cut out, assembled and joined together for the subsequent assembly process. In this chapter the proposed algorithms sequence is presented and further contributed by numerical examples.

Use in Practice

This chapter presents an interesting customer example calculated by using the described and further implemented algorithms.

1.2 OBJECTIVES OF THE THESIS

Here, the thesis objectives are listed, covering the research work performed.

Form Finding

The objective of this part of the thesis is the description of a general form finding algorithm suitable for the implementation. Furthermore, the aim is also the proposal of an advanced stabilization technique for dealing with conical membranes, which needs special treatment of prestress in the regions of high or low points. In addition to the scope of this thesis, the stabilization technique dealing with the optimization of beams and shell shapes is also proposed and introduced.

Structural Analysis

The aim of this part of the thesis is to deal with the wrinkling phenomenon. Thus, the proposal of a suitable algorithm usable for elastic and inelastic materials is required here. The proposed method should be verified by suitable examples.

Cutting Pattern Generation

The objective of this part of the thesis is the investigation of existing algorithms for the cutting pattern generation and the consequent proposal of a suitable procedure for the implementation. Thus, the combined procedure composed of two different algorithms is proposed as an optimal solution technique.

The chapters focused on the mentioned objectives are further complemented with the numerical examples calculated by using the FEA solver by the *FEM consulting* company [IV], incorporated into the RFEM software by the *Dlubal Software* company [III]. Thus, the dissertation presents the theoretical research as well as the proposals of suitable or new algorithms, which were used for the development of the tools for designing and analysing tensile structures in the RFEM software. However, the codes are not a subject of the thesis but they are a property of these private companies.

2 CONTINUUM MECHANICS

2.1 ESSENTIAL QUANTITIES OF CONTINUUM MECHANICS

This section gives the essential formulas for definition of the variational formulation of the principle of the virtual work. For tensile structures, the Lagrangian continuum description is assumed with the consideration of large displacements, large rotations and also with large strains in general.

In the very start, the basic assumptions, quantities and measures for geometrically nonlinear analysis are introduced.

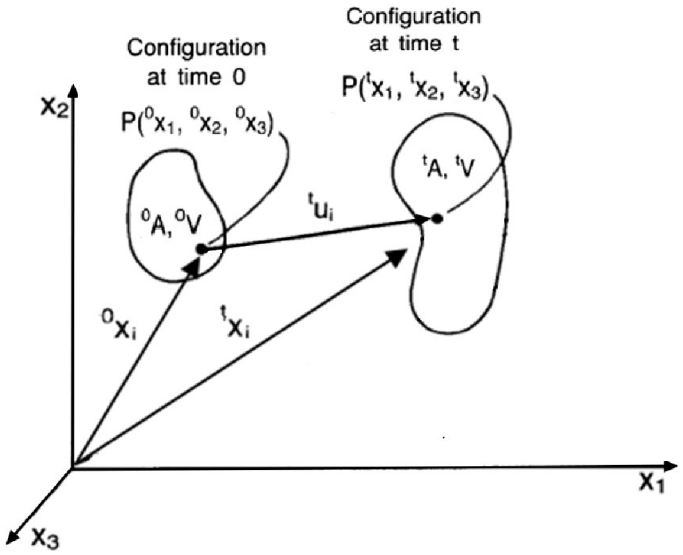

Fig. 3 Original (Material) and Actual (Spatial) Configuration of Body

The particle of the body at time 0 is described by the position vector ${}^0x_i$, when undergoing the deformation ${}^tu_i$ the particle position ${}^tx_i$ is described as follows (Fig. 3):

$$ {}^tx_i = {}^0x_i + {}^tu_i \tag{2.1} $$

Thus, the relation of different configurations in the original and the actual positions is described by the deformation gradient tensor. The matrix notation

$$ {}^t_0\mathbf{F} = \begin{bmatrix} \frac{\partial {}^tx_1}{\partial {}^0x_1} & \frac{\partial {}^tx_1}{\partial {}^0x_2} & \frac{\partial {}^tx_1}{\partial {}^0x_3} \\ \frac{\partial {}^tx_2}{\partial {}^0x_1} & \frac{\partial {}^tx_2}{\partial {}^0x_2} & \frac{\partial {}^tx_2}{\partial {}^0x_3} \\ \frac{\partial {}^tx_3}{\partial {}^0x_1} & \frac{\partial {}^tx_3}{\partial {}^0x_2} & \frac{\partial {}^tx_3}{\partial {}^0x_3} \end{bmatrix} \tag{2.2} $$

and the index notation

$$ {}^t_0F_{ij} = \frac{\partial {}^tx_i}{\partial {}^0x_j} = {}^t_0x_{i,j} \tag{2.3} $$

This tensor describes the straining and the rigid body rotation of material fibres. This is a fundamental quantity of continuum mechanics, used for the definition and relation of different measures and quantities used later.

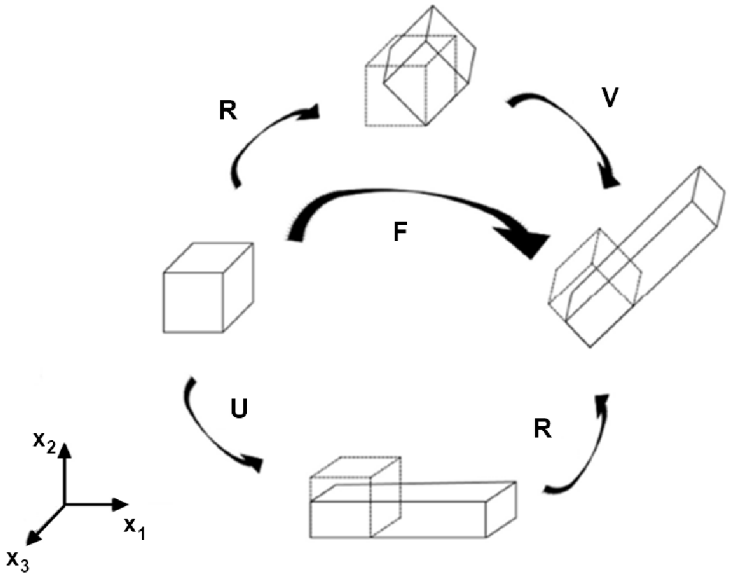

Fig. 4 Polar Decomposition

The deformation gradient ${}^{t}_{0}\mathbf{F}$ can be decomposed into two parts (Fig. 4), capturing the straining ${}^{t}_{0}\mathbf{U}$ first and then the rigid body rotation ${}^{t}_{0}\mathbf{R}$, or capturing the rigid body rotation ${}^{t}_{0}\mathbf{R}$ first and then the straining ${}^{t}_{0}\mathbf{V}$. This process is called polar decomposition.

$$ {}^{t}_{0}\mathbf{F} = {}^{t}_{0}\mathbf{R}\ {}^{t}_{0}\mathbf{U} = {}^{t}_{0}\mathbf{V}\ {}^{t}_{0}\mathbf{R} \tag{2.4} $$

The rotation tensor ${}^{t}_{0}\mathbf{R}$ is orthogonal and the straining tensors ${}^{t}_{0}\mathbf{U}$ and ${}^{t}_{0}\mathbf{V}$ are symmetric.

With the use of the deformation gradient, the right and left Cauchy-Green deformation tensors can be defined:

$$ {}^{t}_{0}\mathbf{C} = {}^{t}_{0}\mathbf{F}^{\mathrm{T}}\ {}^{t}_{0}\mathbf{F} = ({}^{t}_{0}\mathbf{U}^{\mathrm{T}}\ {}^{t}_{0}\mathbf{R}^{\mathrm{T}})({}^{t}_{0}\mathbf{R}\ {}^{t}_{0}\mathbf{U}) = ({}^{t}_{0}\mathbf{U})^{2} \tag{2.5} $$

$$ {}^{t}_{0}\mathbf{B} = {}^{t}_{0}\mathbf{F}\ {}^{t}_{0}\mathbf{F}^{\mathrm{T}} = ({}^{t}_{0}\mathbf{V}\ {}^{t}_{0}\mathbf{R})({}^{t}_{0}\mathbf{R}^{\mathrm{T}}\ {}^{t}_{0}\mathbf{V}^{\mathrm{T}}) = ({}^{t}_{0}\mathbf{V})^{2} \tag{2.6} $$

Both of these tensors are only related to the stretch tensors ${}^{t}_{0}\mathbf{U}$ or ${}^{t}_{0}\mathbf{V}$, which are symmetric, and therefore, both of the Cauchy-Green deformation tensors are also symmetric and invariant under the rigid body rotation. These tensors will be further used for the definition of the strain measures in the reference and current configurations.

As described later, for the variational formulation of the principle of the virtual work, we are dealing with the equilibrium in the unknown configuration. Since we cannot integrate the virtual work over the body with unknown configuration, this equation will be modified and linearized afterwards. For further calculation, different strain and stress measures will be used. Particularly two strain measures, the Green-Lagrange and the Euler-Almansi strain tensors, as well as two conjugated stress measures, the Second Piola-Kirchhoff and Cauchy stress tensors, will be described.

The **Green-Lagrange strain tensor** is related to the chosen reference configuration. Considering the figure above (Fig. 3), the strain caused by the body deformation from the original configuration at time 0 to the actual configuration at time t can be expressed in the matrix notation as

$$ {}^{t}_{0}\mathbf{E} = \frac{1}{2}({}^{t}_{0}\mathbf{F}^{\mathrm{T}}\ {}^{t}_{0}\mathbf{F} - \mathbf{I}) = \frac{1}{2}({}^{t}_{0}\mathbf{C} - \mathbf{I}) \tag{2.7} $$

and in the index notation as

$$ {}^{t}_{0}E_{ij} = \frac{1}{2}\left(\frac{\partial {}^{t}u_i}{\partial {}^{0}x_j} + \frac{\partial {}^{t}u_j}{\partial {}^{0}x_i} + \frac{\partial {}^{t}u_k}{\partial {}^{0}x_i}\frac{\partial {}^{t}u_k}{\partial {}^{0}x_j}\right) = \frac{1}{2}({}^{t}_{0}u_{i,j} + {}^{t}_{0}u_{j,i} + {}^{t}_{0}u_{k,i}\ {}^{t}_{0}u_{k,j}) \tag{2.8} $$

The Green-Lagrange strain tensor is symmetric and for rigid body motion, it is equal to zero.

Note: The upper left index denotes the deformed configuration of the body in time t and the bottom left index denotes the required/chosen reference configuration to which the strain is related.

The **Euler-Almansi strain tensor** is related to the actual configuration. Referring to (Fig. 3), the strain can be expressed in the matrix notation as

$$ {}^{t}_{t}\mathbf{e} = {}^{t}\mathbf{e} = \frac{1}{2}(\mathbf{I} - {}^{t}_{0}\mathbf{F}^{-\mathrm{T}}\ {}^{t}_{0}\mathbf{F}^{-1}) = \frac{1}{2}(\mathbf{I} - \mathbf{B}^{-1}) \tag{2.9} $$

and in the index notation as

$$ {}^{t}_{t}e_{ij} = {}^{t}e_{ij} = \frac{1}{2}\left(\frac{\partial {}^{t}u_i}{\partial {}^{t}x_j} + \frac{\partial {}^{t}u_j}{\partial {}^{t}x_i} + \frac{\partial {}^{t}u_k}{\partial {}^{t}x_i}\frac{\partial {}^{t}u_k}{\partial {}^{t}x_j}\right) = \frac{1}{2}({}^{t}_{t}u_{i,j} + {}^{t}_{t}u_{j,i} + {}^{t}_{t}u_{k,i}\ {}^{t}_{t}u_{k,j}) \tag{2.10} $$

Note: Since the strain is related to the actual configuration, the upper and the bottom left index are the same. Therefore, the bottom left index is redundant and will not be written further.

If the deformations are so small that the nonlinear (second-order) terms of the Green-Lagrange or the Euler-Almansi strain tensor can be neglected, the linear part of these tensors identifies them as an **Infinitesimal strain tensor,** which is equal to the linear deformation tensor. The Infinitesimal strain tensor in the original configuration in the matrix notation can be written as

$$ {}^{t}_{0}\boldsymbol{\varepsilon} = \frac{1}{2}({}^{t}_{0}\mathbf{F} + {}^{t}_{0}\mathbf{F}^{\mathrm{T}}) - \mathbf{I} \tag{2.11} $$

and in the index notation as

$$ {}^{t}_{0}\varepsilon_{ij} = \frac{1}{2}\left(\frac{\partial {}^{t}u_i}{\partial {}^{0}x_j} + \frac{\partial {}^{t}u_j}{\partial {}^{0}x_i}\right) = \frac{1}{2}({}^{t}_{0}u_{i,j} + {}^{t}_{0}u_{j,i}) \tag{2.12} $$

The Infinitesimal strain tensor in the actual configuration in the matrix notation can be written as

$$ {}^{t}_{t}\boldsymbol{\varepsilon} = {}^{t}\boldsymbol{\varepsilon} = \mathbf{I} - \frac{1}{2}({}^{t}_{0}\mathbf{F}^{-1} + {}^{t}_{0}\mathbf{F}^{-\mathrm{T}}) \tag{2.13} $$

and in the index notation as

$$ {}^{t}_{t}\varepsilon_{ij} = {}^{t}\varepsilon_{ij} = \frac{1}{2}\left(\frac{\partial {}^{t}u_i}{\partial {}^{t}x_j} + \frac{\partial {}^{t}u_j}{\partial {}^{t}x_i}\right) = \frac{1}{2}\left({}^{t}_{t}u_{i,j} + {}^{t}_{t}u_{j,i}\right) \tag{2.14} $$

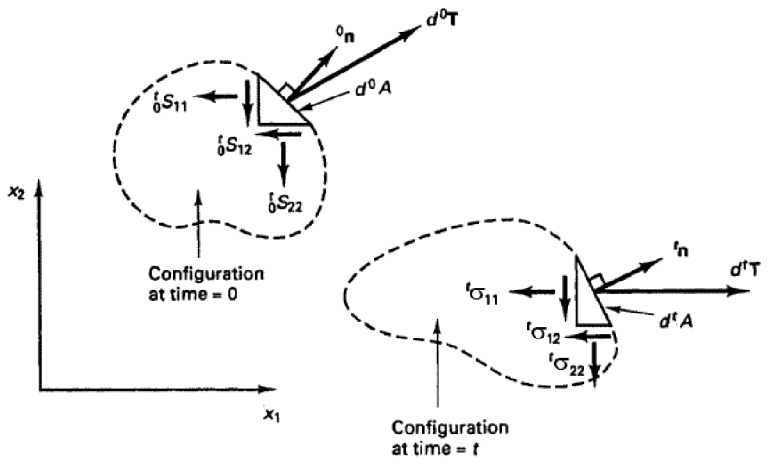

Fig. 5 Second Piola-Kirchhoff and Cauchy Stresses

Assuming the force $\mathrm{d}^{t}\mathbf{T}$ acting on the area $\mathrm{d}^{t}A$ of the body in the actual configuration, the *Cauchy formula* defines the relation

$$ \mathrm{d}^{t}\mathbf{T} = {}^{t}\boldsymbol{\sigma}^{T}\,{}^{t}\mathbf{n}\,\mathrm{d}^{t}A \tag{2.15} $$

where ${}^{t}\boldsymbol{\sigma}$ is the **Cauchy stress** tensor and ${}^{t}\mathbf{n}$ is the normal vector to the area $\mathrm{d}^{t}A$.

The analogical relation defines the force $\mathrm{d}^{0}\mathbf{T}$ acting on the area $\mathrm{d}^{0}A$ of the body in the original configuration

$$ \mathrm{d}^{0}\mathbf{T} = {}^{t}_{0}\mathbf{S}^{T}\,{}^{0}\mathbf{n}\,\mathrm{d}^{0}A \tag{2.16} $$

where ${}^{t}_{0}\mathbf{S}$ is known as the **Second Piola-Kirchhoff stress** tensor and ${}^{0}\mathbf{n}$ is the normal vector to the area $\mathrm{d}^{0}A$.

Considering the kinematic relationship, known as the *Nanson's formula,* and the formula for transformation between forces $\mathrm{d}^{0}\mathbf{T}$ and $\mathrm{d}^{t}\mathbf{T}$

$$ {}^{t}\mathbf{n}\,\mathrm{d}^{t}A = \frac{{}^{0}\rho}{{}^{t}\rho}\,{}^{t}_{0}\mathbf{F}^{-T}\,{}^{0}\mathbf{n}\,\mathrm{d}^{0}A \tag{2.17} $$

$$ \mathrm{d}^{0}\mathbf{T} = {}^{t}_{0}\mathbf{F}^{-1}\,\mathrm{d}^{t}\mathbf{T} \tag{2.18} $$

the relationship between the Cauchy stress and the Second Piola-Kirchhoff stress tensors is defined by the following equations in the matrix notation

$$ {}^{t}\boldsymbol{\sigma} = \frac{{}^{t}\rho}{{}^{0}\rho}\,{}^{t}_{0}\mathbf{F}\,{}^{t}_{0}\mathbf{S}\,{}^{t}_{0}\mathbf{F}^{T} = \frac{1}{\det({}^{t}_{0}\mathbf{F})}\,{}^{t}_{0}\mathbf{F}\,{}^{t}_{0}\mathbf{S}\,{}^{t}_{0}\mathbf{F}^{T} \tag{2.19} $$

$$ {}^{t}_{0}\mathbf{S} = \frac{{}^{0}\rho}{{}^{t}\rho}\,{}^{t}_{0}\mathbf{F}^{-1}\,{}^{t}\boldsymbol{\sigma}\,{}^{t}_{0}\mathbf{F}^{-T} = \det({}^{t}_{0}\mathbf{F})\,{}^{t}_{0}\mathbf{F}^{-1}\,{}^{t}\boldsymbol{\sigma}\,{}^{t}_{0}\mathbf{F}^{-T} \tag{2.20} $$

and in the index notation

$$ {}^{t}\sigma_{mn} = \frac{{}^{t}\rho}{{}^{0}\rho}\ {}^{t}_{0}x_{m,i}\ {}^{t}_{0}x_{n,j}\ {}^{t}_{0}S_{ij} = \frac{1}{det({}^{t}_{0}F)}\ {}^{t}_{0}x_{m,i}\ {}^{t}_{0}x_{n,j}\ {}^{t}_{0}S_{ij} \tag{2.21} $$

$$ {}^{t}_{0}S_{ij} = \frac{{}^{0}\rho}{{}^{t}\rho}\ {}^{t}_{0}x^{-1}_{i,m}\ {}^{t}_{0}x^{-1}_{j,n}\ {}^{t}\sigma_{mn} = det({}^{t}_{0}F)\ {}^{t}_{0}x^{-1}_{i,m}\ {}^{t}_{0}x^{-1}_{j,n}\ {}^{t}\sigma_{mn} \tag{2.22} $$

The first formula can be called as a ‘pull-back’ and the second one as a ’push-forward’ operation.

The above defined quantities will be further used in the following chapters and subchapters of this work. For many cases, there could be other different strain and stress measures defined, as described in [1, 3].

Based on the measures above, the virtual work of the internal forces in the body at time t can be described in different configurations, here in the actual (spatial) or the original (material) configuration as

$$ \delta W^{int} = \int_{{}^{t}V} {}^{t}\sigma_{ij}\ \delta\,{}^{t}\varepsilon_{ij}\ {}^{t}dV = \int_{{}^{0}V} {}^{t}_{0}S_{ij}\ \delta\,{}^{t}_{0}E_{ij}\ {}^{0}dV \tag{2.23} $$

and the virtual work of the external forces is described as

$$ \begin{aligned} \delta W^{ext} &= \int_{{}^{t}V} {}^{t}f_i^V\ \delta u_i\ {}^{t}dV + \int_{{}^{t}S} {}^{t}f_i^S\ \delta u_i^S\ {}^{t}dS + \sum_n {}^{t}F_i\ \delta u_i \\ &= \int_{{}^{0}V} {}^{t}_{0}f_i^V\ \delta u_i\ {}^{0}dV + \int_{{}^{0}S} {}^{t}_{0}f_i^S\ \delta u_i^S\ {}^{0}dS + \sum_n {}^{t}_{0}F_i\ \delta u_i \end{aligned} \tag{2.24} $$

where ${}^{t}V$, ${}^{0}V$ and ${}^{t}S$, ${}^{0}S$ are the volume and the surface in the original and actual configurations, ${}^{t}f_i^V$, ${}^{t}_{0}f_i^V$, ${}^{t}f_i^S$, ${}^{t}_{0}f_i^S$, ${}^{t}F_i$ and ${}^{t}_{0}F_i$ are the volume, surface and nodal external forces respectively, δu_i and δu_i^S are the nodal displacement variations of the body and the body surface.

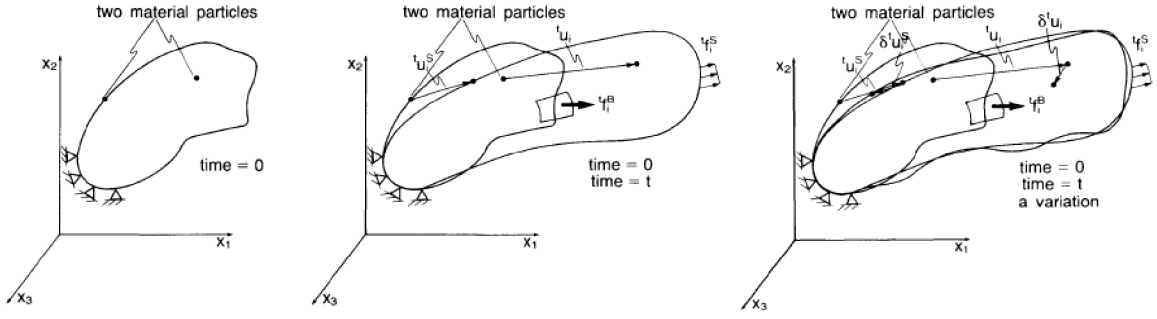

Fig. 6 Deformation of Body and Application of Deformation Variation

For the body in equilibrium, the variation of the overall virtual work disappears, as described by the formula

$$ \delta W = \delta W^{int} - \delta W^{ext} = 0 \tag{2.25} $$

2.2 LINEARIZATION OF GENERAL PRINCIPLE OF VIRTUAL WORK

As described above, we assume for tensile structures that the body is subjected to large displacements, large rotations as well as large strains in general. In the following figure (Fig. 7), the original (time 0), the actual (time t) and the new (time $t + \Delta t$) configurations are depicted.

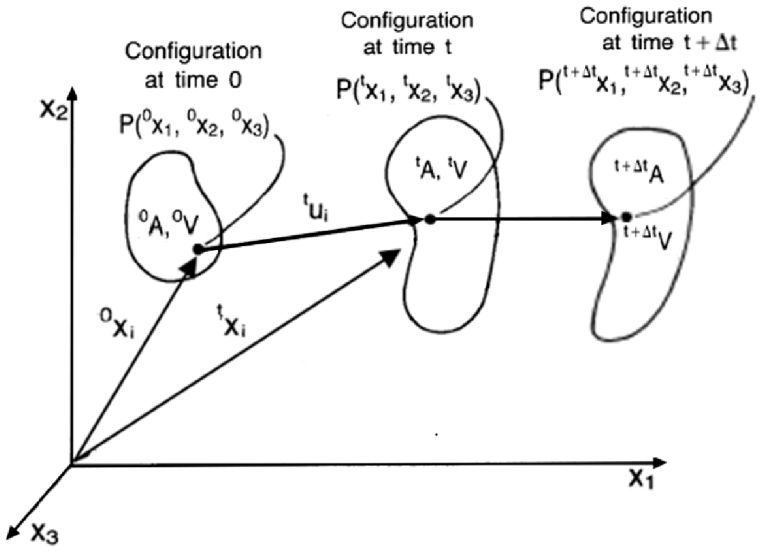

Fig. 7 Original, Actual and New Configurations of Body

The virtual work of the internal and external forces related to the new configuration (time $t + \Delta t$) is described by

$$\delta W^{int} = \int_{t+\Delta t V} {}^{t+\Delta t}\sigma_{ij}\, \delta\, {}^{t+\Delta t}\varepsilon_{ij}\, {}^{t+\Delta t}dV \tag{2.26}$$

$$\delta W^{ext} = \int_{t+\Delta t V} {}^{t+\Delta t}f_i^V\, \delta u_i\, {}^{t+\Delta t}dV + \int_{t+\Delta t S} {}^{t+\Delta t}f_i^S\, \delta u_i^S\, {}^{t+\Delta t}dS + \sum_n {}^{t+\Delta t}F_i\, \delta u_i = {}^{t+\Delta t}\mathcal{R} \tag{2.27}$$

Based on the equilibrium equation of the principle of the virtual work for the new configuration

$$\delta W^{int} = \delta W^{ext} \tag{2.28}$$

$$\int_{t+\Delta t V} {}^{t+\Delta t}\sigma_{ij}\, \delta\, {}^{t+\Delta t}\varepsilon_{ij}\, {}^{t+\Delta t}dV = {}^{t+\Delta t}\mathcal{R} \tag{2.29}$$

Based on the fact that the new configuration (time $t + \Delta t$) is not known, the direct integration of the Cauchy stress tensor and the variation of the Infinitesimal strain tensor over the unknown volume of the body cannot be performed directly. The equilibrium equation needs to be rewritten by using another stress and strain measures, specifically the Second Piola-Kirchhoff stress and the Green-Lagrange strain tensors, which are related to the known configurations.

There are two practical choices for the reference configuration, the original one in time 0 and the actual one in time t. The procedure using the original configurationis known as a **Total**

Lagrangian formulation, the procedure considering the actual configuration is called an **Updated Lagrangian formulation**. In the following, the Updated Lagrangian formulation will be followed and used for rewriting and further linearization of the principle of the virtual work.

$$\int_{{}^{t}V} {}_{t}^{t+\Delta t}S_{ij}\ \delta\, {}_{t}^{t+\Delta t}E_{ij}\ {}^{t}dV = {}^{t+\Delta t}\mathcal{R} \tag{2.30}$$

This equation is physically totally equivalent to the previous one. The decomposition of the unknown Second Piola-Kirchhoff stress and the Green-Lagrange strain tensors will be performed in order to separate the known values in time t and the unknown increments.

$${}_{t}^{t+\Delta t}S_{ij} = {}_{t}^{t}S_{ij} + {}_{t}S_{ij} = {}^{t}\sigma_{ij} + {}_{t}S_{ij} \tag{2.31}$$

$${}_{t}^{t+\Delta t}E_{ij} = {}_{t}^{t}E_{ij} + {}_{t}E_{ij} = {}_{t}E_{ij} \tag{2.32}$$

The increment of the Green-Lagrange strain tensor

$${}_{t}E_{ij} = \frac{1}{2}\left({}_{t}u_{i,j} + {}_{t}u_{j,i} + {}_{t}u_{k,i}\ {}_{t}u_{k,j}\right) \tag{2.33}$$

can be decomposed into its linear (Infinitesimal) and nonlinear parts in terms of the displacement vector u_i

$${}_{t}\varepsilon_{ij} = \frac{1}{2}\left({}_{t}u_{i,j} + {}_{t}u_{j,i}\right) \tag{2.34}$$

$${}_{t}\eta_{ij} = \frac{1}{2}\,{}_{t}u_{k,i}\ {}_{t}u_{k,j} \tag{2.35}$$

Therefore, the following holds

$${}_{t}E_{ij} = {}_{t}\varepsilon_{ij} + {}_{t}\eta_{ij} \tag{2.36}$$

$$\delta\,{}_{t}E_{ij} = \delta\,{}_{t}\varepsilon_{ij} + \delta\,{}_{t}\eta_{ij} \tag{2.37}$$

Using the formulas above, the equation of the principle of the virtual work can be rewritten

$$\int_{{}^{t}V} {}_{t}S_{ij}\ \delta\,{}_{t}\varepsilon_{ij}\ {}^{t}dV + \int_{{}^{t}V} {}_{t}S_{ij}\ \delta\,{}_{t}\eta_{ij}\ {}^{t}dV + \int_{{}^{t}V} {}^{t}\sigma_{ij}\ \delta\,{}_{t}\varepsilon_{ij}\ {}^{t}dV + \int_{{}^{t}V} {}^{t}\sigma_{ij}\ \delta\,{}_{t}\eta_{ij}\ {}^{t}dV = {}^{t+\Delta t}\mathcal{R} \tag{2.38}$$

with no approximation introduced till now.

Since the equation of the principle of the virtual work is generally a complicated nonlinear function of the unknown displacement increment, the linearization is performed by neglecting the higher-order terms in u_i, so an approximate equation is obtained.

The term ${}^{t}\sigma_{ij}$ describes a known value of the actual Cauchy stress in the body. With the given variation δu_i, the variation of the linear term $\delta\,{}_{t}\varepsilon_{ij}$ is also known, however the variation of the term $\delta\,{}_{t}\eta_{ij}$ is linearly dependent on u_i. The Second Piola-Kirchhoff stress increment ${}_{t}S_{ij}$ is

generally a nonlinear function of the Green-Lagrange strain ${}_tE_{ij}$. Using the Taylor series, the stress increment ${}_tS_{ij}$ can be rewritten

$$ {}_tS_{ij} = \frac{\partial {}^tS_{ij}}{\partial {}^tE_{rs}}\ {}_tE_{rs} + \cdots \doteq \frac{\partial {}^tS_{ij}}{\partial {}^tE_{rs}}\ ({}_t\varepsilon_{rs} + {}_t\eta_{rs}) \doteq {}_tC_{ijrs}\ {}_t\varepsilon_{rs} \tag{2.39} $$

while neglecting the higher-order terms of the Taylor series and the second-order part of the Green-Lagrange strain tensor ${}_t\eta_{rs}$. The linearized stress increment ${}_tS_{ij}$ is thus obtained and the linearization the whole equation of the principle of the virtual work can be written as follows:

$$ \int_{{}^tV} {}_tC_{ijrs}\ {}_t\varepsilon_{rs}\ \delta\,{}_t\varepsilon_{ij}\ {}^tdV + \int_{{}^tV} {}^t\sigma_{ij}\ \delta\,{}_t\eta_{ij}\ {}^tdV = {}^{t+\Delta t}\mathcal{R} - \int_{{}^tV} {}^t\sigma_{ij}\ \delta\,{}_t\varepsilon_{ij}\ {}^tdV \tag{2.40} $$

or in the matrix notation

$$ \int_{{}^tV} {}_t\mathbf{C}\ {}_t\boldsymbol{\varepsilon}\ \delta\,{}_t\boldsymbol{\varepsilon}\ {}^t\mathrm{dV} + \int_{{}^tV} {}^t\boldsymbol{\sigma}\ \delta\,{}_t\boldsymbol{\eta}\ {}^t\mathrm{dV} = {}^{t+\Delta t}\boldsymbol{\mathcal{R}} - \int_{{}^tV} {}^t\boldsymbol{\sigma}\ \delta\,{}_t\boldsymbol{\varepsilon}\ {}^t\mathrm{dV} \tag{2.41} $$

The integral with the linearized term of the stress increment ${}_tS_{ij}$ and the variation of $\delta\,{}_t\eta_{ij}$ (linearly dependent in u_i) had to be neglected. The linearly dependent terms remain on the left side, the known values are given to the right side. The term ${}^{t+\Delta t}\mathcal{R}$ is the already described virtual work of external forces at time $t + \Delta t$, the integral on the right hand side is the virtual work of the element internal stresses at time t and the difference of these terms is known as an out-of-balance virtual work term. As a consequence of linearization, the approximative deformation Δu is obtained

$$ {}^{t+\Delta t}u_i \doteq {}^tu_i + \Delta u_i \tag{2.42} $$

This leads to the iteration scheme

$$ {}^{t+\Delta t}u_i^{(k)} = {}^{t+\Delta t}u_i^{(k-1)} + \Delta u_i^{(k)} \tag{2.43} $$

Assuming the load is deformation dependent

$$ \begin{aligned} {}^{t+\Delta t}\mathcal{R} &= \int_{t+\Delta t_V} {}^{t+\Delta t}f_i^V\ \delta u_i\ {}^{t+\Delta t}dV + \int_{t+\Delta t_S} {}^{t+\Delta t}f_i^S\ \delta u_i^S\ {}^{t+\Delta t}dS + \sum_n {}^{t+\Delta t}F_i\ \delta u_i \\ &\doteq \int_{t+\Delta t_V^{(k-1)}} {}^{t+\Delta t}f_i^{V(k-1)}\ \delta u_i\ {}^{t+\Delta t}dV^{(k-1)} \\ &+ \int_{t+\Delta t_S^{(k-1)}} {}^{t+\Delta t}f_i^{S(k-1)}\ \delta u_i^S\ {}^{t+\Delta t}dS^{(k-1)} + \sum_n {}^{t+\Delta t}F_i^{(k-1)}\ \delta u_i \\ &= {}^{t+\Delta t}\mathcal{R}^{(k-1)} \end{aligned} \tag{2.44} $$

the linearized equation of the principle of the virtual work can be rewritten into the following form of the Newton iteration scheme

$$\int_{{}^{t+\Delta t}V^{(k-1)}} {}^{t+\Delta t}C_{ijrs}^{(k-1)}\,\Delta_{t+\Delta t}\varepsilon_{rs}^{(k)}\,\delta_{t+\Delta t}\varepsilon_{ij}^{(k-1)}\,{}^{t+\Delta t}dV^{(k-1)}$$

$$+\int_{{}^{t+\Delta t}V^{(k-1)}} {}^{t+\Delta t}\sigma_{ij}^{(k-1)}\,\delta\Delta_{t+\Delta t}\eta_{ij}^{(k)}\,{}^{t+\Delta t}dV^{(k-1)} \tag{2.45}$$

$$={}^{t+\Delta t}\mathcal{R}^{(k-1)}-\int_{{}^{t+\Delta t}V^{(k-1)}} {}^{t+\Delta t}\sigma_{ij}^{(k-1)}\,\delta_{t+\Delta t}\varepsilon_{ij}^{(k-1)}\,{}^{t+\Delta t}dV^{(k-1)}$$

where

$${}^{t+\Delta t}u_i^{(0)}={}^{t}u_i \tag{2.46}$$

$${}^{t+\Delta t}\sigma_{ij}^{(0)}={}^{t}\sigma_{ij} \tag{2.47}$$

$${}^{t+\Delta t}\varepsilon_{ij}^{(0)}={}^{t}\varepsilon_{ij} \tag{2.48}$$

The term t and Δt are the generalized load or/and time state and increment, the counter k denotes the iteration number. If the dynamic analysis is to be performed, the virtual work of inertia forces is assumed in the equilibrium equation described above

$${}^{t+\Delta t}\mathcal{J}^{(k)}=\int_{{}^{t+\Delta t}V} {}^{t+\Delta t}\rho\;{}^{t+\Delta t}\ddot{u}_i^{(k)}\,\delta u_i\;{}^{t+\Delta t}dV=\int_{{}^{0}V} {}^{0}\rho\;{}^{t+\Delta t}\ddot{u}_i^{(k)}\,\delta u_i\;{}^{0}dV \tag{2.49}$$

3 FINITE ELEMENT PROCEDURE

The previous chapter Continuum Mechanics focused on the brief description of the physical basis of the mathematical modeling of structures. This chapter deals with the continuum discretization in space, or in time, of the previously depicted formulas in order to obtain the finite number of the equilibrium equations, which are to be solved.

3.1 CONTINUUM DISCRETIZATION

The objective of this process is to replace the continuum by finite elements (FE) (Fig. 8) and to evaluate the equilibrium in the finite number of nodes, depending on the required accuracy, thus on the fineness of the mesh.

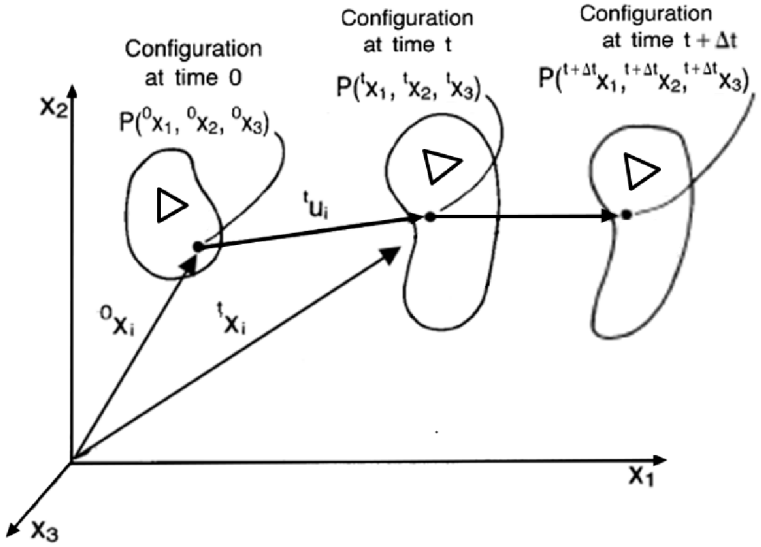

Fig. 8 Continuum Discretization by Finite Elements (Triangular FE)

The variation of the linearized general equation of the virtual work for continuum (2.41)

$$\int_{{}^tV} {}_t\mathbf{C}\ {}_t\boldsymbol{\varepsilon}\ \delta_t\boldsymbol{\varepsilon}\ {}^tdV + \int_{{}^tV} {}^t\boldsymbol{\sigma}\ \delta_t\boldsymbol{\eta}\ {}^tdV = {}^{t+\Delta t}\boldsymbol{\mathcal{R}} - \int_{{}^tV} {}^t\boldsymbol{\sigma}\ \delta_t\boldsymbol{\varepsilon}\ {}^tdV$$

is therefore modified to the form, where the variation is expressed by the summation the virtual work variation for the individual elements

$$\sum_k^m \int_{{}^tV_k} {}_t\mathbf{C}_k\ {}_t\boldsymbol{\varepsilon}_k\ \delta_t\boldsymbol{\varepsilon}_k\ {}^tdV_k + \sum_k^m \int_{{}^tV_k} {}^t\boldsymbol{\sigma}_k\ \delta_t\boldsymbol{\eta}_k\ {}^tdV_k = {}^{t+\Delta t}\mathcal{R} - \sum_k^m \int_{{}^tV_k} {}^t\boldsymbol{\sigma}_k\ \delta_t\boldsymbol{\varepsilon}_k\ {}^tdV_k \qquad (3.1)$$

Where k and m are the FE number and the total amount of FE respectively.

The evaluation of the element contributions, thus the formation of the required matrices and vectors, is an important phase of the whole analysis solution. There can be different FE formulations identified, specifically the generalized coordinate and isoparametric finite elements. The usage of the isoparametric elements is more common and usually more efficient,

although it can be sometime of interest to follow the generalized coordinate choice, especially in the case of beam elements.

The following subchapter includes a short introduction of the basic principle of the isoparametric elements and presents rewriting of the individual contributions (3.1).

3.2 ISOPARAMETRIC FINITE ELEMENTS

"The principal idea of the isoparametric finite element formulation is to achieve the relationship between the element displacements at any point and the element nodal point displacements directly through the use of interpolation functions (also called shape functions)." [1].

$$x_i = \sum_{l}^{n} h_l \, \hat{x}_i{}^{l} \tag{3.2}$$

$$u_i = \sum_{l}^{n} h_l \, \hat{u}_i{}^{l} \tag{3.3}$$

and in the matrix form

$$\mathbf{x} = \mathbf{H}\,\hat{\mathbf{x}} \tag{3.4}$$

$$\mathbf{u} = \mathbf{H}\,\hat{\mathbf{u}} \tag{3.5}$$

$$\hat{\mathbf{x}}^{\mathrm{T}} = [x_1^1 \quad x_2^1 \quad x_3^1 \quad x_1^2 \quad x_2^2 \quad x_3^2 \quad \cdots \quad x_1^n \quad x_2^n \quad x_3^n] \tag{3.6}$$

$$\hat{\mathbf{u}}^{\mathrm{T}} = [u_1^1 \quad u_2^1 \quad u_3^1 \quad u_1^2 \quad u_2^2 \quad u_3^2 \quad \cdots \quad u_1^n \quad u_2^n \quad u_3^n] \tag{3.7}$$

where x_i or $\mathbf{x}$ and u_i or $\mathbf{u}$ are the positions and displacements at any node respectively, $\hat{x}_i^l$ or $\hat{\mathbf{x}}$ and $\hat{u}_i^l$ or $\hat{\mathbf{u}}$ are the position and displacement of the element nodes, h_l and $\mathbf{H}$ are the displacement interpolation functions and the displacement interpolation matrix, l and n are the node number and the number of element nodes.

All the finite element matrices $\mathbf{K}_{\mathrm{L}}$, $\mathbf{K}_{\mathrm{NL}}$, $\mathbf{M}$, $\mathbf{C}$, internal forces $\mathbf{F}$ contributions, surface and body load effects $\mathbf{R}$ are calculated by using these interpolation functions, precisely said using the displacement interpolation matrix $\mathbf{H}$, the linear $\mathbf{B_L}$ and the nonlinear $\mathbf{B_{NL}}$ strain interpolation matrices, which are derived and assembled on the basis of the elements shape functions.

The isoparametric elements can be formulated as continuum or structural elements. Whereas for the continuum elements, the displacements are interpolated in terms of the nodal point displacements, for structural elements, the displacements are interpolated in terms of the midsurface displacements and rotations.

The general procedure is described on a 2D isoparametric continuum element, where two broadly used of them are shown in the following figure (Fig. 9). The global x_i and the local $\bar{x}_i$ Cartesian systems are depicted, where the local Cartesian system is defined in such a way that the local $\bar{x}_3$ axis coincide with the element normal direction n.

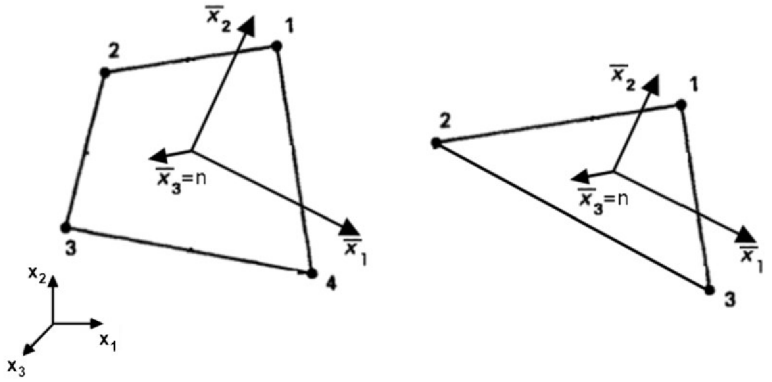

Fig. 9 2D Continuum Isoparametric Elements in Global x_i and Local $\bar{x}_i$ Cartesian System

For derivation of the following quantities, the Updated Lagrangian formulation is assumed. Further, the planar (local) axial system of the element is used, therefore the transformation between the global $\hat{\mathbf{u}}$ and the local $\bar{\hat{\mathbf{u}}}$ nodal displacement is introduced by the transformation matrix $\mathbf{T}$

$$ {}_t\hat{\mathbf{u}} = \mathbf{T}\ {}_t\bar{\hat{\mathbf{u}}} \tag{3.8} $$

$$ {}_t\bar{\hat{\mathbf{u}}} = \mathbf{T}^{\mathrm{T}}\ {}_t\hat{\mathbf{u}} \tag{3.9} $$

$$ {}_t\bar{\hat{\mathbf{u}}}^{\mathrm{T}} = [{}_t\bar{u}_1^1 \quad {}_t\bar{u}_2^1 \quad {}_t\bar{u}_3^1 \quad {}_t\bar{u}_1^2 \quad {}_t\bar{u}_2^2 \quad {}_t\bar{u}_3^2 \quad \cdots \quad {}_t\bar{u}_1^n \quad {}_t\bar{u}_2^n \quad {}_t\bar{u}_3^n] \tag{3.10} $$

$$ {}_t\mathbf{T} = \begin{bmatrix} \mathbf{T}^{\mathrm{l}} & \mathbf{0} & \vdots & \mathbf{0} \\ \mathbf{0} & \mathbf{T}^{\mathrm{l}} & \vdots & \mathbf{0} \\ \vdots & \vdots & \vdots & \vdots \\ \mathbf{0} & \mathbf{0} & \vdots & \mathbf{T}^{\mathrm{l}} \end{bmatrix} \tag{3.11} $$

$$ {}_t\mathbf{T}^{\mathrm{l}} = \begin{bmatrix} cos(x_1\bar{x}_1) & cos(x_1\bar{x}_2) & cos(x_1\bar{x}_3) \\ cos(x_2\bar{x}_1) & cos(x_2\bar{x}_2) & cos(x_2\bar{x}_3) \\ cos(x_3\bar{x}_1) & cos(x_3\bar{x}_2) & cos(x_3\bar{x}_3) \end{bmatrix} \tag{3.12} $$

$$ \mathbf{0} = \begin{bmatrix} 0 & 0 & 0 \\ 0 & 0 & 0 \\ 0 & 0 & 0 \end{bmatrix} \tag{3.13} $$

The displacement interpolation matrix is defined by putting together the displacement interpolation functions

$$ \bar{\mathbf{H}} = \begin{bmatrix} h_1 & 0 & 0 & h_2 & 0 & 0 & \cdots & h_n & 0 & 0 \\ 0 & h_1 & 0 & 0 & h_2 & 0 & \cdots & 0 & h_n & 0 \\ 0 & 0 & h_1 & 0 & 0 & h_2 & & 0 & 0 & h_n \end{bmatrix} \tag{3.14} $$

Furthermore, the Green-Lagrange incremental strain tensor is expressed in the local coordinate system by using the formulas depicted in (2.33), (2.34) and (2.35)

$$ {}_t\bar{\mathbf{E}}_{11} = {}_t\bar{\boldsymbol{\varepsilon}}_{11} + {}_t\bar{\boldsymbol{\eta}}_{11} = {}_t\bar{u}_{1,1} + \frac{1}{2}\left(\left({}_t\bar{u}_{1,1}\right)^2 + \left({}_t\bar{u}_{2,1}\right)^2 + \left({}_t\bar{u}_{3,1}\right)^2\right) \tag{3.15} $$

$$ {}_t\bar{\mathbf{E}}_{22} = {}_t\bar{\boldsymbol{\varepsilon}}_{22} + {}_t\bar{\boldsymbol{\eta}}_{22} = {}_t\bar{u}_{2,2} + \frac{1}{2}\left(\left({}_t\bar{u}_{1,2}\right)^2 + \left({}_t\bar{u}_{2,2}\right)^2 + \left({}_t\bar{u}_{3,2}\right)^2\right) \tag{3.16} $$

$$ {}_t\bar{\mathbf{E}}_{12} = {}_t\bar{\boldsymbol{\varepsilon}}_{12} + {}_t\bar{\boldsymbol{\eta}}_{12} = \frac{1}{2}\left({}_t\bar{u}_{1,2} + {}_t\bar{u}_{2,1}\right) + \frac{1}{2}\left({}_t\bar{u}_{1,1}\ {}_t\bar{u}_{1,2} + {}_t\bar{u}_{2,1}\ {}_t\bar{u}_{2,2} + {}_t\bar{u}_{3,1}\ {}_t\bar{u}_{3,2}\right) \tag{3.17} $$

To express the linear part of the Green-Lagrange incremental strain tensor, the linear strain interpolation matrix is derived by taking the partial derivatives of the shape functions

$$ {}_t\bar{\mathbf{B}}_{\mathrm{L}} = \begin{bmatrix} {}_th_{1,1} & 0 & 0 & {}_th_{2,1} & 0 & 0 & \cdots & {}_th_{n,1} & 0 & 0 \\ 0 & {}_th_{1,2} & 0 & 0 & {}_th_{2,2} & 0 & & 0 & {}_th_{n,2} & 0 \\ {}_th_{1,2} & {}_th_{1,1} & 0 & {}_th_{2,2} & {}_th_{2,1} & 0 & & {}_th_{n,2} & {}_th_{n,1} & 0 \end{bmatrix} \tag{3.18} $$

$$ {}_t\bar{\boldsymbol{\varepsilon}} = \begin{bmatrix} {}_t\bar{\boldsymbol{\varepsilon}}_{11} & {}_t\bar{\boldsymbol{\varepsilon}}_{22} & 2{}_t\bar{\boldsymbol{\varepsilon}}_{12} \end{bmatrix} = {}_t\bar{\mathbf{B}}_{\mathrm{L}}\ {}_t\hat{\bar{\mathbf{u}}} \tag{3.19} $$

where

$$ {}_th_{l,i} = \frac{\partial h_l}{\partial {}^tx_i} \tag{3.20} $$

By using the introduced formulas, the first integral of the equation (3.1) can be rewritten in terms of the nodal displacement vector

$$ \begin{aligned} \int_{{}^tV_k} {}_t\mathbf{C}_k\ {}_t\boldsymbol{\varepsilon}_k\ \delta_t\boldsymbol{\varepsilon}_k\ {}^t\mathrm{d}V_k &= \delta_t\hat{\bar{\mathbf{u}}}_k^{\mathrm{T}} \int_{{}^tV_k} {}_t\bar{\mathbf{B}}_{Lk}^{\mathrm{T}}\ {}_t\mathbf{C}_k\ {}_t\bar{\mathbf{B}}_{Lk}\ {}^t\mathrm{d}V_k\ {}_t\hat{\bar{\mathbf{u}}}_k = \delta_t\hat{\mathbf{u}}_k^{\mathrm{T}}\ {}_t\mathbf{T}_k^{\mathrm{T}}\ {}_t\bar{\mathbf{K}}_{Lk}\ {}_t\mathbf{T}_k\ {}_t\hat{\mathbf{u}}_k \\ &= \delta_t\hat{\mathbf{u}}_k^{\mathrm{T}}\ {}_t\mathbf{K}_{Lk}\ {}_t\hat{\mathbf{u}}_k \end{aligned} \tag{3.21} $$

where ${}_t\bar{\mathbf{K}}_{Lk}$ and ${}_t\mathbf{K}_{Lk}$ are the linear (denoted by the index L) stiffness matrixes of the element k in time t in the local and global Cartesian coordinate system respectively.

To consider the nonlinear part of the Green-Lagrange incremental strain tensor, the nonlinear strain interpolation matrix is derived as follows:

$$ {}_t\bar{\mathbf{B}}_{\mathrm{NL}} = \begin{bmatrix} {}_th_{1,1} & 0 & 0 & {}_th_{2,1} & 0 & 0 & & {}_th_{n,1} & 0 & 0 \\ {}_th_{1,2} & 0 & 0 & {}_th_{2,2} & 0 & 0 & & {}_th_{n,2} & 0 & 0 \\ 0 & {}_th_{1,1} & 0 & 0 & {}_th_{2,1} & 0 & \cdots & 0 & {}_th_{n,1} & 0 \\ 0 & {}_th_{1,2} & 0 & 0 & {}_th_{2,2} & 0 & & 0 & {}_th_{n,2} & 0 \\ 0 & 0 & {}_th_{1,1} & 0 & 0 & {}_th_{2,1} & & 0 & 0 & {}_th_{n,1} \\ 0 & 0 & {}_th_{1,2} & 0 & 0 & {}_th_{2,2} & & 0 & 0 & {}_th_{n,2} \end{bmatrix} \tag{3.22} $$

where

$$ {}_t\bar{\mathbf{B}}_{\mathrm{NL}}\ {}_t\hat{\bar{\mathbf{u}}} = \begin{bmatrix} {}_t\bar{u}_{1,1} & {}_t\bar{u}_{1,2} & {}_t\bar{u}_{2,1} & {}_t\bar{u}_{2,2} & {}_t\bar{u}_{3,1} & {}_t\bar{u}_{3,2} \end{bmatrix}^{\mathrm{T}} \tag{3.23} $$

For the integration of the virtual work caused by the nonlinear strain increment, the Cauchy stress matrix has to be modified to the following form:

$$ {}^{t}\overline{\boldsymbol{\sigma}} = \begin{bmatrix} {}^{t}\sigma_{11} & {}^{t}\sigma_{12} & 0 & 0 & 0 & 0 \\ {}^{t}\sigma_{12} & {}^{t}\sigma_{22} & 0 & 0 & 0 & 0 \\ 0 & 0 & {}^{t}\sigma_{11} & {}^{t}\sigma_{12} & 0 & 0 \\ 0 & 0 & {}^{t}\sigma_{12} & {}^{t}\sigma_{22} & 0 & 0 \\ 0 & 0 & 0 & 0 & {}^{t}\sigma_{11} & {}^{t}\sigma_{12} \\ 0 & 0 & 0 & 0 & {}^{t}\sigma_{12} & {}^{t}\sigma_{22} \end{bmatrix} \tag{3.24} $$

By using the introduced formulas, the second integral of the equation (3.1) can be rewritten in terms of the nodal displacements vector

$$ \begin{aligned} \int_{{}^{t}V_k} {}^{t}\boldsymbol{\sigma}_k \, \delta_t\boldsymbol{\eta}_k \, {}^{t}dV_k &= \delta_t\hat{\overline{\mathbf{u}}}_k^{T} \int_{{}^{t}V_k} {}_{t}\overline{\mathbf{B}}_{NLk}^{T} \, {}^{t}\overline{\boldsymbol{\sigma}}_k \, {}_{t}\overline{\mathbf{B}}_{NLk} \, {}^{t}dV_k \; {}_{t}\hat{\overline{\mathbf{u}}}_k = \delta_t\hat{\mathbf{u}}_k^{T} \, {}_{t}\mathbf{T}_k^{T} \, {}_{t}\overline{\mathbf{K}}_{NLk} \, {}_{t}\mathbf{T}_k \, {}_{t}\hat{\mathbf{u}}_k \\ &= \delta_t\hat{\mathbf{u}}_k^{T} \, {}_{t}\mathbf{K}_{NLk} \, {}_{t}\hat{\mathbf{u}}_k \end{aligned} \tag{3.25} $$

where ${}_{t}\overline{\mathbf{K}}_{NLk}$ and ${}_{t}\mathbf{K}_{NLk}$ are the nonlinear (denoted by the index NL) stiffness matrices of the element k in time t in the local and global Cartesian coordinate system respectively.

The virtual work integral of the known actual internal stresses, written in the Voight notation of Cauchy stress tensor, is expressed as

$$ {}^{t}\vec{\overline{\boldsymbol{\sigma}}} = \begin{bmatrix} {}^{t}\sigma_{11} \\ {}^{t}\sigma_{22} \\ {}^{t}\sigma_{12} \end{bmatrix} \tag{3.26} $$

$$ \int_{{}^{t}V_k} {}^{t}\boldsymbol{\sigma}_k \, \delta_t\boldsymbol{\varepsilon}_k \, {}^{t}dV_k = \delta_t\hat{\overline{\mathbf{u}}}_k^{T} \int_{{}^{t}V_k} {}_{t}\overline{\mathbf{B}}_{Lk} \, {}^{t}\vec{\overline{\boldsymbol{\sigma}}}_k \, {}^{t}dV_k = \delta_t\hat{\mathbf{u}}_k^{T} \, {}_{t}\mathbf{T}_k^{T} \, {}^{t}\overline{\mathbf{F}} = \delta_t\hat{\mathbf{u}}_k^{T} \, {}^{t}\mathbf{F}_k \tag{3.27} $$

The surface, body and inertia forces can also be rewritten as

$$ \int_{{}^{t}V_k} {}^{t+\Delta t}_{t}\mathbf{f}_k^{V} \, \delta_t\mathbf{u}_k \, {}^{t}dV_k = \delta_t\hat{\overline{\mathbf{u}}}_k^{T} \int_{{}^{t}V_k} \overline{\mathbf{H}}_k \, {}^{t+\Delta t}_{t}\overline{\mathbf{f}}_k^{V} \, {}^{t}dV_k = \delta_t\hat{\mathbf{u}}_k^{T} \, {}_{t}\mathbf{T}_k^{T} \, {}^{t+\Delta t}_{t}\overline{\mathbf{R}}_k^{V} = \delta_t\hat{\mathbf{u}}_k^{T} \, {}^{t+\Delta t}_{t}\mathbf{R}_k^{V} \tag{3.28} $$

$$ \int_{{}^{t}S_k} {}^{t+\Delta t}_{t}\mathbf{f}_k^{S} \, \delta_t\mathbf{u}_k \, {}^{t}dS_k = \delta_t\hat{\overline{\mathbf{u}}}_k^{T} \int_{{}^{t}S_k} \overline{\mathbf{H}}_k^{S} \, {}^{t+\Delta t}_{t}\overline{\mathbf{f}}_k^{S} \, {}^{t}dS_k = \delta_t\hat{\mathbf{u}}_k^{T} \, {}_{t}\mathbf{T}_k^{T} \, {}^{t+\Delta t}_{t}\overline{\mathbf{R}}_k^{S} = \delta_t\hat{\mathbf{u}}_k^{T} \, {}^{t+\Delta t}_{t}\mathbf{R}_k^{S} \tag{3.29} $$

$$ \begin{aligned} \int_{{}^{t}V_k} {}_{t}\rho_k \, {}^{t+\Delta t}\ddot{\mathbf{u}}_k \, \delta_t\mathbf{u}_k \, {}^{t}dV_k &= \delta_t\hat{\overline{\mathbf{u}}}_k^{T} \int_{{}^{t}V_k} {}_{t}\rho_k \, \overline{\mathbf{H}}_k^{T} \, \overline{\mathbf{H}}_k \, {}^{t}dV_k \; {}^{t+\Delta t}\hat{\ddot{\overline{\mathbf{u}}}}_k \\ &= \delta_t\hat{\mathbf{u}}_k^{T} \, {}_{t}\mathbf{T}_k^{T} \, {}_{t}\overline{\mathbf{M}}_k \, {}_{t}\mathbf{T}_k \, {}^{t+\Delta t}\hat{\ddot{\mathbf{u}}}_k = \delta_t\hat{\mathbf{u}}_k^{T} \, {}_{t}\mathbf{M}_k \, {}^{t+\Delta t}\hat{\ddot{\mathbf{u}}}_k = \delta_t\hat{\mathbf{u}}_k^{T} \, \mathbf{M}_k \, {}^{t+\Delta t}\hat{\ddot{\mathbf{u}}}_k \end{aligned} \tag{3.30} $$

where ${}^{t}\mathbf{F}^{V}$ and ${}^{t}\mathbf{F}^{S}$ are the vectors of nodal contributions for the body and surface forces and ${}_{t}\mathbf{M}$ is the mass matrix. In the consequence of the mass preservation assumption, the mass matrix does not change and holds the identity ${}_{t}\mathbf{M} = {}_{t_0}\mathbf{M} = \mathbf{M}$ and therefore, this matrix does not need to be recalculated during the analysis.

3.3 DISCRETIZATION OF EQUATION OF VIRTUAL WORK

Using the equations derived in Chapter 3.2, the formula (3.1) can be rewritten into the following form:

$$\sum_{k}^{m} \delta_t \hat{\mathbf{u}}_k^T \, {}_t\mathbf{K}_{Lk} \, {}_t\hat{\mathbf{u}}_k + \sum_{k}^{m} \delta_t \hat{\mathbf{u}}_k^T \, {}_t\mathbf{K}_{NLk} \, {}_t\hat{\mathbf{u}}_k = \sum_{k}^{m} \delta_t \hat{\mathbf{u}}_k^T \left({}^{t+\Delta t}_{t}\mathbf{R}_k^V + {}^{t+\Delta t}_{t}\mathbf{R}_k^S \right) + \sum_{p}^{q} \delta_t \hat{\mathbf{u}}_p^T \left({}^{t+\Delta t}_{t}\mathbf{R}_p^N \right) - \sum_{k}^{m} \delta_t \hat{\mathbf{u}}_k^T \, {}^t\mathbf{F}_k \tag{3.31}$$

With the localization procedure, the elements contributions can be assembled into the form of global matrices and vectors

$$\delta_t \hat{\mathbf{u}}^T \, {}_t\mathbf{K}_L \, {}_t\hat{\mathbf{u}} + \delta_t \hat{\mathbf{u}}^T \, {}_t\mathbf{K}_{NL} \, {}_t\hat{\mathbf{u}} = \delta_t \hat{\mathbf{u}}^T \left({}^{t+\Delta t}_{t}\mathbf{R}^V + {}^{t+\Delta t}_{t}\mathbf{R}^S + {}^{t+\Delta t}_{t}\mathbf{R}^N \right) - \delta_t \hat{\mathbf{u}}^T \, {}^t\mathbf{F} \tag{3.32}$$

$$\delta_t \hat{\mathbf{u}}^T \, {}_t\mathbf{K}_L \, {}_t\hat{\mathbf{u}} + \delta_t \hat{\mathbf{u}}^T \, {}_t\mathbf{K}_{NL} \, {}_t\hat{\mathbf{u}} = \delta_t \hat{\mathbf{u}}^T \, {}^{t+\Delta t}_{t}\mathbf{R} - \delta_t \hat{\mathbf{u}}^T \, {}^t\mathbf{F} \tag{3.33}$$

As the consequence that the variation $\delta_t \hat{\mathbf{u}}^T$ can be arbitrary, the identity matrix is chosen and the equation above takes the form

$$\left({}_t\mathbf{K}_L + {}_t\mathbf{K}_{NL} \right) {}_t\hat{\mathbf{u}} = {}^{t+\Delta t}_{t}\mathbf{R} - {}^t\mathbf{F} \tag{3.34}$$

$${}_t\mathbf{K} \, {}_t\hat{\mathbf{u}} = {}^{t+\Delta t}_{t}\mathbf{R} - {}^t\mathbf{F} \tag{3.35}$$

For the case of dynamic analysis, the equation is extended of the inertia and the damping effect

$$\sum_{k}^{m} \mathbf{M}_k \, {}^{t+\Delta t}\ddot{\hat{\mathbf{u}}}_k = \mathbf{M} \, {}^{t+\Delta t}\ddot{\hat{\mathbf{u}}} \tag{3.36}$$

$$\sum_{k}^{m} {}_t\mathbf{C}_k \, {}^{t+\Delta t}\dot{\hat{\mathbf{u}}}_k = {}_t\mathbf{C} \, {}^{t+\Delta t}\dot{\hat{\mathbf{u}}} \tag{3.37}$$

In the following sections of this thesis, the global nodal deformations ${}_t\hat{\mathbf{u}}$ will be further written without the hat ${}_t\mathbf{u}$ as the subsequent chapters consider the case of discretized equations, so the distinction between the continuum and discretized deformations is not needed.

$${}_t\mathbf{K} \, {}_t\mathbf{u} = {}^{t+\Delta t}_{t}\mathbf{R} - {}^t\mathbf{F} \tag{3.38}$$

or

$$\mathbf{M} \, {}^{t+\Delta t}\ddot{\mathbf{u}} + {}_t\mathbf{C} \, {}^{t+\Delta t}\dot{\mathbf{u}} + {}_t\mathbf{K} \, {}_t\mathbf{u} = {}^{t+\Delta t}_{t}\mathbf{R} - {}^t\mathbf{F} \tag{3.39}$$

There are three basic requirements that has to be satisfied at the end of each load, or time, increment

- Equilibrium
- Compatibility (compatible mesh layout and satisfaction of the boundary conditions)
- Stress-strain low

3.4 SOLUTION OF NONLINEAR EQUILIBRIUM EQUATIONS IN STATIC ANALYSIS

To achieve the equilibrium solution in the nonlinear static analysis, the most crucial requirement is the zero 'right-hand side', thus the zero (in the context of the convergence criteria) unbalanced forces vector

$$\Delta\mathbf{R} = {}^{t+\Delta t}_{t}\mathbf{R} - {}^{t}\mathbf{F} \tag{3.40}$$

assuming the iterations in each load increment

$$\Delta\mathbf{R}^{(k-1)} = {}^{t+\Delta t}\mathbf{R}^{(k-1)} - {}^{t+\Delta t}\mathbf{F}^{(k-1)} \tag{3.41}$$

where t and Δt denote the load level and the increment respectively, k is the iteration counter and ${}^{t+\Delta t}\mathbf{R}^{(k-1)}$ is the vector of the applied deformation dependent loads (if no deformation dependent load is present, the vector takes the form ${}^{t+\Delta t}\mathbf{R}$, which does not change during the particular load level).

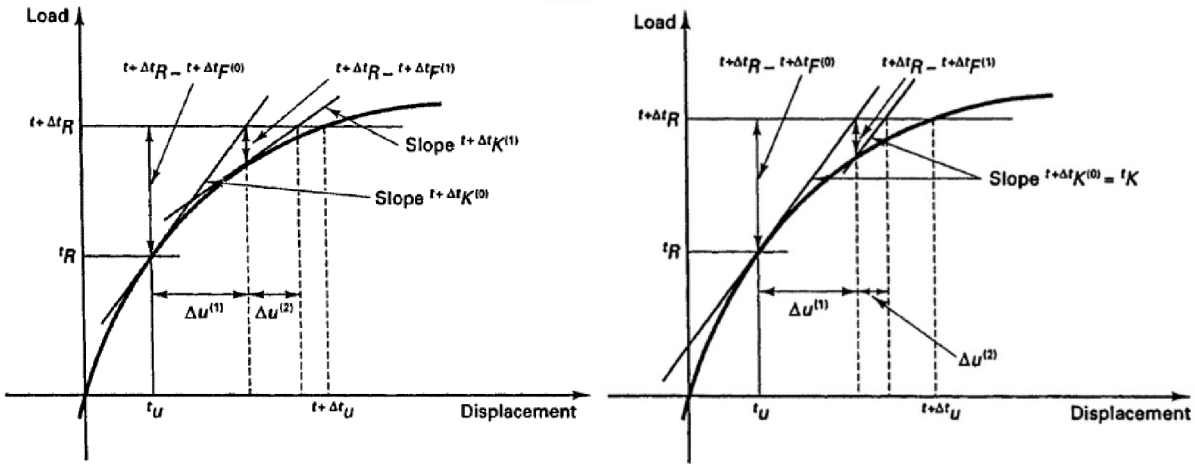

Fig. 10 Full Newton-Raphson Method and Modified Newton-Raphson Method [1]

For solution of the nonlinear equations in the static analysis (3.38), there are many iterative methods and the most common one is the Newton-Raphson iteration scheme and its modifications (Fig. 10).

$${}_{t+\Delta t}\mathbf{K}^{(k-1)}\,\Delta\mathbf{u}^{k} = \Delta\mathbf{R}^{(k-1)} \tag{3.42}$$

$${}_{\tau}\mathbf{K}\,\Delta\mathbf{u}^{k} = \Delta\mathbf{R}^{(k-1)} \tag{3.43}$$

$${}_{0}\mathbf{K}\,\Delta\mathbf{u}^{k} = \Delta\mathbf{R}^{(k-1)} \tag{3.44}$$

where $\Delta\mathbf{u}^{k}$ denotes the deformation increment in the iteration k. The converged deformation increment ${}_{t}\mathbf{u}$ of the time step $t + \Delta t$ and the total deformation of the structure are subsequently calculated

$${}_{t}\mathbf{u} = \sum_{i=1}^{k} \Delta\mathbf{u}^{i} \tag{3.45}$$

$$^{t+\Delta t}\mathbf{u} = {}^{t}\mathbf{u} + {}_{t}\mathbf{u} = {}^{t}\mathbf{u} + \sum_{i=1}^{k} \Delta \mathbf{u}^{i} \tag{3.46}$$

Note: Even though the modifications of the Newton-Raphson method are effective in many cases, the observations during the development proved the full Newton-Raphson method is suitable for tensile structures. The stiffness changes are considerable and it is not efficient to keep the fixed stiffness, and it even does not usually lead to the convergence

3.5 SOLUTION OF NONLINEAR EQUILIBRIUM EQUATIONS IN DYNAMIC ANALYSIS

For the solution of the dynamic response of tensile structures, the direct integration methods are assumed. The methods are divided into two main groups, namely **Implicit Methods** and **Explicit Methods**. In the group of the implicit methods, the Newmark method is broadly used, further the Houbolt method, Wilson method, Bathe method, etc. can be identified and used. In the group of the explicit methods, the Central difference method is well-known and usually used. In the following, the implicit Newmark method and the explicit Central difference method are described.

The main difference between these two methods is the time when the solution of the nonlinear equilibrium equations is considered. While the implicit methods are assuming the equilibrium in time $t + \Delta t$ to solve the deformation increment in the same time (3.39), the explicit methods are assuming the equilibrium in time t to solve the deformation increment in time $t + \Delta t$.

$$\mathbf{M}\, {}^{t+\Delta t}\ddot{\mathbf{u}} + {}_{t}\mathbf{C}\, {}^{t+\Delta t}\dot{\mathbf{u}} + {}_{t}\mathbf{K}\, {}_{t}\mathbf{u} = {}^{t+\Delta t}_{t}\mathbf{R} - {}^{t}\mathbf{F}$$

$$\mathbf{M}\, {}^{t}\ddot{\mathbf{u}} + {}_{t}\mathbf{C}\, {}^{t}\dot{\mathbf{u}} + {}^{t}\mathbf{F} = {}^{t}_{t}\mathbf{R} \tag{3.47}$$

Both well-known methods, one from each group, are briefly introduced bellow.

3.5.1 Newmark Method

This method uses the following formulas for the calculation of velocity and deformation in time $t + \Delta t$ [4].

$$^{t+\Delta t}\dot{\mathbf{u}} = {}^{t}\dot{\mathbf{u}} + [(1-\delta)\,{}^{t}\ddot{\mathbf{u}} + \delta\, {}^{t+\Delta t}\ddot{\mathbf{u}}]\,\Delta t \tag{3.48}$$

$$^{t+\Delta t}\mathbf{u} = {}^{t}\mathbf{u} + {}^{t}\dot{\mathbf{u}}\,\Delta t + \left[\left(\frac{1}{2} - \alpha\right){}^{t}\ddot{\mathbf{u}} + \alpha\, {}^{t+\Delta t}\ddot{\mathbf{u}}\right]\Delta t^{2} \tag{3.49}$$

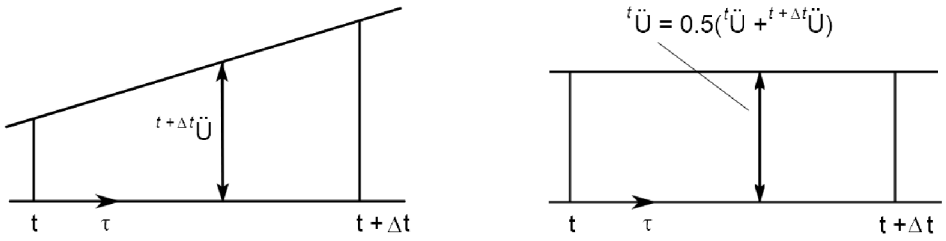

Fig. 11 Linear Acceleration (left) and Constant Average Acceleration (Trapezoidal Rule) Methods [1]

Different coefficients δ and α could be used. The linear acceleration method (Fig. 11) uses $\delta = 1/2$ and $\alpha = 1/6$, the constant average acceleration method (also known as the trapezoidal rule) uses the parameters $\delta = 1/2$ and $\alpha = 1/4$ and the formulas above are rewritten as

$$^{t+\Delta t}\mathbf{u} = {}^{t}\mathbf{u} + \frac{\Delta t}{2}({}^{t}\dot{\mathbf{u}} + {}^{t+\Delta t}\dot{\mathbf{u}}) \tag{3.50}$$

$$^{t+\Delta t}\dot{\mathbf{u}} = {}^{t}\dot{\mathbf{u}} + \frac{\Delta t}{2}({}^{t}\ddot{\mathbf{u}} + {}^{t+\Delta t}\ddot{\mathbf{u}}) = \frac{2}{\Delta t}({}^{t+\Delta t}\mathbf{u} - {}^{t}\mathbf{u}) - {}^{t}\dot{\mathbf{u}} \tag{3.51}$$

$$^{t+\Delta t}\ddot{\mathbf{u}} = \frac{4}{(\Delta t)^2}({}^{t+\Delta t}\mathbf{u} - {}^{t}\mathbf{u}) - \frac{4}{\Delta t}{}^{t}\dot{\mathbf{u}} - {}^{t}\ddot{\mathbf{u}} \tag{3.52}$$

Considering the iterations in every time increment as described in equations (3.45) and (3.46), the formulas are rewritten as

$$^{t+\Delta t}\dot{\mathbf{u}}^{(k)} = \frac{2}{\Delta t}\left({}^{t+\Delta t}\mathbf{u}^{(k-1)} + \Delta\mathbf{u}^{k} - {}^{t}\mathbf{u}\right) - {}^{t}\dot{\mathbf{u}} \tag{3.53}$$

$$^{t+\Delta t}\ddot{\mathbf{u}}^{(k)} = \frac{4}{(\Delta t)^2}\left({}^{t+\Delta t}\mathbf{u}^{(k-1)} + \Delta\mathbf{u}^{k} - {}^{t}\mathbf{u}\right) - \frac{4}{\Delta t}{}^{t}\dot{\mathbf{u}} - {}^{t}\ddot{\mathbf{u}} \tag{3.54}$$

Using these formulas, the equilibrium equation (3.39) is modified

$$\begin{aligned}\widetilde{\mathbf{K}}\,\Delta\mathbf{u}^{k} = {}^{t+\Delta t}\mathbf{R}^{(k-1)} - {}^{t+\Delta t}\mathbf{F}^{(k-1)} - \mathbf{M}\left(\frac{4}{(\Delta t)^2}\left({}^{t+\Delta t}\mathbf{u}^{(k-1)} - {}^{t}\mathbf{u}\right) - \frac{4}{\Delta t}\,{}^{t}\dot{\mathbf{u}} + {}^{t}\ddot{\mathbf{u}}\right)\\ + {}_{t+\Delta t}\mathbf{C}^{(k-1)}\left(\frac{2}{\Delta t}\left({}^{t+\Delta t}\mathbf{u}^{(k-1)} - {}^{t}\mathbf{u}\right) - {}^{t}\dot{\mathbf{u}}\right) = \Delta\widetilde{\mathbf{R}}^{(k-1)}\end{aligned} \tag{3.55}$$

$$\widetilde{\mathbf{K}}\,\Delta\mathbf{u}^{k} = \Delta\widetilde{\mathbf{R}}^{(k-1)} \tag{3.56}$$

As well as in the static analysis, the modified stiffness matrix $\widetilde{\mathbf{K}}$ in equations (3.55) and (3.56), enriched with the inertia and damping effects, can be solved by using different modifications of the Newton-Raphson method, analogically to formulas (3.42), (3.43) and (3.44). Therefore, the further formulas are possible ways of the nonlinear Newmark method solution (Full Newton-Raphson Method, Modified Newton-Raphson Method, Initial Stress Method)

$$\left(\frac{4}{\Delta t^2}\,\mathbf{M} + \frac{2}{\Delta t}\,{}_{t+\Delta t}\mathbf{C}^{(k-1)} + {}_{t+\Delta t}\mathbf{K}^{(k-1)}\right)\Delta\mathbf{u}^{k} = \Delta\widetilde{\mathbf{R}}^{(k-1)} \tag{3.57}$$

$$\left(\frac{4}{\Delta t^2}\,\mathbf{M} + \frac{2}{\Delta t}\,{}_{\tau}\mathbf{C} + {}_{\tau}\mathbf{K}\right)\Delta\mathbf{u}^{k} = \Delta\widetilde{\mathbf{R}}^{(k-1)} \tag{3.58}$$

$$\left(\frac{4}{\Delta t^2}\,\mathbf{M} + \frac{2}{\Delta t}\,{}_{0}\mathbf{C} + {}_{0}\mathbf{K}\right)\Delta\mathbf{u}^{k} = \Delta\widetilde{\mathbf{R}}^{(k-1)} \tag{3.59}$$

Note: As in the case of the nonlinear static analysis, the full Newton-Raphson iteration scheme is highly recommended when solving the nonlinear implicit dynamic of tensile structures.

3.5.2 Central Difference Method

Another possible integration scheme is the central difference method, as a method of the explicit integration group. The velocity and the acceleration in time t are described

$$ {}^{t}\dot{\mathbf{u}} = \frac{1}{2\Delta t}({}^{t+\Delta t}\mathbf{u} - {}^{t-\Delta t}\mathbf{u}) \tag{3.60} $$

$$ {}^{t}\ddot{\mathbf{u}} = \frac{1}{(\Delta t)^2}({}^{t+\Delta t}\mathbf{u} - 2{}^{t}\mathbf{u} + {}^{t-\Delta t}\mathbf{u}) \tag{3.61} $$

Using these formulas, the equation (3.47) takes the following form

$$ \left(\frac{1}{\Delta t^2}\mathbf{M} + \frac{1}{2\Delta t}\,{}_{t}\mathbf{C}\right){}^{t+\Delta t}\mathbf{u} = {}^{t}\mathbf{R} - {}^{t}\mathbf{F} + \frac{2}{(\Delta t)^2}\mathbf{M}\,{}^{t}\mathbf{u} - \left(\frac{1}{(\Delta t)^2}\mathbf{M} - \frac{1}{2\Delta t}\,{}_{t}\mathbf{C}\right){}^{t-\Delta t}\mathbf{u} = \Delta\widetilde{\mathbf{R}} \tag{3.62} $$

This method is effecient when using the diagonal mass $\mathbf{M}$ and the diagonal damping ${}_{t}\mathbf{C}$ matrixes, as every new nodal deformation can be solved independently

$$ {}^{t+\Delta t}\mathbf{u}_{i} = \left(\frac{1}{\frac{1}{(\Delta t)^2}\,m_{ii} + \frac{1}{2\Delta t}\,c_{ii}}\right)\Delta\widetilde{\mathbf{R}}_{i} \tag{3.63} $$

In contrary to the Newmark method, which is unconditionally stable, the central difference method is only conditionally stable. The condition to be satisfied is the time step Δt

$$ \Delta t \leq \Delta t_{cr} \tag{3.64} $$

This integration scheme can be used for both the nonlinear dynamic and also the static analysis, known as the Dynamic relaxation, where the mass and the damping factors are the artificial values chosen in such a way to obtain good convergence behaviour.

4 FORM FINDING

It was already mentioned in the introduction of this thesis that membrane structures belong to the group of structures, whose shapes cannot be chosen freely, as the shape is inherently connected to the equilibrium of forces within the given boundary conditions. For a civil engineer or an architect designing these structures, the equilibrium of the internal and external forces within the frame of the defined boundaries are the shaping parameters as well as the degree of freedom. The typical double curvature is the characteristic aesthetic appearance as well as the necessity of the structures to be satisfied, in connection with the internal forces, to reach the required load bearing capacity. Some of the basic shapes are displayed in the following figure (Fig. 12).

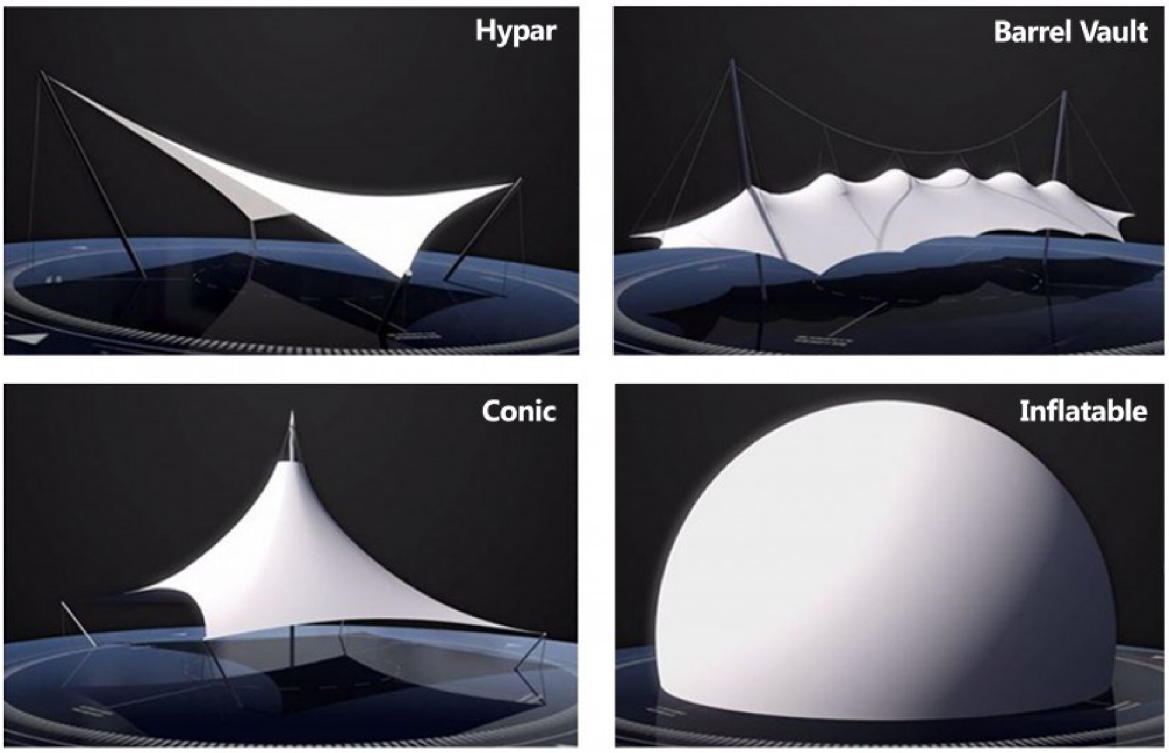

Fig. 12 Categorization of Membrane Structure Shapes [V]

In the past, physical models were used to find the appropriate shapes for membrane, cable, shell or combined structures. The hanging models used by Antoni Gaudí, hanging membranes by Heinz Isler [5], or the fascination with the shapes of isotropic stress field presented by the soap film analogy investigated by Frei Otto [6, 7, 8] were the ways of the shape designing by these and other brilliant brains until the advent of computer methods. The rapid development of the computer methods for the shape designing, called a form finding analysis, started in the 1970s and until now, many methods were proposed.

4.1 OVERVIEW OF EXISTING FORM FINDING METHODS

A number of methods have been proposed for the form finding procedure. Some of them assumed the process as a general nonlinear finite element analysis with the consideration of large deformations and the defined material, calculated by the implicit procedure, as could be

observed in the work by J. H. Argyris, T. Angelopoulos and B. Bichat [9], presented for 1D elements, or in the work by B. Tabarrok and Z. Qin [10], assumed for 1D and 2D elements.

Another possible way, the *Dynamic Relaxation (DR)*, was introduced by M. R. Barnes [11, 12], where the explicit solution procedure is used and the equilibrium is reached by using the artificial inertia and damping (the kinetic damping is particularly recommended).

The most extensive group of the methods for form finding is considered as a materially independent process, where the equilibrium of the predefined (or specially defined) forces, loads and boundaries is only assumed. The well-known *Force Density Method (FDM)* proposed by K. Linkwitz and H. J. Schek [13, 14] for 1D elements was the first of that group. This method was derived from the equilibrium equations of the nodes connected by cable elements, and the relation between the lengths and the forces of the cables was introduced and named as a force density. By this way, the method is distinguished by its linearity and the solving process is rapid. Assuming the updating the force density within iterations, the method can be extended to a nonlinear form. This method has inspired many other authors, who extended the idea of it, namely J. Sánchez, M. Á. Serna and P. Morer proposed the *Preliminary Form-Finding and Surface-Fitting Method (PFSM)* and the *Multi-Step Force Density Method and Surface-Fitting Approach (MFDS)* [15], R. M. O. Pauletti and P. M. Pimenta proposed the *Natural Force Density Method (NFDM)* [16], and B. Maurin and R. Motro proposed the *Surface Stress Density Method (SSDM)* [17]. A very general approach was derived by the authors R. B. Haber and J. F. Abel, who proposed the *Assumed Geometric Stiffness Method (AGSM)* and its nonlinear form *Iterative Smoothing Method (ISM)* [18, 19], which are consistently derived from the continuum mechanics basis (2.38), and these are really natural in the sense of the FEM software implementation. It can be proven that the *Force Density Method (FDM)* as well as the later contributions derived from this method are a special case of this generalized method *(AGSM* or *ISM)*. The work of the authors R. B. Haber and J. F. Abel was also an inspiration for the contribution of T. Nouri-Baranger, who proposed the *Stress Ratio Method (SRM)* [20] and stated that this method is a special case of *AGSM*. Also the authors K. U. Bletzinger and E. Ramm [21] followed the consistent derivation of the form finding method from the continuum mechanics basis and proposed the *Updated Reference Strategy (URS)* method, which can be understood as a possible extension of *(AGSM)* by the homotopy mapping for working with the known and searched configurations. When only assuming the reference configuration, the *URS* identifies itself with the *(AGSM resp. ISM)*. The author team around K. U. Bletzinger has published further investigations in [22, 23, 24, 25].

A very interesting and valuable contribution, dealing with summarizing, categorization and even comparing the existing methods for networks, was written by the authors D. Veenendaal and P. Block [26]. Here, three essential groups of the form finding methods are identified and consequently named as the *Stiffness Matrix Method (SM)*, *Geometric Stiffness Methods (GSM),* and *Dynamic Equilibrium Methods (DM)*. The categorization can be seen in the following figure (Fig. 13), overtaken from the mentioned work. In a generalized way, all the methods can be understood as different, or even special, solving procedures of the general continuum equilibrium equation.

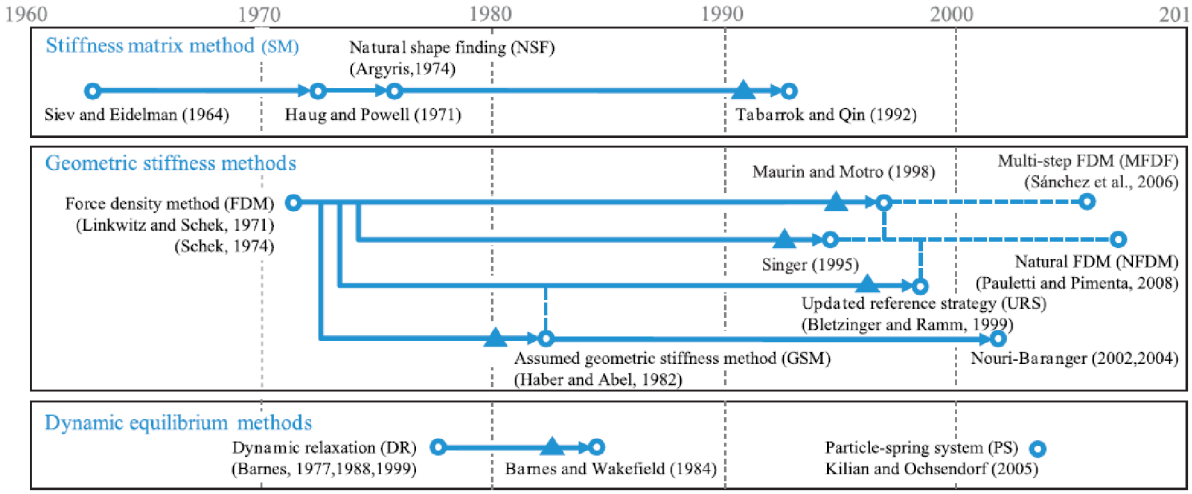

Fig. 13 'Development and categorization of form finding methods with key references Arrows denote descendence, dotted lines denote independent but related methods and triangles a first formulation using surface elements.' according to D. Veenendaal and P. Block [26].

In the following, three of the above-mentioned methods from the group of GSM, namely the FDM, AGSM with ISM and URS, will be described briefly.

4.1.1 Force Density Method (FDM)

The force density method, proposed by K. Linkwitz and H. J. Schek [13, 14] and published in 1971 or 1974, is derived from the equilibrium equations of the forces in net nodes, as can be seen in the figure (Fig. 14), overtaken from the contribution by the author team of L. Grüendig, E. Moncrieff., P. Singer and D. Ströbel [27].

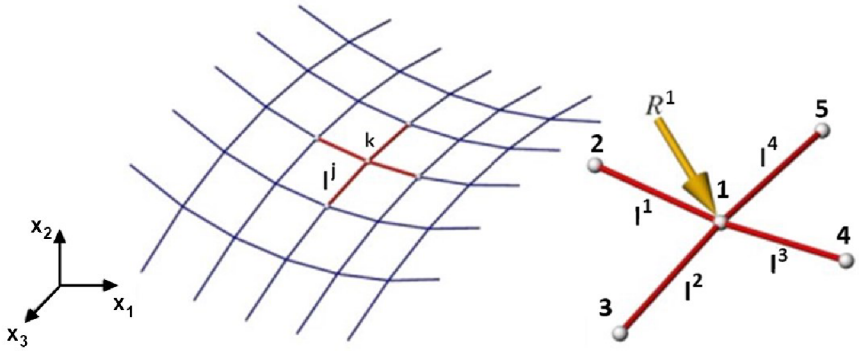

Fig. 14 Cable Structure (left) and Extracted Part of Cable Network (right), Modified Illustration from [27]

If a part of the net is extracted from the general network (Fig. 14), the equilibrium equations in the node $k = 1$ can be written as

$$\sum_{j}^{m} N^j \cos\left(l^j x_i\right) = R_i^k \tag{4.1}$$

$$N^1 \cos(l^1 x_i) + N^2 \cos(l^2 x_i) + N^3 \cos(l^3 x_i) + N^4 \cos(l^4 x_i) = R_i^1 \tag{4.2}$$

where j, m, k and i are the number of the particular element and the total elements amount, the node number and the Cartesian axis direction respectively, N^j and l^j are the normal force and the length of the element j, R_i^k is the external force acting on the node k in the i^{th} direction x_i

of the global Cartesian system, the term $cos(l^j x_i)$ is cosine of the angle between the cable j and the global axis x_i.

The equations can be rewritten into the following form:

$$\frac{N^1}{l^1}(x_i^2 - x_i^1) + \frac{N^2}{l^2}(x_i^3 - x_i^1) + \frac{N^3}{l^3}(x_i^4 - x_i^1) + \frac{N^4}{l^4}(x_i^5 - x_i^1) = R_i^1 \tag{4.3}$$

Since the lengths of the individual cables are dependent on the unknown nodal positions, the equilibrium equation is still nonlinear. Therefore, the authors of this method K. Linkwitz and H. J. Schek [13, 14] proposed a consequent linearization. The ratio of the internal force N^j in the cable and its length l^j is replaced by the quantity q^j, named *force density*, which also gave the name to this method.

$$\frac{N^j}{l^j} = q^j \tag{4.4}$$

Assuming this replacement for all the cables, the linearized form of the equilibrium can be rewritten and the unknown nodal position x_i^1 can be calculated

$$q^1(x_i^2 - x_i^1) + q^2(x_i^3 - x_i^1) + q^3(x_i^4 - x_i^1) + q^4(x_i^5 - x_i^1) = R_i^1 \tag{4.5}$$

The nodal equilibrium described above can be written in the general matrix form as described in [14] (by using a slightly different indexation). The general network (Fig. 14) consists of m cables (branches) and n nodes. The topology of the construction can be described by the branch-node matrix $\mathbf{C}$ [28, 29], which describes the connectivity of the individual nodes and cables. Each cable (branch) j defines two records c_{jk} on the line j of the matrix $\mathbf{C}$. The records for the start and end nodes take on the values $+1$ or -1 in the appropriate columns k, other positions of that row j are equal to zero.

$$c_{jk} = \begin{cases} +1 & k \in j_{start} \\ -1 & k \in j_{end} \\ 0 & \emptyset \end{cases} \tag{4.6}$$

Further, the vector of the nodal positions in the specific Cartesian axis direction is denoted $\mathbf{x}_i$, the diagonal matrix $\mathbf{Q}$ contains the force densities and the vector $\mathbf{R}_i$ is assembled from the external force contributions in the particular directions.

In the contribution of H. J. Schek [14], the division of the branch-node matrix $\mathbf{C}$ and the position vector $\mathbf{x}_i$ are assumed to separate the free (movable) $\tilde{\mathbf{x}}_i$ and the fixed $\bar{\mathbf{x}}_i$ nodal positions as well as the $\tilde{\mathbf{C}}$ and $\bar{\mathbf{C}}$ representing the columns assigned to the free and fixed nodes. The equilibrium equation can be written and further modified as follows:

$$\tilde{\mathbf{C}}^T\,\mathbf{Q}\,\tilde{\mathbf{C}}\,\tilde{\mathbf{x}}_i + \tilde{\mathbf{C}}^T\,\mathbf{Q}\,\bar{\mathbf{C}}\,\bar{\mathbf{x}}_i = \tilde{\mathbf{R}}_i \tag{4.7}$$

$$\tilde{\mathbf{D}}\,\tilde{\mathbf{x}}_i + \bar{\mathbf{D}}\,\bar{\mathbf{x}}_i = \tilde{\mathbf{R}}_i \tag{4.8}$$

$$\tilde{\mathbf{D}}\,\tilde{\mathbf{x}}_i = \tilde{\mathbf{R}}_i - \bar{\mathbf{D}}\,\bar{\mathbf{x}}_i \tag{4.9}$$

$$\tilde{\mathbf{x}}_i = \tilde{\mathbf{D}}^{-1}\left(\tilde{\mathbf{R}}_i - \bar{\mathbf{D}}\,\bar{\mathbf{x}}_i\right) \tag{4.10}$$

Formula (4.10) represents the linear equilibrium equation for solving new nodal positions of the general network. Since the assumption of the force density was prescribed, the resulting forces in the particular cables j of such obtained configuration are calculated as

$$N^j = l^j\, q^j \tag{4.11}$$

A very interesting behaviour of this method is, that the resulting shape is completely independent of the initial approximation of the shape, as the shape is purely defined by the predefined force densities $\mathbf{Q}$, topology description $\mathbf{C}$, external loads $\mathbf{R}_i$ and the specified boundary conditions.

By modifying the force densities after the solving procedure, the nonlinear form of Equation (4.10) can be obtained since the force density matrix $\mathbf{Q}(\mathbf{x})$ becomes nonlinear. Such an iterative form of the *force density method (FDM)* provides the possibility to influence the resulting forces, thus also the equilibrium shape, in order to avoid under-tensioned or over-tensioned areas. The force densities can be modified after the individual iterations according to the user-defined force requirements, as this physical quantity is easier to predefine for a civil engineer or an architect than the force density itself.

As this subchapter is focused on a brief introduction of the *FDM* method principles, the individual steps in deriving the equations are not presented. The insight into the formulation and derivation of the formulas mentioned above are described in the contributions by K. Linkwitz and H. J. Schek [13, 14].

4.1.2 Assumed Geometric Stiffness Method (AGSM) and Iterative Smoothing Method (ISM)

The *assumed geometric stiffness method (AGSM)*, as well as its nonlinear version *iterative smoothing method (ISM)*, was proposed by the authors R. B. Haber and J. F. Abel in 1982 [18, 19]. In the first of these contributions, the authors stated that *'the force density method provides and efficient linear solution to the initial equilibrium problem for cable structures composed of bar elements'*, and also *'this approach cannot be extended to cover curved cable elements or membrane behavior. A new method, based on assumed geometric stiffness matrices, will be developed in this section. The new method contains the force density method as a special case, and can be applied to any finite element structural model'*, as an evaluation of the previous method restrictions.

This method is consistently derived from the general equation of the virtual work (2.30) or (2.38), rewritten in the matrix notation

$$\int_{{}^tV} {}_t\mathbf{S}\,\delta_t\boldsymbol{\varepsilon}\,{}^t\mathrm{dV} + \int_{{}^tV} {}_t\mathbf{S}\,\delta_t\boldsymbol{\eta}\,{}^t\mathrm{dV} + \int_{{}^tV} {}^t\boldsymbol{\sigma}\,\delta_t\boldsymbol{\varepsilon}\,{}^t\mathrm{dV} + \int_{{}^tV} {}^t\boldsymbol{\sigma}\,\delta_t\boldsymbol{\eta}\,{}^t\mathrm{dV} = {}^{t+\Delta t}\boldsymbol{\mathcal{R}} \tag{4.12}$$

Considering the essential physical statement that the shape is defined by the equilibrium of forces and is therefore completely independent of the material, the first and the second term of Equation (2.38) can be cancelled, as they represent the internal forces increment, which is zero

when using the zero constitutive matrix ${}_t\mathbf{C}$. Furthermore, when assuming the given tensor of the Cauchy stress ${}^t\boldsymbol{\sigma}$, the third term is known and will be moved to the right hand side

$$\int_{{}^tV} {}^t\boldsymbol{\sigma}\, \delta_t\boldsymbol{\eta}\, {}^t\mathrm{dV} = {}^{t+\Delta t}\boldsymbol{\mathcal{R}} - \int_{{}^tV} {}^t\boldsymbol{\sigma}\, \delta_t\boldsymbol{\varepsilon}\, {}^t\mathrm{dV} \tag{4.13}$$

Even though this equation can be solved by the standard way described in Chapter *Finite Element Procedure*, the authors proposed the following procedure. The virtual work equilibrium is associated with the deformed configuration, which is obtained by collapsing all the nodes of the structure to the global origin of the Cartesian system. This deformation can be expressed by setting the vector of the displacements $\mathbf{u}$ equal to the negative vector of the nodal positions $-\mathbf{x}$.

As a consequence, the discretized equation does not have the usual meaning of the Updated Lagrangian procedure, where the vector of the nodal deformations $\Delta\mathbf{u}^k$ is obtained in each iteration, which defines the relation between the current and the new configuration. Instead, the vector of the nodal positions $\mathbf{x}^k$ is obtained.

$${}_{t+\Delta t}\mathbf{K}_{NL}^{(k-1)}\, \mathbf{x}^k = -\Delta\mathbf{R}^{(k-1)} \tag{4.14}$$

If a designer would specify directly the required geometric stiffness, the procedure of *AGSM* would be linear as well as the *FDM*, when the force density is predefined. However, this quantity is not natural to define from the user's point of view, so the stiffness matrix is derived from the required stress and thus the geometric stiffness matrix become a nonlinear function, therefore the method become nonlinear as well. In the contribution of the authors R. B. Haber and J. F. Abel [18], this procedure is named *Iterative Smoothing Method (ISM)*.

A similar separation of the equations as performed in *FDM* is proposed here, where the free nodal positions are indexed with the letter *A* and fixed with the letter *B*. The same applies to the residual forces. The stiffness matrix is also separated, where the submatrix $\mathbf{K}_{AA}$ belongs to the free nodes, $\mathbf{K}_{BB}$ belongs to the fixed nodes, and $\mathbf{K}_{AB}$ and $\mathbf{K}_{BA}$ represent the coupling of them. By performing the condensation procedure of the fixed node positions $\mathbf{x}_B$, which are known, the following equation can be further rewritten

$${}_{t+\Delta t}\begin{bmatrix}\mathbf{K}_{AA} & \mathbf{K}_{AB}\\ \mathbf{K}_{BA} & \mathbf{K}_{BB}\end{bmatrix}_{NL}^{(k-1)} \begin{Bmatrix}\mathbf{x}_A\\ \mathbf{x}_B\end{Bmatrix}^k = -\begin{Bmatrix}\Delta\mathbf{R}_A\\ \Delta\mathbf{R}_B\end{Bmatrix}^{(k-1)} \tag{4.15}$$

$${}_{t+\Delta t}[\mathbf{K}_{AA}]_{NL}^{(k-1)}\, \{\mathbf{x}_A\}^k = -\{\Delta\mathbf{R}_A\}^{(k-1)} - {}_{t+\Delta t}[\mathbf{K}_{AB}]_{NL}^{(k-1)}\, \{\mathbf{x}_B\}^k \tag{4.16}$$

$$\{\mathbf{x}_A\}^k = \left({}_{t+\Delta t}[\mathbf{K}_{AA}]_{NL}^{(k-1)}\right)^{-1} \left(-\{\Delta\mathbf{R}_A\}^{(k-1)} - {}_{t+\Delta t}[\mathbf{K}_{AB}]_{NL}^{(k-1)}\, \{\mathbf{x}_B\}^k\right) \tag{4.17}$$

It is possible to observe the similarity in the expressions (4.10) and (4.17). However, the method is general as Equation (4.17) is derived from the basis of the FEM analyses.

As already mentioned previously, the equation can be solved by the standard procedure of the Updated Lagrangian formulation without changing the physical meaning.

4.1.3 Updated Reference Strategy (URS)

The *updated reference strategy (URS)* was proposed by the authors K. U. Bletzinger and E. Ramm [21], followed by the further contributions of the author team around K. U. Bletzinger [22, 23, 24, 25]. As well as the previous method, the *URS* was also consistently derived from the continuum mechanics basis (2.38).

As already stated, the shape of the tensile structures is given by the equilibrium of forces in the space. Assuming that the stress field in the final configuration is known, the equation of the virtual work is written with respect to the unknown final position as follows:

$$\int_{t+\Delta t V} {}^{t+\Delta t}\boldsymbol{\sigma}\, \delta_{t+\Delta t}\mathbf{e}\, {}^{t+\Delta t}dV = {}^{t+\Delta t}\boldsymbol{\mathcal{R}} \tag{4.18}$$

Thus, the shape would only be unknown, not the internal stress state. However, this equation cannot be solved directly, since the singularity appears in the tangential direction of the unknown surface, as the floating of nodes in this tangential direction does not affect the spatial shape and thus even the equilibrium prescribed by this equation. This fact was presented in many contributions of the author team mentioned above and is demonstrated by the following figure (Fig. 15), overtaken from the contribution [22].

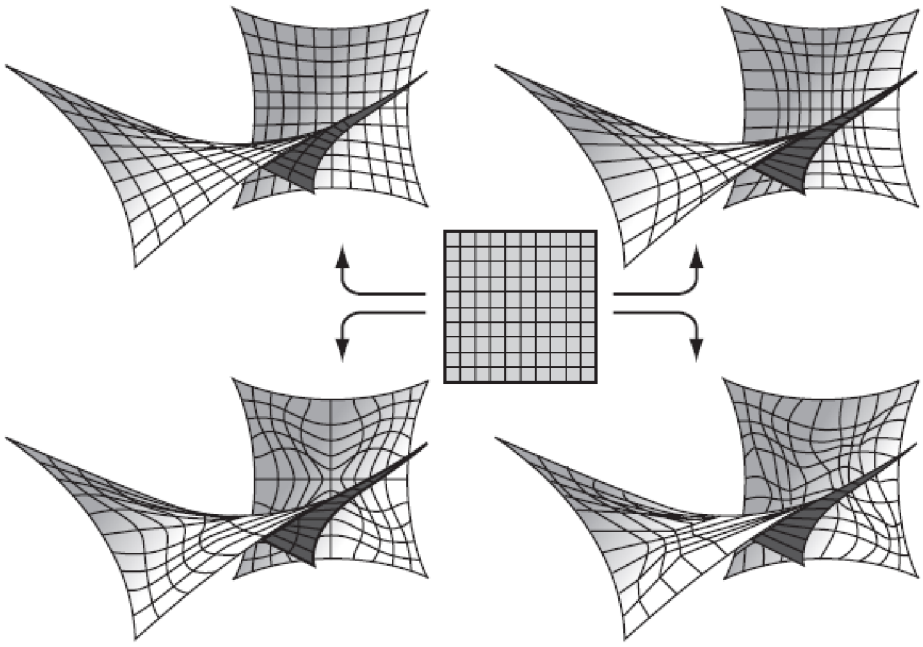

Fig. 15 Floating Mesh [22]

Equation (4.18) in context of the known reference configuration can be rewritten to obtain the consequent relation

$$\int_{tV} {}^{t+\Delta t}_{t}\mathbf{S}\, \delta_t\mathbf{E}\, {}^{t}dV = {}^{t+\Delta t}\boldsymbol{\mathcal{R}} \tag{4.19}$$

Since the physical meaning of the equation does not change, as the second Piola-Kirchhoff stress tensor is obtained by the pull-back operation, even the singularity will not disappear.

$$ {}^{t+\Delta t}_{t}\mathbf{S} = \det\left({}^{t+\Delta t}_{t}\mathbf{F}\right) {}^{t+\Delta t}_{t}\mathbf{F}^{-1}\ {}^{t+\Delta t}\boldsymbol{\sigma}\ {}^{t+\Delta t}_{t}\mathbf{F}^{-T} \tag{4.20} $$

$$ \int_{{}^{t}V} \det\left({}^{t+\Delta t}_{t}\mathbf{F}\right) {}^{t+\Delta t}_{t}\mathbf{F}^{-1}\ {}^{t+\Delta t}\boldsymbol{\sigma}\ {}^{t+\Delta t}_{t}\mathbf{F}^{-T}\ \delta_{t}\mathbf{E}\ {}^{t}\mathrm{dV} = {}^{t+\Delta t}\boldsymbol{\mathcal{R}} \tag{4.21} $$

Therefore, the regularization is proposed to solve this problem, which is based on the addition of the stabilization term, that is formulated as an integral with the known second Piola-Kirchhoff stress tensor ${}^{t}_{t}\mathbf{S}$ on the reference configuration. Thus, by using the Cauchy stress ${}^{t}\boldsymbol{\sigma} = {}^{t}_{t}\mathbf{S}$, since the second Piola-Kirchhoff stress in time t is related to the configuration in the same time t. The weighting factor λ is used to relate these two definitions of the internal work

$$ \lambda \int_{{}^{t}V} \det\left({}^{t+\Delta t}_{t}\mathbf{F}\right) {}^{t+\Delta t}_{t}\mathbf{F}^{-1}\ {}^{t+\Delta t}\boldsymbol{\sigma}\ {}^{t+\Delta t}_{t}\mathbf{F}^{-T}\ \delta_{t}\mathbf{E}\ {}^{t}\mathrm{dV} + (1-\lambda) \int_{{}^{t}V} {}^{t}\boldsymbol{\sigma}\ \delta_{t}\mathbf{E}\ {}^{t}\mathrm{dV} = {}^{t+\Delta t}\boldsymbol{\mathcal{R}} \tag{4.22} $$

The factor λ forms a relationship between the prescription of the user-required stress (Cauchy stress) in the known and unknown configurations. If the homotopy factor $\lambda > 0$, Equation (4.22) is nonlinear and requires the internal iterative loops in each iteration of the FEA.

If the homotopy factor $\lambda = 0$, the method is linear in each FEA iteration and principally coincides with the *AGSM* method described above, even though it differs in the solution procedure itself.

$$ \int_{{}^{t}V} {}^{t}\boldsymbol{\sigma}\ \delta_{t}\mathbf{E}\ {}^{t}\mathrm{dV} = {}^{t+\Delta t}\boldsymbol{\mathcal{R}} \tag{4.23} $$

$$ \int_{{}^{t}V} {}^{t}\boldsymbol{\sigma}\ \delta_{t}\boldsymbol{\eta}\ {}^{t}\mathrm{dV} = {}^{t+\Delta t}\boldsymbol{\mathcal{R}} - \int_{{}^{t}V} {}^{t}\boldsymbol{\sigma}\ \delta_{t}\boldsymbol{\varepsilon}\ {}^{t}\mathrm{dV} \tag{4.24} $$

As the prescription of the user-required prestress $\boldsymbol{\sigma}$ causes the deformations towards the equilibrium position, the Cauchy stress prescribed in the known configuration by such a defined value ${}^{t}\boldsymbol{\sigma} = \boldsymbol{\sigma}$ in time t can be expressed as the second Piola-Kirchhoff stress tensor ${}_{t+\Delta t}{}^{t}\mathbf{S}$ in the newly calculated configuration. These vectors differ numerically in their magnitudes ${}^{t}\boldsymbol{\sigma} \neq {}_{t+\Delta t}{}^{t}\mathbf{S}$ until the equilibrium is reached. As soon as the structure reaches the equilibrium position, the deformation gradient identifies itself with the identity matrix and the relation of the vectors remains ${}_{t+\Delta t}{}^{t}\mathbf{S} = {}^{t}\boldsymbol{\sigma} = \boldsymbol{\sigma}$. Thus, the shape for the predefined stress distribution $\boldsymbol{\sigma}$ is finally obtained.

4.1.4 Hybrid Methods

Three methods of the GSM group were described and the procedures of SM and DM could also be described. However, it is not necessary to only restrict the form finding for one method, as the obvious overlapping could be seen when the methods of the different groups are consistently derived from the general equation of the virtual work. As the physical basis is the same, specifically reaching the equilibrium shape, the appropriate hybrid method can be developed. Such a statement can be found in the contribution by D. Veenendaal and P. Block [26], which states: *'By examining the relation between methods and how they solve the initial equilibrium*

problem, it may occur to the reader where new possibilities lie for future development of new approaches. The framework allows hybrid solutions combining strengths of existing methods.'

4.2 SEARCHING FOR EQUILIBRIUM PRESTRESS

In the text above, form finding was considered as searching for a shape when the equilibrium prestress is explicitly known and thus given. However, this is generally not a true, except the isotropic prestress. The constant orthotropic prestress cannot exist in the surface with double curvature, so the general anisotropic stress field has to be reached if the isotropic prestress does not satisfy the engineering or architectural requirements for the given tensile structure. Such a user entry is not realistic and therefore, the constant values in the orthogonal directions, called warp and weft, are the usual software entries.

The authors J. Linhard, K. U. Bletzinger [22] stated that *'...it is not possible to generate a doubly curved surface with constant anisotropic prestress distribution, but if the prestress is allowed to vary around its mean value, many interesting and physically stable shapes can be generated',* and also the authors R. B. Haber and J. F. Abel [18] presented a really general statement: *'The problem of finding a reference configuration that satisfies the laws of equilibrium has been termed form finding or shape finding by some. This nomenclature does not adequately describe methods in which variables besides the shape are adjusted to satisfy equilibrium. For this reason, the selection of an appropriate reference configuration will be referred to here as the initial equilibrium problem'*. Indeed, the **initial equilibrium problem** solving is much more suitable description of this process, and besides the shape, the calculation also comprises finding of the equilibrium of forces itself.

If the constant anisotropic stress field would be *prescribed* and *enforced* during consequent iterations, all the methods would diverge, which is represented by sliding the nodes to some regions and thus by collapsing of the mesh. In fact, it does not matter which specific method of the groups described above [recall: *Stiffness Matrix Method (SM)*, *Geometric Stiffness Methods (GSM),* and *Dynamic Equilibrium Methods (DM)*] is used if the prescribed values are strictly required.

There are many possible ways for stabilization techniques [22, 26, 31, 38], which are briefly described below.

4.2.1 Specifying Number of Form Finding Steps

A natural solution is to allow the user to influence the number of form finding steps. Although this is the simplest way, it is very powerful stabilization technique, which allows a user to trace the shaping process. However, this method is more a safety break than an advanced tool, and it is more comfortable for a civil engineer or an architect to avoid this, if possible.

4.2.2 Elastic Control

This way is an essential part of the *stiffness methods (SM)* [9, 10], and usable in the *dynamic equilibrium methods (DM)* as well [12]. If the constitutive relation is left within the form finding loops, it can be used in two different ways. Let's call them *natural* and *controlling*.

The first one, the *natural* way, assumes that the constitutive law has a direct impact on the resulting stress field, that is, the element elongation and shortening cause increasing and decreasing of the resulting stress in comparison with the prescribed stress. This constitutive law is artificial and usually very small, and turns the form finding process into the standard FEA. However, with increasing the stiffness, the resulting shape is increasingly dependent on the initial model position and some regions could be understressed or overstressed. This is a drawback of this stabilization technique.

The second method, called a *controlling* way here, uses the constitutive law as a brake of the unwanted diverging of the model described above. The material stiffness does not influence the prestress during the form finding steps here, nevertheless the incorporation of this term slows down the in-plane sliding of FE nodes. It also decreases the speed of the whole form finding process, but still the method has a considerable influence on keeping a good mesh quality for a long time. Though the method helps to avoid fast sliding of the in-plane mesh nodes, it does not lead to the equilibrium prestress in fact, since the prestress is not influenced here, and without changing the forces, this method would also lead to the unwanted mesh distortions though it is slower than without this elastic control. Therefore, if the deformations in the normal direction become minor in comparison to the tangential direction, the shaping process should be replaced by the equilibrium finding process, which closely approximates the required unrealizable prestress values by the equilibrium values. This can be done by taking into account the force changes caused by the artificial material.

The elastic control method is a powerful tool for the form finding process. The first way is easier to implement, but it leads to worse results in general. The second way is sensitive in terms of the algorithm tuning for appropriate switching, but leads to better results in general.

4.2.3 Element Size Control

Another possibility for stabilization, when non-equilibrium prestress is prescribed, can be the element size control, as proposed for example in the following contributions [22, 25, 26, 38]. This method can be used in the way, that the predefined forces stops to be enforced when a particular element reaches the limit deformation. The last reached stress in the actual configuration for the *geometric stiffness methods (GSM)* (the Cauchy stress calculated from the second Piola-Kirchhoff stress defined in the last reference configuration before the limit deformation was reached) can be used for further iterations, or the forces caused by the artificial material can be encountered for the *stiffness matrix methods (SM)* or the *dynamic equilibrium methods (DM)* when the limit deformation is reached, for example.

This method is also a strong way of avoiding the divergence in the form finding analysis, even so a disadvantage can be seen in the fact, that the nonphysical prestress starts to be influenced up to the moment when the limit distortion is reached. Up to this point, the tangential movement, or sliding of nodes, is not influenced.

4.2.4 Other Methods

There could be found other proposals for solving the problems described above. For example, inserting *control strings* [26], or inserting an *artificial damping* when the *dynamic equilibrium*

method (DM) is used [31], or by incorporation of the *constrained problems* [14, 32, 33, 34, 35, 36].

4.2.5 Projection Method

A possible way for searching the equilibrium can be seen in defining the general anisotropic prestress by a realizable manner, specifically by defining the equilibrium in the configuration, where it is possible to do it analytically and use this for the projection into the spatial configuration. This is a really general method, which leads to the definition of the spatial equilibrium indirectly, but uniquely and without using the safety brakes.

Even though this was not the only stabilization technique implemented in the form finding algorithms of the above-mentioned FEA solver during the development work (there were three stabilization methods used as described later), the detailed investigation and development works were performed to formulate and implement this tool. Therefore, the next chapter will be focused on the description of this particular stabilization method, before introducing the chapter of the whole form finding implementation description.

4.3 PROJECTION METHOD

A proposal of this special stabilization technique, which defines the spatial equilibrium in the implicit manner, is based on determining the equilibrium in an arbitrarily oriented plane. Thus, the analytically defined planar equilibrium is further projected into finite elements in their spatial configuration. Therefore, the integral of the particular FE force components parallel to such a plane has to be equal to the integral of forces in the fictitious FE, which is obtained by the projection of the real element into the defined projection plane with the analytically prescribed equilibrium prestress

$$\int_{{}^{t}V} {}^{t}\boldsymbol{\sigma}_{||}\, {}^{t}\mathrm{dV} = \int_{{}^{t}P} {}^{t}_{p}\mathbf{S}\, {}^{t}\mathrm{dP} \tag{4.25}$$

where ${}^{t}P$ is the surface obtained by the projection of the structure into the specified plane in time t and ${}^{t}_{p}\mathbf{S}$ is the analytically predefined second Piola-Kirchhoff stress of the assumed FE in such an artificial reference configuration. The overall predefined stress field ${}_{p}\mathbf{S}$ does not change during the form finding analysis, so it represents an equilibrium stress in an infinite projection plane in fact, but the position of the assumed FE projection to such a plane changes its position and since this field ${}_{p}\mathbf{S}$ could be generally anisotropic, the used FE prestress ${}^{t}_{p}\mathbf{S}$ depends on its actual projected position into ${}^{t}P$. ${}^{t}\boldsymbol{\sigma}_{||}$represents stress components of the given FE in its actual position, which are parallel to the defined projection plane ${}^{t}P$. From knowing the stress ${}^{t}\boldsymbol{\sigma}_{||}$, the actual membrane stress ${}^{t}\boldsymbol{\sigma}$ for each FE can be derived directly (Fig. 16).

The process could also be described by using an artificial deformation gradient ${}^{t}_{p}\mathbf{F}$. This tensor describes a virtual deformation, which would be performed to move the fictitious FE, obtained by the projection of the real FE into the projection plane, back to the real FE position in the particular iteration. As this tensor ${}^{t}_{p}\mathbf{F}$ is known for the actual configuration of the current iteration, as well as the prestress ${}^{t}_{p}\mathbf{S}$ in such a reference configuration is known, the real

prestress ${}^{t}\boldsymbol{\sigma}$ in the actual FE configuration can be obtained by the stress transformation formula (2.19)

$$ {}^{t}\boldsymbol{\sigma} = \frac{{}^{t}\rho}{{}_{p}\rho}\, {}_{p}^{t}\mathbf{F}\, {}_{p}^{t}\mathbf{S}\, {}_{p}^{t}\mathbf{F}^{T} = \frac{1}{\det\left({}_{p}^{t}\mathbf{F}\right)}\, {}_{p}^{t}\mathbf{F}\, {}_{p}^{t}\mathbf{S}\, {}_{p}^{t}\mathbf{F}^{T} \tag{4.26} $$

Using this implicit manner of the spatial equilibrium prestress definition, the input values for the general formulas are defined

$$ \int_{{}^{t}V} {}^{t}\boldsymbol{\sigma}\, \delta_{t}\boldsymbol{\eta}\, {}^{t}dV = {}^{t+\Delta t}\boldsymbol{\mathcal{R}} - \int_{{}^{t}V} {}^{t}\boldsymbol{\sigma}\, \delta_{t}\boldsymbol{\varepsilon}\, {}^{t}dV \tag{4.27} $$

This leads to the unique solution, which is independent of the initial shape configuration. This is a great advantage of this *projection method* stabilization technique, as such a behaviour is usually considered as valid for the isotropic prestress only, because if the unrealizable prestress is prescribed (for example, constant orthotropic pretension in the space), the resulting prestress values are affected by the used stabilization techniques and does not have its unique solution.

The isotropic (Fig. 37), the constant orthotropic, or even the general anisotropic radial prestress in equilibrium (Fig. 45) can be formulated analytically for the arbitrarily oriented projection plane. This method is especially suitable for the conical shapes, where it leads to smoothly changing prestress between the base and the top of the cone, as presented in the example *4.6.4 Projection Method*.

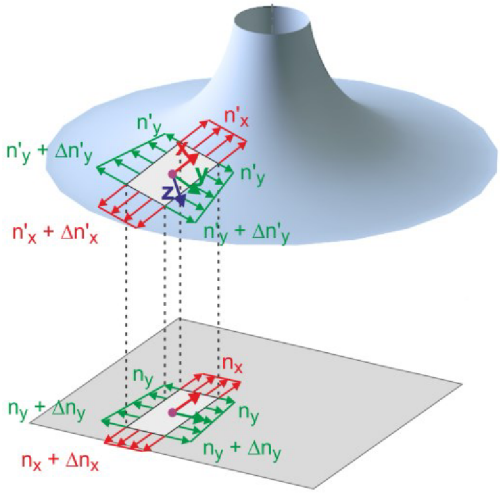

Fig. 16 Prestress Defined in Projection Plane and Prestress in Membrane Structure

4.4 PUSHING METHOD FOR COMPRESSION REQUIREMENTS IN FORM FINDING PROCESS

During the research and the development works of the form finding process of membrane structures, including shaping the cables and gas chambers as well, the shape optimization of the conventional structures was also additionally investigated. Since for both the arches and the shells, the load bearing capacity is increased when the in-plane resistance is preferred form the bending resistance.

A physically new phenomenon has to be dealt with here, as in the contrast to the tensile definitions, which could be considered as a stable equilibrium state finding, the unstable equilibrium searching is the case when the compression requirements are prescribed. Since the tensile forces try to reach the stable equilibrium from the arbitrary unequilibrium position, as illustrated in the left part of the figure below, the compression forces try to diverge far away from the given unequilibrium position, as illustrated by the right part of the figure below (Fig. 17).

In this case, the stabilization procedure has to be used to ensure reaching the required equilibrium. Already from the ancient times, the mirroring of the shapes under tension was used to obtain the shapes under compression. Thus, the procedure of replacing the negative forces by tensile forces and inverting the load could be the way for the structures loaded exclusively by the compressive normal forces, since it is the analogical process to the mirrored physical models used in the past.

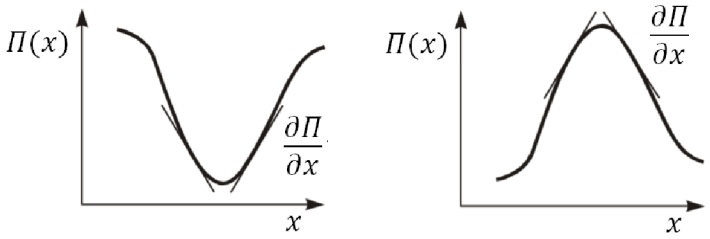

Fig. 17 Stable and Unstable Equilibrium Position

Such a simple procedure has one considerable disadvantage, specifically the cases when the mixed requirements are used, where the tension is defined for membranes and the compression for supporting arches, for example. Inverting the whole task would change the compression requirement for the arches into tension, however, the tension in membranes would be inverted into compression. So, the same problem stays here.

Therefore, the proposed stabilization, called here as a *pushing method,* tries to push up the structure to the maximum energy position, which is represented by the top position in the right part of the figure above (Fig. 17). The process consists physically of two artificial modifications during assembling the equilibrium equations, described in *3.3 Discretization of Equation of Virtual Work* and *3.4 Solution of Nonlinear Equilibrium Equations in Static Analysis*. The first modification inserts an artificial geometric stiffness into the elements with the compression requirement, for which the zero bending stiffness is assumed in this proposal during the form finding process itself. The geometrical stiffness derived from the absolute value of the internal normal force was considered in the algorithms used. The second, more sensitive and important modification, deals with inverting the unbalanced forces in the appropriate FE nodes, where the unstable equilibrium is expected [106].

$$\Delta \mathbf{R} = {}^{t+\Delta t}_{t}\mathbf{R} - {}^{t}\mathbf{F} \tag{4.28}$$

$$\Delta \mathbf{R}_i = \begin{cases} \Delta \mathbf{R}_i = -\Delta \mathbf{R}_i & i \in U \\ \Delta \mathbf{R}_i & i \in S \end{cases} \tag{4.29}$$

where i is the number of particular FE node, U and S are the groups of nodes, where the unstable and stable equilibrium is expected.

It is crucial to do this inversion as postprocessing after the standard assemblage process of the unbalanced forces is ready, since it is necessary to preserve the magnitude, but change the direction. Finally, the decision of the group membership for the individual nodes is quite a sensitive task. In this proposal, it is suggested that this is performed according to the hierarchy algorithm. This algorithm is assigning the nodes into groups according to the assumed role of the structural part in the structure and its form finding requirement. For example, the algorithm assumes that a beam is the supporting object for shells or membranes, so if all mentioned structural objects meet in one FE node, the assignment is done according to the beam object form finding requirement. Further, the geometrical requirements are superior to the force requirements, etc.

During the development, more different methods were proposed and investigated. For example, the methods dealing with the actual force or the energy changes were less reliable, since they were quite sensitive on the shape changes of the other structural parts. Since the initial model position in the form finding analysis could be really far from the equilibrium one, these algorithms had quite a problem to find the 'right way'.

The examples presenting the results reached by using the proposed *pushing method* stabilization technique are presented below 4.6.6 and 4.6.7, where the second example exhibits one more interesting phenomenon, namely a possible existence of nonunique equilibrium positions, when the mixed requirement is prescribed.

4.5 IMPLEMENTED FORM FINDING METHODS

Note: Based on the research work during the doctoral study, focused on the investigation of numerical methods, the form finding process and the algorithmization procedures of the consequent development was performed in the FEA core by the FEM consulting company [IV], which is used in the RFEM software by the Dlubal Software company[III].

Two form finding methods were implemented in the mentioned solver, the first one used as a *default* procedure, considering all the structural parts, the second one used as a *preliminary* form finding, considering only the structural parts with the definition of the required forces.

4.5.1 Preliminary Form Finding

To implement the *preliminary form finding,* the *GSM* group was chosen, specifically the *AGSM* with *ISM*. As the subchapter name declares, this method was intended for a fast shaping of the structural parts with the form finding force requirements. Other structural parts are ignored and this allows to minimize the number of equations for a rapid shaping procedure.

This tool can be used separately in the RFEM software environment for the topology shaping and thus the visualization of the shape when changing the forces or boundary condition. Also, the *preliminary* method can be used in the interaction with the *default form finding*, which is general and takes into account the entire structure defined.

For stabilizing the non-equilibrium prestress definition, the *preliminary form finding* uses three possible stabilizations: first, the simple influencing of step numbers by a user, further the calculation interruption based on the deformation monitoring algorithm, and also a possible usage of the projection method.

4.5.2 Default Form Finding

The *default form finding* can be classified as a *hybrid method*, which balances between the *GSM* and *SM* groups according the user setting of the *speed of convergence* in the *Calculation Parameters/Form-Finding* dialog box of the RFEM software.

The development was inspired by the above-described methods URS without the internal loops (4.24) and AGSM with ISM solved by the Newton-Raphson algorithms instead of the above-written (4.17) procedure (that both physically overlaps in this specification are materially independent and consistently derived from the equation of the virtual work), and their physical meaning is dominant when a high *speed of convergence* is set by a software user. Therefore, with this setting, the implemented hybrid form finding moves towards the GSM group.

The SM group was also an inspiration, in the modified form, as the incorporation of the artificial material (internally driven by the algorithms based on the decreasing parameter of the *speed of convergence*) has a considerable advantage. Usually, the SM methods are implemented with the *natural* way of the *elastic control* (4.2.2), which makes the resulting shape dependent on the initial model position [9]. Since this was not intended, the *controlling* way was implemented into the FEA core with further tuning, since the equilibrium has to be finally reached, even if the unphysical prestress has been defined. The mentioned advantage lies in a more natural and stable enforcing of geometrical requirements given by a civil engineer or an architect. This behaviour starts to be predominant when specifying a low *speed of convergence*. Although the calculation needs more iterations, the process is thus more robust.

For stabilizing the non-equilibrium prestress definition, the *default form finding* uses the *controlling* way of the *elastic control,* whose influence is dependent on the *speed of convergence* setting, the deformation monitoring and the equilibrium finding when deformations normal to the plane starts to be minor in comparison with the tangential deformations and the possible usage of the projection method can be included as well. Of course, the setting of a number of the form finding steps can also be influenced.

The *default form finding* is fully incorporated into the general FEA solver (this is the great difference compared with the *preliminary form finding*) and considers the structure supporting the membranes, cables, gas chambers, etc., which are subjected to the form finding. Thus, the supporting structure, with arbitrary geometry, nonlinearities, etc., is taken into account.

4.6 EXAMPLES

In the following, there are some examples of form finding analyses presented in context with the particular phenomena, either physical or implementation nature. First, different phenomena are shown on rather simple structure for a clear presentation of the intended issues, and later, more complex structures are shown to also present the abilities of the implemented algorithms.

4.6.1 Catenoid Benchmark

The first example deals with a catenoid surface, which arise by rotation of the catenary curve about an axis. As it is a minimal surface, the isotropy prestress defines such a shape as well.

This example was chosen as the analytical solution is known and thus it serves as a benchmark. Moreover, the convergence speed can be also presented here for the *GSM (preliminary) form finding* and the *hybrid (default) form finding* with different settings. More verification examples can be found on the website [VIII].

The analytical surface of the catenoid in the three dimensional Cartesian coordinate system can be describe by the following equations:

$$x = a\ cosh\left(\frac{z}{a}\right)\ cos(v) \tag{4.30}$$

$$y = a\ cosh\left(\frac{z}{a}\right)\ sin(v) \tag{4.31}$$

where x, y, z are the positions in the Cartesian coordinate system, $v \in (-\pi, \pi)$ is the angle of rotation about z axis, and a is the constant to be determined. Assuming the rotation symmetry of the Catenoid surface, the relation can be expressed in the x coordinate axis only

$$x = a\ cosh\left(\frac{z}{a}\right) \tag{4.32}$$

The surface, described by the equations above, can exist if the ratio of the height h to the radius of the base r fulfill this requirement $h < 1.32548\,r$. Behind this ratio, the surface collapses [37]. In this example, the following values are chosen: $r = 1.00\ m$, $h = 1.20\ m$. Knowing the solution in $z_{max} = h/2$

$$r = a\ cosh\left(\frac{h}{2a}\right) \tag{4.33}$$

The value of $a = 0.461689\ m$ is solved numerically. If the initial shape of the analysed structure is a cylinder (Fig. 18), the maximal deformation from the cover in the middle of the height is $u_{analytical} = r - a = 1.00 - 0.745071 = 0.254929\ m$.

The equilibrium shape for the isotropic prestress $n_x = n_y = 1.00\ kN/m$ was calculated with both implemented methods, the *GSM preliminary form finding* and the *HM default form finding*, where three different *speed of convergence* were used (Fig. 20). The maximum deformation in the middle of the catenoid height has the value $u = 254.484\ mm$ (Fig. 19) and the difference with the analytical solution is $error = 0.18\%$, using the standard precision setting and the presented FE mesh (1536 triangle FE, 832 nodes). When refining the FE mesh, the error converges to zero.

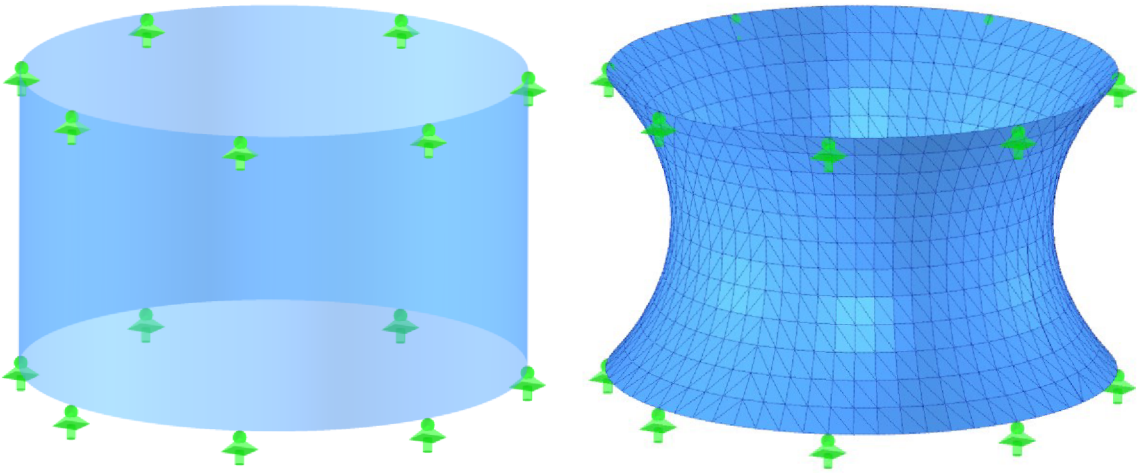

Fig. 18 Model in Initial Position (left), FE Mesh in Equilibrium Shape (right)

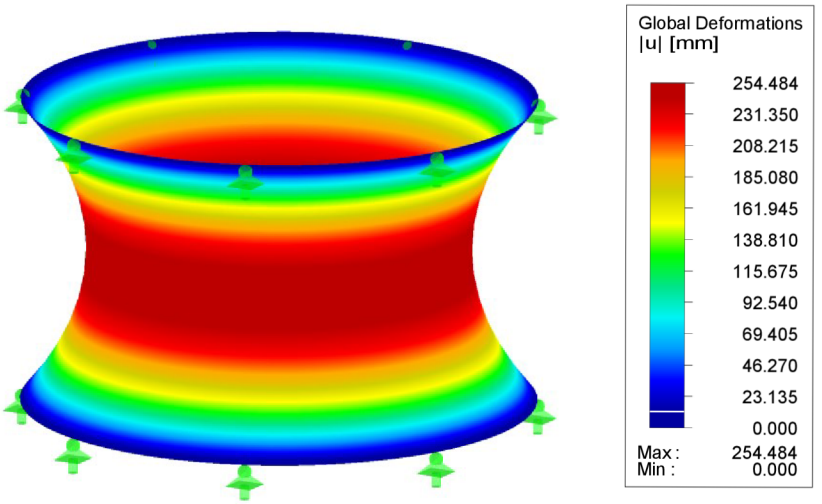

Fig. 19 Deformation in Form Finding Analysis (right)

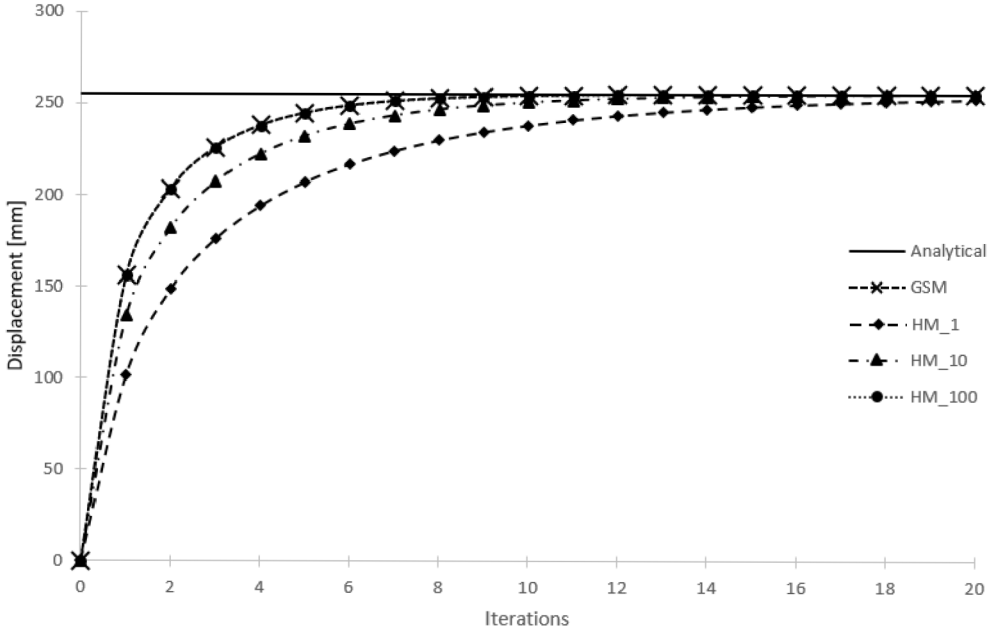

Fig. 20 Convergence Behaviour of GSM and HM Form Finding

4.6.2 Independence of Equilibrium Shape on Initial Model Position

As mentioned above, the resulting shape is dependent exclusively on the predefined equilibrium of forces and the given boundary conditions. This fact is presented in the next example of a hypar shaped membrane (Fig. 12), where two different initial configurations were chosen (Fig. 21). The isotropy prestress of the membrane is $n_x = n_y = 1.00\,kN/m$ and the tension in the cables is $N = 10.00\,kN$. Since different deformations are required for reaching the equilibrium, it does not make sense to compare them. Instead, the final geometry is compared directly (Fig. 22), which proves the identity resulting positions. Again, the convergence behaviour is presented in also (Fig. 23).

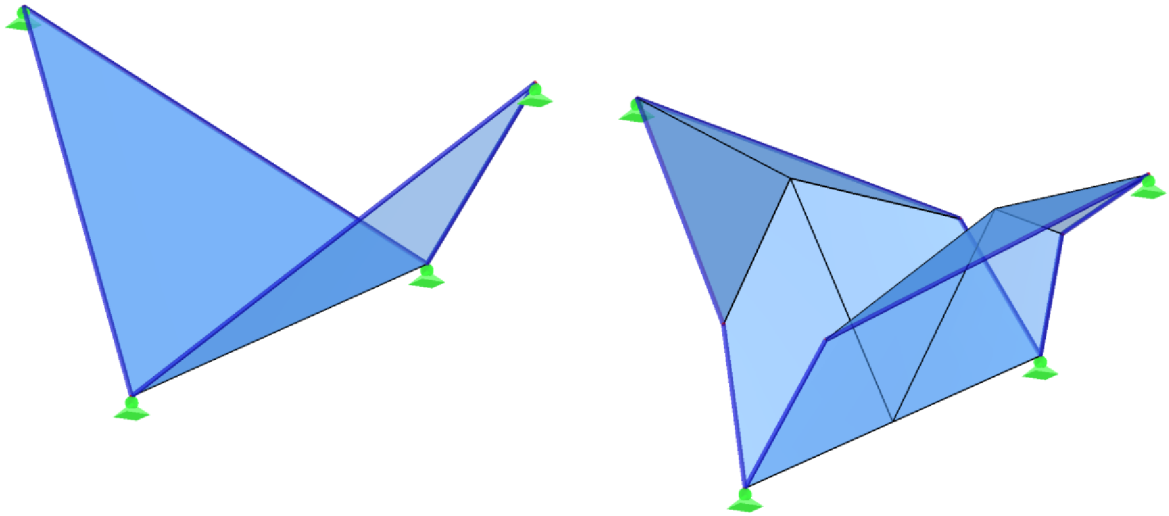

Fig. 21 Initial Geometry of Two Hypar Membranes

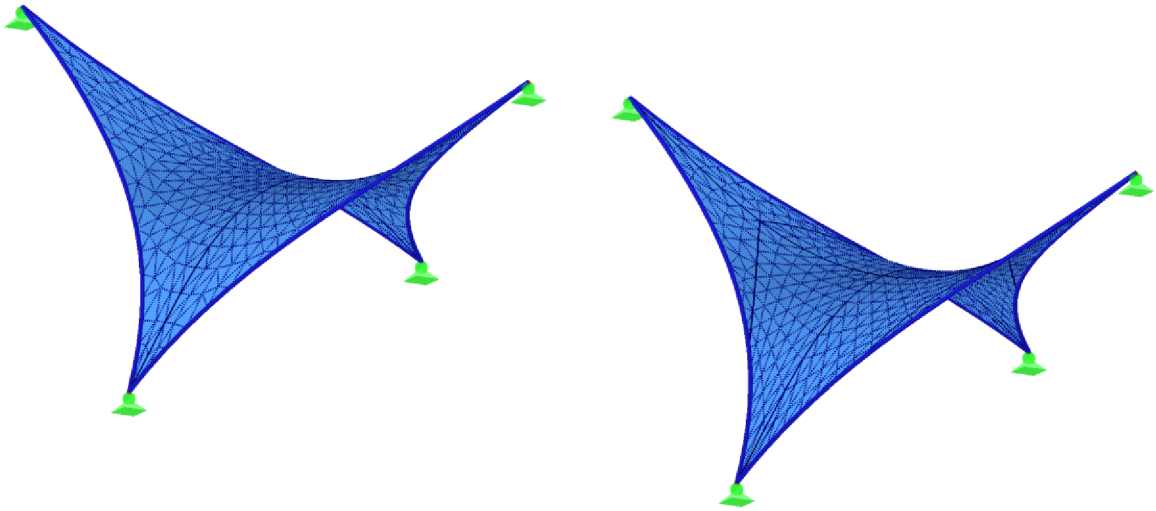

Fig. 22 Final Geometry and FE Mesh of Two Hypar Membranes (1D FE: 152, 2D FE: 1100, FE Nodes: 628)

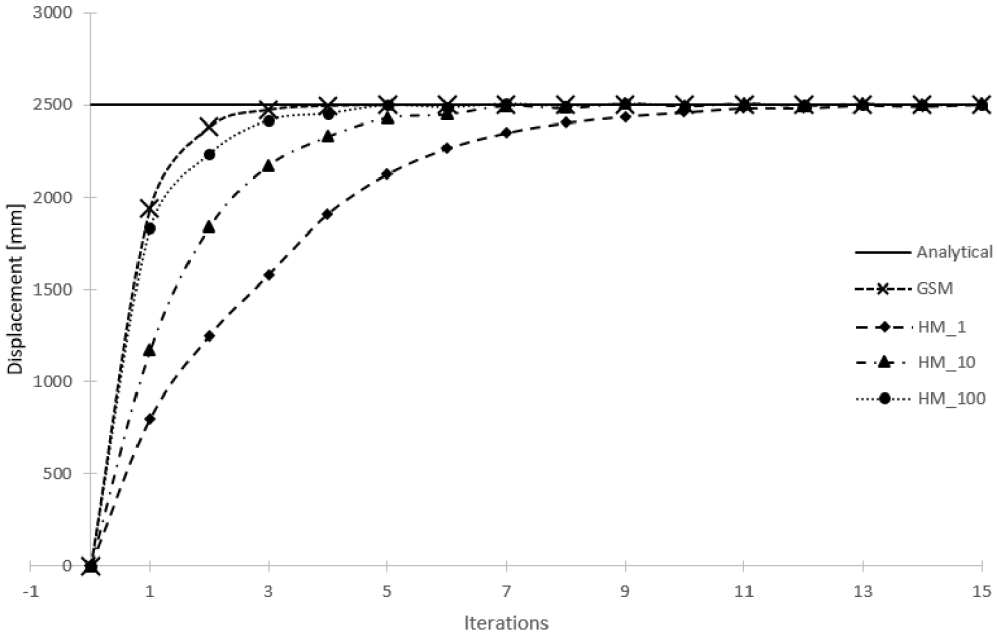

Fig. 23 Convergence Behaviour of GSM and HM Form Finding

4.6.3 Orthotropic Prestress

The left hypar-shaped membrane structure (Fig. 21) is overtaken for this example, presenting the issue of the constant orthotropic prestress impossibility in double-curved surfaces. The values of $n_x = 2.00\,kN/m$ and $n_y = 1.00\,kN/m$ are used for the membrane prestress and the requirement of the relative sag is prescribed for the cables $s_{rel} = 8.00\,\%$.

If the constant orthotropic prestress is strongly enforced, uncontrolled model distortions occur (Fig. 24). However, a close approximation of these values can lead to equilibrium, as presented in the following figures (Fig. 25, Fig. 26). The normal forces in the cables for satisfying the geometric requirement are found (Fig. 27). The normal forces vary along the cable lengths, as necessary for the equilibrium with the membrane.

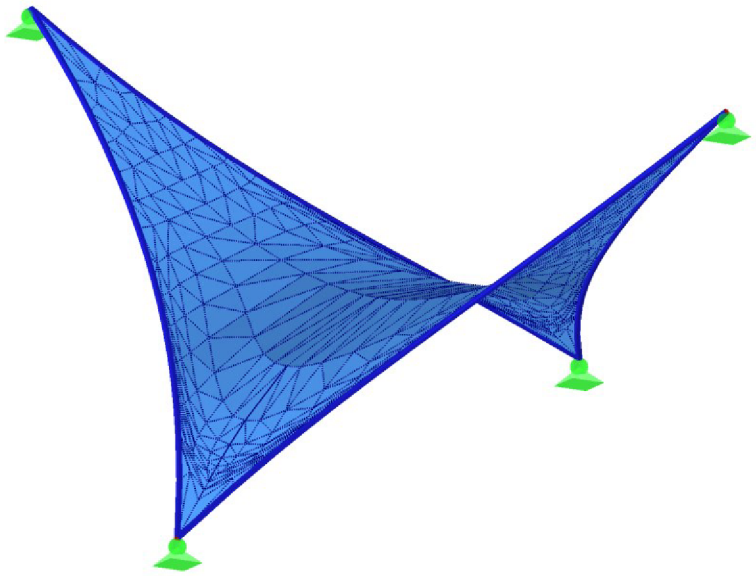

Fig. 24 Analysis Divergence Characterised by Uncontrolled Mesh Distortions

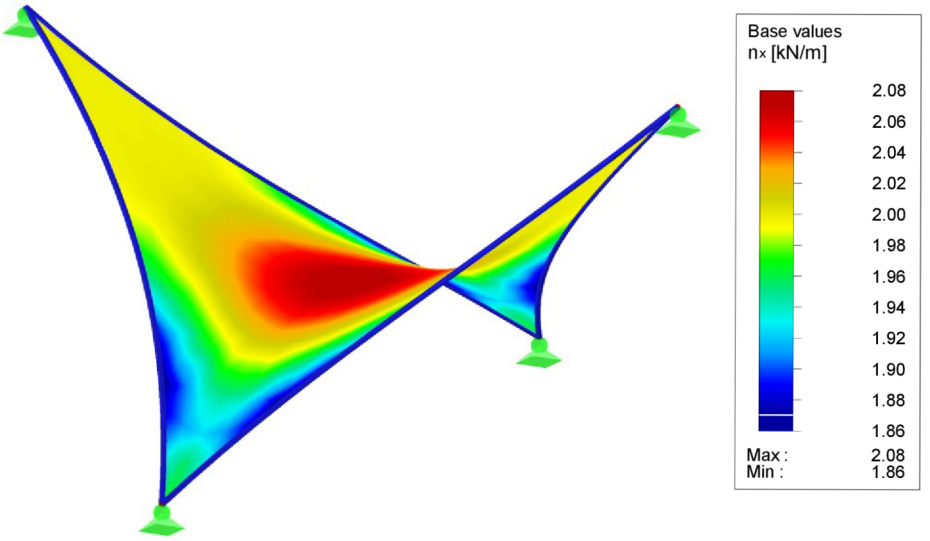

Fig. 25 Prestress n_x Approximating Predefined Values $n_x = 2.00\ kN/m$

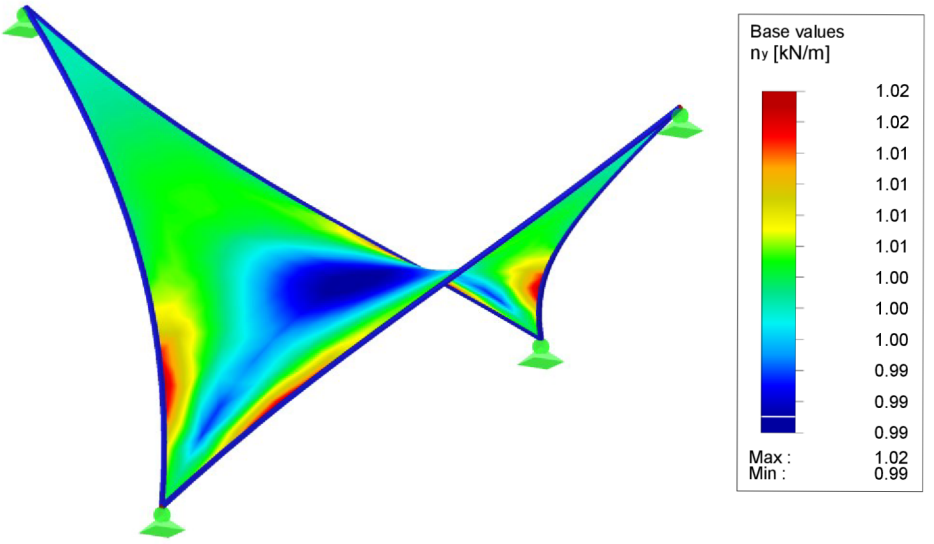

Fig. 26 Prestress n_y Approximating Predefined Values $n_y = 1.00\ kN/m$

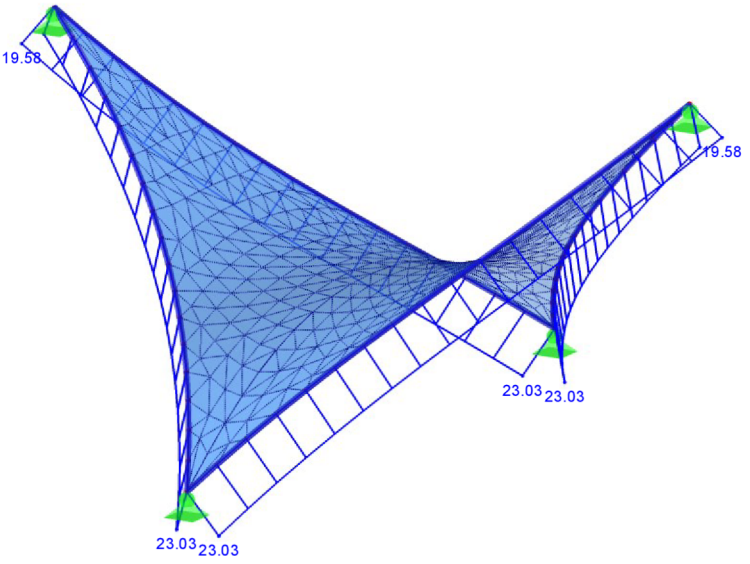

Fig. 27 Prestress N Satisfying Predefined Cables Sag Value $s_{rel} = 8.00\ \%$

4.6.4 Projection Method

The following example shows two umbrellas, the left one with the square base made of cables, and the right one with the circular base made of a steel frame (Fig. 28).

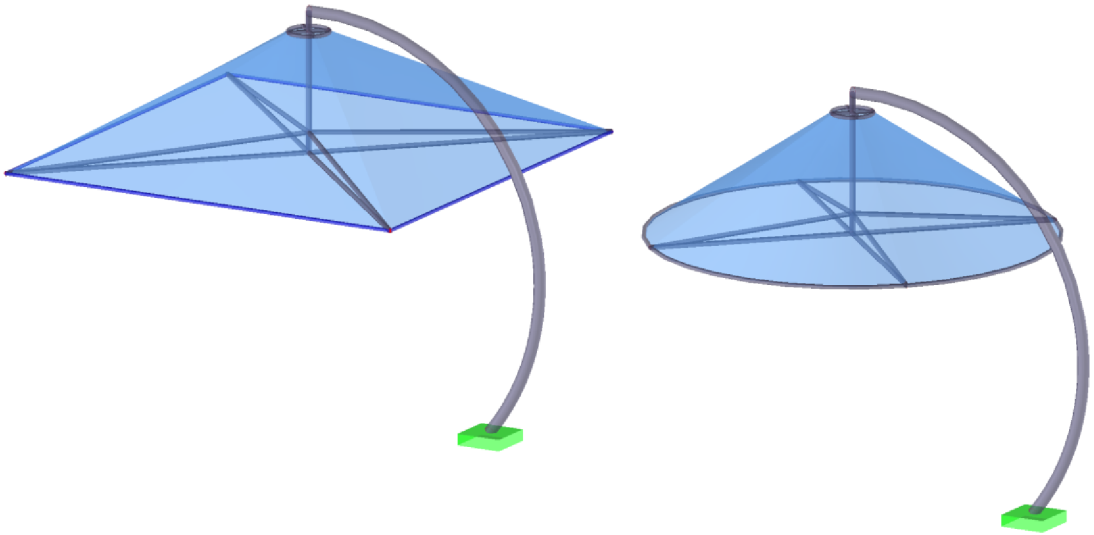

Fig. 28 Initial Models Positions of Membrane Umbrellas (Light Blue: Membrane, Blue: Cables, Gray: Beams)

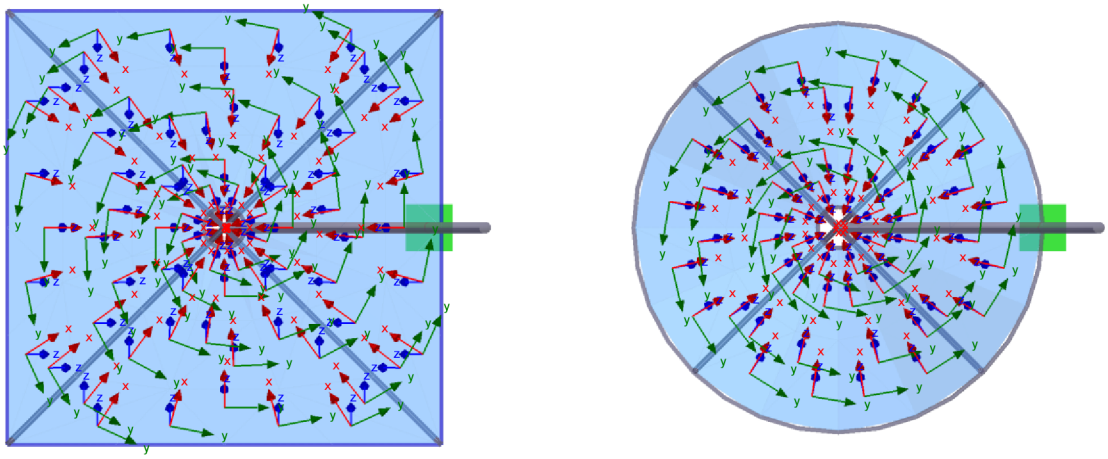

Fig. 29 Axis Orientation: x (Radial), y (Tangential)

Such a conical shapes are typical by necessity of the stress concentration in the regions of the top or bottom rings, thus the prestress vary much more than in the previous example (4.6.3), where quite a close approximation of the given values was reached. Here, the given prestress values $n_x = n_y = 1.00\ kN/m$ will be far away from the resulting prestress of the membrane. To be complete, the prestress $N = 5.00\ kN$ for the boundary cables is required.

A stabilization procedure needs to be applied. As mentioned above, the possible ways are *Specifying Number of Form Finding Steps* (4.2.1), Elastic Control in the *natural* way (4.2.2), *Element Size Control* (4.2.3), *Projection Method* (4.2.5), etc. In the following, for the sake of the comparison, the number of iterations is restricted first and the example is then calculated with the *Projection Method*.

The final geometry (Fig. 30) and results of the form finding process with the restricted number of calculation steps can be seen in following figures (Fig. 31 – Fig. 35).

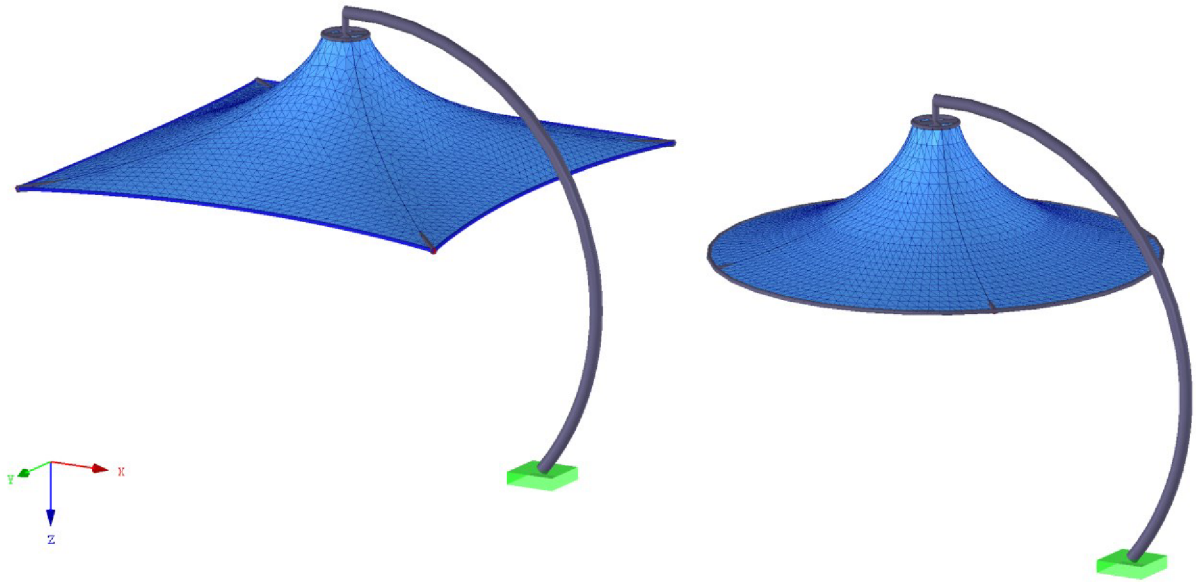

Fig. 30 Final Geometry and FE Mesh: Stabilization: Specifying Number of Form Finding Steps

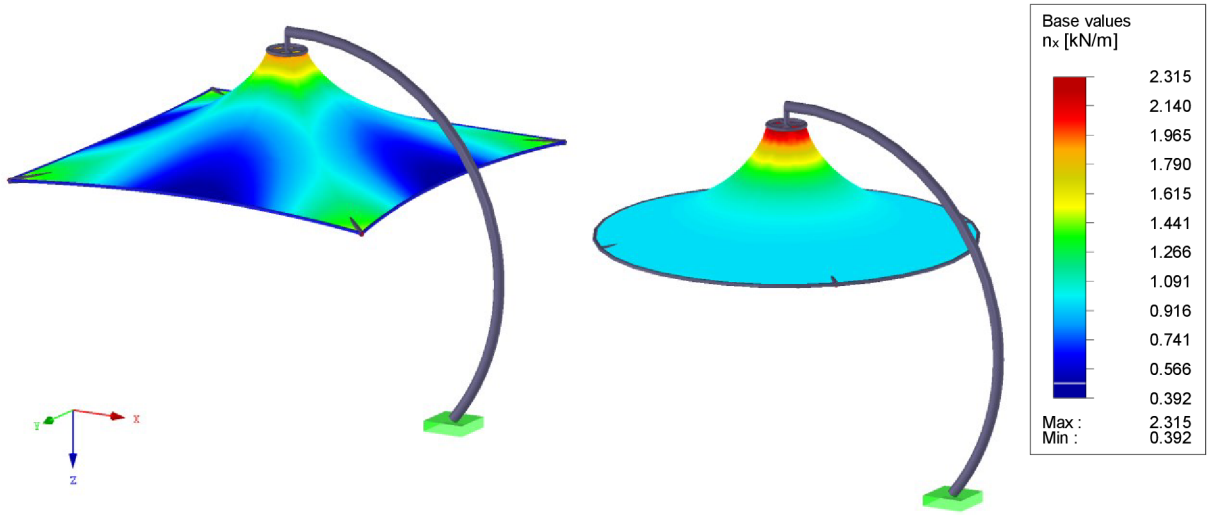

Fig. 31 Normal Forces in x Direction; Stabilization: Specifying Number of Form Finding Steps

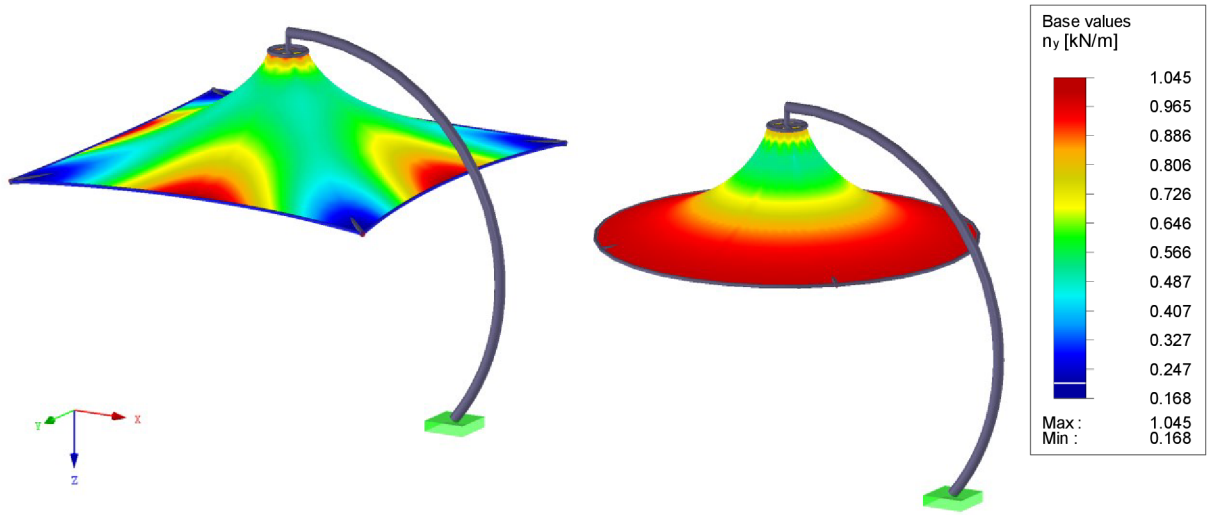

Fig. 32 Normal Forces in y Direction; Stabilization: Specifying Number of Form Finding Steps

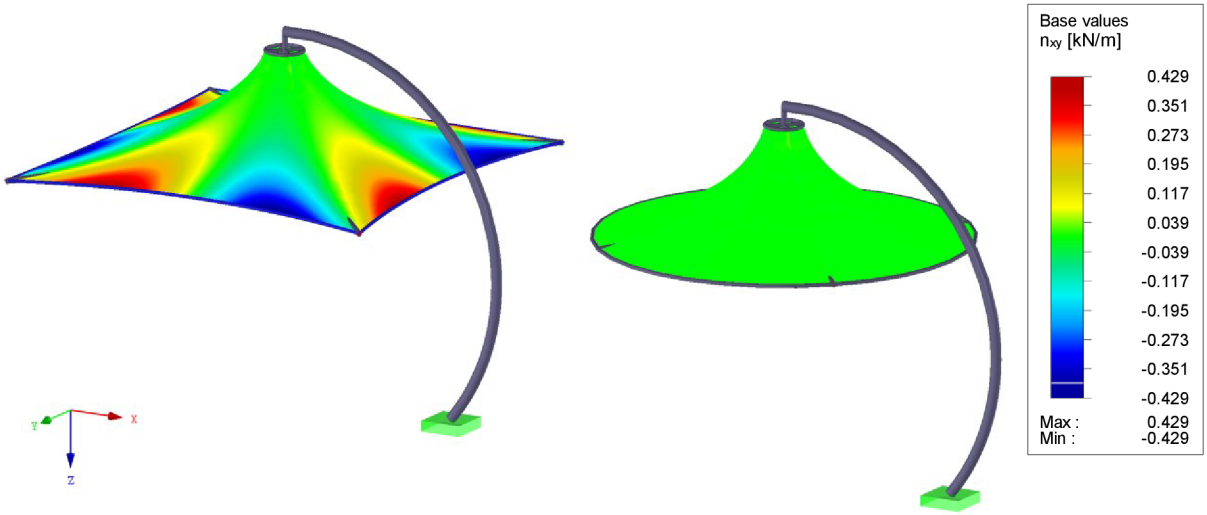

Fig. 33 Shear Forces; Stabilization: Specifying Number of Form Finding Steps

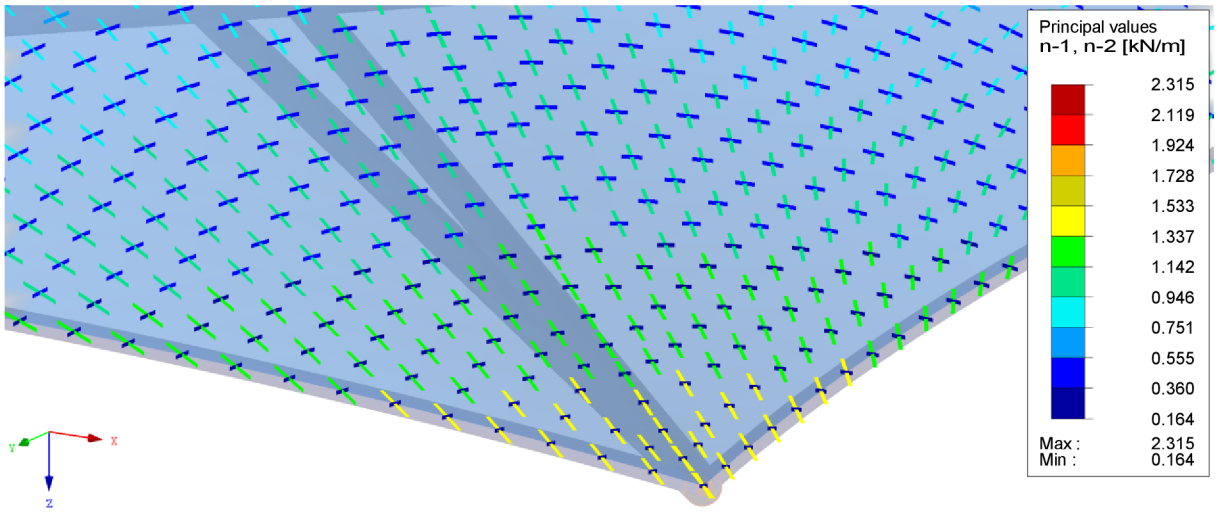

Fig. 34 Principal Forces Vectors in Corner of Left Membrane; Stabilization: Specifying Number of Form Finding Steps

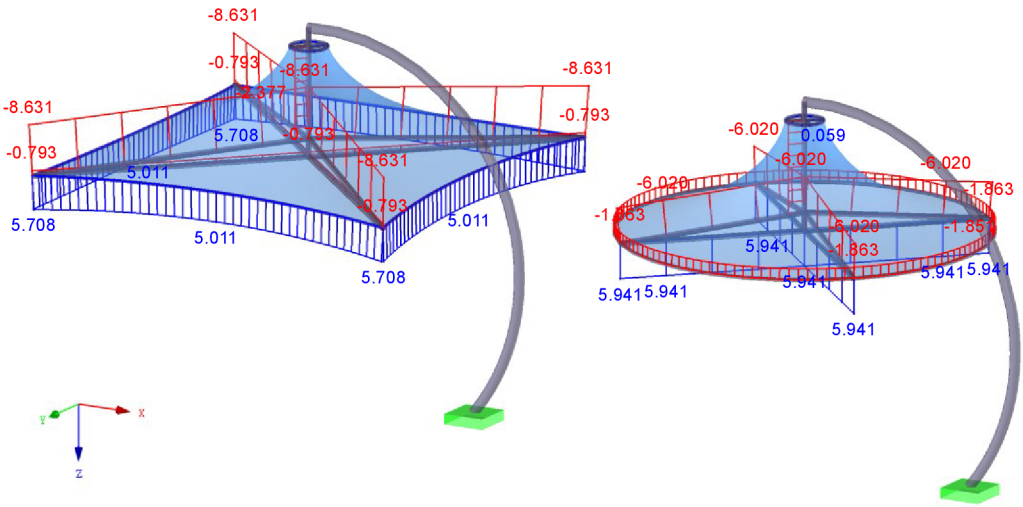

Fig. 35 Normal Forces; Stabilization: Specifying Number of Form Finding Steps

While observing these two umbrellas, it can be seen that quite nice prestress can be reached for the axially symmetric structure. However, when observing the results of the left structure, no smooth prestress is reached and the locations with the overtension and undertension can be detected. As an example, the undertensioned region in the y direction of all four corners is observable in (Fig. 32), or the vectors of principal forces in one corner of the left membrane (Fig. 34). This method is therefore not an optimum solution for the general membrane structures with high or low points.

The next form finding analysis is performed with the *Projection Method* (4.2.5) stabilization technique. In the figure (Fig. 36), the circular cutout of the infinite projection plane is presented. The membranes prestress values $n_x = n_y = 1.00\ kN/m$ are specified in the given projection planes and the cable prestress of the left membrane $N = 5.00\ kN$.

Note 1: It is important to note that this is only a cutout of the infinite projection plane, whose orientation in the space is uniquely defined by the normal vector. The precise position of this plane is not important, only its orientation plays a role. Moreover, the equilibrium in the whole projection plane is satisfied, so when the model of the membrane moves, it always has its projection to the mentioned plane.

Note 2: When the radial direction of the FE local axes of the membrane structure is defined by a line (by two nodes), the two nodes are used for the definition of the mentioned normal vector. Thus, using of this method is user-friendly.

The equilibrium of isotropic prestress in the projection plane is presented in (Fig. 37), the final geometry in (Fig. 38) and the results of the form finding analysis can be seen in figures (Fig. 39, Fig. 40, Fig. 41, Fig. 42, Fig. 43).

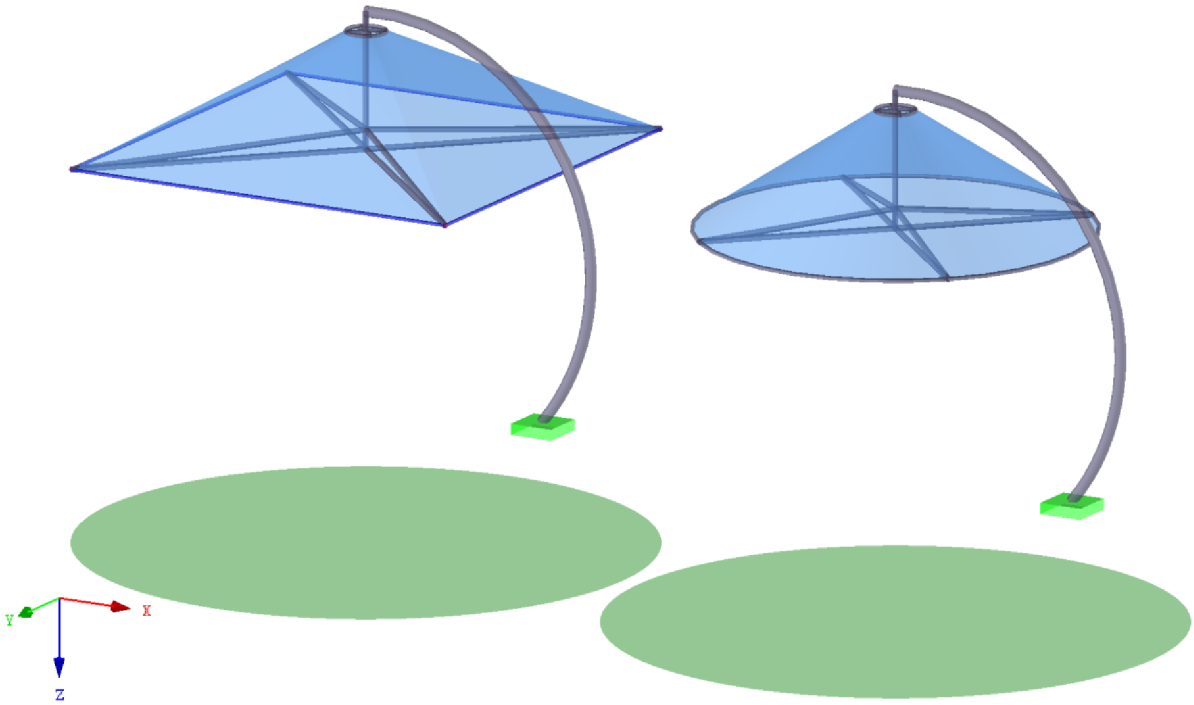

Fig. 36 Projection Planes for Prestress Definition (green)

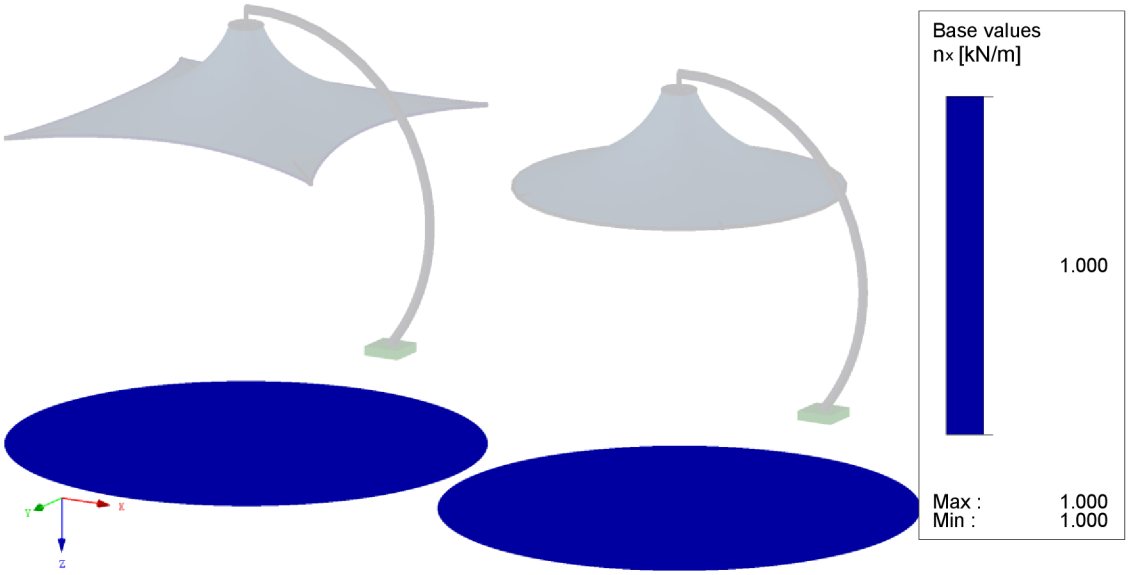

Fig. 37 Isotropic Prestress Definition in Projection Plane (Note: $n_y = n_x$)

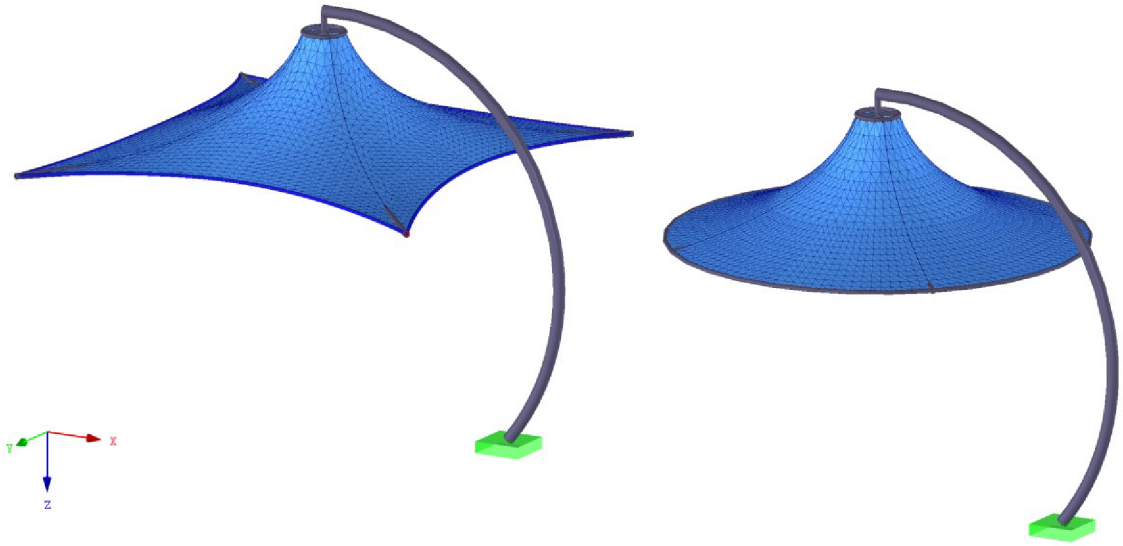

Fig. 38 Final Geometry and FE Mesh: Stabilization: Projection Method

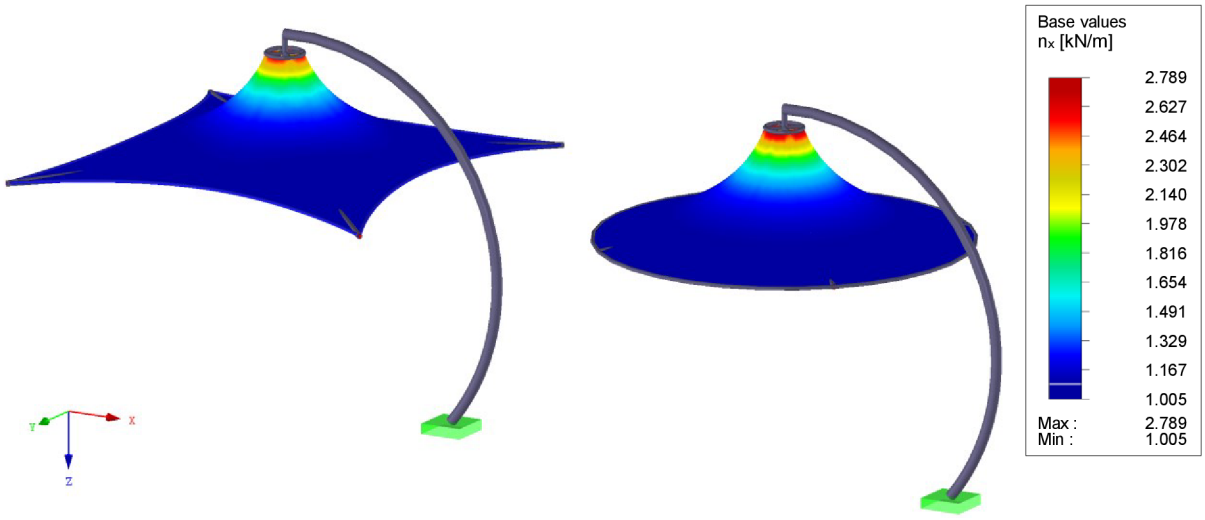

Fig. 39 Normal Forces in x Direction; Stabilization: Projection Method

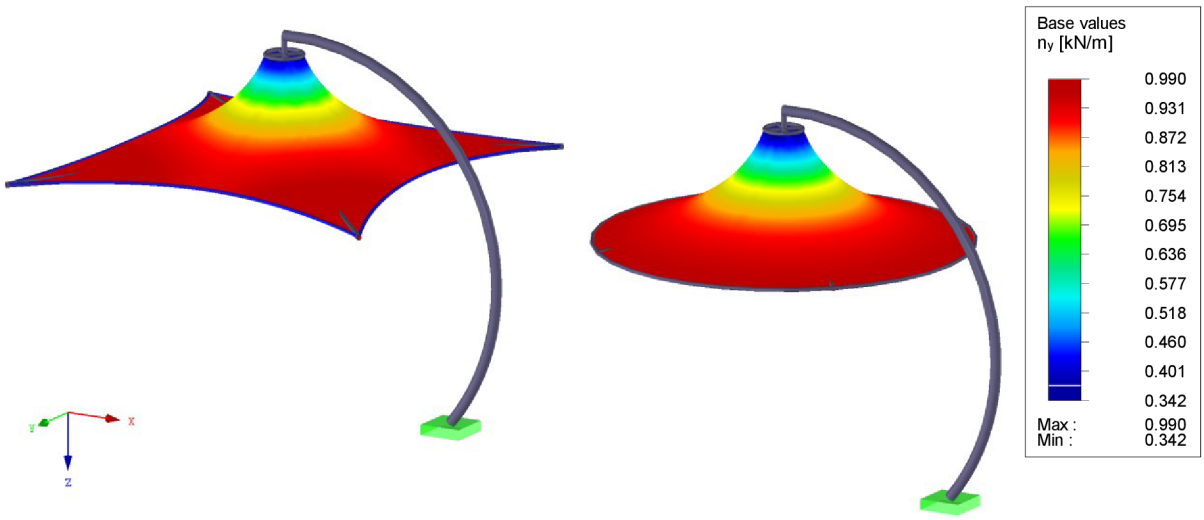

Fig. 40 Normal Forces in y Direction; Stabilization: Projection Method

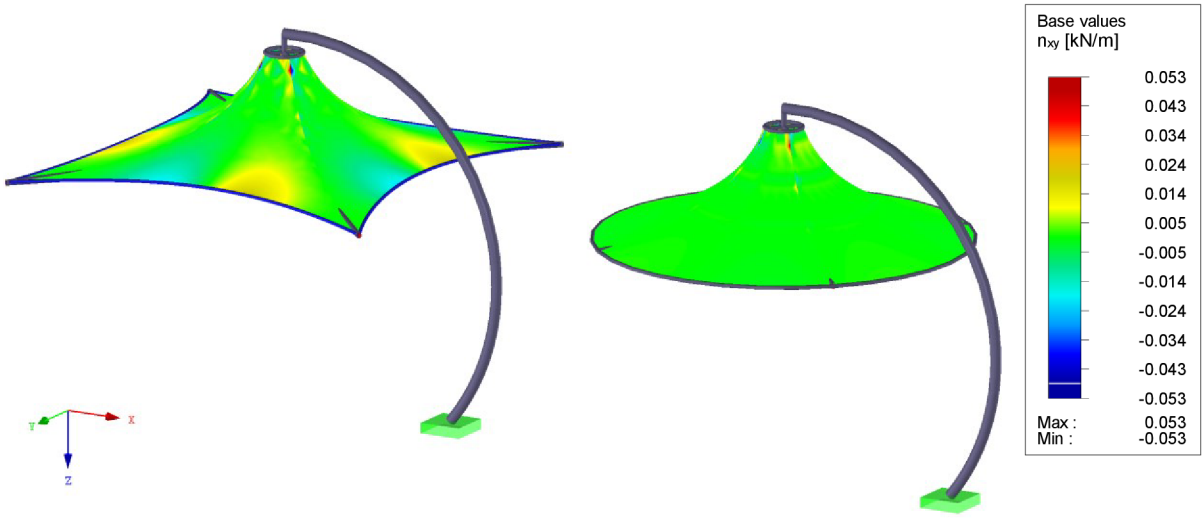

Fig. 41 Shear Forces; Stabilization: Projection Method

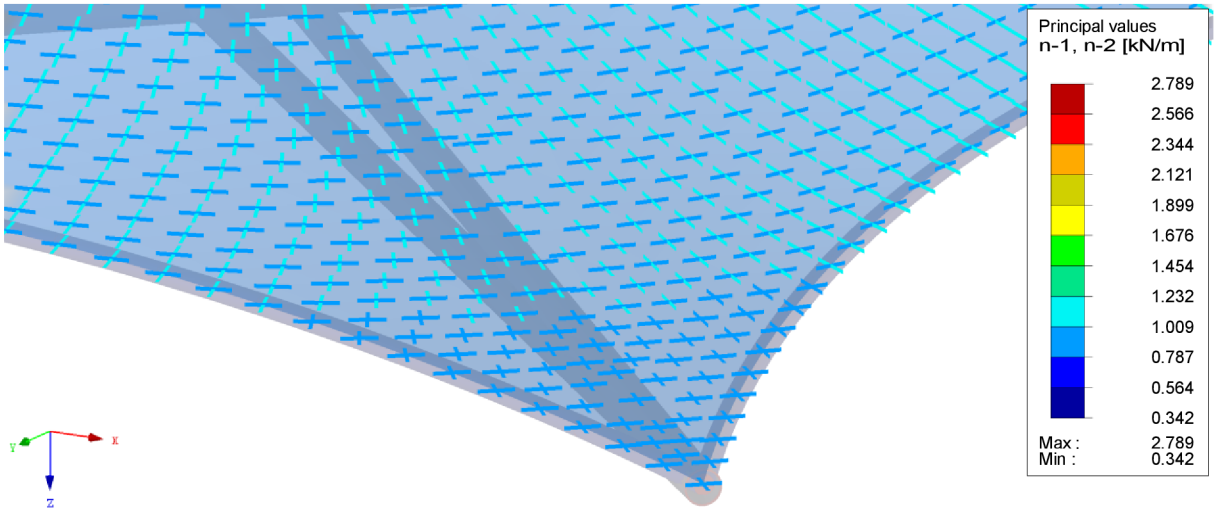

Fig. 42 Principal Forces Vectors in Corner of Left Membrane ; Stabilization: Projection Method

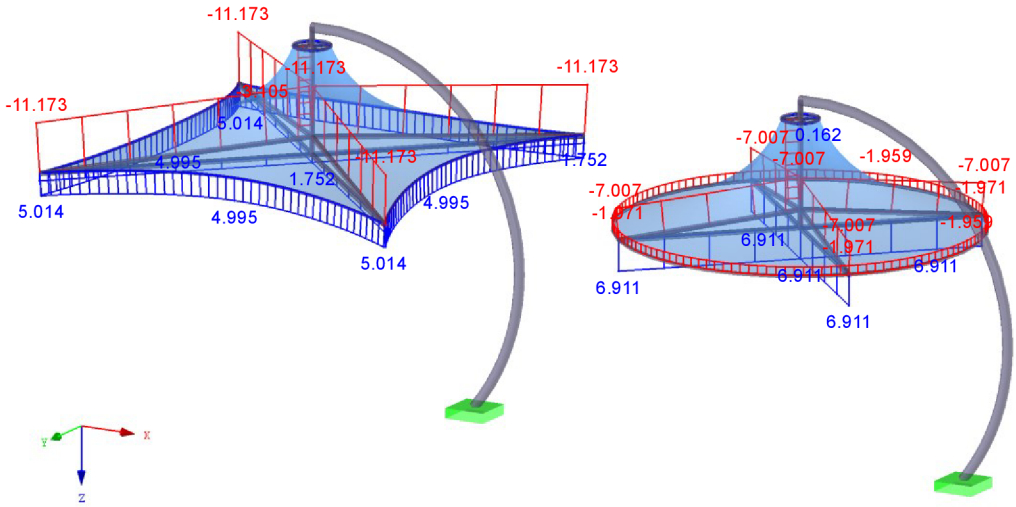

Fig. 43 Normal Forces; Stabilization: Projection Method

While observing the umbrellas, it can be seen that nice and smooth prestress is reached for both models. In the regions with the necessary rapid change of curvatures, specifically the top of the cones, the prestress is increased for the x direction (Fig. 39), while the prestress in the y direction (Fig. 40) decreases to prevent the strangulation effect. However, in the regions without the necessity for rapid curvature changes, the prestress is practically isotropic (as was the task input), therefore, the undertensioned regions in the corners does not occur (comparison well observable in figures Fig. 34 and Fig. 42). Assuming the specified axis directions, the shear stresses are considerably low (Fig. 41).

In comparison with other stabilization techniques, the projection method has one considerable advantage. ***This type of the prestress definition leads to the uniquely defined spatial equilibrium***, even so it is not known in advance. However, as well as the isotropy prestress, the *Projection Method* (4.2.5) stabilization technique leads to the independence of the resulting shape of the initial model position.

To illustrate other possible equilibrium definition in the projection plane, other case is presented briefly. The average prestress values in the projection plane $n_x = 2.00\,kN/m$, $n_y = 1.00\,kN/m$ and $N = 10.00\,kN$ (Fig. 45). The prestress values in the projection plane cannot have a nature of constant orthotropic prestress, so the analytical equations for the calculation of the equilibrium anisotropic prestress in projection planes are implemented, as can be seen in the bottom part of (Fig. 45). The final geometry (Fig. 44) and the vectors of principal spatial equilibrium forces in the membrane, derived from the equilibrium in the projection plane, are presented below (Fig. 45).

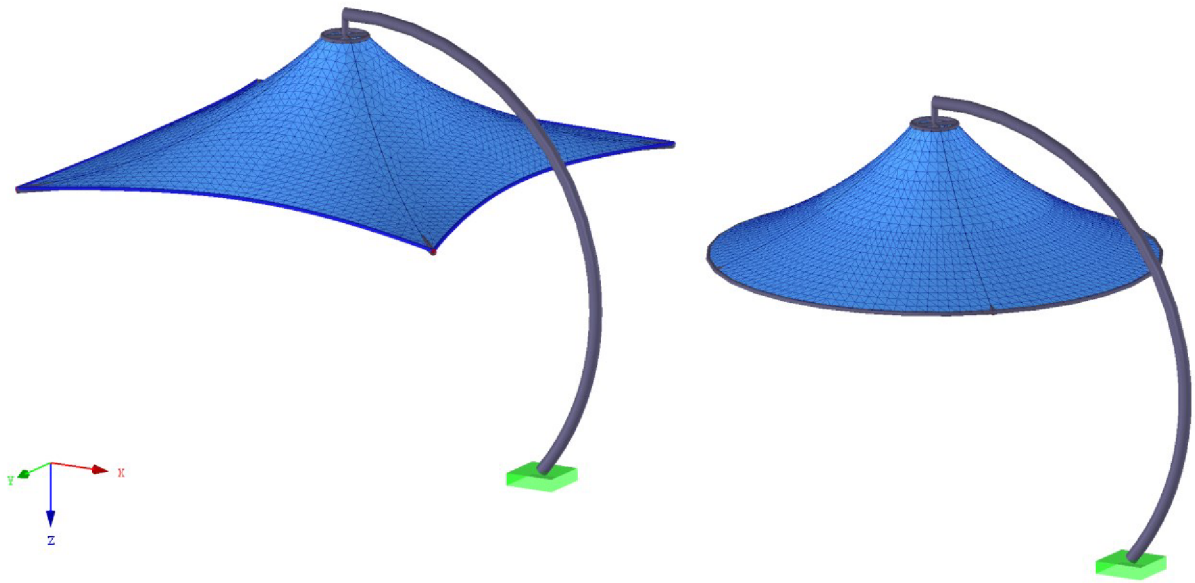

Fig. 44 Final Geometry and FE Mesh for Task $n_x = 2.00\ kN/m$, $n_y = 1.00\ kN/m$ and $N = 10.00\ kN$; Stabilization: Projection Method

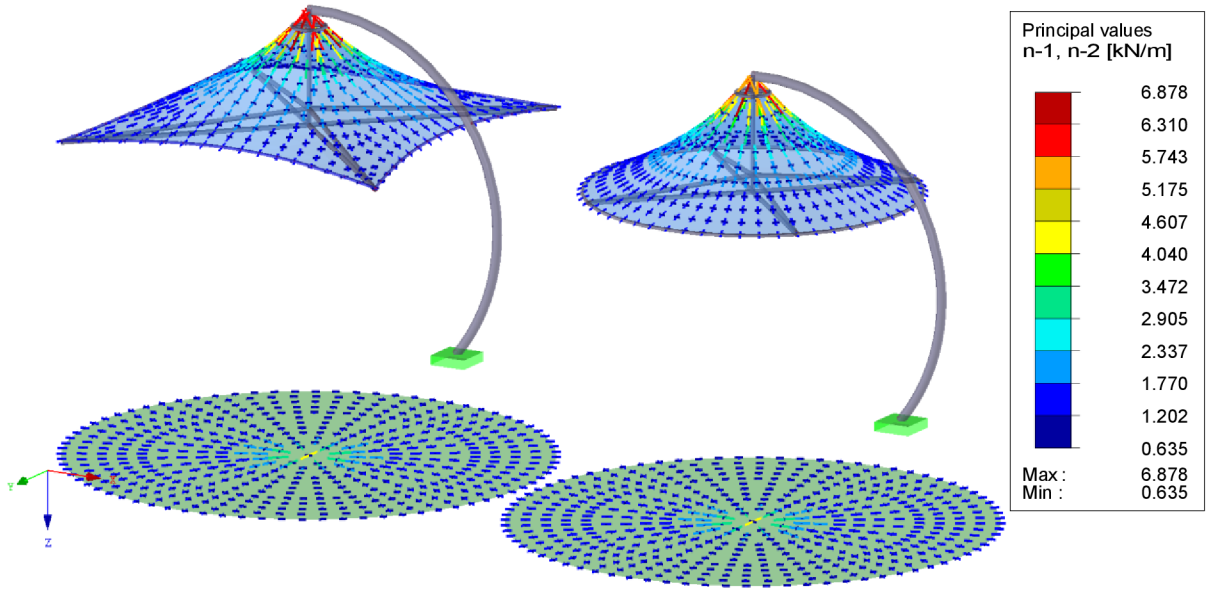

Fig. 45 Vectors of Principal Forces for Task $n_x = 2.00\ kN/m$, $n_y = 1.00\ kN/m$ and $N = 10.00\ kN$; Stabilization: Projection Method

4.6.5 Gas Chambers

Above, the form finding requirements were presented on the examples with membranes and cables. Here, the form-finding of a simple gas chamber is shown. The prestress of the ETFE foil is assumed as $n_x = n_y = 0.40\,kN/m$ and the pressure requirement $p = 250.00\,Pa$ is used. As well the required volume can be defined to find the final geometry. The initial model, final geometry and pressure in the gas chamber after form finding is presented below.

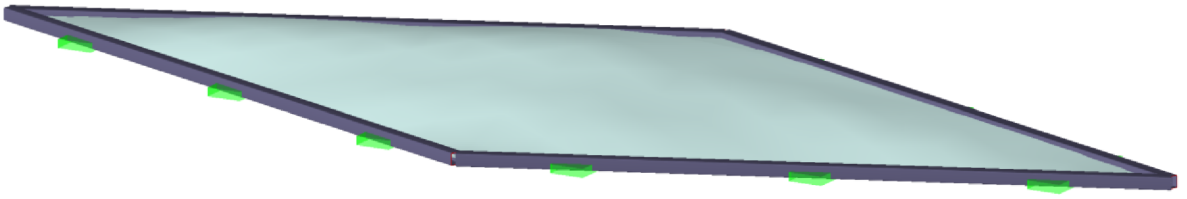

Fig. 46 Initial Model of Gas Chamber

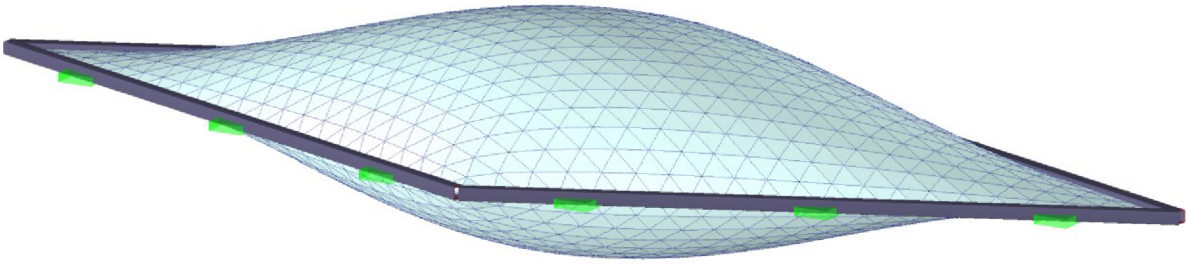

Fig. 47 Final Geometry and FE Mesh of Gas Chamber

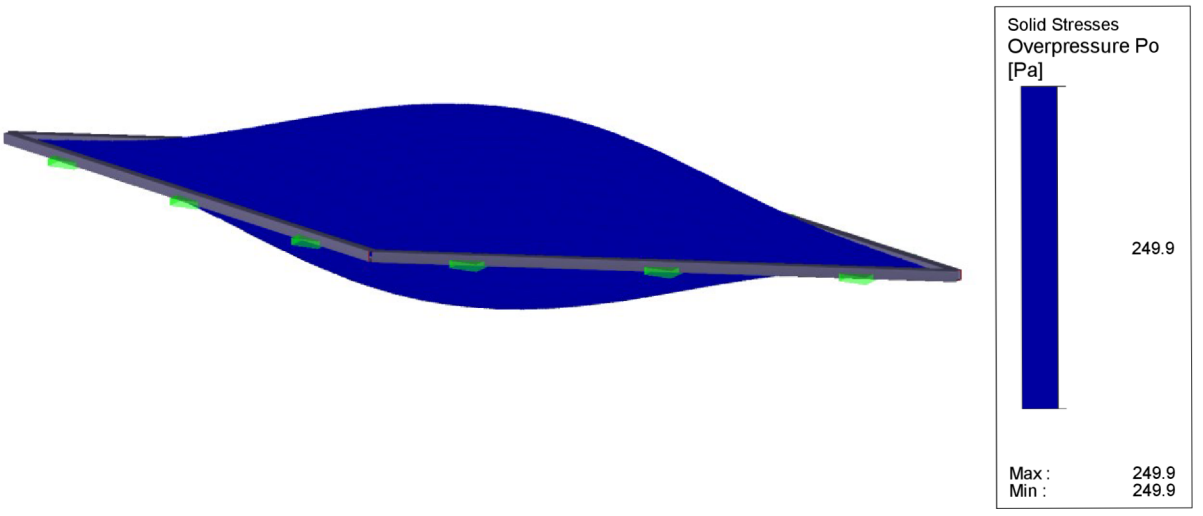

Fig. 48 Resulting Overpressure

4.6.6 Form finding for Structures Under Compression

The form finding of shell structures with boundary beams is presented here. The input values are $n_x = n_y = -9.00\,kN/m$ for the concrete shell with the thickness $t = 70.00\,mm$, $N = -150.00\,kN$ as an average value for the boundary beams and the gravity acceleration $g = 10.00\,m/s^2$. The triangle edge lengths of the initial model are $l = 19.60\,m$.

The initially planar structure (Fig. 49) is deformed to an equilibrium position (Fig. 50), bending moments in the shell (Fig. 51) as well as in the beams are virtually zero, the shell compression is presented in (Fig. 52, Fig. 53) and the compression in the boundary beams in (Fig. 54). Thus, the shape is optimized to act purely in the normal directions when the gravity load is applied.

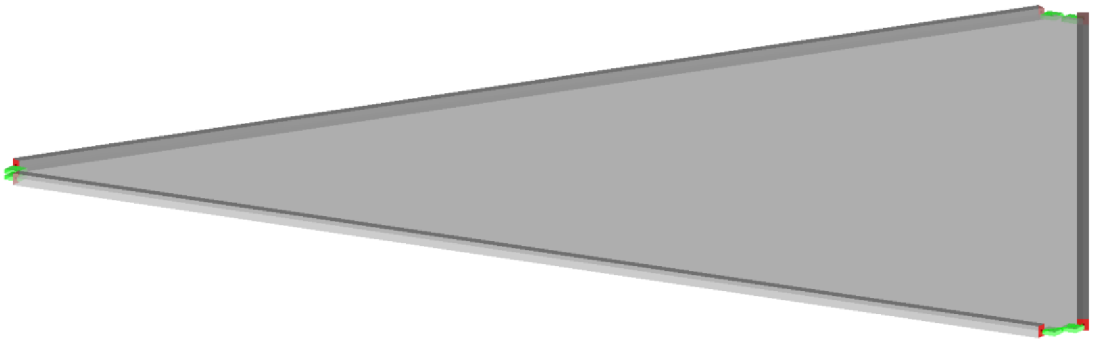

Fig. 49 Initial Model

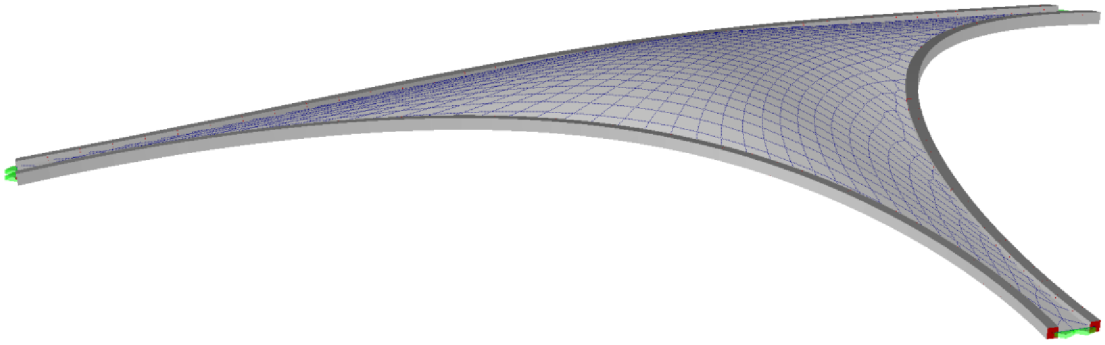

Fig. 50 Final Geometry and FE Mesh Discretization

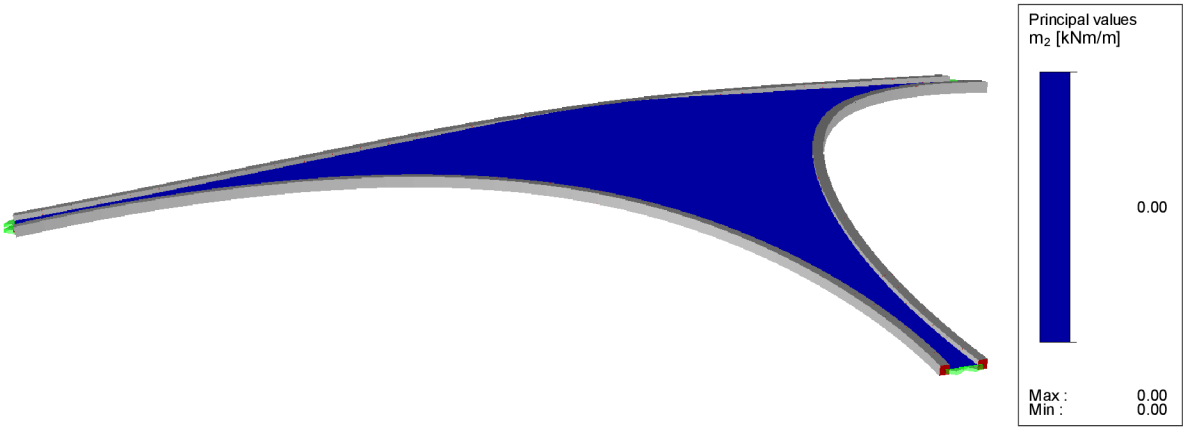

Fig. 51 Principal Moment m_2

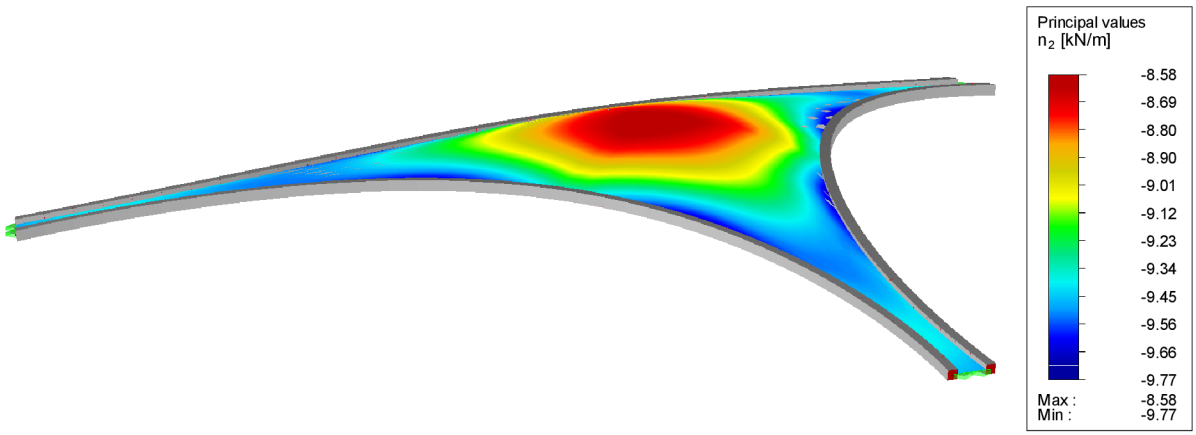

Fig. 52 Principal Normal Force n_2

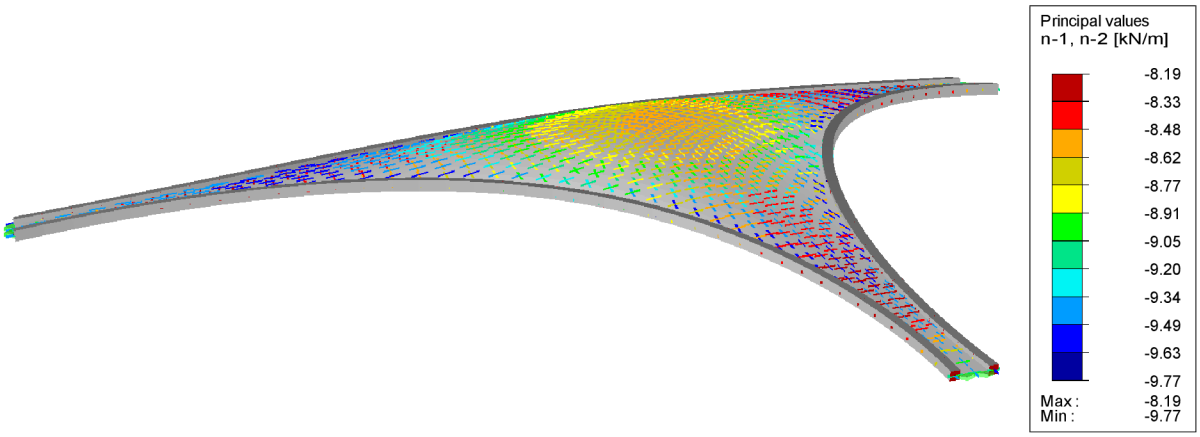

Fig. 53 Vectors of Principal Normal Forces n_1 and n_2

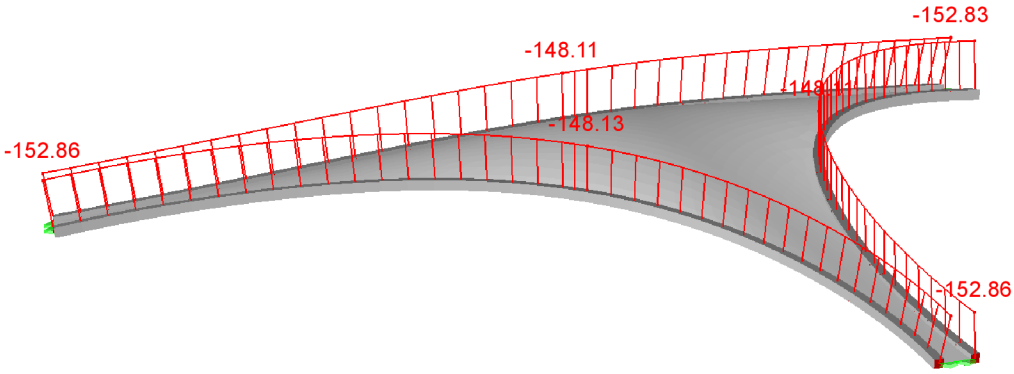

Fig. 54 Normal Forces N $[kN]$

4.6.7 Possibility of Multiple Equilibrium Solutions for Some Form Finding Analyses

The example to be presented now, specifically a membrane on arches, combines more individual form finding requirements and presents a very interesting physical phenomenon.

First, the implemented and thus available physical and geometrical requirements for the form finding analyses are listed here, to provide the overview of the possibilities:

- Cable/Beam (1D): normal force (positive or negative), sag (relative or absolute), length (relative or absolute).
- Membrane/Shell (2D): normal force or stress (positive or negative)
- Gas chambers (3D): pressure (resulting or increment), volume (resulting or increment)

Note: All the requirements are available in the HM form finding, while the force requirements are available in the GSM form finding algorithms.

Now, the prestress of the analysed membrane structure is defined as an orthotropic one with the values $n_x = 2.50\,kN/m$ and $n_y = 2.00\,kN/m$, the cables have the defined relative sag $s_{rel} = 10.00\,\%$ (and acts in tension), the arches of the top model are considered as the supporting structure (no form finding definition) and the arches of the middle and bottom model has the form finding definition of the resulting length $l = 13.37\,m$ under compression (Fig. 55) (this length is considered to be the same as the length of the top model arches). Thus, the example consists of the structural entities both under the positive and the negative required resulting

values. This analysis requires a special procedure. Moreover, the phenomenon of multiple equilibrium solutions is highlighted here (Fig. 56).

The resulting values of the prestress in both directions approximates the defined values and the shear stress has low magnitude (Fig. 57, Fig. 58, Fig. 59). However, the main differences are observable in the shape and the internal forces of beam arches (Fig. 60, Fig. 61). While the first (top) model is exposed to all the beam internal forces, the beams in two other models acts virtually under compression only, since their shape was optimised to behave like this. The structures with the mixed requirements (tension and compression) also often do not have one unique solution, but more equilibrium shapes could be found here (note: although there are only two shapes shown here, four possible solutions exist for this task) and the process converges from the initial position to the closest minimum of energy. Thus, the slight difference between middle and bottom models results in different equilibrium shape after the form finding analysis.

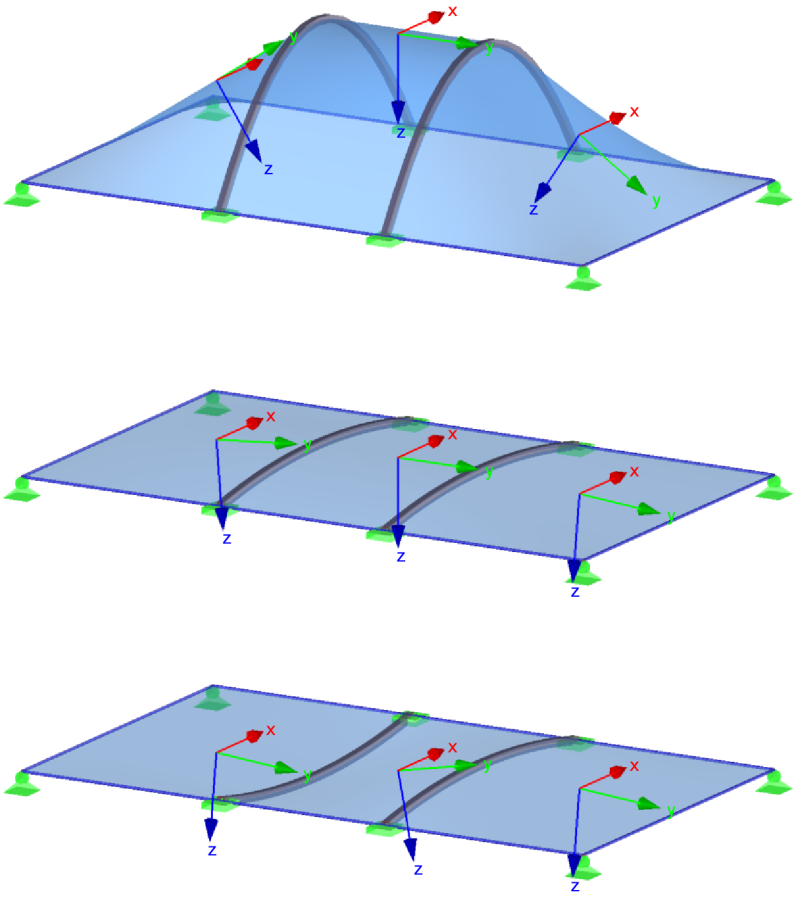

Fig. 55 Initial Model Positions with x and y Axis Orientation

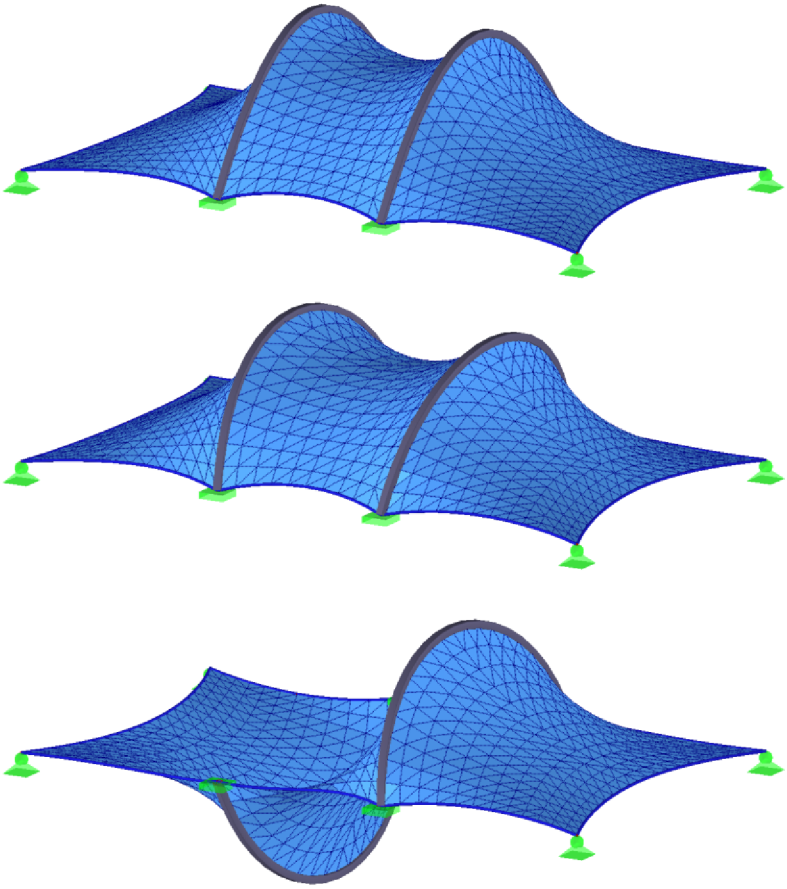

Fig. 56 Final Geometry and FE Mesh Discretization

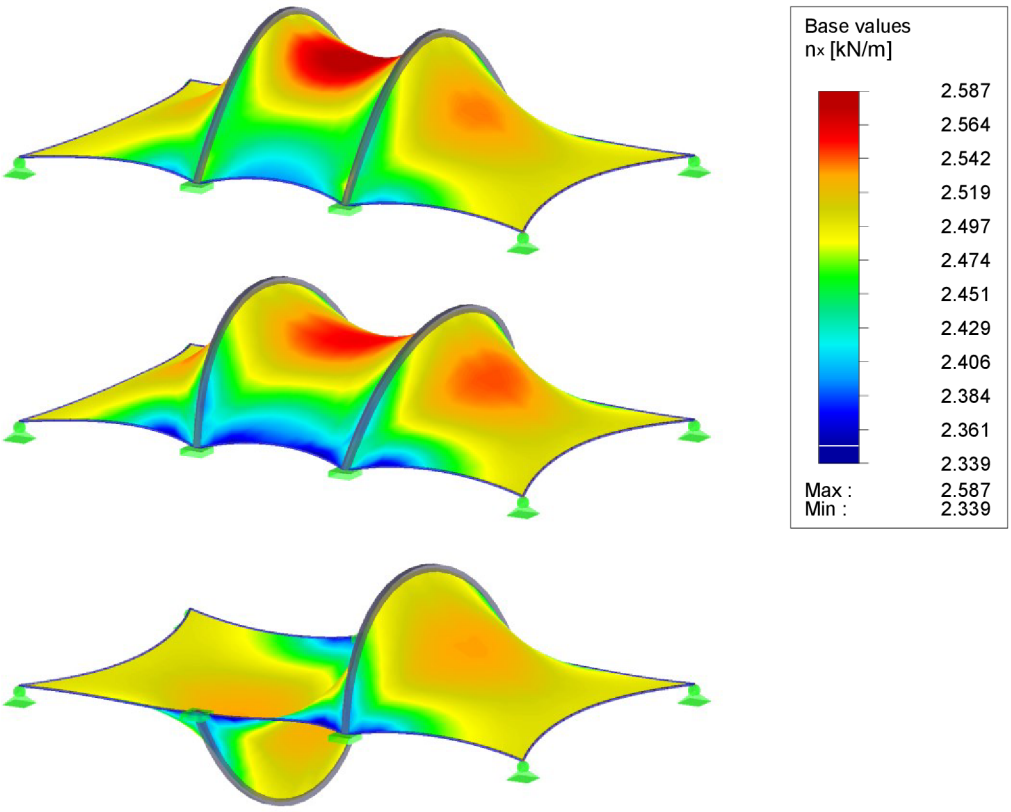

Fig. 57 Normal Forces in x Direction $[kN/m]$

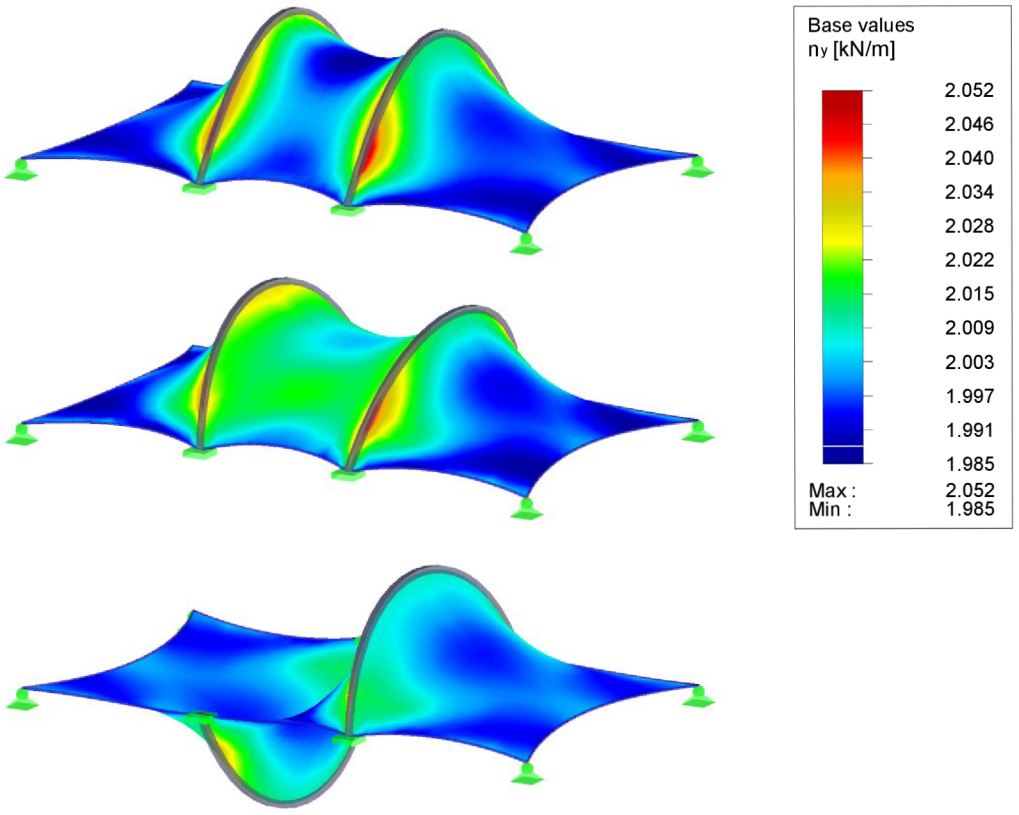

Fig. 58 Normal Forces in y Direction $[kN/m]$

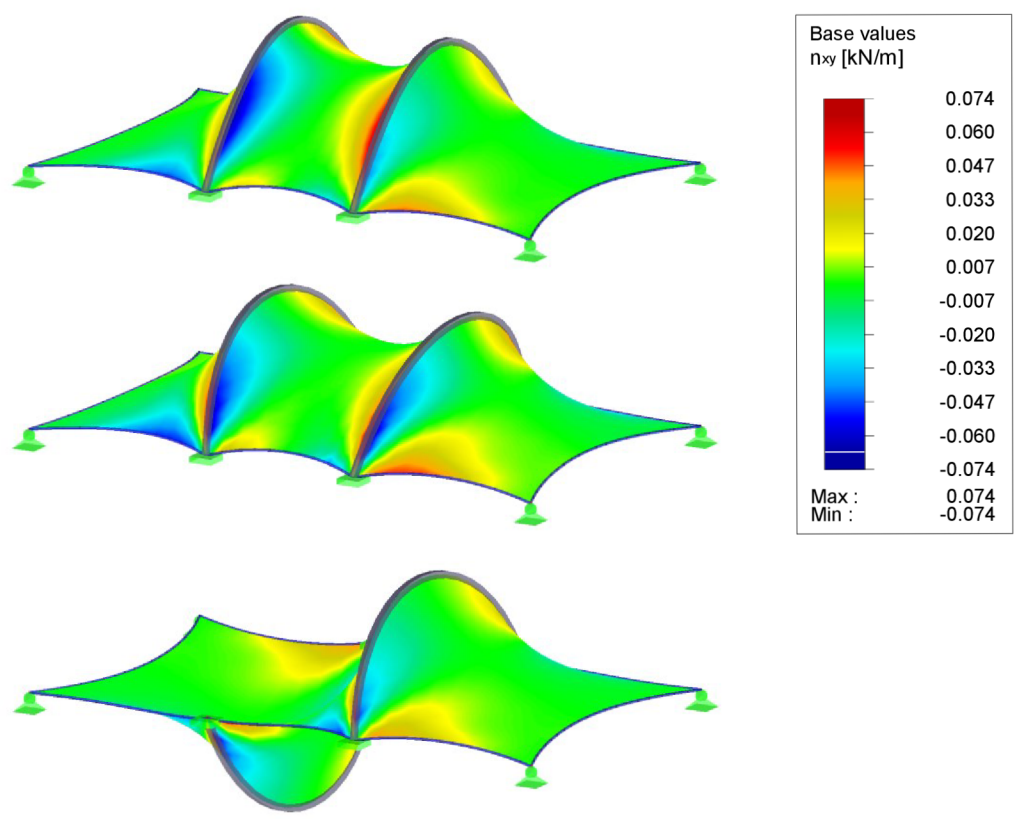

Fig. 59 Shear Forces $[kN/m]$

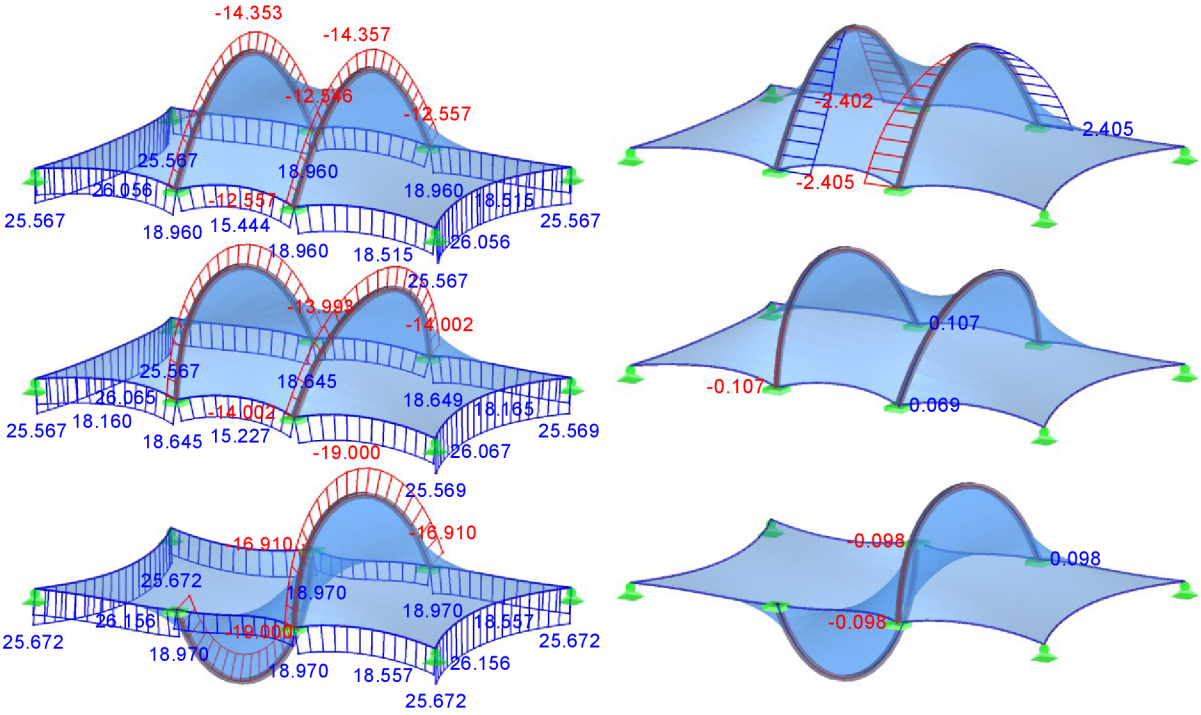

Fig. 60 Normal Forces N $[kN]$ (left), Shear Forces V_y $[kN]$ (right)

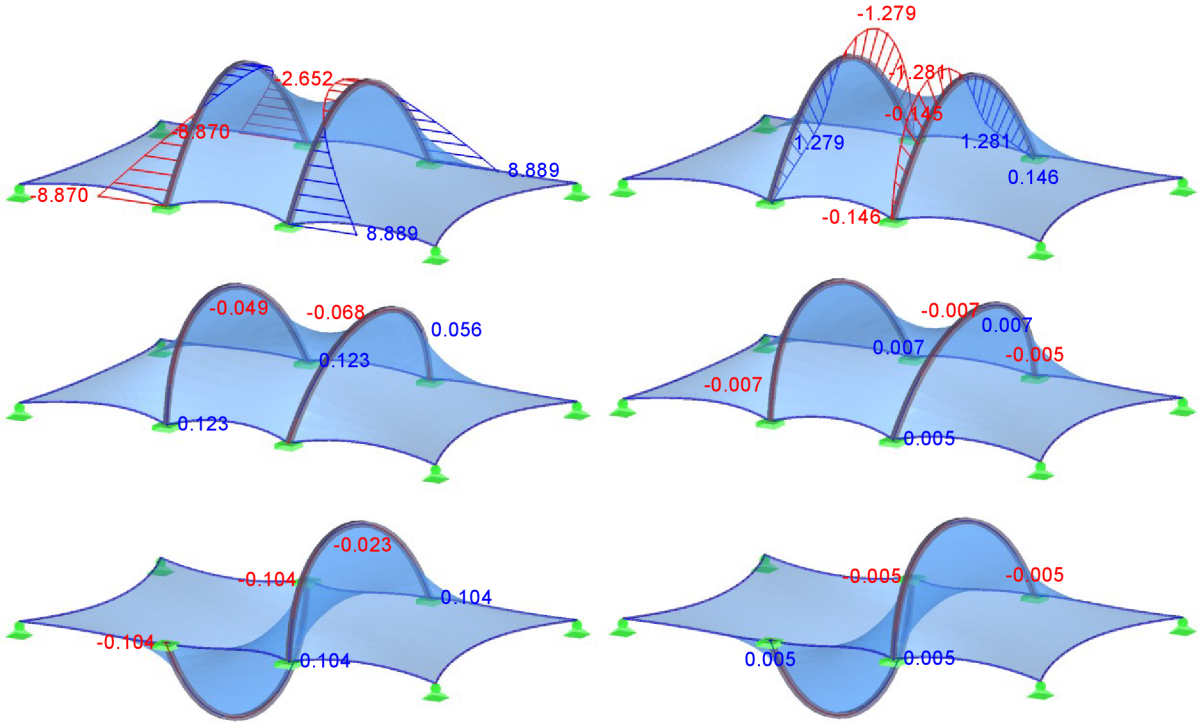

Fig. 61 Bending Moments M_z $[kN/m]$ (left), Torsion Moments M_x $[kN/m]$ (right)

In the graph bellow (Fig. 62), it can be seen that the higher is the *speed of convergence*, the more sensitive is the structure to the oscillations and sometime even instabilities. Here, the model is also stable for the highest speed, however, in the case of more complex and especially sensitive structures, the process can be prone to instabilities and thus, the lower speed of convergence ensures the higher stability of the implemented algorithms.

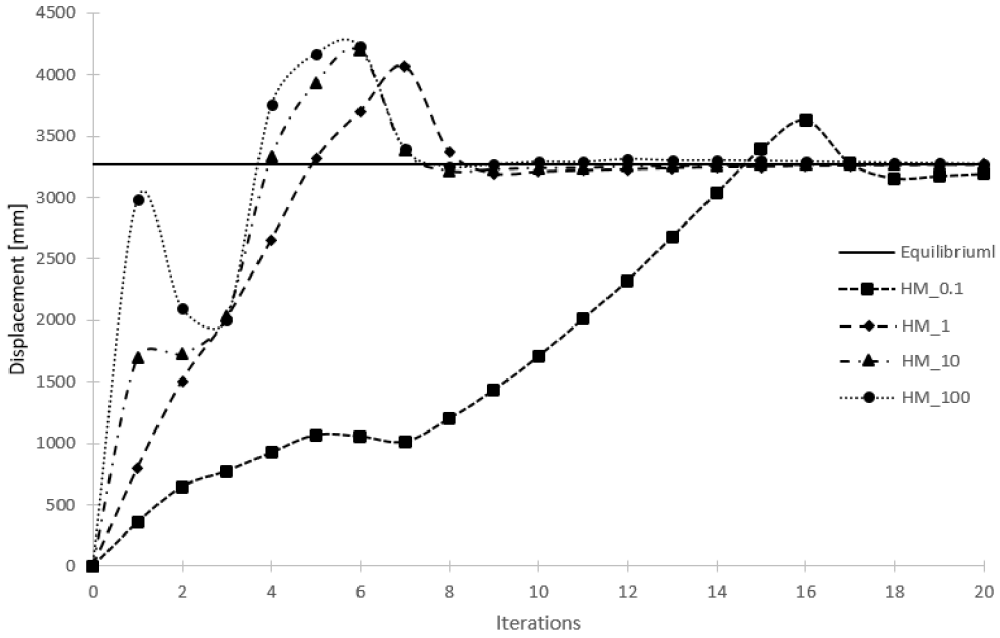

Fig. 62 Convergence Behaviour for Different Setting of HM Form Finding Speed of Convergence

4.6.8 Regeneration of Local FE Axial System

For the example presented in this subchapter, a really crazy initial model position was intentionally chosen as it improves the visibility of the described operation, namely the FE local axial system regeneration. The prestress values are not of interest here, as this issue is generally valid. The initial model has a user-defined local axis direction. Here, the line connecting the bottom supports is a defining line for aligning the local x FE Cartesian direction. The initial model position is presented in the figure (Fig. 63). As the model deforms, the axial system rotates in the space and can change its directions extremely (Fig. 64, Fig. 65).

As the form finding is an initial equilibrium problem solving procedure, the local axial system orientation is not kept during the analysis, but should be regenerated in each iteration in order to keep the orientation as specified by a civil engineer or an architect. It has a great importance on both the material orientation in the subsequent analyses and on the resulting shape, since the local axes are connected with the values prescribed for the form finding process itself. Thus, the local axes regeneration has to be performed.

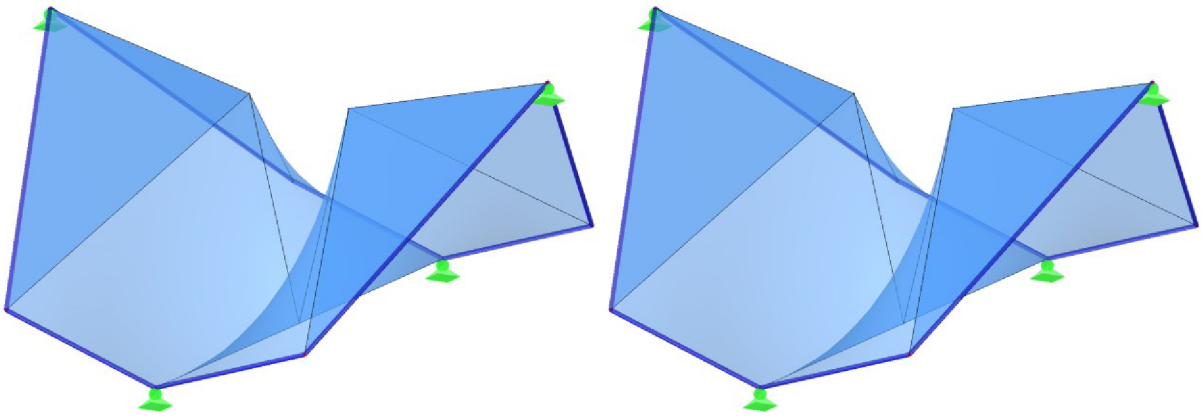

Fig. 63 Initial Position of Models (left)

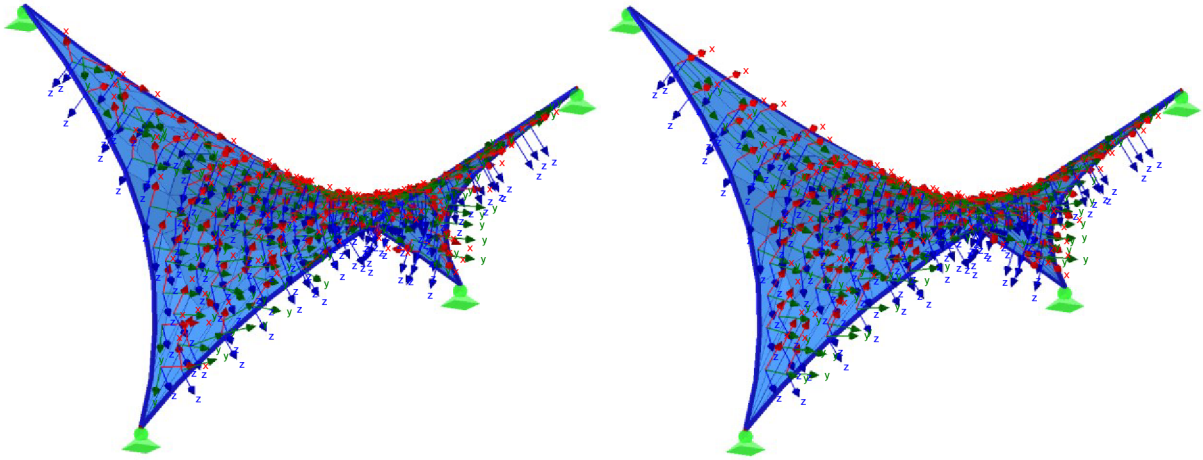

Fig. 64 Final Geometry – Local Axial System Obtained by: Deformation of Original Axial System (left), Regenerated Local Axial System (right); Isometry View

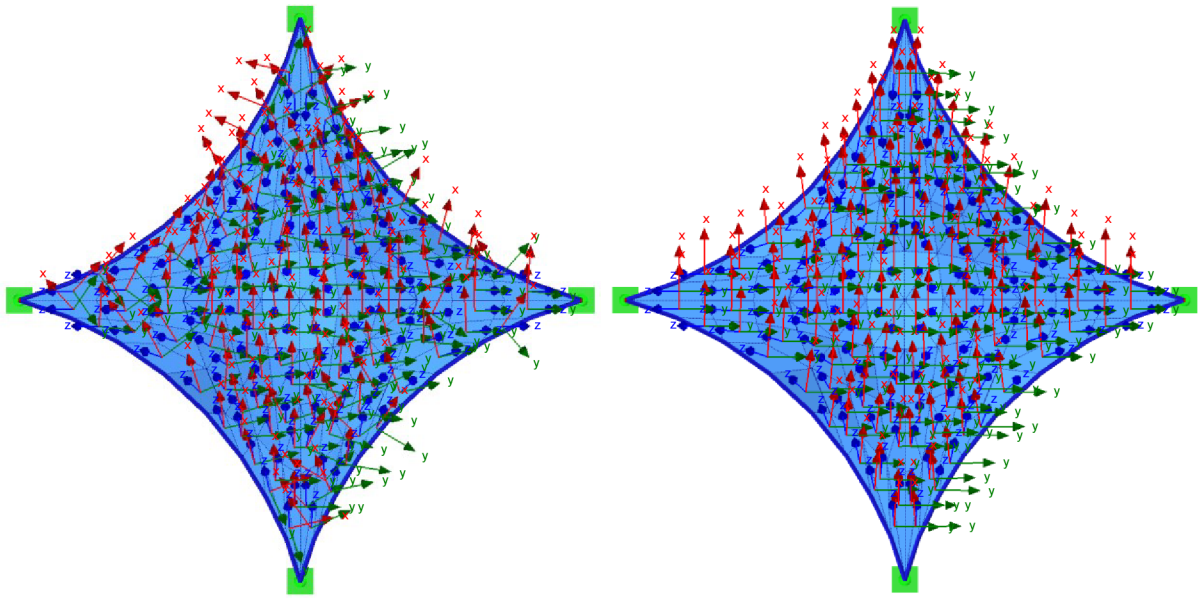

Fig. 65 Final Geometry – Local Axial System Obtained by: Deformation of Original Axis System (left), Regenerated Local Axial System (right); Top View

4.6.9 Material Assignment After Form Finding Analysis

As already mentioned, the form finding analysis is a materially independent process. However, the form finding results are the initial equilibrium state of the given structure for the subsequent analyses, which are materially dependent. Thus, the inverse task in comparison to the usual structural analysis has to be performed on the material level, since the appropriate strains need to be estimated for the actual equilibrium of forces. The strains undergone during the form finding analysis does not have any physical meaning, so, the real physical strains are calculated when the form finding convergence is reached from the resulting stresses

$$\boldsymbol{\varepsilon} = \mathbf{C}^{-1}\,\boldsymbol{\sigma} \tag{4.34}$$

where $\boldsymbol{\varepsilon}$ is the unknown strain state, $\boldsymbol{\sigma}$ is the resulting stress of the form finding analysis, and $\mathbf{C}^{-1}$ is the inverse of the constitutive matrix.

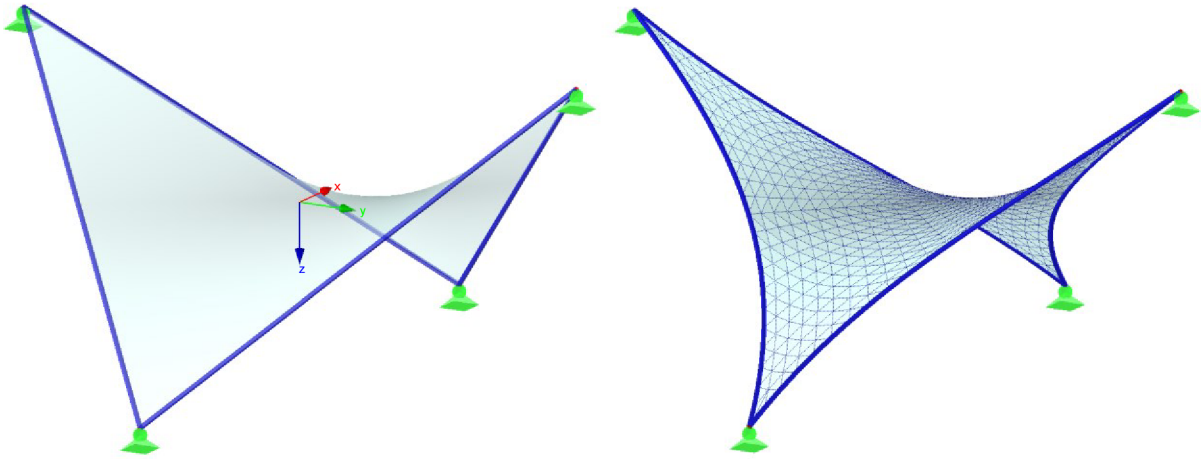

Fig. 66 Initial Position of Model (left), Final Geometry with FE Mesh (right)

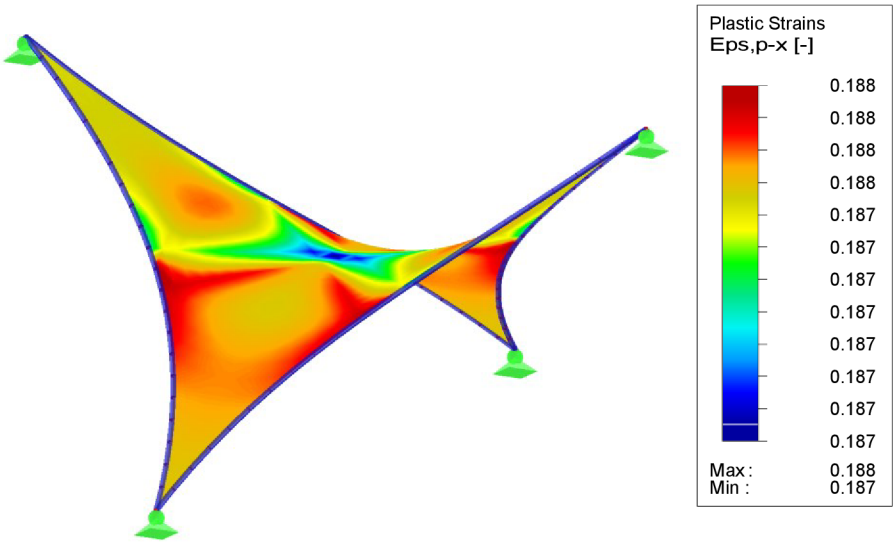

Fig. 67 Determined Total Strains ε_x

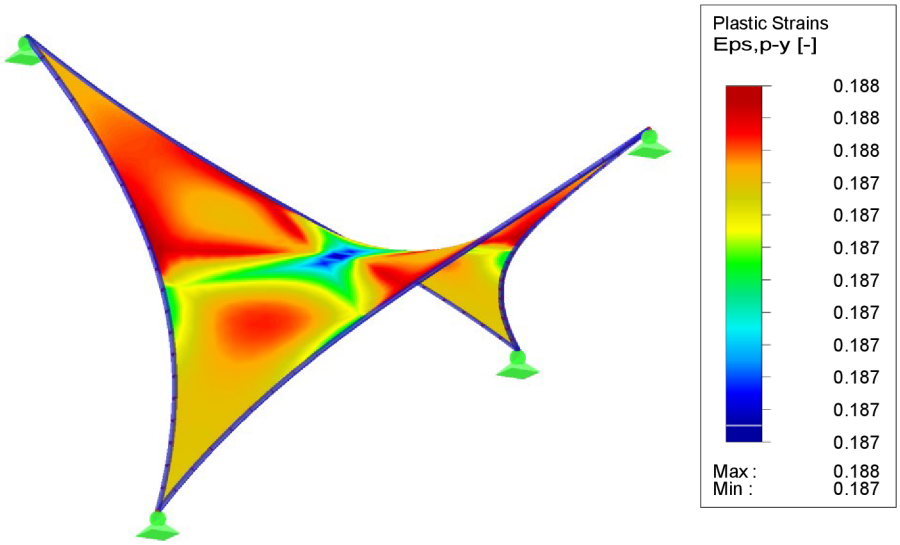

Fig. 68 Determined Plastic Strains $\varepsilon_{pl,x}$

In the example here, the membrane (Fig. 66) prestress has the values $\sigma_x = \sigma_y = 1.50\ MPa$, the material used is defined as an isotropic plastic with the following constants $E = 12.00\ MPa$, $\upsilon = 0.40$, $f_y = 1.00\ MPa$, $E_p = 1.20\ MPa$, and the chosen strain hypothesis is *Von Mises*. In this example, very low material stiffness was used to obtain higher strain values (Fig. 67, Fig. 68).

The process is valid for any available material model. For nonlinear models, the iteration procedure has to be performed when seeking the appropriate strain values (for example, with the *Newton-Raphson* iteration scheme) in each integration node of the analysed FE.

4.6.10 Examples of Complex Structures

The examples already presented were rather simple structures for a straightforward description of the intended issue, phenomenon or implementation necessity to be algorithmizated during the development process. Now, there are few other structures of more complex compositions shown for illustrative purposes (Fig. 69 – Fig. 76). Therefore, the initial and equilibrium shapes are shown without a detailed description.

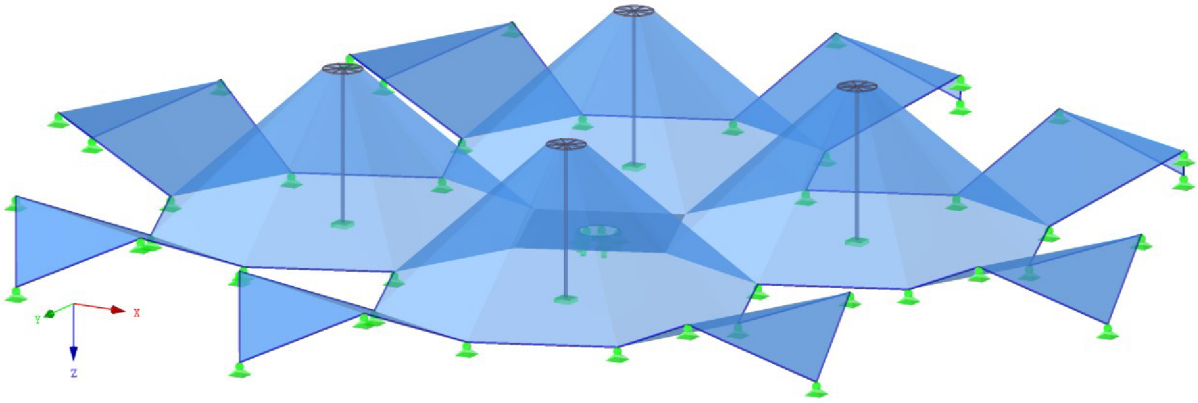

Fig. 69 Composition of Conical and Hypar Membranes – Initial Position [44]

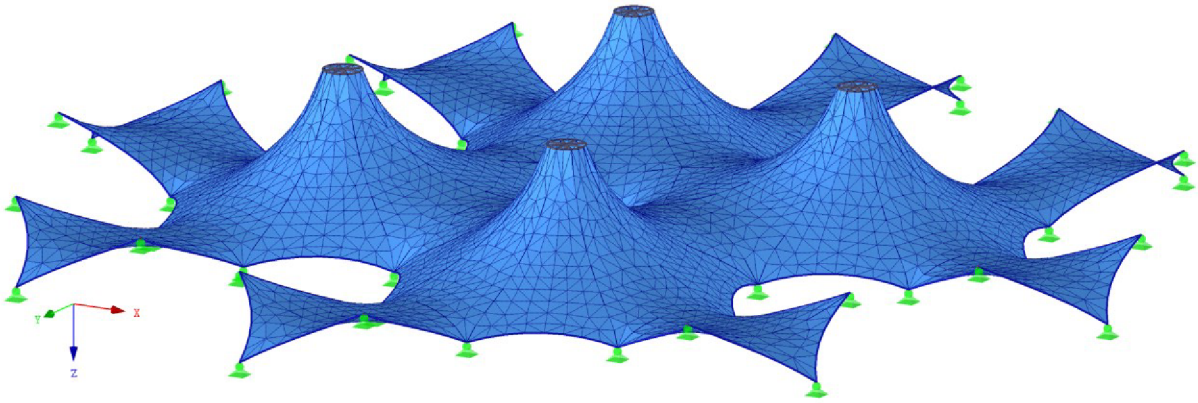

Fig. 70 Composition of Conical and Hypar Membranes – Equilibrium Position [44]

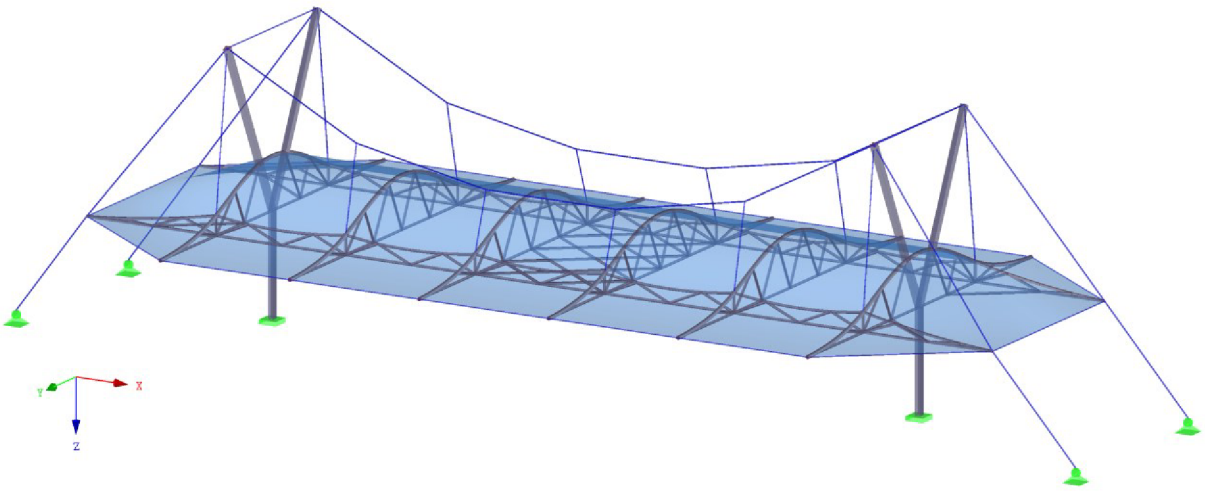

Fig. 71 Bus Station Roofing – Initial Position [44, IX]

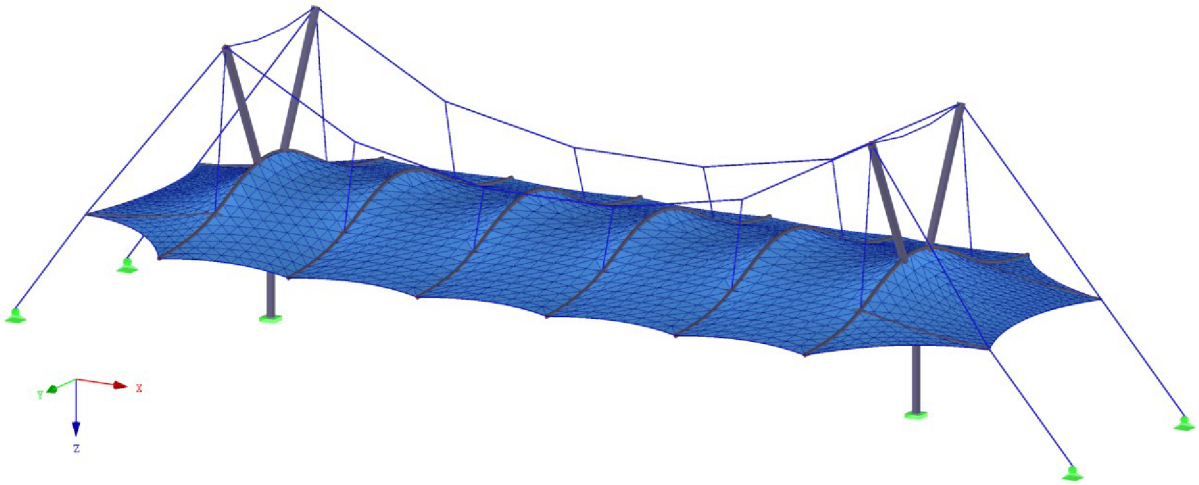

Fig. 72 Bus Station Roofing – Equilibrium Position and Vectors of Principal Forces [44, IX]

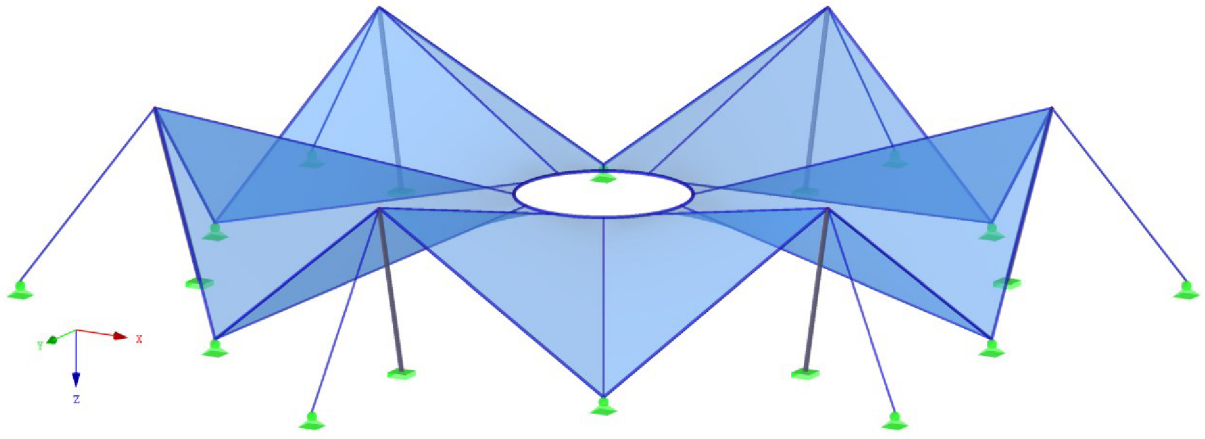

Fig. 73 Tanzbrunnen – Initial Shape

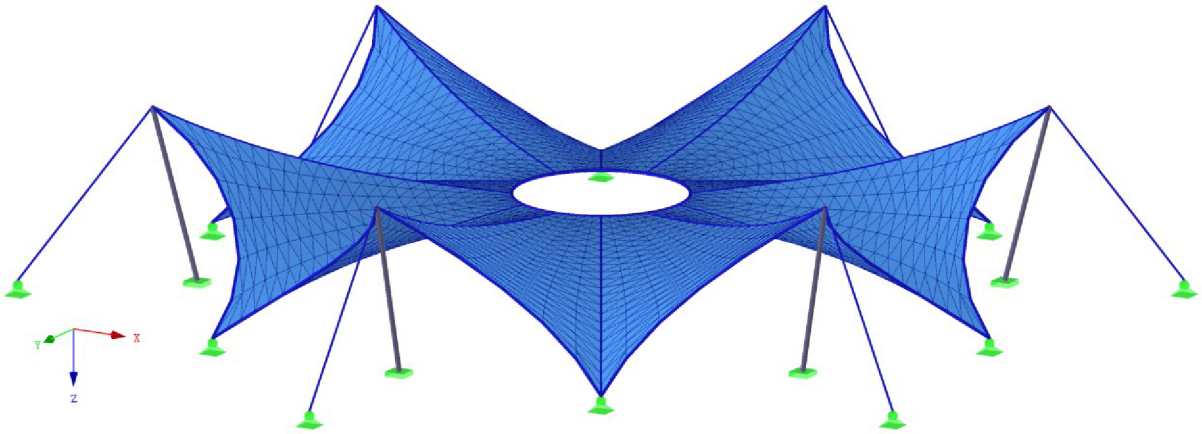

Fig. 74 Tanzbrunnen – Equilibrium Position

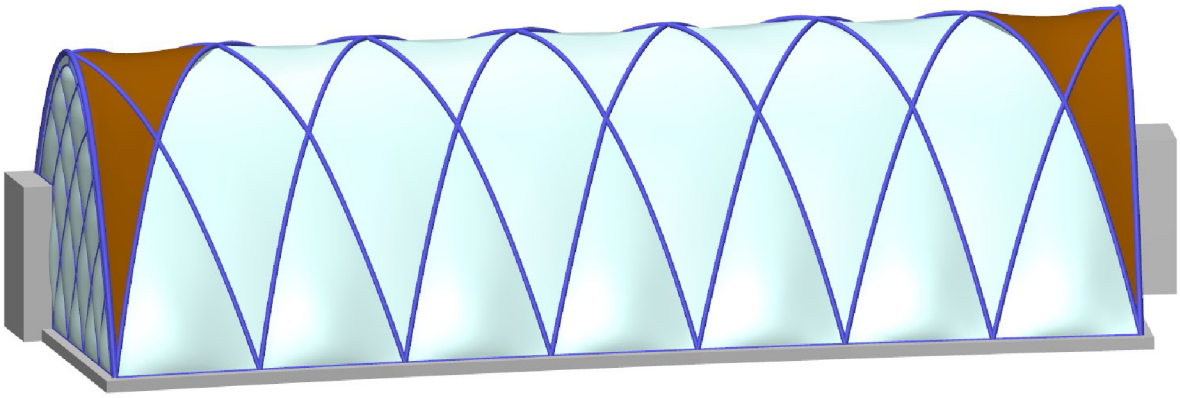

Fig. 75 Greenhouse Made of Pressurized ETFE Cushions – Initial Model [44]

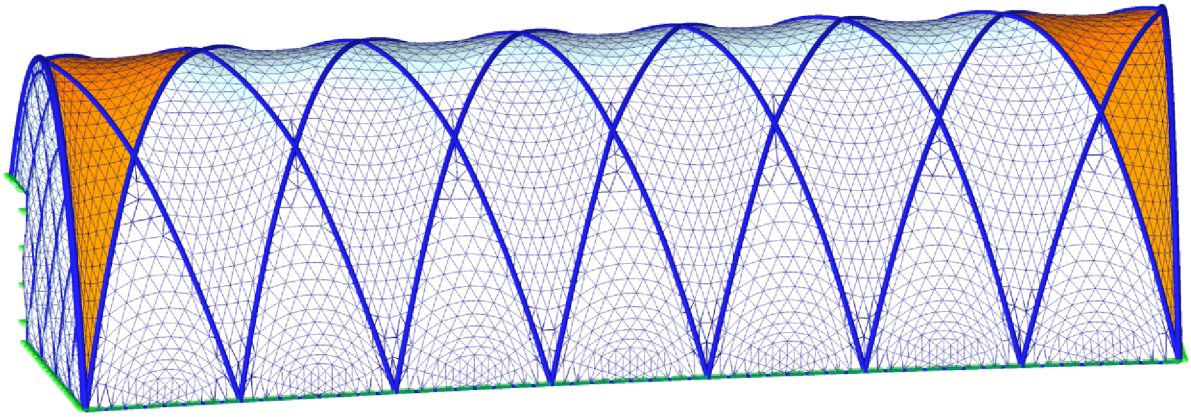

Fig. 76 Greenhouse Made of Pressurized ETFE cushions – Equilibrium Position [44]

5 STRUCTURAL ANALYSIS

The membrane structures are a really special in analysis requirements, which is the consequence of their virtually zero bending stiffness. That implies the singularity when the material stiffness matrix is only taken into account. Thus, the geometric stiffness matrix needs to be regular, which implies tension in the whole membrane. Therefore, if compression occurs, a special treatment has to be performed in the implemented codes. This is done by applying an artificial minimal tension in the numerical analysis.

However while the geometrical nonlinearities could be accounted by a general description of the chapters *Continuum Mechanics* and*Finite Element Procedure* , using the Updated Lagrangian formulation (ULF) or the Total Lagrangian formulation (TLF), being quite standard in terms of the continuum mechanics, the material nonlinearity of membrane structures is quite unique issue. If a membrane loses its pretension, the compression is released by the surface wrinkling and the standard membrane theory does not describe such a state. This is one of the most important and difficult tasks of the structural analysis of such a type of structures.

As this short introduction suggests, the description and studying of the wrinkling phenomenon was one of the crucial parts of this thesis. Thus, this chapter includes the subchapter that deals with the introduction into the physical problem and the current state of the art. Later, the subchapter with the proposed solving technique called ***Wrinkling Separation*** and ***Elastic Prediction Modification*** is presented, where the formulated method is completed by verification examples. Further, the next subchapter present analyses focused on the wrinkling phenomenon. At the end of this chapter, the results of static and dynamic analyses of the Tanzbrunnen membrane structure with consideration the proposed technique, are presented.

5.1 WRINKLING OF MEMBRANE SURFACES

The special behaviour of the membrane material is the subject of research for many decades. The pioneer contribution to this field, studied on the flat sheet metal girders with very thin metal web, was already presented by the author H. Wagner [45], who proposed the *Tension Field Theory (TF)*. The TF assumes that a membrane has zero flexural stiffness. While the membrane is stretched, the classic membrane theory for the evaluation of the stress state is valid, however, when the compression is about to appear, in the consequence of the zero flexural stiffness assumption, the compression is immediately released by the buckling effect, thus by the development of little waves aligned with the tensile direction.

Essentially, there are two ways for solving the wrinkled state of the membrane in FEA. The first way is to use an extremely dense FE discretization and the in-plane stiffness in both the tension and the compression directions, while the bending stiffness is zero. Such a mesh allows the material to follow the little waves, but this is inadequate costly solution and it inevitably depends on the mesh. The second way, which is further categorised, focuses on the separation of the total strain into the elastic and wrinkling part. Such a solution allows for using the FE discretization, where the particular elements are much bigger than the wrinkles. Even so the particular wrinkles are not modelled here, the method is not so strongly dependent on the mesh

as in the case of the previous method and, in terms of the continuum analysis, the global stress state is precisely described by such a *'smeared wrinkle'* analysis.

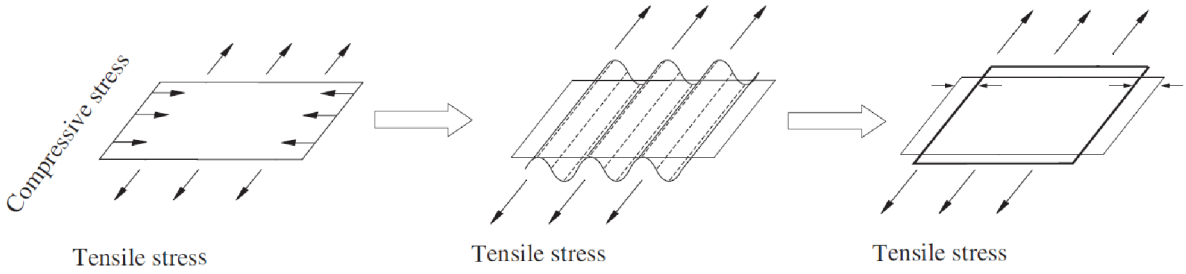

Fig. 77 Applied Stress (left), Real Physical Deformation (Wrinkling) of Membrane (middle), In-Plane Deformation/Strain (right). [46]

The figure (Fig. 77) shows the described physical process, where the compressive stresses are released by the local buckling effect followed by the appearance of wrinkles. If the presented square is assumed to be a quadrangle FE, the out-of-plane deformations presented in the middle of the figure cannot be properly modelled and the in-plane strains presented in the right part of the figure are obtained. Such strains do not properly represent the real physical behaviour and thus, it is necessary to decompose the deformation into an elastic and a wrinkling part (Fig. 78).

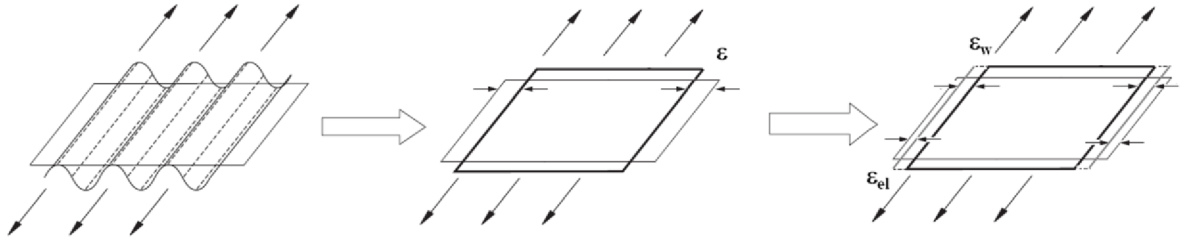

Fig. 78 Real Physical Deformation (Wrinkling) of Membrane (left), Total In-Plane Deformation/Strain (middle), Separation of Total Deformation/Strain into Elastic and Wrinkling Part (right) [46]

The methods of proper strain decomposition have been the subject of many researchers for decades, and the possible methods are briefly mentioned bellow, separated into two main groups, namely *Kinematics Modifications (KM)* and *Material Modifications (MM)* [42].

5.1.1 Kinematic Modifications (KM)

This method, proposed by C.H. Wu and T.R. Cansfield [47] and further extended by D.G. Roddeman et al [48, 49], is based on the modification of the total deformation gradient ${}^{t}_{0}\mathbf{F}$ to eliminate the nonphysical in-plane strains caused by the wrinkling effect.

The orthonormal vectors n_1 and n_2 denotes the principal directions of the Cauchy stress, $\bar{l}$ represents the real deformed length while l is the fictive non-wrinkled length and b is the deformed width. As derived in the contribution by D.G. Roddeman et al [48], the original deformation gradient ${}^{t}_{0}\mathbf{F}$ is subsequently modified

$$ {}^{t}_{0}\bar{\mathbf{F}} = (\mathbf{I} + \beta\, \mathbf{n}_1\mathbf{n}_1)\ {}^{t}_{0}\mathbf{F} \tag{5.1} $$

where $\mathbf{I}$ denotes the identity matrix, β is the parameter, which express a measure of the membrane wrinkling and is never negative because if the wrinkles disappear, the modified

deformation gradient ${}^{t}_{0}\bar{\mathbf{F}}$ unifies with the standard deformation gradient ${}^{t}_{0}\mathbf{F}$ and also, it can be said that $\bar{l}$ can only be greater or equal to l, never smaller. The β parameter is determined by the coupled nonlinear conditions, as described in the paper mentioned above.

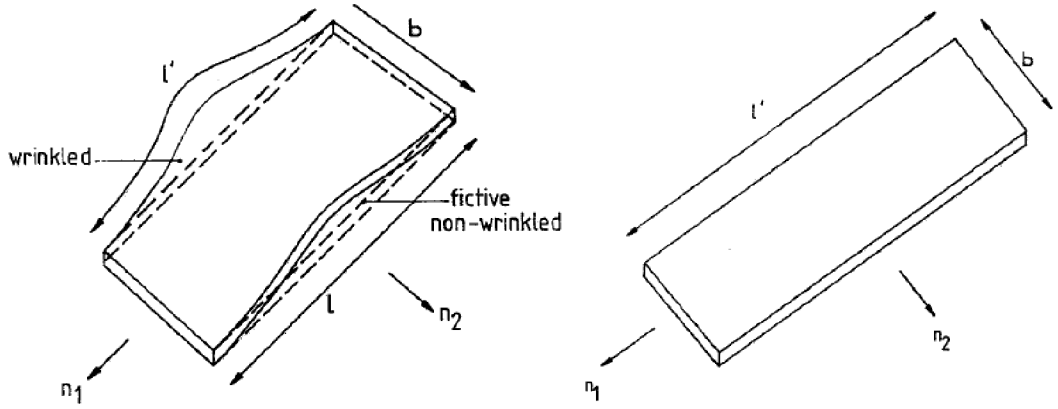

Fig. 79 Wrinkled Membrane with Deformed Length $\bar{l}$, Fictive Non-Wrinkled Membrane Length l and Deformed Width b (left). Wrinkled Membrane Part Straight in Tangent Plane Determined by n_1 and n_2 (right). [48]

Thus, the main idea of this method can be illustrated by the description written in the contribution [48]: *'The tensor* $(\mathbf{I} + \beta\, \mathbf{n}_1\mathbf{n}_1)$ *lengthens the fictive non-wrinkled membrane part to become just as long as the real wrinkled membrane part.'* This can be seen on the right side of the figure above (Fig. 79).

Using the modified deformation gradient ${}^{t}_{0}\bar{\mathbf{F}}$, different measures of the modified strain tensors can be calculated as, for example, the Green-Lagrange and the infinitesimal strain tensors are rewritten in the following formulas, analogous to (2.7) and (2.11)

$$ {}^{t}_{0}\mathbf{E} = \frac{1}{2}({}^{t}_{0}\bar{\mathbf{F}}^{T}\, {}^{t}_{0}\bar{\mathbf{F}} - \mathbf{I}) \tag{5.2} $$

$$ {}^{t}_{0}\boldsymbol{\varepsilon} = \frac{1}{2}({}^{t}_{0}\bar{\mathbf{F}} + {}^{t}_{0}\bar{\mathbf{F}}^{T}) - \mathbf{I} \tag{5.3} $$

Consequently, the different measures of the real/physical stresses in the wrinkled membrane are also calculated. It is important to note that no material assumption was used when deriving this method. Further interesting contribution related to this method was published by H. Schoop et al [50].

5.1.2 Material Modifications (MM)

In contrast to the previous method where the deformation gradient was modified to obtain the real non-wrinkled configuration by the kinematic modifications (KM), the material modification (MM) methods consider the wrinkling phenomenon as a special case of perfect plasticity, and therefore, the total strain $\boldsymbol{\varepsilon}$ (*note: the fictive strain in the language of the method mentioned above*) is decomposed into the elastic $\boldsymbol{\varepsilon}_e$ and the wrinkling $\boldsymbol{\varepsilon}_w$ part. The wrinkling is a zero strain energy process. The standard strain decomposition, known in the material nonlinearity, is written as

$$ \boldsymbol{\varepsilon} = \boldsymbol{\varepsilon}_e + \boldsymbol{\varepsilon}_w \tag{5.4} $$

Many approaches for the material modification (MM) process were proposed by various authors. For example, the contribution of the authors T. Akita et al [46] uses a special projection technique, which separates the elastic and the wrinkling parts of the strain and maps the original constitutive matrix to the modified one (Fig. 80). By this method, the nonphysical stresses belonging to the wrinkling strain are released.

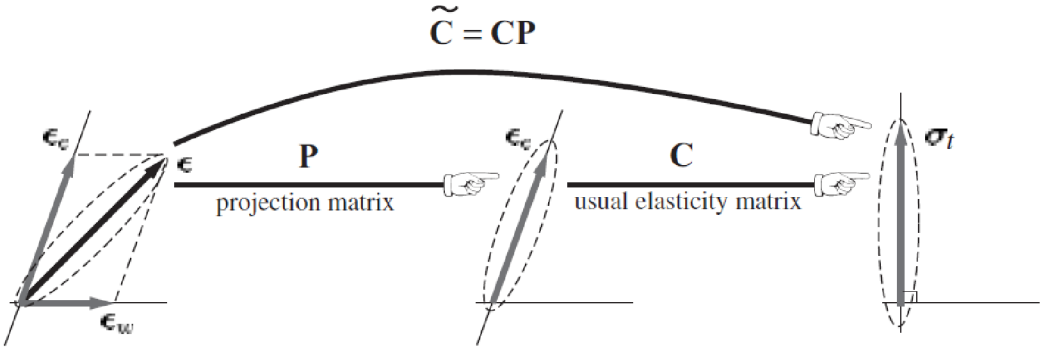

Fig. 80 Visualization of Strain Decomposition with Usage of Projection Matrix $\mathbf{P}$ *and Consequent Stress Calculation with Constitutive Matrix* $\mathbf{C}$*, or Direct Stress Calculation with Usage of Modified Constitutive Matrix* $\tilde{\mathbf{C}}$ *[46].*

The derivation of the projection matrix **P** can be found in [46]. This contribution was also an inspiration for the work by A. Jrusjrungkiat [42] and A. Jrusjrungkiat et al [51].

There are further proposed approaches, where the modified strass-strain relation in a wrinkled membrane is mostly used for dealing with the wrinkling phenomenon.

The way of the material modification (MM) is the method published more widely, such as in [52, 53, 54, 55, 56, 57, 58, 59], and many others. An interesting contribution which compares different methods from both groups was written by Y. Miyazaki [60]. Many other proposals, presented analyses, derivations of the analytical examples and their comparisons can be found in the following contributions [60, 61, 62, 63, 64, 65, 66, 67, 68, 69, 70, 71].

At the end of this chapter, it is necessary to conclude that the majority of the proposed methods are not general in the sense of using them for the anisotropy and the nonlinearity of the material used for a membrane. Some of them are usable exclusively for linear isotropic materials, another also for anisotropic linear material models, but the general methods are rare. Moreover, when studying the research articles, the fact that many methods merely approximate the real physical stress state in the wrinkled membrane can be observed on the presented numerical examples which are compared with the analytical solutions. These facts are the reason for the work of many researchers and their subsequent publications in this field.

5.2 WRINKLING CRITERIA

In order to determine the actual state of the membrane, the wrinkling criteria were developed to distinguish whether the membrane is in a taut, wrinkled or slack state (Fig. 81), and they are widely used for both of the above-mentioned groups of the methods for dealing with the artificial stress caused by fictitious strain [42, 52, 55, 59, 72, 73, 74, 75].

Tab. 1 Wrinkling Criteria to Distinguish Membrane Status

Membrane state	Principal stress criteiron	Principal strain criterion	Mixed criterion
Taut	$S_{min} > 0$	$E_{min} > 0$	$S_{min} > 0$
Wrinkled	$S_{min} \leq 0$ and $S_{max} > 0$	$E_{min} \leq 0$ and $E_{max} > 0$	$S_{min} \leq 0$ and $E_{max} > 0$
Slack	$S_{min} \leq 0$ and $S_{max} \leq 0$	$E_{min} \leq 0$ and $E_{max} \leq 0$	$E_{max} \leq 0$

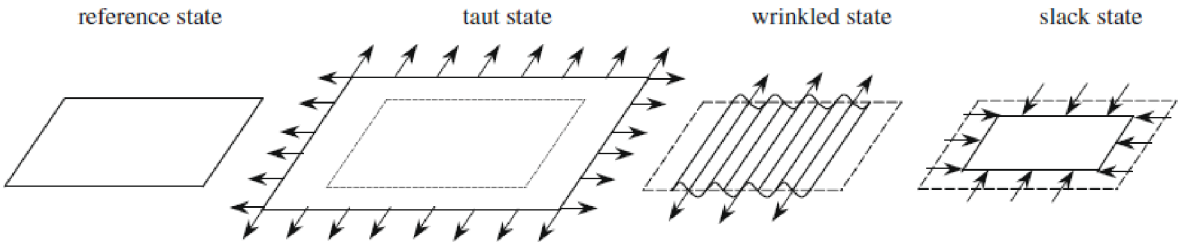

Fig. 81 State of Membrane: Taut, Wrinkled and Slack [42]

The principal stress and principal strain criterion can be misleading as the principal stress criterion is not reliable when detecting the wrinkled or slack state, while the principal strain criterion is not reliable when detecting the taut or wrinkled state. Therefore, the mixed criterion is considered and widely used as a suitable choice.

This status recognition is a tool further used for determining which type of the algorithm should be applied to the actual state of the particular FE integration node.

5.3 PLANE STRESS STATE IN CLASSIC MEMBRANE THEORY

Before the next chapter including a description of the proposed method is presented, the basic formulas used later are listed here [1, 2, 3, 76], starting with the stress-strain law for the elastic and plastic materials, continuing with the constitutive matrix for the isotropic and orthotropic materials

$$\boldsymbol{\sigma} = \mathbf{C}\,\boldsymbol{\varepsilon}_{\mathrm{e}} \tag{5.5}$$

$$\boldsymbol{\sigma} = \mathbf{C}\,(\boldsymbol{\varepsilon} - \boldsymbol{\varepsilon}_{\mathrm{p}}) \tag{5.6}$$

$$\mathbf{C} = \begin{bmatrix} C_{1111} & C_{1122} & C_{1112} \\ C_{2211} & C_{2222} & C_{2212} \\ C_{1211} & C_{1222} & C_{1212} \end{bmatrix} \tag{5.7}$$

where $\boldsymbol{\sigma}$ denotes the actual stress, $\boldsymbol{\varepsilon}$, $\boldsymbol{\varepsilon}_{\mathrm{e}}$, $\boldsymbol{\varepsilon}_{\mathrm{p}}$ are the total, elastic and plastic strain components respectively, $\mathbf{C}$ is the plane stress constitutive relation, which can be described for the isotropic or orthotropic materials as follows:

$$\mathbf{C} = \begin{bmatrix} \dfrac{E}{1-\nu^2} & \dfrac{\nu E}{1-\nu^2} & 0 \\ \dfrac{\nu E}{1-\nu^2} & \dfrac{E}{1-\nu^2} & 0 \\ 0 & 0 & G \end{bmatrix} = \frac{E}{1-\nu^2} \begin{bmatrix} 1 & \nu & 0 \\ \nu & 1 & 0 \\ 0 & 0 & \dfrac{1-\nu}{2} \end{bmatrix} \tag{5.8}$$

$$\mathbf{C} = \begin{bmatrix} \frac{E_x}{1-\nu_{xy}\nu_{yx}} & \frac{\nu_{xy}E_y}{1-\nu_{xy}\nu_{yx}} & 0 \\ \frac{\nu_{yx}E_x}{1-\nu_{xy}\nu_{yx}} & \frac{E_y}{1-\nu_{xy}\nu_{yx}} & 0 \\ 0 & 0 & G_{xy} \end{bmatrix} = \frac{1}{1-\nu_{xy}\nu_{yx}} \begin{bmatrix} E_x & \nu_{xy}E_y & 0 \\ \nu_{yx}E_x & E_y & 0 \\ 0 & 0 & (1-\nu_{xy}\nu_{yx})G_{xy} \end{bmatrix} \tag{5.9}$$

where E, E_x, E_y are the elasticity moduli, and ν, ν_{xy}, ν_{yx} denote the transverse contraction coefficients for the isotropic and orthotropic constitutive laws.

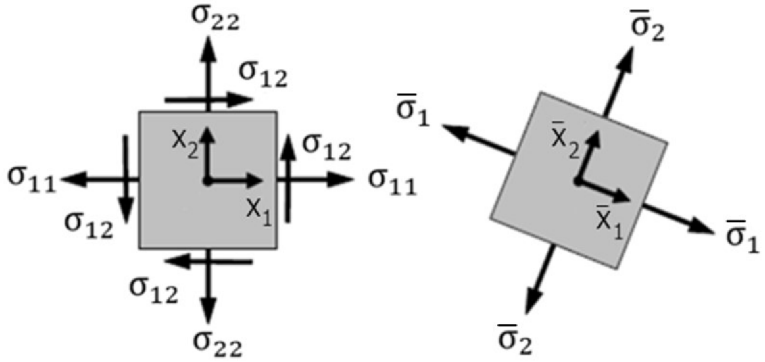

Fig. 82 Stress State in Planar and Main Directions ([77] with Modifications)

The figure above (Fig. 82) displays the stress state in the planar and main directions. The principle stress values can be determined by evaluating the eigenvalue problem of the stress state. Bellow, the stress is written in the matrix notation

$$\boldsymbol{\sigma} = \begin{bmatrix} \sigma_{11} & \sigma_{12} \\ \sigma_{21} & \sigma_{22} \end{bmatrix} \tag{5.10}$$

$$(\boldsymbol{\sigma} - \sigma_0 \mathbf{I})\,\mathbf{n} = \mathbf{0} \tag{5.11}$$

Since the normal vector $\mathbf{n}$ relates to the unit length, the tensor in the brackets has to be singular, thus the following relation has to be fulfilled:

$$\det(\boldsymbol{\sigma} - \sigma_0 \mathbf{I}) = \begin{bmatrix} \sigma_{11} - \sigma_0 & \sigma_{12} \\ \sigma_{21} & \sigma_{22} - \sigma_0 \end{bmatrix} = (\sigma_0)^2 - (\sigma_{11} + \sigma_{22})\,\sigma_0 + (\sigma_{11}\sigma_{22} - (\sigma_{12})^2) \tag{5.12}$$

where $\mathbf{I}$ is the unit matrix, and σ_0 denotes the eigenvalues, thus the magnitude of the principal stresses in the first and the second main direction $\bar{\sigma}_1$ and $\bar{\sigma}_2$

$$\bar{\sigma}_{1,2} = \frac{(\sigma_{11} + \sigma_{22})}{2} \pm \sqrt{\left(\frac{\sigma_{11} - \sigma_{22}}{2}\right)^2 + (\sigma_{12})^2} \tag{5.13}$$

Bellow, the well-known vizualisation of the stress state using the Mohr circle (Fig. 83) is attached.

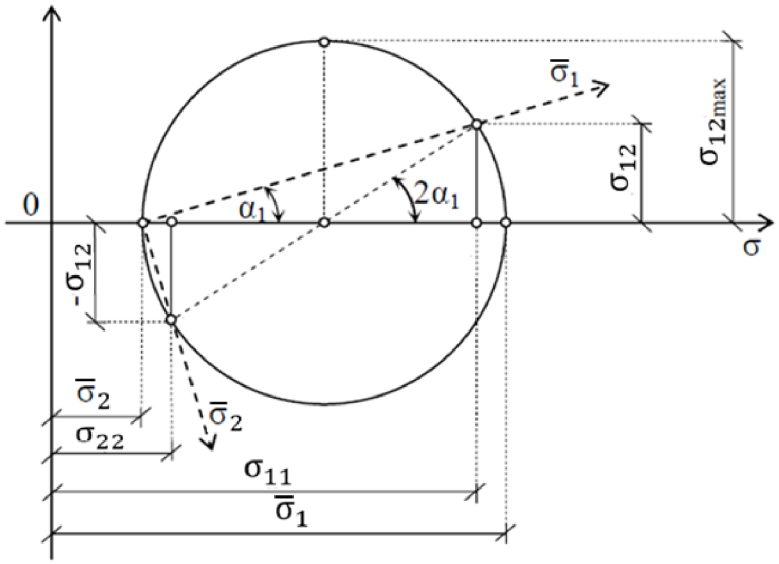

Fig. 83 Mohr Circle for Stress Transformation

The angle between the planar and the main directions α is given by the following equation:

$$\alpha = \frac{1}{2} tan^{-1}\left(\frac{2\sigma_{12}}{\sigma_{11} - \sigma_{22}}\right) \tag{5.14}$$

For the sake of distinguishing the physical values in the planar Cartesian coordinate system of the element and in the main stress directions, a bar is used. Whenever the value is written without the bar, it denotes the planar Cartesian coordinate system directions, and when the bar is used, the physical values are considered as transformed into the direction of the main stresses.

$$\boldsymbol{\sigma} = [\, \sigma_{11} \quad \sigma_{22} \quad \sigma_{12} \,]^{\mathrm{T}} \tag{5.15}$$

$$\bar{\boldsymbol{\sigma}} = [\, \bar{\sigma}_1 \quad \bar{\sigma}_2 \quad 0 \,]^{\mathrm{T}} \tag{5.16}$$

The transformation of the membrane strains and the stress strain matrix between the planar Cartesian coordinate system and the axial system given by the directions of the main stresses is performed by the following transformation matrix:

$$\mathbf{T}_\varepsilon = \begin{bmatrix} cos^2\,\bar{x}_1x_1 & cos^2\,\bar{x}_1x_2 & cos\,\bar{x}_1x_1\,cos\,\bar{x}_1x_2 \\ cos^2\,\bar{x}_2x_1 & cos^2\,\bar{x}_2x_2 & cos\,\bar{x}_2x_1\,cos\,\bar{x}_2x_2 \\ 2\,cos\,\bar{x}_1x_1\,cos\,\bar{x}_2x_1 & 2\,cos\,\bar{x}_1x_2\,cos\,\bar{x}_2x_2 & cos\,\bar{x}_1x_1\,cos\,\bar{x}_2x_2 + cos\,\bar{x}_2x_1\,cos\,\bar{x}_1x_2 \end{bmatrix} \tag{5.17}$$

where $\bar{x}_i$ and x_i denote the main and the planar Cartesian coordinate axes, so the matrix can be rewritten by using the angle α

$$\mathbf{T}_\varepsilon = \begin{bmatrix} cos^2\,\alpha & sin^2\,\alpha & sin\,\alpha\ cos\,\alpha \\ sin^2\,\alpha & cos^2\,\alpha & -sin\,\alpha\ cos\,\alpha \\ -2\,sin\,\alpha\ cos\,\alpha & 2\,sin\,\alpha\ cos\,\alpha & cos^2\,\alpha - sin^2\,\alpha \end{bmatrix} \tag{5.18}$$

The strains transformation is given by the equations

$$\bar{\boldsymbol{\varepsilon}} = \mathbf{T}_\varepsilon\, \boldsymbol{\varepsilon} \tag{5.19}$$

$$\boldsymbol{\varepsilon} = \mathbf{T}_\varepsilon^{-1}\, \bar{\boldsymbol{\varepsilon}} \tag{5.20}$$

And the transformation of the constitutive matrix can be written as

$$\bar{\mathbf{C}} = \mathbf{T}_{\varepsilon}^{-\mathrm{T}}\, \mathbf{C}\, \mathbf{T}_{\varepsilon}^{-1} \tag{5.21}$$

$$\mathbf{C} = \mathbf{T}_{\varepsilon}^{\mathrm{T}}\, \bar{\mathbf{C}}\, \mathbf{T}_{\varepsilon} \tag{5.22}$$

5.4 YIELDING CRITERIA FOR ISOTROPIC NONLINEAR ELASTIC AND PLASTIC MATERIAL MODELS

Some of the well-known yielding criteria for the isotropic nonlinear elastic and plastic material models are listed here in the form of the figures attached below (Fig. 84, Fig. 85, Fig. 86). Their detailed description can be found in the literature, for example [1, 3]. It is possible to combine these models with the further described ***Wrinkling Separation*** and ***Elastic Prediction Modification*** procedures for an appropriate representation of such combined nonlinearities, namely the wrinkling and the yielding process together, as described in Subchapter (5.5.2).

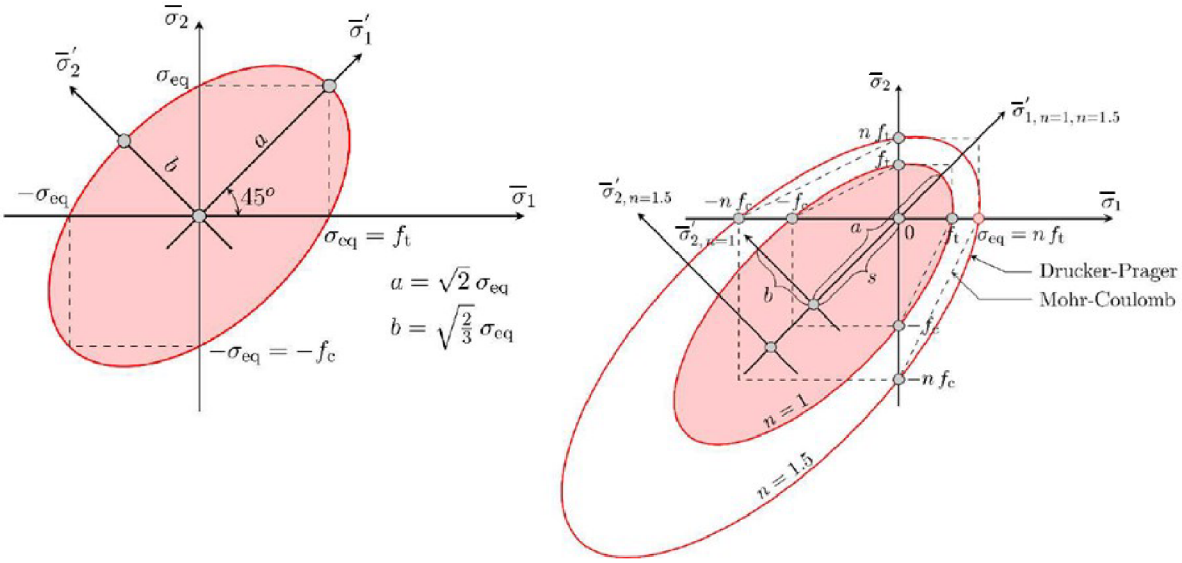

Fig. 84 Visualization of Von Mises and Drucker-Prager Yielding Criteria in Plane of $\bar{\sigma}_1$ and $\bar{\sigma}_2$ ($\bar{\sigma}_3 = 0$) [76]

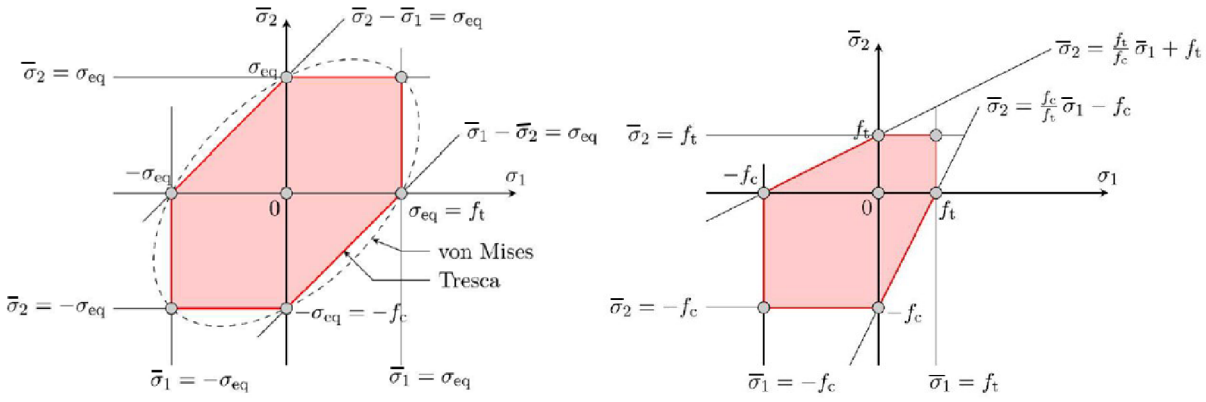

Fig. 85 Visualization of Tresca and Mohr-Coulomb Yielding Criteria in Plane of $\bar{\sigma}_1$ and $\bar{\sigma}_2$ ($\bar{\sigma}_3 = 0$) [76]

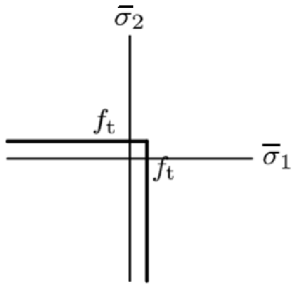

Fig. 86 Visualization of Rankine Yielding Criterion in Plane of $\bar{\sigma}_1$ and $\bar{\sigma}_2$ ($\bar{\sigma}_3 = 0$)

5.5 WRINKLING SEPARATION AND ELASTIC PREDICTION MODIFICATION

As a part of this thesis, the proposal of a new technique dealing with the wrinkling phenomenon described above was made. This method, called **Wrinkling Separation** and **Elastic Prediction Modification** processes, could be categorized among the material modification (MM) techniques. The actual strain is decomposed into the real in-plane and wrinkling components and the fictitious stress is decomposed into the real and nonphysical parts, released by the local buckling process. The presented method will be further followed by numerical examples.

Following the mixed wrinkling criterion, the actual state of the membrane is determined. If the membrane is tensioned in both directions, the classic membrane theory is used, whereas if both principal strains are negative, the slack status is detected and all the stress components are released by the wrinkling effect, and the tangent stiffness becomes a zero matrix. If the wrinkled status is detected, the real stress state is the unknown to be determined.

Redrawing the above presented figure of the wrinkling process (Fig. 78) into the following form shown in the figure below (Fig. 87), the real sequence of the physical processes is described. As the membrane is tensioned in one direction, the transverse elastic deformation is proceeding first according to the Poisson effect. Until now, no wrinkling occurs. However, when the transverse contraction continues beyond this limit value, the compression occurs and at the same time, this compression is released by the wrinkling effect. The real stress state is already given by the first step of this sequence as the wrinkling process itself does not influence neither the contracted nor the stretched direction. Thus, the stress state on the border of the first and the second sequence step is the aim of the following process.

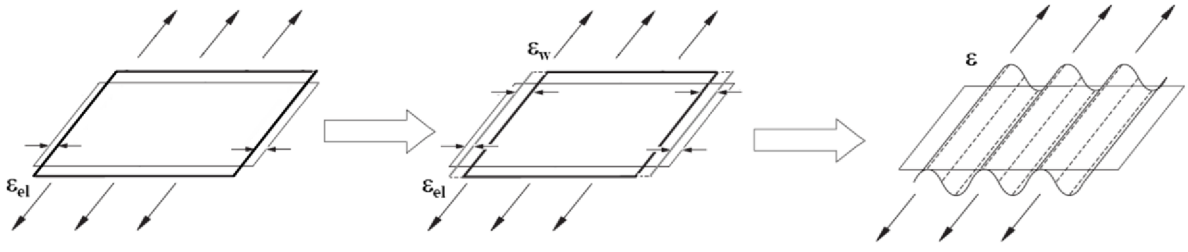

Fig. 87 Transverse Contraction (left), Additional Contraction Causing Wrinkling Effect (middle and right)

5.5.1 Wrinkling Separation Procedure for Anisotropic Linear Elastic Material Models

The whole process is described on the level of each FE integration point from the moment the total strain is known until the moment the real physical stress is determined, the total strain is

decomposed and the constitutive matrix is derived. First, the elastic stress estimation in the planar Cartesian coordinate system is performed

$$\boldsymbol{\sigma} = \mathbf{C}\,\boldsymbol{\varepsilon} \tag{5.23}$$

Further, the stress is transformed into the main directions

$$\boldsymbol{\sigma} \rightarrow \bar{\boldsymbol{\sigma}} = [\,\bar{\sigma}_1 \quad \bar{\sigma}_2 \quad 0\,]^{\mathrm{T}} \tag{5.24}$$

Now, the case when the lower principle stress $\bar{\sigma}_2 < 0$ and the higher principle strain $\tilde{\varepsilon}_1 > 0$ (where generally the principle directions do not coincide as denoted by different accents) is assumed, denoting the membrane is in the wrinkled state. The actual stress is unknown as the elastic estimation $\boldsymbol{\sigma} \rightarrow \bar{\boldsymbol{\sigma}}$ using the classic membrane theory does not give the proper values.

For the actual stress state estimation, the **Wrinkling Separation** procedure uses the above-defined assumption that the negative stress $\bar{\sigma}_2$ is released by the local buckling effect and thus the real elastic stress $\bar{\sigma}_2^{\,e} = 0$. As the value of $\bar{\sigma}_1$ is influenced by the coefficient of the transverse contraction even for the wrinkling part of the strain, its value is not correct and thus the elastic stress $\bar{\sigma}_1^{\,e}$ is set as unknown $\bar{\sigma}_1^{\,e} = ?$. Furthermore, the actual strain and the constitutive matrix are transformed into the direction of the principle stresses as denoted by the bar accent.

$$\bar{\boldsymbol{\varepsilon}} = \mathbf{T}_{\varepsilon}\,\boldsymbol{\varepsilon} = [\,\bar{\varepsilon}_{11} \quad \bar{\varepsilon}_{22} \quad \bar{\varepsilon}_{12}\,]^{\mathrm{T}} \tag{5.25}$$

$$\bar{\mathbf{C}} = \mathbf{T}_{\varepsilon}^{-\mathrm{T}}\,\mathbf{C}\,\mathbf{T}_{\varepsilon}^{-1} = \begin{bmatrix} \bar{C}_{1111} & \bar{C}_{1122} & \bar{C}_{1112} \\ \bar{C}_{2211} & \bar{C}_{2222} & \bar{C}_{2212} \\ \bar{C}_{1211} & \bar{C}_{1222} & \bar{C}_{1212} \end{bmatrix} \tag{5.26}$$

where $\bar{\varepsilon}_{12} \neq 0$ and $\bar{\mathbf{C}}$ is the full occupied matrix for the general linear anisotropic material model. However, since the membrane is in the wrinkled state, the elastic stress $\bar{\sigma}_1^{\,e}$ is positive. As the membrane does not wrinkle in the direction of the first principal stress $\bar{\sigma}_1$, the strain component $\bar{\varepsilon}_{11}$ does not require further decomposition, and it holds $\bar{\varepsilon}_{11}^{\,e} = \bar{\varepsilon}_{11}$ and $\bar{\varepsilon}_{11}^{\,w} = 0$, where the indexes *e* and *w* denote the elastic and the wrinkling strain parts. Following these physical assumptions, the limit state of the wrinkling initialization depicted on the left side of the figure (Fig. 87) is given by the equation

$$\begin{bmatrix} \bar{\sigma}_1^{\,e} = ? \\ 0 \\ 0 \end{bmatrix} = \begin{bmatrix} \bar{C}_{1111} & \bar{C}_{1122} & \bar{C}_{1112} \\ \bar{C}_{2211} & \bar{C}_{2222} & \bar{C}_{2212} \\ \bar{C}_{1211} & \bar{C}_{1222} & \bar{C}_{1212} \end{bmatrix} \begin{bmatrix} \bar{\varepsilon}_{11}^{\,e} = \bar{\varepsilon}_{11} \\ \bar{\varepsilon}_{22}^{\,e} = ? \\ \bar{\varepsilon}_{12}^{\,e} = ? \end{bmatrix} \tag{5.27}$$

This system of three equations with three unknowns, namely the elastic stress $\bar{\sigma}_1^{\,e}$ and the elastic strains $\bar{\varepsilon}_{22}^{\,e}$ and $\bar{\varepsilon}_{12}^{\,e}$, represent the state when wrinkling starts to appear. By solving this system, the elastic part is obtained and the wrinkling part is separated out. For solving this, the equation (5.27) is modified as follows:

$$\begin{bmatrix} \bar{\sigma}_A^{\,e} = ? \\ 0 \end{bmatrix} = \begin{bmatrix} \bar{C}_{AA} & \bar{C}_{AB} \\ \bar{C}_{BA} & \bar{C}_{BB} \end{bmatrix} \begin{bmatrix} \bar{\varepsilon}_A^{\,e} = \bar{\varepsilon}_{11} \\ \bar{\varepsilon}_B^{\,e} = ? \end{bmatrix} \tag{5.28}$$

Solving the unknown elastic strains $\bar{\varepsilon}_{22}^{e}$ and $\bar{\varepsilon}_{12}^{e}$

$$0 = \bar{C}_{BA}\,\bar{\varepsilon}_{11} + \bar{C}_{BB}\,\bar{\varepsilon}_{B}^{e} \tag{5.29}$$

$$\bar{\varepsilon}_{B}^{e} = -\bar{C}_{BB}^{-1}\,\bar{C}_{BA}\,\bar{\varepsilon}_{11} \tag{5.30}$$

$$\begin{bmatrix} \bar{\varepsilon}_{22}^{e} \\ \bar{\varepsilon}_{12}^{e} \end{bmatrix} = -\begin{bmatrix} \bar{C}_{2222} & \bar{C}_{2212} \\ \bar{C}_{1222} & \bar{C}_{1212} \end{bmatrix}^{-1} \begin{bmatrix} \bar{C}_{2211} \\ \bar{C}_{1211} \end{bmatrix} \bar{\varepsilon}_{11} \tag{5.31}$$

Solving the unknown elastic stress $\bar{\sigma}_{1}^{e}$

$$\bar{\sigma}_{1}^{e} = \bar{\sigma}_{A}^{e} = \bar{C}_{1111}\,\bar{\varepsilon}_{11} + \bar{C}_{1122}\,\bar{\varepsilon}_{22}^{e} + \bar{C}_{1112}\,\bar{\varepsilon}_{12}^{e} \tag{5.32}$$

Following the **wrinkling separation** process described above, the artificial stress associated with the in-plane strain representing the buckling effect is separated out and the elastic parts of the stress and the strain tensors are obtained

$$\bar{\boldsymbol{\sigma}}^{\mathrm{e}} = [\,\bar{\sigma}_{1}^{e} \quad 0 \quad 0\,]^{\mathrm{T}} \tag{5.33}$$

$$\bar{\boldsymbol{\varepsilon}}^{\mathrm{e}} = [\,\bar{\varepsilon}_{11} \quad \bar{\varepsilon}_{22}^{e} \quad \bar{\varepsilon}_{12}^{e}\,]^{\mathrm{T}} \tag{5.34}$$

And here, the separated stress and strain values

$$\bar{\boldsymbol{\sigma}}^{\mathrm{w}} = [\,\bar{\sigma}_{1}^{w} \quad \bar{\sigma}_{2} \quad 0\,]^{\mathrm{T}} = [\,(\bar{\sigma}_{1} - \bar{\sigma}_{1}^{e}) \quad \bar{\sigma}_{2} \quad 0\,]^{\mathrm{T}} \tag{5.35}$$

$$\bar{\boldsymbol{\varepsilon}}^{\mathrm{w}} = [\,0 \quad \bar{\varepsilon}_{22}^{w} \quad \bar{\varepsilon}_{12}^{w}\,]^{\mathrm{T}} = [\,0 \quad (\bar{\varepsilon}_{22} - \bar{\varepsilon}_{22}^{e}) \quad (\bar{\varepsilon}_{12} - \bar{\varepsilon}_{12}^{e})\,]^{\mathrm{T}} \tag{5.36}$$

Having obtained the actual stress state in its principal directions, the transformation of the stresses and strains into the planar coordinate system can be performed

$$\boldsymbol{\sigma}^{\mathrm{e}} = \mathbf{T}_{\sigma}^{-1}\,\bar{\boldsymbol{\sigma}}^{\mathrm{e}} = \mathbf{T}_{\varepsilon}^{\mathrm{T}}\,\bar{\boldsymbol{\sigma}}^{\mathrm{e}} \tag{5.37}$$

$$\boldsymbol{\varepsilon}^{\mathrm{e}} = \mathbf{T}_{\varepsilon}^{-1}\,\bar{\boldsymbol{\varepsilon}}^{\mathrm{e}} \tag{5.38}$$

$$\boldsymbol{\sigma}^{\mathrm{w}} = \mathbf{T}_{\sigma}^{-1}\,\bar{\boldsymbol{\sigma}}^{\mathrm{w}} = \mathbf{T}_{\varepsilon}^{\mathrm{T}}\,\bar{\boldsymbol{\sigma}}^{\mathrm{w}} \tag{5.39}$$

$$\boldsymbol{\varepsilon}^{\mathrm{w}} = \mathbf{T}_{\varepsilon}^{-1}\,\bar{\boldsymbol{\varepsilon}}^{\mathrm{w}} \tag{5.40}$$

When rewriting the constitutive law into the following form, the similarity with the general nonlinear material models can be seen.

$$\boldsymbol{\sigma} = \mathbf{C}\,(\boldsymbol{\varepsilon} - \boldsymbol{\varepsilon}^{\mathrm{w}}) \tag{5.41}$$

As written above, if the membrane status is taut, the original constitutive matrix is valid $\mathbf{C}_{\mathrm{t}} = \mathbf{C}$, and if the membrane status is slack, the constitutive matrix $\mathbf{C}_{\mathrm{s}}$ becomes a zero matrix.

$$\mathbf{C}_{\mathrm{t}} = \mathbf{C} = \begin{bmatrix} C_{1111} & C_{1122} & C_{1112} \\ C_{2211} & C_{2222} & C_{2212} \\ C_{1211} & C_{1222} & C_{1212} \end{bmatrix} \tag{5.42}$$

$$\mathbf{C}_{\mathrm{s}} = \begin{bmatrix} 0 & 0 & 0 \\ 0 & 0 & 0 \\ 0 & 0 & 0 \end{bmatrix} \tag{5.43}$$

If the membrane is in the wrinkled status, the constitutive matrix $\mathbf{C}_{\mathrm{w}}$ can be calculated numerically

$$\mathbf{C}_{\mathrm{w}} = \begin{bmatrix} \frac{\partial \sigma_{11}}{\partial \varepsilon_{11}} & \frac{\partial \sigma_{11}}{\partial \varepsilon_{22}} & \frac{\partial \sigma_{11}}{\partial \varepsilon_{12}} \\ \frac{\partial \sigma_{22}}{\partial \varepsilon_{11}} & \frac{\partial \sigma_{22}}{\partial \varepsilon_{22}} & \frac{\partial \sigma_{22}}{\partial \varepsilon_{12}} \\ \frac{\partial \sigma_{12}}{\partial \varepsilon_{11}} & \frac{\partial \sigma_{12}}{\partial \varepsilon_{22}} & \frac{\partial \sigma_{12}}{\partial \varepsilon_{12}} \end{bmatrix} \tag{5.44}$$

Moreover, it can be proven that for the isotropic material, the following analytical constitutive relation holds

$$\mathbf{C}_{\mathrm{w}} = \begin{bmatrix} E & 0 & 0 \\ 0 & 0 & 0 \\ 0 & 0 & k\,G \end{bmatrix} = \begin{bmatrix} E & 0 & 0 \\ 0 & 0 & 0 \\ 0 & 0 & k\,\frac{E}{2(1+\nu)} \end{bmatrix} \tag{5.45}$$

where k is the coefficient of the shear softening, which is dependent on the degree of wrinkling, thus on the relation of the elastic and total strains

$$k = \frac{\varepsilon_{12}^{e}}{\varepsilon_{12}} = \frac{\varepsilon_{11}^{e} - \varepsilon_{22}^{e}}{\varepsilon_{11} - \varepsilon_{22}} \tag{5.46}$$

For the sake of the FEA numerical stability, the real tangential stiffness $\mathbf{C}_{\mathrm{s}}$ or $\mathbf{C}_{\mathrm{w}}$ cannot be used directly as it leads to the oscillations of forces and the deformations during the calculation, and the analysis often even does not converge at all. Thus, the artificial stiffness modification applies in order to avoid such behaviour. The selection of such artificial stiffness can be modified according to the required analysis robustness. These modifications should be understood as the algorithmically tuning of the given software behaviour.

The calculation process is demonstrated with a simple example below, where the selected material is assumed to represent the woven fabric. More complex examples and their results are presented in the next subchapter, so this example was chosen as a basic one, where the principle directions are aligned with the planar directions (Fig. 88). The size of each square membrane is $a = 1.00\,m$, thickness $t = 1.00\,mm$. The imposed deformations are $u_x^1 = u_x^2 = u_x^3 = 10.00\,mm$, $u_y^2 = 20.00\,mm$ and $u_y^3 = 80.00\,mm$ (the upper index denoting the particular model). The first model deforms in the u_y^1 direction according to the elastic transverse contraction coefficient. The other membranes are in the wrinkled state.

$$E_x = 1000.0\ kN/m, E_y = 800.0\ kN/m, G = 100.0\ kN/m, \nu_{xy} = 0.20 \tag{5.47}$$

$$\mathbf{C} = \begin{bmatrix} 1033.1 & 165.3 & 0 \\ & 826.4 & 0 \\ sym. & & 100.0 \end{bmatrix} kN/m \tag{5.48}$$

First, the classic membrane theory is used for the calculation of the elastic stress prediction, which is shown in the following figures (Fig. 89, Fig. 90, Fig. 91).

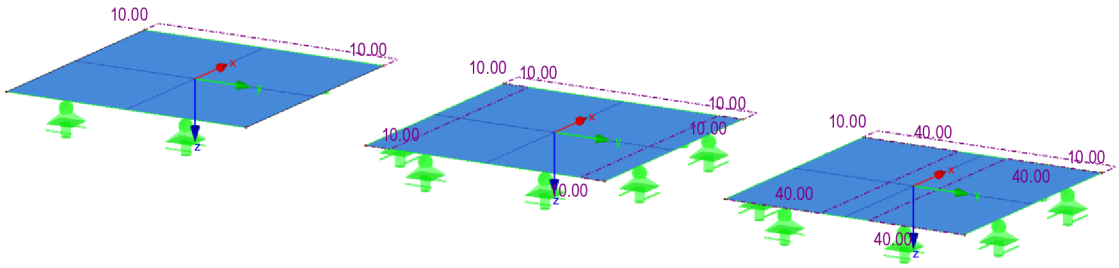

Fig. 88 Three Square Membranes, FE Mesh and Planar Directions Definition, Imposed Deformation Visualization

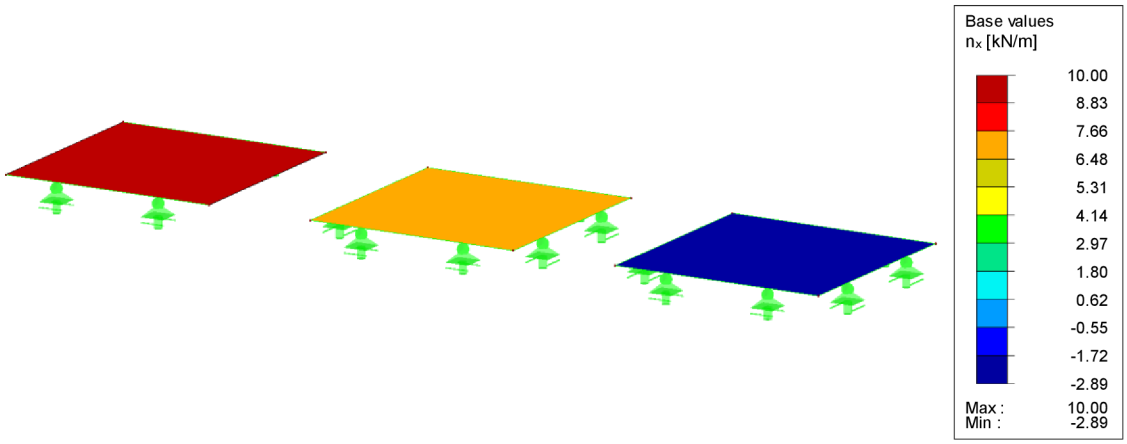

Fig. 89 Elastic Prediction of n_x kN/m

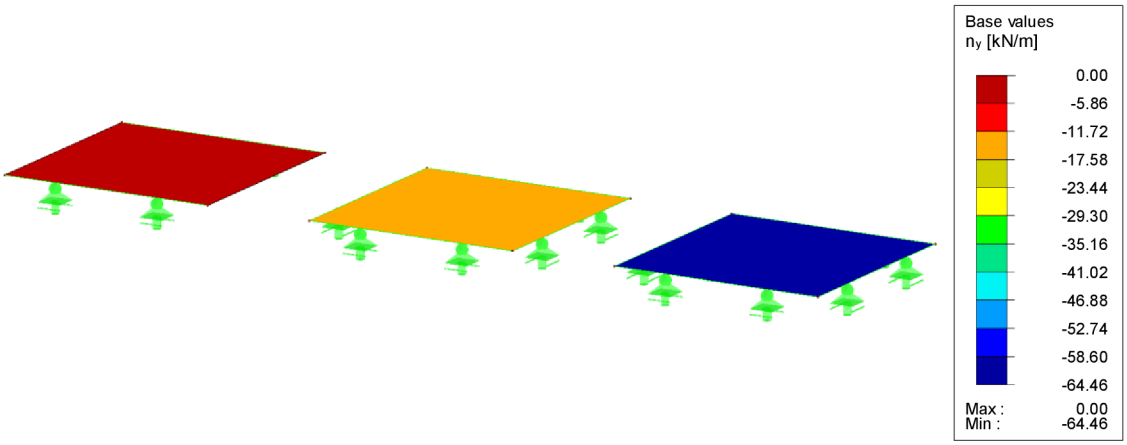

Fig. 90 Elastic Prediction of n_y kN/m

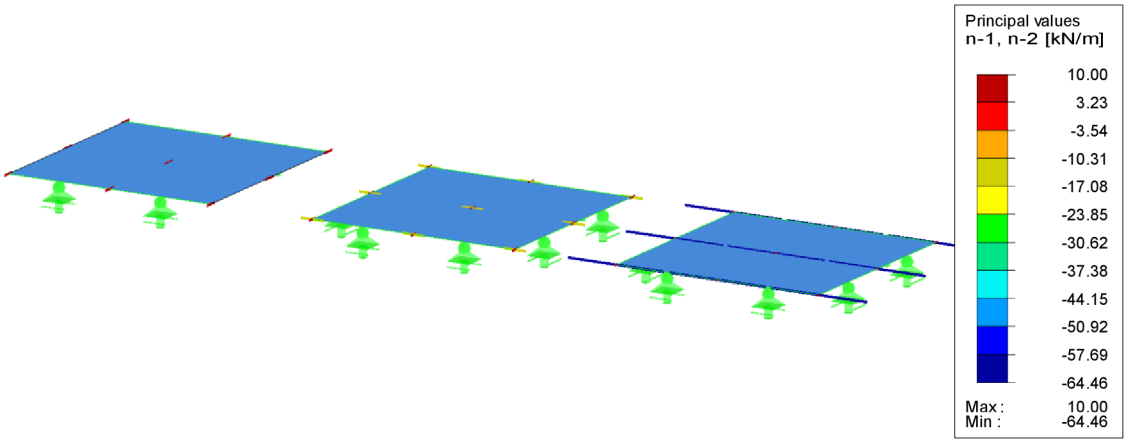

Fig. 91 Vectors Visualizing Elastic Prediction of Principal Forces n_1 and n_2 kN/m

As the membranes 2 and 3 are classified to be in the wrinkled state, the above-described calculation scheme of the wrinkling separation is performed. Therefore, the unnatural effect caused by the in-plane strain belonging to the wrinkling is separated out and the resulting elastic stresses are presented in the figures (Fig. 92, Fig. 93, Fig. 94).

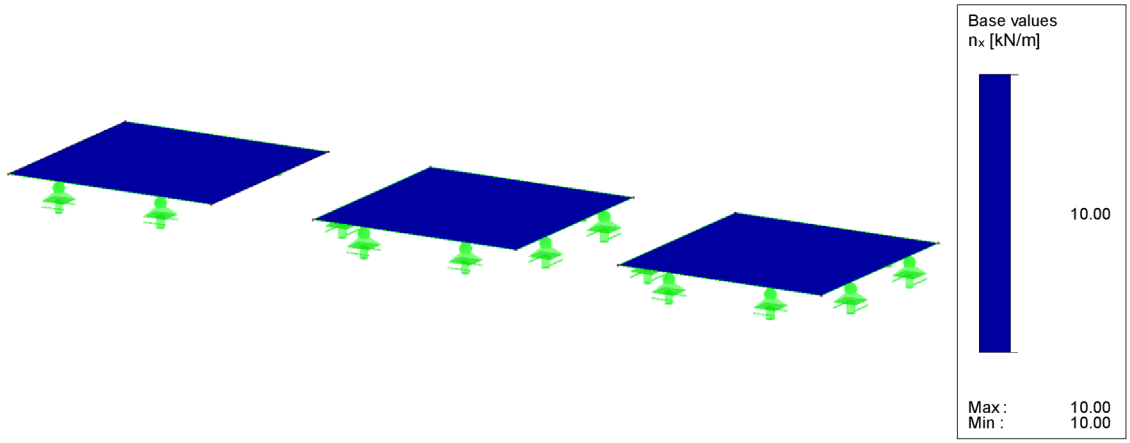

Fig. 92 Elastic Part of Force n_x kN/m

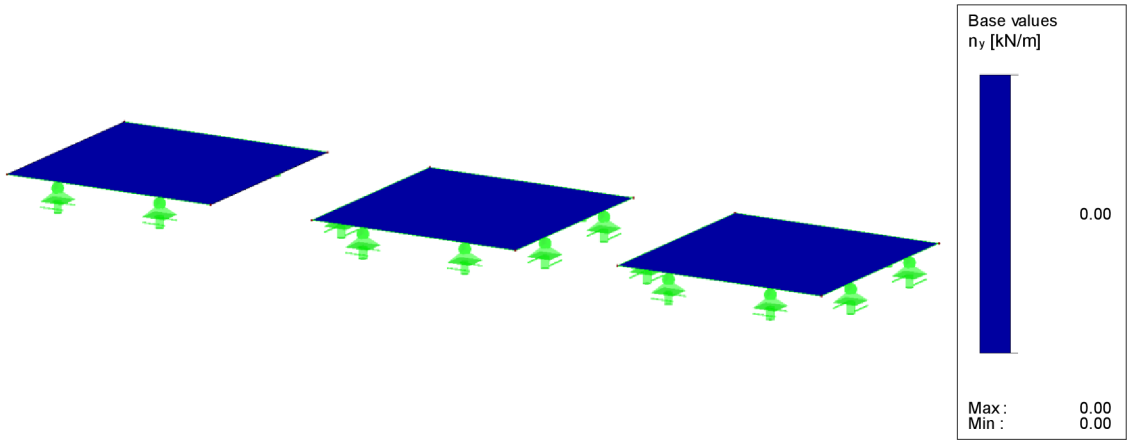

Fig. 93 Elastic Part of Force n_y kN/m

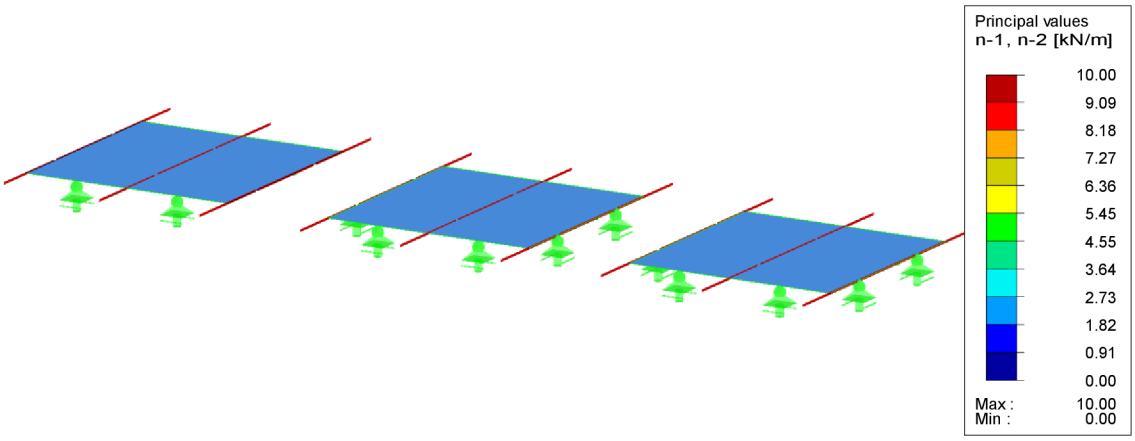

Fig. 94 Vectors Visualizing Elastic Part of Principal Forces n_1 and n_2 kN/m

Since the uniaxial tension is caused by the same value of in-plane strain $\varepsilon_x = 0.01$, the resulting forces have to be same, as presented above. This return algorithm into the common stress state

is visualized by the following graph (Fig. 95), where all elastic predictions are connected with the final elastic stress by the lines with the arrows.

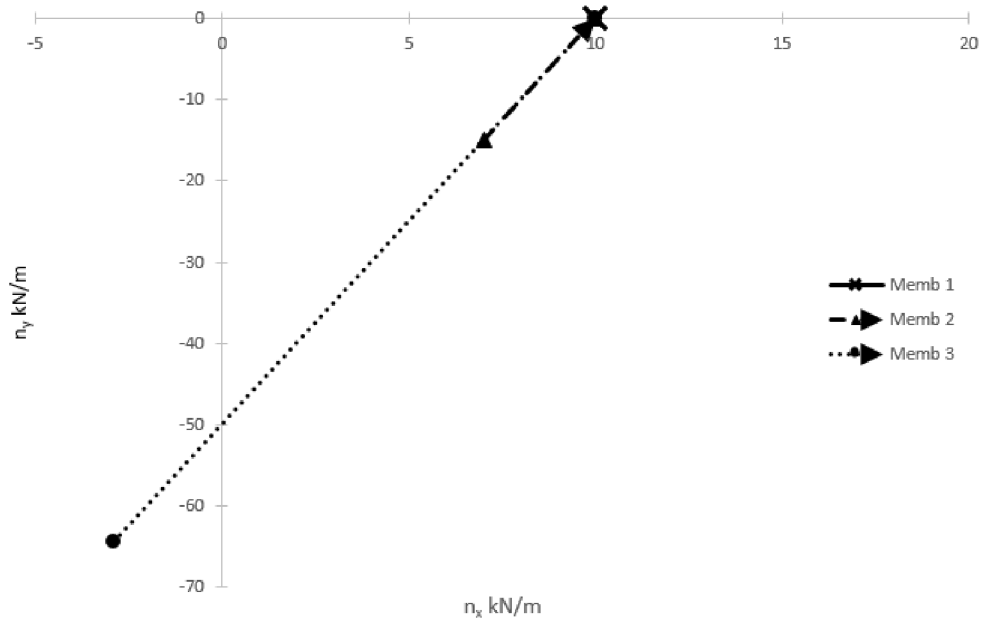

Fig. 95 Graph of Elastic Prediction and Consequent Return Process to Real Elastic Stress State

5.5.2 Elastic Prediction Modification for Nonlinear Elastic and Plastic Material Models

In the previous subchapter (5.5.1), the Wrinkling separation process was presented for the anisotropic linear elastic material models. In this subchapter, the process is also extended for the application in the case of the nonlinear elastic or plastic material models. The additional decomposition of the total strain written in the previous subchapter (5.41) is extended with the plastic strain $\boldsymbol{\varepsilon}^{\mathrm{p}}$.

$$\boldsymbol{\sigma} = \mathbf{C}\,(\boldsymbol{\varepsilon} - \boldsymbol{\varepsilon}^{\mathrm{p}} - \boldsymbol{\varepsilon}^{\mathrm{w}}) \tag{5.49}$$

Some of the possible material models combinations suitable for membrane structures are presented in the figure below (Fig. 96), namely Von Mises/Rankine, Drucker-Prager/Rankine, Tresca/Rankine or Mohr-Coulomb/Rankine yielding criteria.

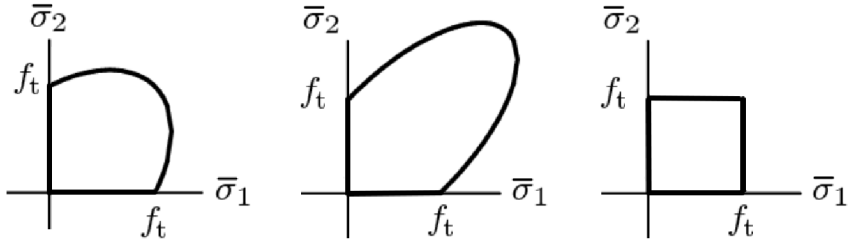

Fig. 96 Combined Yielding Criteria in Plane of $\bar{\sigma}_1$ and $\bar{\sigma}_2$ ($\bar{\sigma}_3 = 0$): Von Mises/Rankine (left), Drucker-Prager/Rankine (middle) and Tresca or Mohr-Coulomb/Rankine (right)

The essence of combining these criteria with the Wrinkling separation process lies in a suitable treatment or the appropriate modification of the actual elastic prediction. As well as the standard membrane theory formulas cannot be used for the linear material models and the modification presented is necessary (5.27), also the standard elastic prediction cannot be used for the return

algorithms on the plasticity surfaces and thus the modification of the elastic prediction is a crucial issue.

The proposed calculation procedure is represented by the attached figures (Fig. 97, Fig. 98) and can be described by the consequent flowchart. For the sake of different elastic prediction distinctions, the left index is added. Moreover, to be consistent in the notation of the formulas, the bar above the stress vectors and components is used, since the main directions are assumed in the following formulas.

I. the calculation of the standard elastic prediction ${}^{\mathrm{I}}\bar{\boldsymbol{\sigma}} = [\,{}^{I}\bar{\sigma}_1 \quad {}^{I}\bar{\sigma}_2 \quad 0\,]^{\mathrm{T}}$
II. the modification of the elastic prediction by the wrinkling separation procedure ${}^{\mathrm{II}}\bar{\boldsymbol{\sigma}} = [\,{}^{II}\bar{\sigma}_1 \quad 0 \quad 0\,]^{\mathrm{T}}$
III. Performing the return algorithm to the yielding surface representing the chosen criterion with consideration of the additional elastic prediction modification ${}^{\mathrm{III}}\bar{\boldsymbol{\sigma}} = [\,{}^{III}\bar{\sigma}_1 \quad {}^{III}\bar{\sigma}_2 \quad 0\,]^{\mathrm{T}}$ and thus converging to the final stress state $\bar{\boldsymbol{\sigma}}^{\mathrm{e}} = [\,\bar{\sigma}_1^{e} \quad \bar{\sigma}_2^{e} \quad 0\,]^{\mathrm{T}}$.

Since the first two steps are the same as in the previous subchapter (5.5.1), the last step needs to be described in more detail.

Let's assume the return process from the elastic prediction modified by the wrinkling separation algorithm ${}^{\mathrm{II}}\bar{\boldsymbol{\sigma}} = [\,{}^{II}\bar{\sigma}_1 \quad 0 \quad 0\,]^{\mathrm{T}}$. The stress change caused by the yielding process can be described as

$$\boldsymbol{\Delta\bar{\sigma}} = [\Delta\bar{\sigma}_1 \quad \Delta\bar{\sigma}_2 \quad 0] \tag{5.50}$$

When observing this process in two following figures (Fig. 97, Fig. 98), the origination of the tensile force $\Delta\sigma_2$ in the wrinkled direction is obvious. However, the fictitious compression component $\bar{\sigma}_2^{\mathrm{w}}$ of the eliminated fictitious stress state $\bar{\boldsymbol{\sigma}}^{w} = [\bar{\sigma}_1^{w} \quad \bar{\sigma}_2^{w} \quad 0]$ was separated out by the wrinkling separation procedure (note: $\bar{\sigma}_2^{w} = {}^{I}\bar{\sigma}_2$). Thus, the tension increment $\Delta\bar{\sigma}_2$ cannot be the final stress state. In other words, the stress increment in the wrinkled direction caused by the yielding process is absorbed by the wrinkling smoothing process. Thus, the elastic prediction ${}^{\mathrm{II}}\bar{\boldsymbol{\sigma}}$ is further modified to ${}^{\mathrm{III}}\bar{\boldsymbol{\sigma}}$. Two essential cases can be described by the following formulas:

$$\bar{\sigma}_2^{w} + \Delta\bar{\sigma}_2 \leq 0 \;\longrightarrow\; {}^{\mathrm{III}}\bar{\boldsymbol{\sigma}} = [\,{}^{III}\bar{\sigma}_1 \quad {}^{III}\bar{\sigma}_2 \quad 0\,]^{\mathrm{T}} = [\,{}^{II}\bar{\sigma}_1 \quad -\Delta\bar{\sigma}_2 \quad 0\,]^{\mathrm{T}} \tag{5.51}$$

$$\bar{\sigma}_2^{w} + \Delta\bar{\sigma}_2 > 0 \;\longrightarrow\; {}^{\mathrm{III}}\bar{\boldsymbol{\sigma}} = [\,{}^{III}\bar{\sigma}_1 \quad {}^{III}\bar{\sigma}_2 \quad 0\,]^{\mathrm{T}} = [\,{}^{II}\bar{\sigma}_1 \quad {}^{I}\bar{\sigma}_2 \quad 0\,]^{\mathrm{T}} \tag{5.52}$$

The green lines (Fig. 97, Fig. 98) connecting the stress points ${}^{\mathrm{I}}\bar{\boldsymbol{\sigma}}$ and ${}^{\mathrm{II}}\bar{\boldsymbol{\sigma}}$ represent the separated $\bar{\boldsymbol{\sigma}}^{w} = [\,\bar{\sigma}_1^{w} \quad \bar{\sigma}_2^{w} \quad 0\,]$ components. While the stress $\bar{\sigma}_1^{w}$, represented by the horizontal green line, does not possess any physical meaning as it is caused by the transverse contraction effect which disappears when the wrinkling process is initialized, the second component $\bar{\sigma}_2^{w}$, represented by the vertical green line, can be understood as a stress deficit to smooth out the wrinkles. It is obvious that the figure (Fig. 97) represents the case when the wrinkles are not soothed out by the yielding process and the membrane is still tensioned in one direction only. However, the second figure (Fig. 98) represents the case when the wrinkles are totally absorbed by the yielding process and the resulting stress state is the membrane tensioned in both directions.

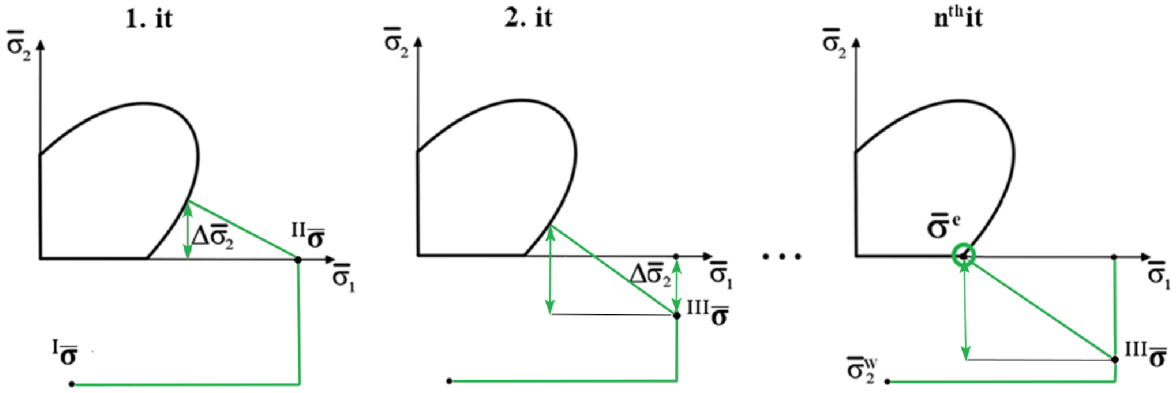

Fig. 97 Standard Elastic Prediction ${}^{I}\bar{\boldsymbol{\sigma}}$ and Elastic Prediction after Wrinkling Separation ${}^{II}\bar{\boldsymbol{\sigma}}$ (left), Iterative Modification of Elastic Prediction ${}^{III}\bar{\boldsymbol{\sigma}}$ (middle and right), Final Elastic Prediction ${}^{III}\bar{\boldsymbol{\sigma}}$ and Resulting Stress State $\bar{\boldsymbol{\sigma}}^{e}$ (right). Iteration Counter (Above).

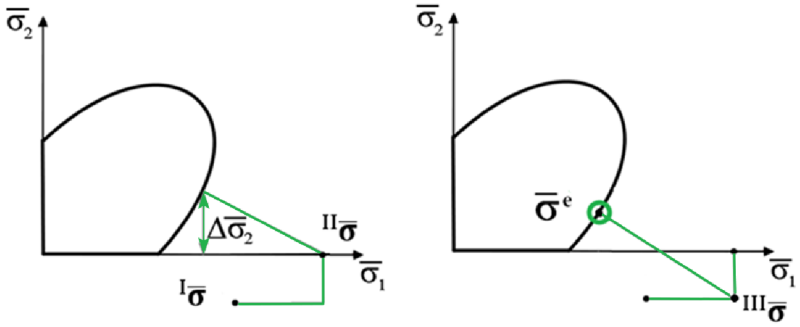

Fig. 98 Standard Elastic Prediction ${}^{I}\bar{\boldsymbol{\sigma}}$ and Elastic Prediction After Wrinkling Separation ${}^{II}\bar{\boldsymbol{\sigma}}$ (left), Modification of Elastic Prediction ${}^{III}\bar{\boldsymbol{\sigma}}$ and Resulting Stress State $\bar{\boldsymbol{\sigma}}^{e}$ (right).

Although the iterative procedure was mentioned (Fig. 97) for the description purpose of the method and physical process, it is not necessary to perform the calculation by this way and it is possible to proceed directly. The normal vector in the node, which is defined by the intersection of the Rankine criterion with some other (the yielding node on the $\bar{\sigma}_1$ axis), is calculated. Two cases can occur:

1. If the normal line to the yielding criterion used for the material description in tension (created in the position of the intersection with the axis $\bar{\sigma}_1$) intersects the vertical green line first, this node defines the final elastic stress prediction ${}^{III}\bar{\boldsymbol{\sigma}}$ directly (Fig. 97 right). This is the case of the wrinkled membrane even with the consideration of the yielding process.
2. If this normal line to the yielding criterion intersects the horizontal green line first, the final elastic stress prediction is defined as ${}^{III}\bar{\boldsymbol{\sigma}} = [\ {}^{II}\bar{\sigma}_1 \quad {}^{I}\bar{\sigma}_2 \quad 0\ ]^{\mathrm{T}} = [\ {}^{II}\bar{\sigma}_1 \quad \bar{\sigma}_2^{w} \quad 0\ ]^{\mathrm{T}}$ (Fig. 98). This is the case when the yielding process smooth out the wrinkles and the membrane become tensioned in both directions.

For the algorithmization purposes, such a direct process is preferred as it ensures a higher calculation performance than the iterative procedure.

Finally, the real stress state is estimated and the transformation into the planar Cartesian coordinate directions can be performed, holding the well-known equation $\boldsymbol{\sigma} = \mathbf{C}\,(\boldsymbol{\varepsilon} - \boldsymbol{\varepsilon}^{\mathrm{p}} - \boldsymbol{\varepsilon}^{\mathrm{w}})$, which was extended with the strain representing the wrinkling $\boldsymbol{\varepsilon}^{\mathrm{w}}$.

The main advantage of the proposed method of the **wrinkling separation** and the consequent **elastic prediction modification** lies in its modularity. As this process originates from the mentioned modification of the elastic prediction, it does not change the definition of the used material yielding criterion itself. The return algorithms and the constitutive matrices can be then used in a standard manner.

The process of the wrinkling smoothing is presented by the following simple example. More complex situations are further presented in the subsequent chapter, which is only focused on the presentation of examples. For this simple example, the Von Mises/Rankine yielding criterion is assumed and the following material properties are used

$$E = 900.0\ MPa, \nu = 0.3, t = 300.0\ \mu m$$
$$f_{y,t} = 10.0\ MPa, E_p = 0.0\ MPa$$
$$\mathbf{C} = \begin{bmatrix} 989.0 & 296.7 & 0 \\ & 989.0 & 0 \\ sym. & & 346.2 \end{bmatrix} MPa \tag{5.53}$$

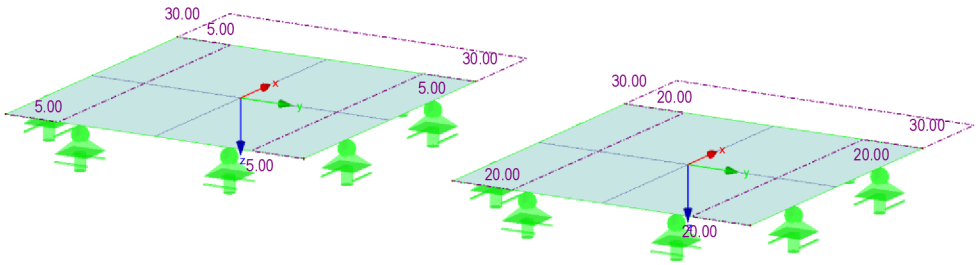

Fig. 99 Two Square Membranes, FE Mesh and Planar Directions Definition, Imposed Deformations Visualization

The two square membranes are defined and the imposed load is applied according to the presented figure (Fig. 99). The fact that both membranes are in the wrinkled state before starting the yielding process is demonstrated by two following figures (Fig. 100, Fig. 101), where the elastic stress prediction ${}^{\mathrm{I}}\bar{\boldsymbol{\sigma}}$ according to the standard membrane theory is presented.

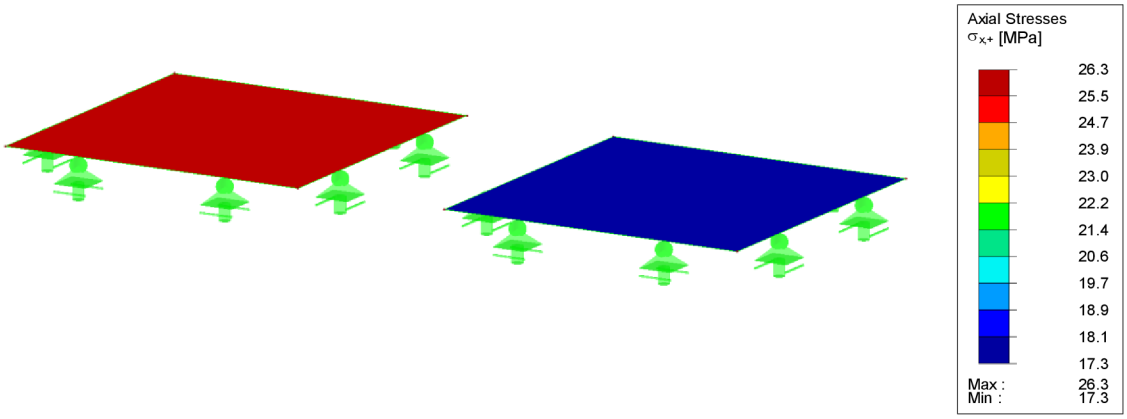

Fig. 100 Standard Elastic Prediction ${}^{\mathrm{I}}\sigma_x$

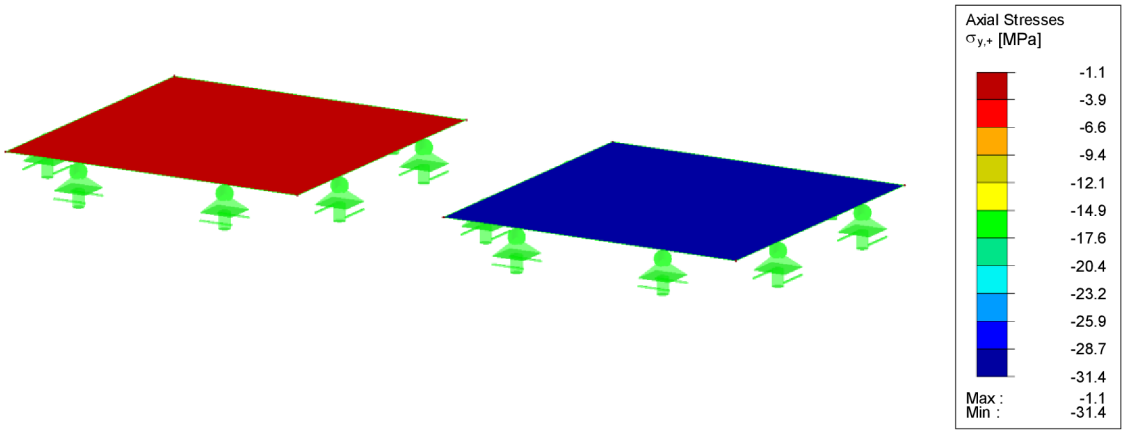

Fig. 101 Standard Elastic Prediction ${}^{I}\sigma_y$

When performing the yielding process, wrinkles in the left membrane are smoothed out, while the right membrane is still wrinkled, as it can be demonstrated by resulting stresses (Fig. 102, Fig. 103, Fig. 104).

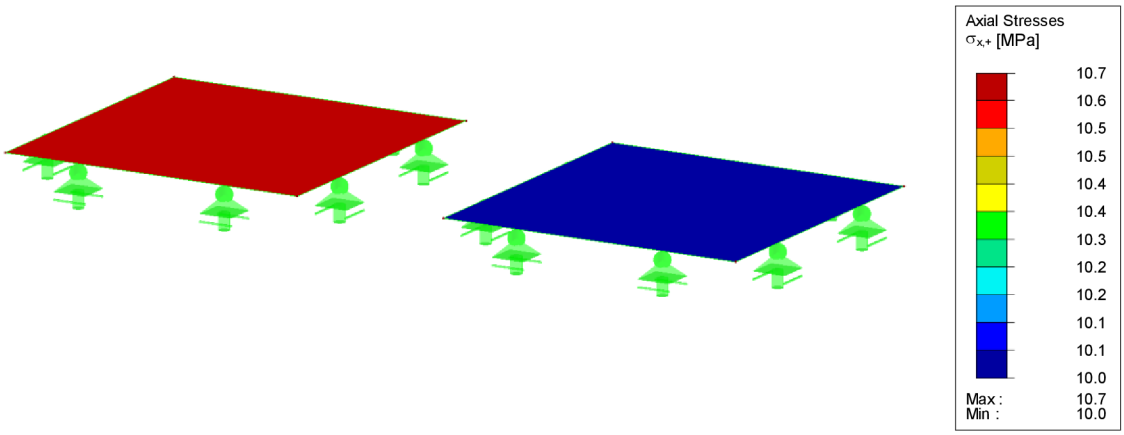

Fig. 102 Resulting Stress σ_x

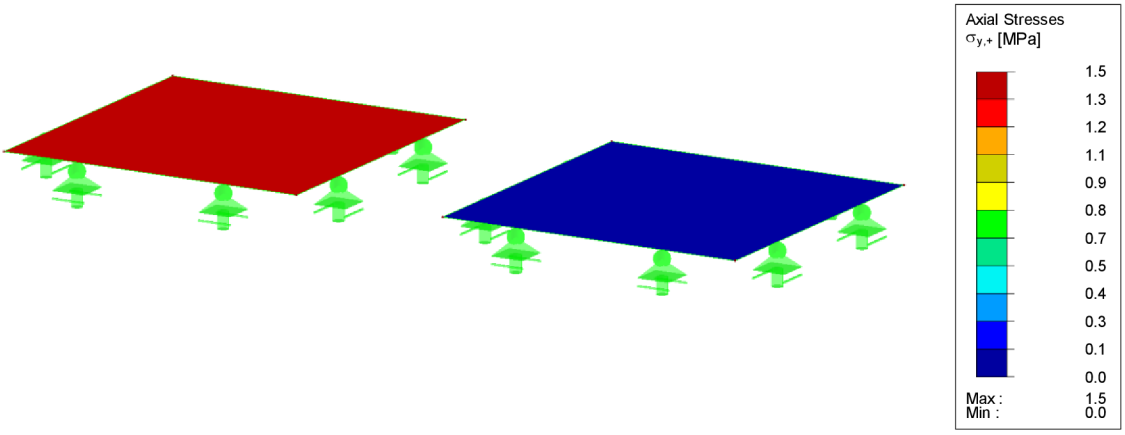

Fig. 103 Resulting Stress σ_y

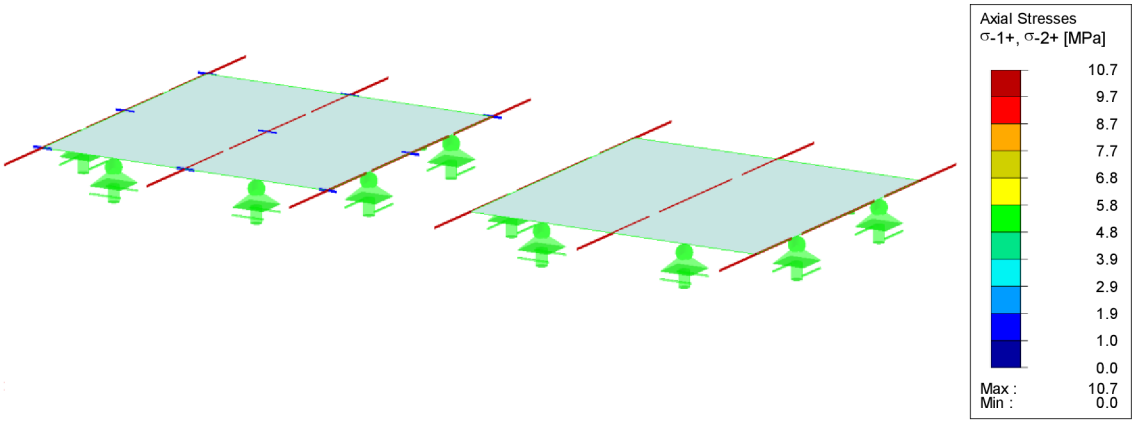

Fig. 104 Vectors of Resulting Principal Stress σ_1 and σ_2

5.6 NUMERICAL EXAMPLES

This chapter presents numerical examples. First, the wrinkling separation procedure for the linear elastic material models is verified on an example with the analytical solution available. Further, other examples are presented covering also the nonlinear material models.

5.6.1 Pure Bending of Rectangular Membrane

As the first example, the well-known and often used pure bending of the stretched rectangular membrane is chosen (Fig. 105). This example has an analytical solution [78] and therefore, it serves as a benchmark when evaluating the wrinkling separation process for elastic materials.

The membrane is initially prestressed in both directions with the value of n_0. The prestress is applied by the continuous load acting on the top and bottom borders and by the force $P = h\,n_0$ acting on the left and right edges. A beam with the high flexural and zero normal stiffness is used for the P force transmission into the membrane. The membrane height is denoted by h. Furthermore, the value of the nodal moment M is increased in the middle of the left and right edges. By applying this moment, the isotropic pretension changes and when reaching a certain value, the bottom region starts to wrinkle. The height of the wrinkling region b changes continuously until the limit value $b = h$ is reached.

The proportion of the wrinkled region magnitude b to the height of the rectangular membrane h is described by

$$\frac{b}{h} = \begin{cases} 0. & \frac{M}{Ph} < \frac{1}{6} \\ \frac{3M}{Ph} - \frac{1}{2} & \frac{1}{6} \leq \frac{3M}{Ph} < \frac{1}{2} \end{cases} \tag{5.54}$$

The proportion of the resulting horizontal tension n_x to the original pretension n_0 according to the y coordinate is defined as

$$\frac{n_x}{n_0} = \begin{cases} \frac{2(y/h - b/h)}{(1 - b/h)^2} & \frac{b}{h} < \frac{y}{h} \leq 1 \\ 0. & 0. \leq \frac{y}{h} \leq \frac{b}{h} \end{cases} \tag{5.55}$$

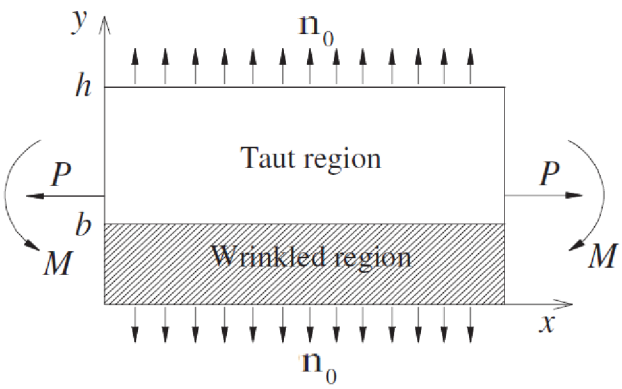

Fig. 105 Pure Bending of Stretched Rectangular Membrane [46]

Since the membrane is symmetric along the vertical line situated in the middle of the structure, the right half will only be analyzed numerically (Fig. 106). The height $h = 1.0\ m$, the length of the selected half is $l = 2.0\ m$ (this parameter is not relevant for the results, so this is only the information about the particular model), the pretension $n_0 = 1.00\ kN/m$. The first model is considered to be created from the isotropic linear elastic material model representing the linear part of the ETFE stress-strain response with the values $E = 900.0\ MPa, \nu = 0.45, t = 300.0\ \mu m$. Even these particular material values do not influence the monitored results of the presented example, as the formulas above do not use any of this information. However, this information is still mentioned to have an engineering idea or touching with the used material, since the orthotropic material will be used later, even with a different axis orientation and the mentioned material independence of this example will be proven. The selected FE size is $l_{FE} = 0.05\ m$, so the structure is composed of $n = 800$ bilinear isoparametric FE.

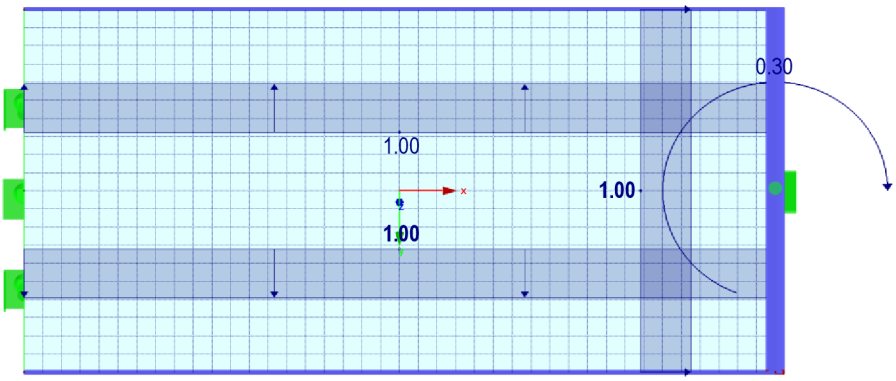

Fig. 106 Right Half of Rectangular Membrane, FE Mesh, Local Cartesian Coordinate System Orientation and Applied Forces and Moment

The results in the form of figures are presented for three discrete states. First, for the initial pretension when $M = 0.0\ kNm$ (Fig. 107), then for the limit state when the wrinkling initialization has started $M = Ph/6\ kNm$ (Fig. 108), and finally for the relation $b/h = 1/2$, which implies $M = Ph/3$ (Fig. 109). Other calculations with the gradual changes of the applied moment M are presented in the form of graphs (Fig. 110, Fig. 111).

Fig. 107 Internal Forces n_x Distribution for $M = 0.0\ kNm$

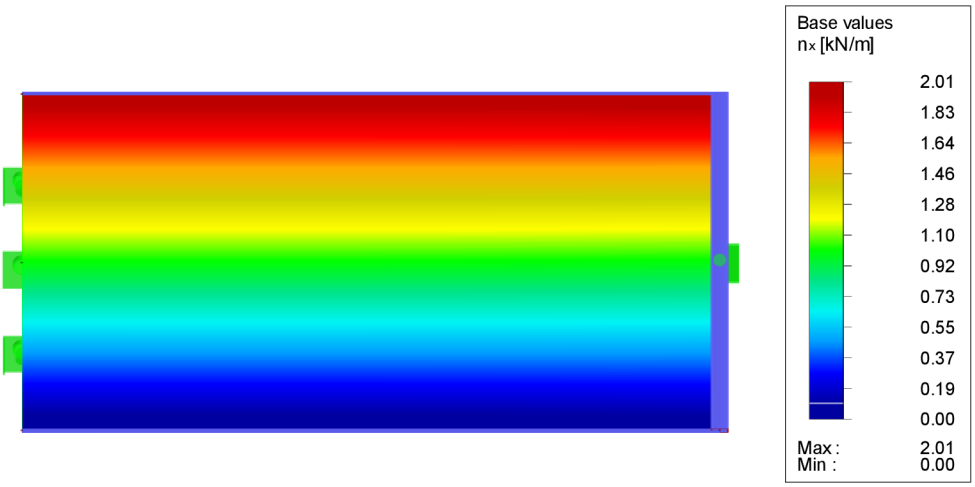

Fig. 108 Internal Forces n_x Distribution for $M = Ph/6$

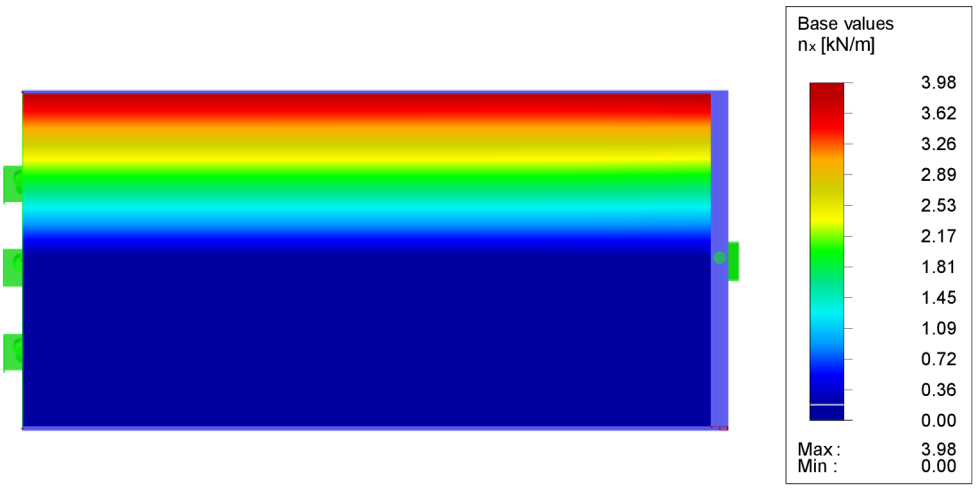

Fig. 109 Internal Forces n_x Distribution for $M = Ph/3$, thus $b/h = 1/2$

In the following, two graphs are presented, where the first one presents spreading of the wrinkled region bandwidth b in dependence on the applied moment M (Fig. 110). The comparison of the analytical and the numerical solution can be observed. The second graph presents the actual internal force n_x distribution over the vertical cut for three different applied

moments M (Fig. 111). Again, the comparison of the analytical and the numerical solution is available. Both attached graphs prove the reliability and the accuracy of the proposed wrinkling separation process.

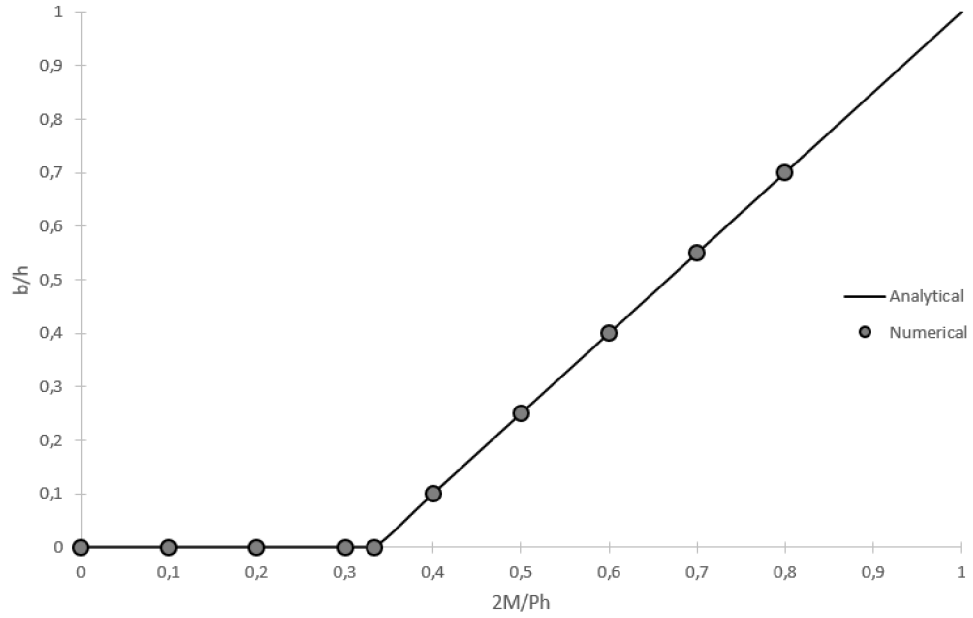

Fig. 110 Spreading of Wrinkled Region Bandwidth b in Dependence on Applied Moment M

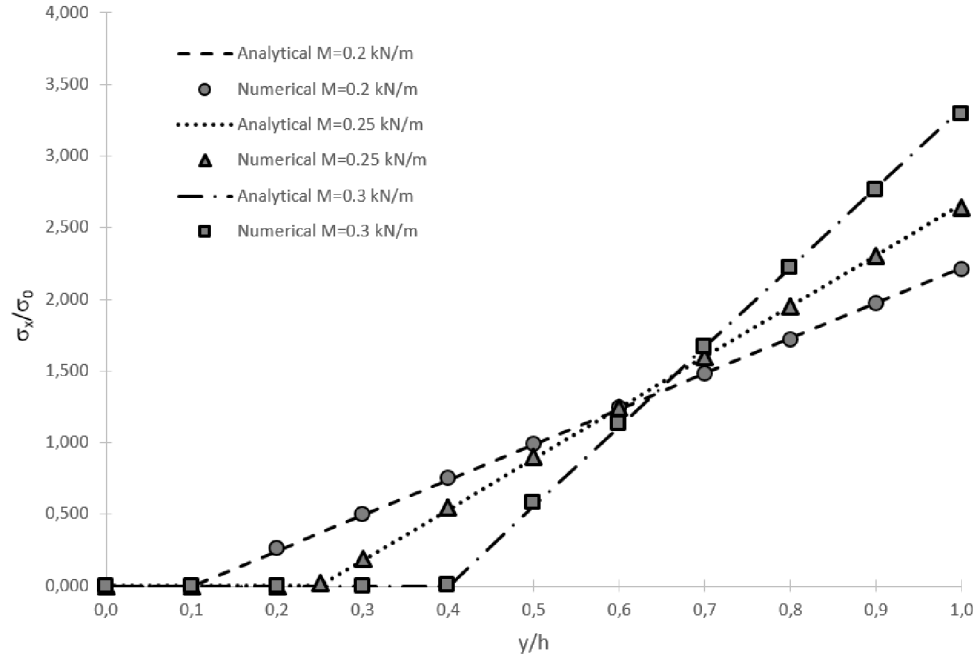

Fig. 111 Comparison of Analytical and Numerical Results of Internal Forces n_x on Vertical Cut for Three Different Applied Moments M

In the end of this example, two other analyses are presented, where nothing changes but the material definition. While the material properties of the presented example are assumed to represent the linear stress-strain diagram part of the isotropic ETFE foil material, the following two examples use the linear orthotropic material definition, which can be a representation for response of the woven fabric with top cover.

The properties are defined as $E_x = 1000.0\,kN/m$, $E_y = 800.0\,kN/m$, $G = 100.0\,kN/m$, $\nu_{xy} = 0.20, t = 1.0\,mm$. As mentioned previously, the presented formulas are materially independent and hold for any elastic material and orthotropic direction definition (Fig. 112). Of course, the deformations are different but they are not a subject of this benchmark analysis.

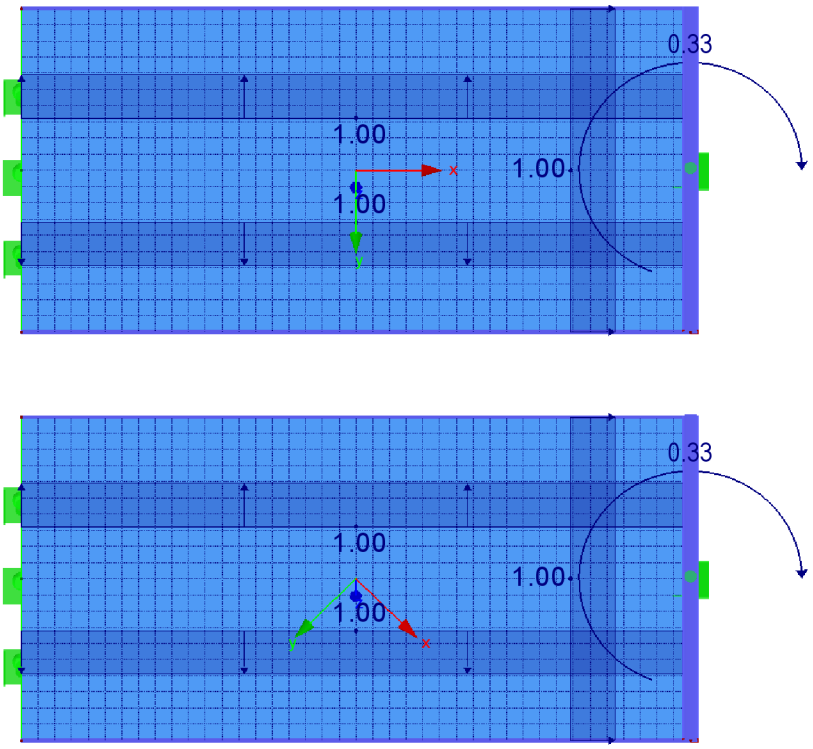

Fig. 112 FE Model with Changed Material Definition (Both) and Changed Orthotropic Direction (Bottom)

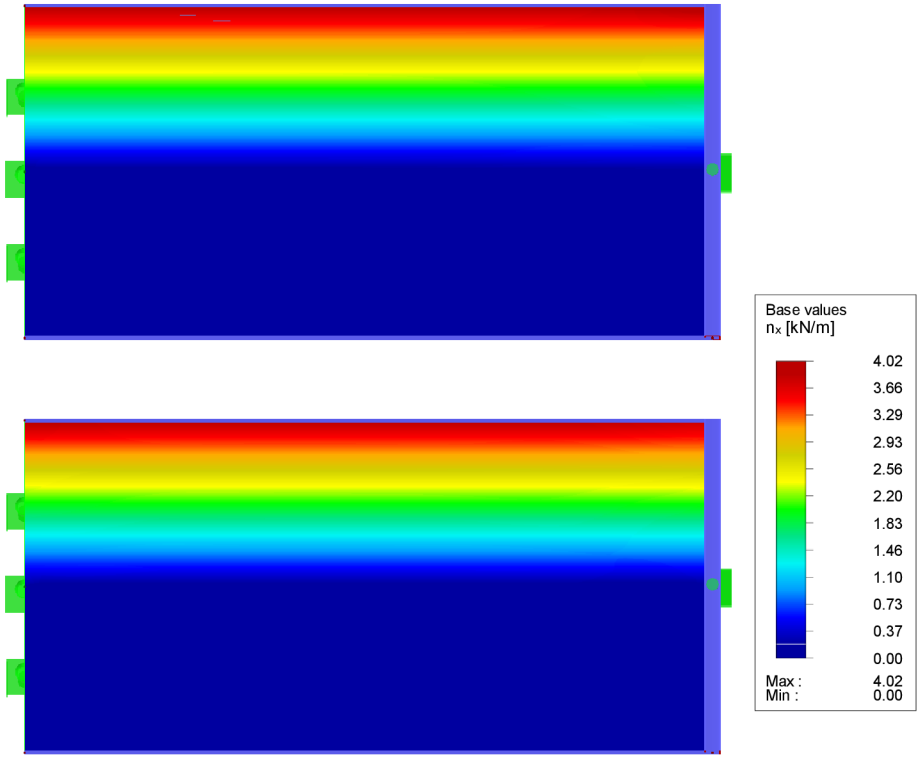

Fig. 113 Internal Forces n_x Distribution for $M = Ph/3$, Thus $b/h = 1/2$

The analysis was performed for the nodal moment with the value $M = Ph/3$. Comparing the results presented in the attached figures (Fig. 109, Fig. 113), it can be observed that the internal forces for the isotropic and both direction definitions of the orthotropic material are the same.

5.6.2 Shear Test of Rectangular Membrane for Orthotropic Elastic Material

In the second example, the shear test of the rectangular membrane is performed. As there is no analytical solution defined, another proof of the result reliability is used.

Recalling the statement written in the beginning of this chapter, where it is written: *'Essentially, there are two ways for solving the wrinkled state of the membrane in FEA. The first way is to use an extremely dense FE discretization and the in-plane stiffness in both the tension and the compression directions, while the bending stiffness is zero. Such a mesh allows the material to follow the little waves, but this is inadequate costly solution and it inevitably depends on the mesh. The second way, which can be further categorised, focuses on the separation of the total strain into the elastic and wrinkling part. Such a solution allows for using the FE discretization, where the particular elements are much bigger than the wrinkles. Even so the particular wrinkles are not modelled here, the method is not so strongly dependent on the mesh as in the case of the previous method and, in terms of the continuum analysis, the global stress state is precisely described by such a "smeared wrinkle" analysis.'*

A similar statement can be found in the contribution of the authors D.J. Steigmann and A.C. Pipkin [62]: *'To estimate the load-carrying capacity of a wrinkled membrane without obtaining unneeded information about its precise shape, Wagner [45] formulated tension field theory, in which the wrinkles are treated as being spaced infinitesimally close together.'*

Thus, the method reliability and accuracy can be proven by comparing the results performed by both of these analysis ways. Furthermore, the mesh dependence is presented here in the form of a graph.

In this example, the following properties of a coated woven fabric are assumed $E_x = 2000.0\,kN/m$, $E_y = 1000.0\,kN/m$, $G = 200.0\,kN/m$, $\nu_{xy} = 0.20$, $t = 1.0\,mm$. The length of the rectangular membrane is defined as $l = 2.0\,m$ and the height is $h = 1.0\,m$. The horizontal imposed deformation in the top part of the membrane is defined with the value $\Delta = 100.0\,mm$. For imposing a little imperfection in the direction perpendicular to the membrane and thus initiating the formation of wrinkles, a really small area load is applied, specifically $f = 0.01\,N/m^2$, thus the load of only 2.0 grams in the total magnitude is used, negligible when comparing with the value of the resulting forces caused by the imposed deformation. For this analysis, the triangular isoparametric constant strain FE are used. The figure below (Fig. 114) shows the FE mesh with the given size $l_{FE} = 0.10\,m$, thus $n = 400$, however different mesh sizes are further used to compare the mesh dependence.

Note: The nearly unnoticeable perpendicular load for wrinkling initialization is only necessary in the case the shell elements with the zero bending stiffness are used. The wrinkling separation procedure does not need this crutch.

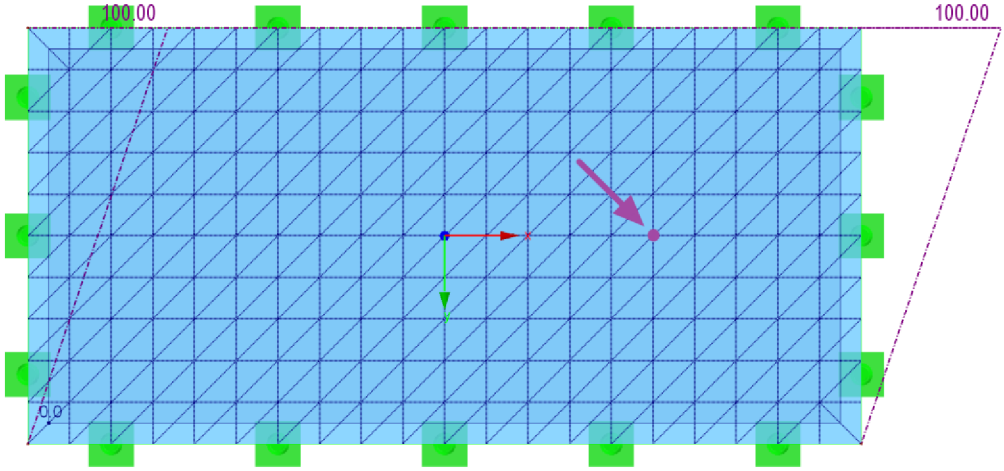

Fig. 114 Rectangular Membrane, FE Mesh, Local Cartesian Coordinate System Orientation, Imposed Deformation and Applied Perpendicular Forces, Node for Result Presentation (purple dot)

As there are different FE meshes during studying this example, it is not possible to focus on one particular element and instead, the results are presented in the particular grid point (the point for result presentation).

Since the diagonals run from left to right, the discretization is not symmetric and thus two cases of loading are studied. First, the imposed deformation is assumed from left to right, as shown in the figure (Fig. 114), then the direction is reversed and the deformation is applied from right to left (in the same magnitude). The aim of this process is focused on studying the mesh dependence as well as changing the element sizes.

The results for the mesh size $l_{FE} = 0.10\ m$ and the first mode of shear loading is presented in the form of figures (Fig. 115 - Fig. 120), while the results of different mesh length definitions are presented in the form of the graph attached (Fig. 122).

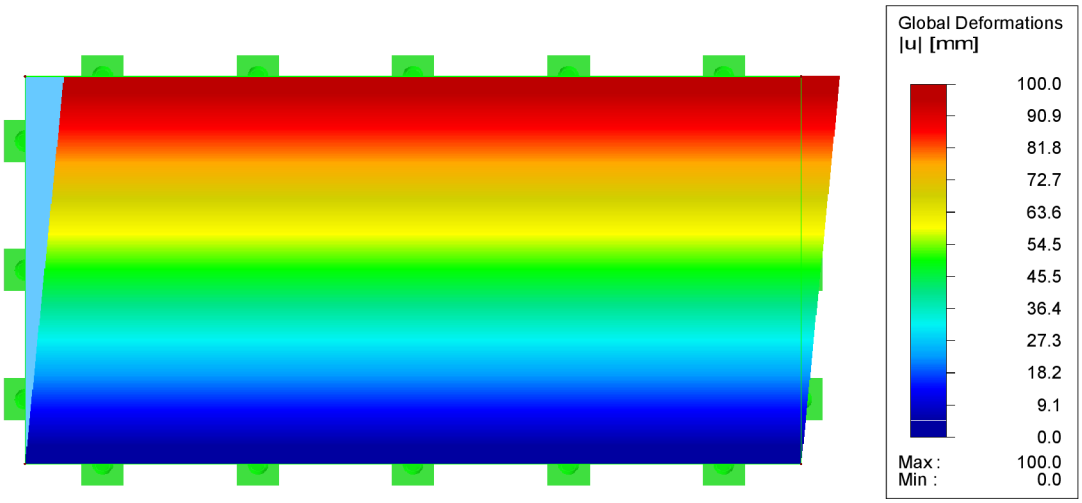

Fig. 115 Wrinkling Separation: Global Deformations u

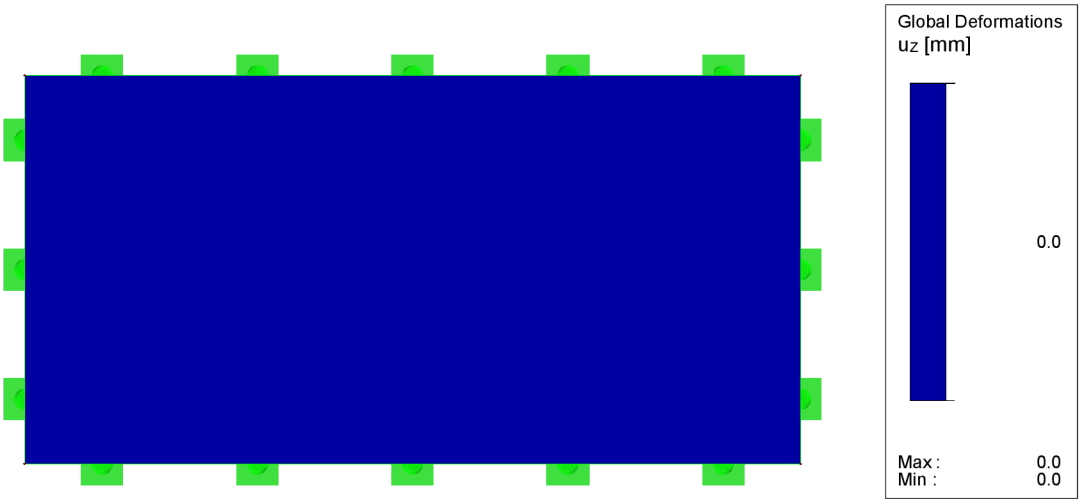

Fig. 116 Wrinkling Separation: Deformations Perpendicular to Membrane u_z

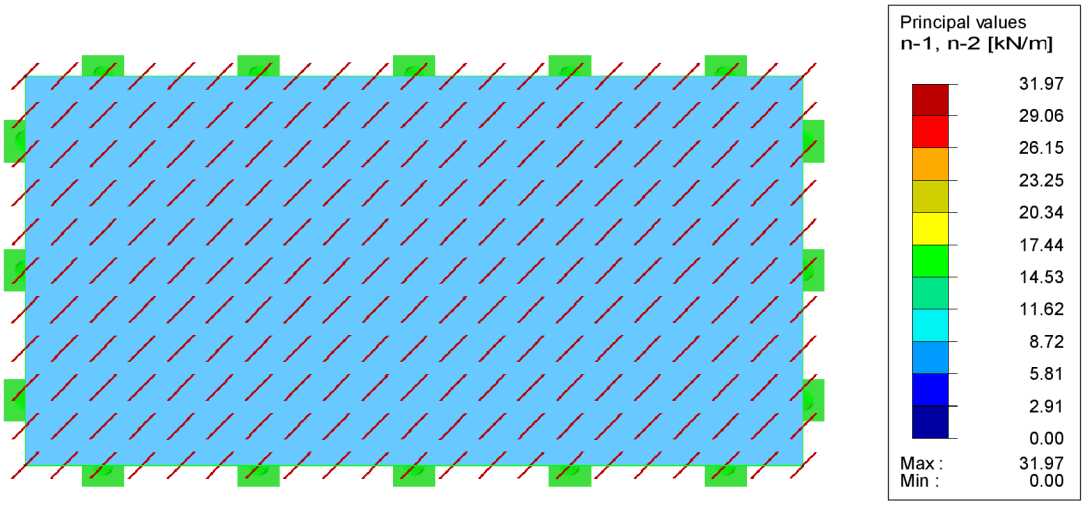

Fig. 117 Wrinkling Separation: Vectors of Principal Internal Forces n_1 and n_2

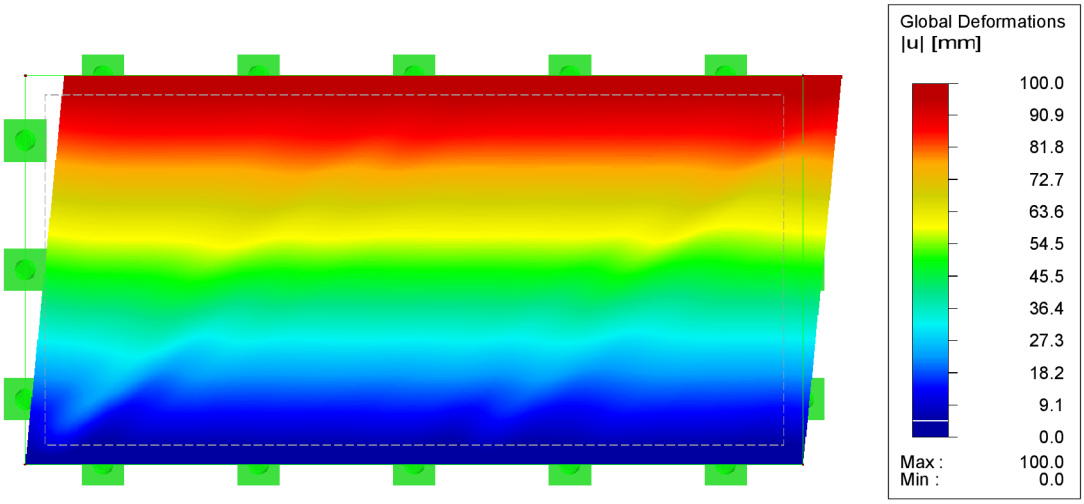

Fig. 118 Shell Element with Zero Bending Stiffness: Global Deformations u

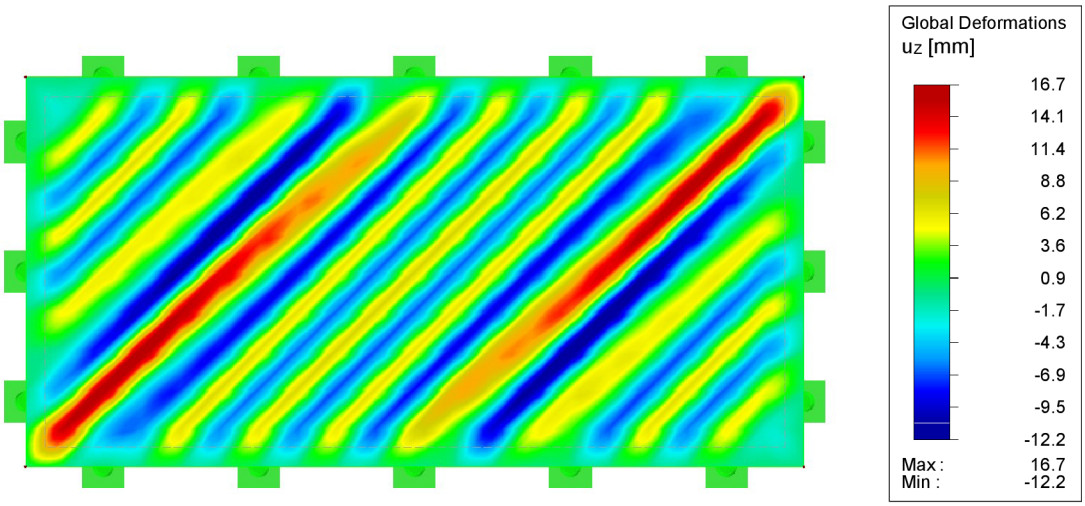

Fig. 119 Shell Element with Zero Bending Stiffness: Deformations Perpendicular to Membrane u_z

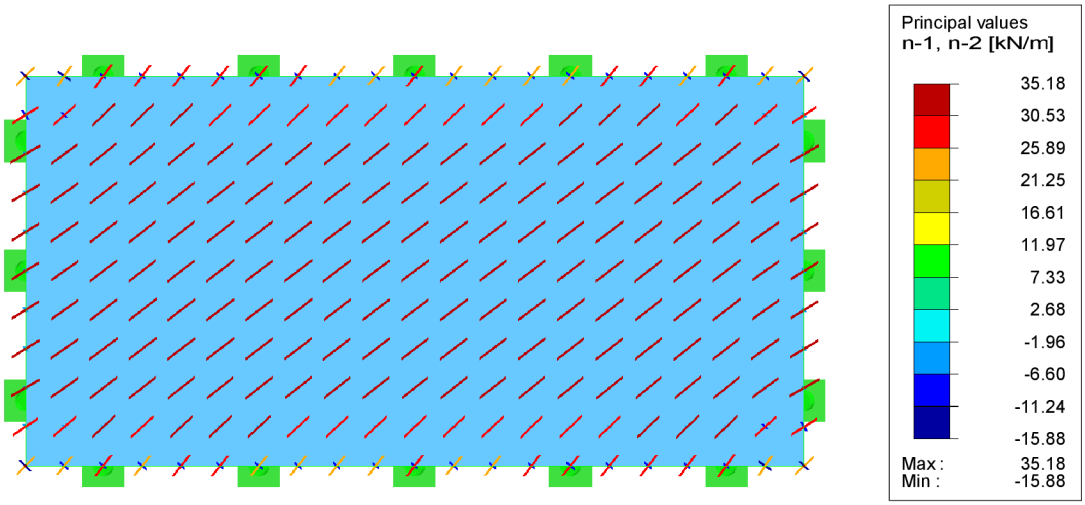

Fig. 120 Shell Element with Zero Bending Stiffness: Vectors of Principal Internal Forces n_1 *and* n_2

Comparing the graphical results, several notes can be written there. First, the zero perpendicular deformation u_z can be observed for the *wrinkling separation* procedure (Fig. 116), which is

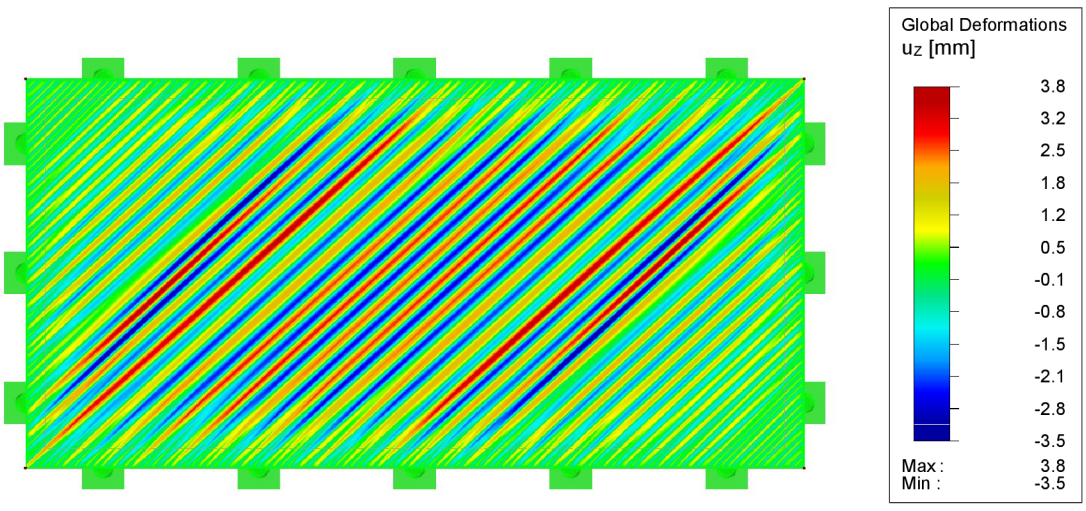

Fig. 121 Shell Element with Zero Bending Stiffness: Deformations Perpendicular to Membrane u_z *for* $l_{FE} = 0.01\ m$

consistent with the above-mentioned assumption of the tension field theory that the wrinkling of a membrane is replaced by the in-plane deformation. Instead, the inevitable wrinkles are observed in the case the equal tensile and compressive stiffness, but zero flexural stiffness are used (Fig. 119). When observing this perpendicular deformation for $l_{FE} = 0.10\ m$ (Fig. 119) and for $l_{FE} = 0.01\ m$ (Fig. 121), the fact that the wave size is restricted by the FE size is obvious. Applying the further refinement, the wrinkles are located closer to each other and the perpendicular deformation tends to zero.

The second important observation can be seen when comparing the resulting forces. While in the case of *the wrinkling separation* procedure, the internal forces are absolutely homogeneous with the values $n_1 = 31.97\ kN/m$ and $n_2 = 0.00\ kN/m$ in the whole membrane (Fig. 117), the force variation can be seen in the case of the *shell elements with zero bending stiffness*, where there is also the compression occurring on the border as the omnidirectional supports do not allow for the wrinkles here (Fig. 120). However, the tendency of the results is the same and the good agreement with the most of the membrane surface is evident.

The shear test of a rectangular membrane with the orthotropic elastic material was further studied for different FE mesh refinements, whose settings can be seen in the table below (Tab. 2). The comparison of the results obtained is measured for the first principal force n_1 in the highlighted grid point (Fig. 114, Fig. 122).

Tab. 2 Description of Eight Performed Analyses FE Data

Analysis number	1	2	3	4	5	6	7	8
FE size l_{FE} (mm)	500	400	300	200	100	50	25	12.5
Number of 2D FE	16	25	44	100	400	1600	6400	25600
Number of FE nodes	15	24	42	66	231	861	3321	13041
Equations number	45	72	126	198	693	2583	9963	39123

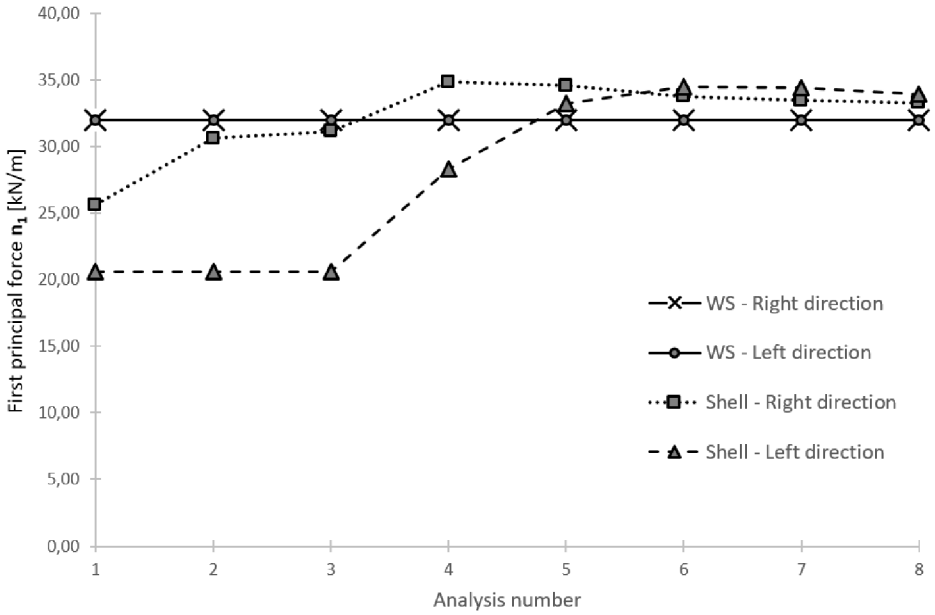

Fig. 122 Resulting Values of First Principal Force n_1 in Grid Point (Fig. 114) for Eight Different FE Refinements

Four analyses were calculated for each FE mesh setting, since the imposed deformation was applied from left to right (right direction) and from right to left (left direction), further both the wrinkling separation process (WS) and the shell with zero flexural stiffness (Shell) cases were also used.

Several conclusions can be made on the basis of the presented graph. First, the wrinkling separation procedure is independent of the mesh, while the usage of the shell with the zero bending stiffness is distinguished by a considerable FE mesh dependence as the inevitable perpendicular deformations are directly restricted by the FE mesh used. Furthermore, when used the shell elements, a well-seen difference of the different imposed load direction is presented, which is the consequence of the alignment of the wrinkles with the FE mesh diagonals in the right direction, while the left direction causes the wrinkles which are crossing the diagonal direction (Fig. 114). However, both shell models converge to the results of the wrinkling separation procedure when the extensive refinement is used.

5.6.3 Shear Test of Rectangular Membrane for Isotropic Nonlinear Elastic and Plastic Material

The same geometry of the model and the imposed load conditions as in the previous example (Fig. 114) are now subjected to the analysis with the isotropic nonlinear elastic combined yielding criterion Von Mises/Rankine. This example is performed by using the above-described wrinkling separation procedure and the elastic prediction modification. The material used here is considered as a bilinear approximation of the ETFE stress-strain diagram with the parameters $E = 900.0\,MPa, \nu = 0.45, t = 300.0\,\mu m$, the yielding stress $f_{y,t} = 21.0\,MPa$ and the elasticity modulus after yielding $E_p = 90.0\,MPa$. The results of the mesh size $l_{FE} = 0.10\,m$ are again presented in the graphical form (Fig. 123 - Fig. 128).

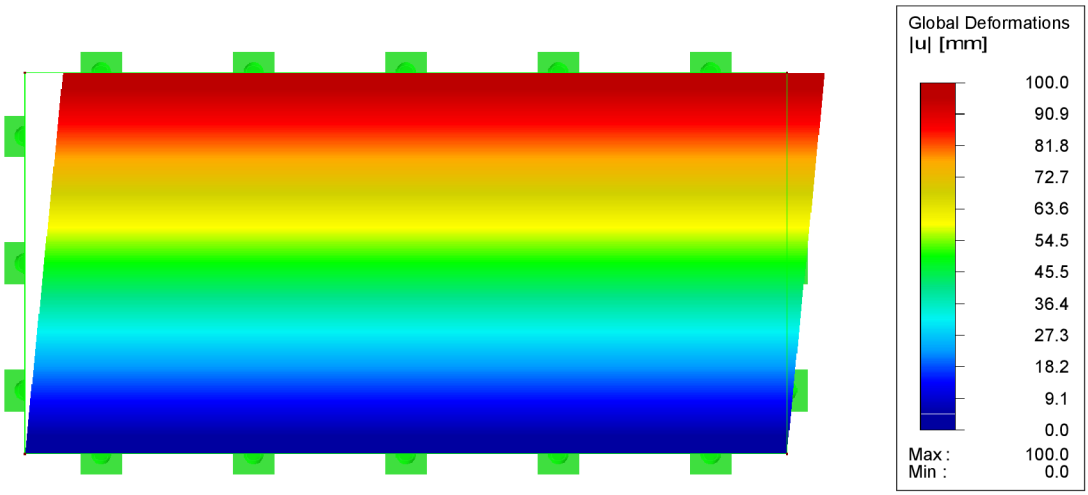

Fig. 123 Wrinkling Separation: Global Deformations u

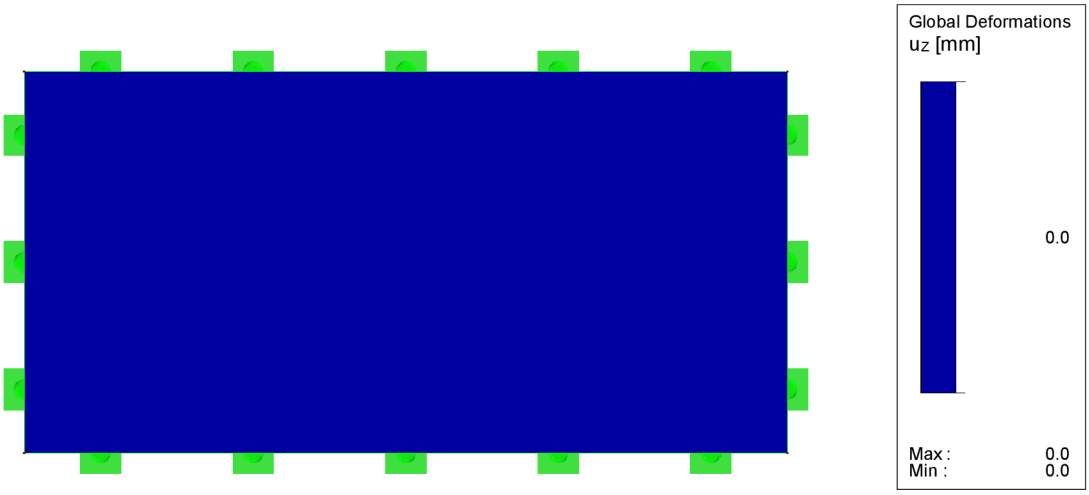

Fig. 124 Wrinkling Separation: Deformations Perpendicular to Membrane u_z

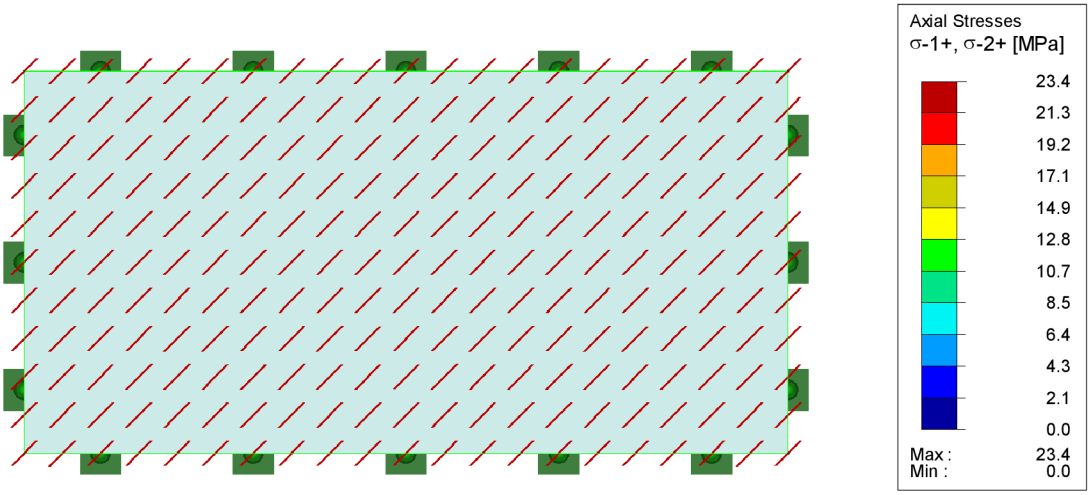

Fig. 125 Wrinkling Separation: Vectors of Principal Stresses σ_1 and σ_2

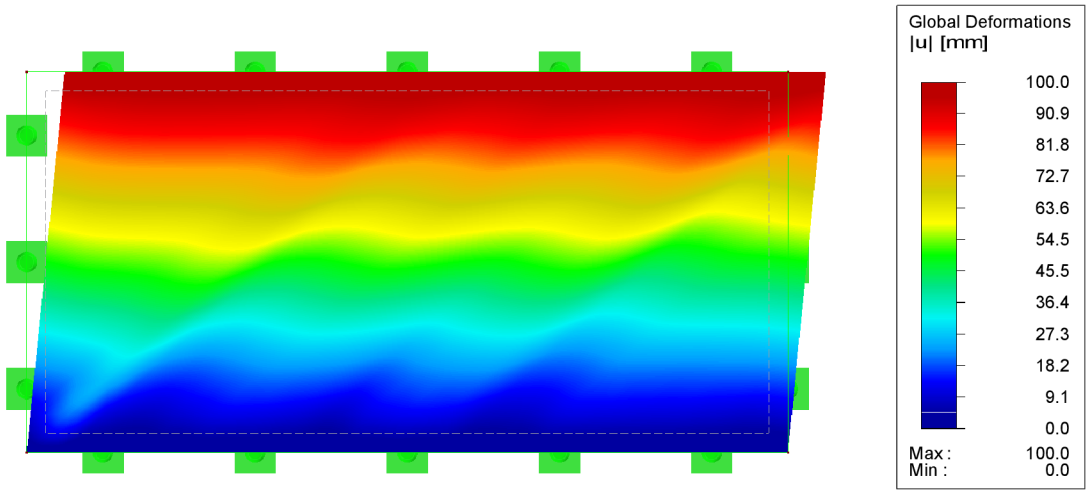

Fig. 126 Shell Element with Zero Bending Stiffness: Global Deformations u

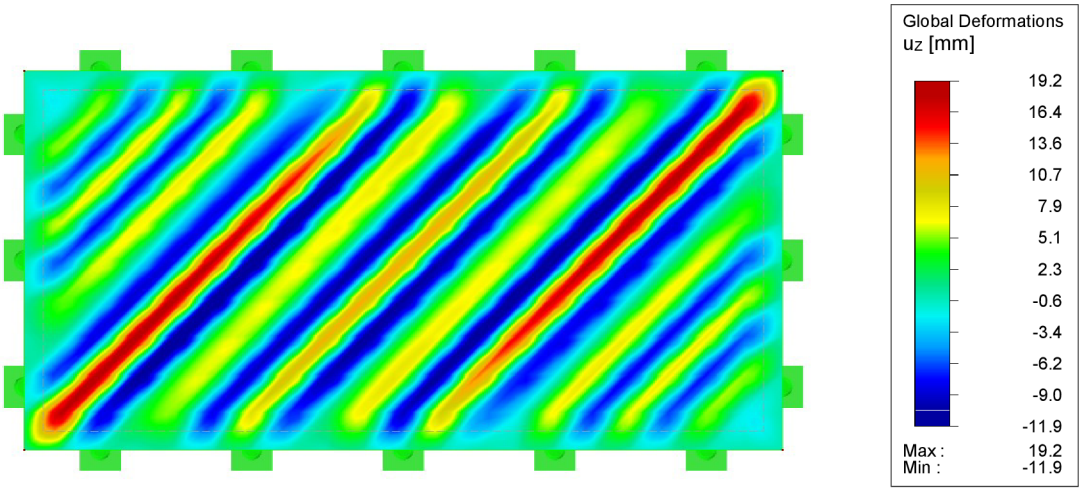

Fig. 127 Shell Element with Zero Bending Stiffness: Deformations Perpendicular to Membrane u_z

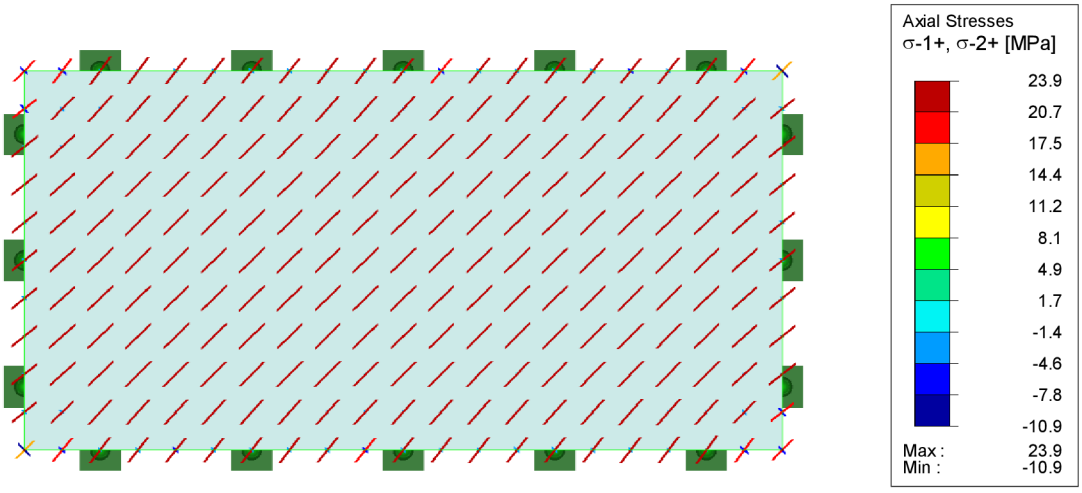

Fig. 128 Shell Element with Zero Bending Stiffness: Vectors of Principal Stresses σ_1 and σ_2

When using the tenth of the size of the previously used FE $l_{FE} = 0.01\ m$ and the shell elements with the zero bending stiffness, the wrinkles are smaller and spaced closer to each other, as can be seen when comparing the figures (Fig. 127) and (Fig. 129).

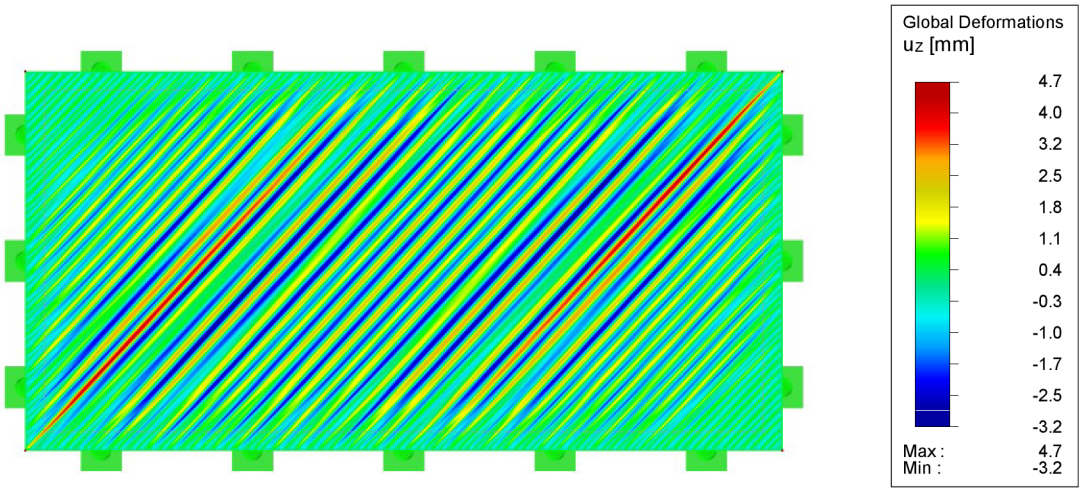

Fig. 129 Shell Element with Zero Bending Stiffness: Deformations Perpendicular to Membrane u_z for $l_{FE} = 0.01\ m$

An analogous comparison of the resulting values as presented in the previous example is made for the different mesh refinements and imposed load orientation. The example details and results are attached below (Tab. 3, Fig. 130).

Tab. 3 Description of Eight Performed Analyses FE Data

Analysis number	1	2	3	4	5	6	7	8
FE size l_{FE} (mm)	500	400	300	200	100	50	25	12.5
Number of FE	16	25	44	100	400	1600	6400	25600
Number of FE nodes	15	24	42	66	231	861	3321	13041
Equations number	45	72	126	198	693	2583	9963	39123

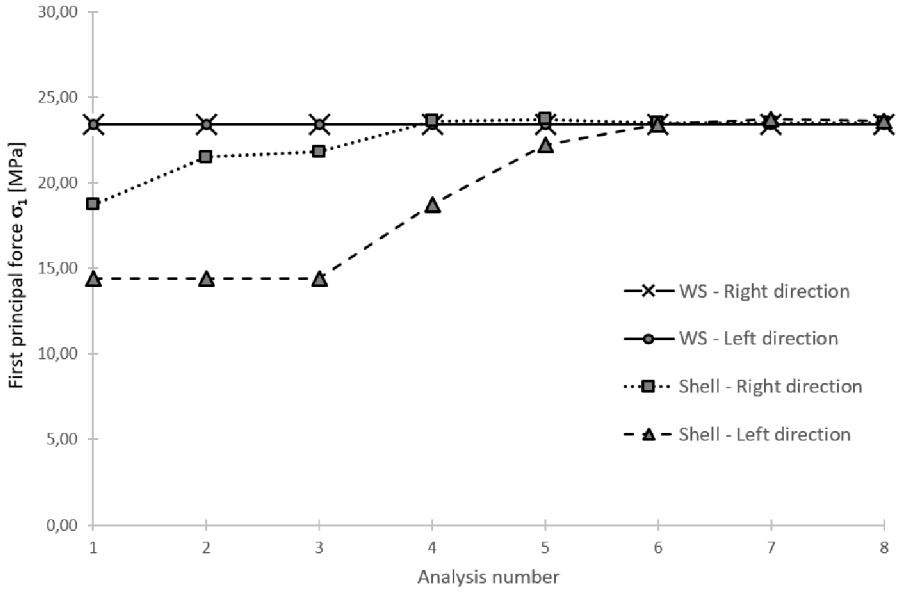

Fig. 130 Resulting Values of First Principal Force n_1 in Grid Point (Fig. 114) for Eight Performed Analyses

As well as in the previous example, when using the shell elements with the zero flexural stiffness, the diagonal directions have a considerable influence on the resulting stresses if the FE mesh is not refined enough. With the consequent decreasing of the FE length value, the shell solution converges to the wrinkling separation procedure solution, which is again independent of the mesh.

There are completely identical results obtained when using the combined plastic yielding criterion Von Mises/Rankine, instead of the nonlinear elastic material definition.

5.7 STATIC AND DYNAMIC ANALYSIS OF MEMBRANE STRUCTURES

While the previous chapter was focused on the verification of the proposed method for dealing with the wrinkling phenomenon, this chapter presents the structure analysis of the whole membrane structure, starting with the static analysis and then presenting the results of the dynamic analysis.

The analyzed model is inspired by the Tanzbrunnen structure [I, II] and the PVC/PES Type III is assumed in the analysis, defined by the material characteristics $E_x = 1000.0\,kN/m,$

$E_y = 700.0\,kN/m$, $G = 70.0\,kN/m$, $\nu_{xy} = 0.20$, $t = 1.0\,mm$ The radius defining horizontal distance of the high or low points from the middle is $r = 10.0\,m$, the low points are situated in

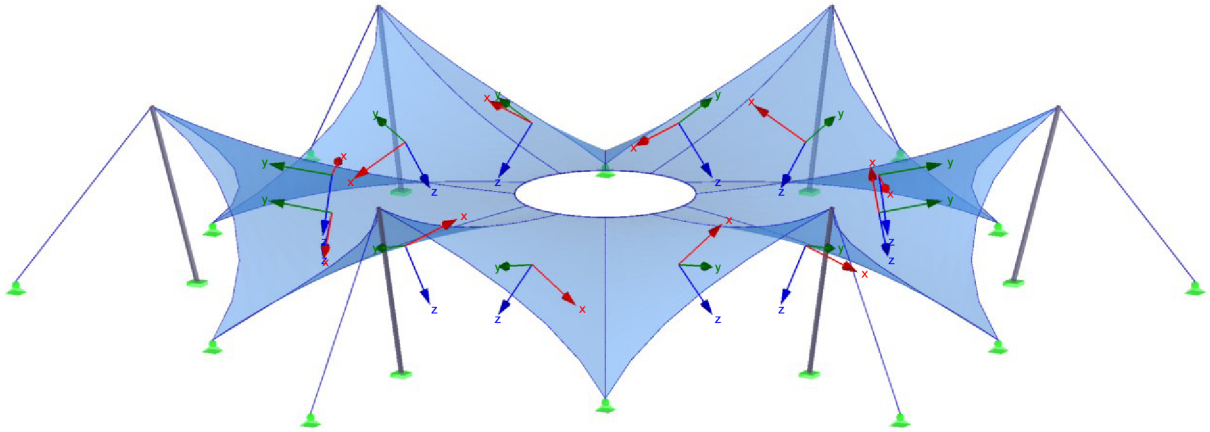

Fig. 131 Geometry of Membrane Structure After Form Finding and Orthotropy Directions

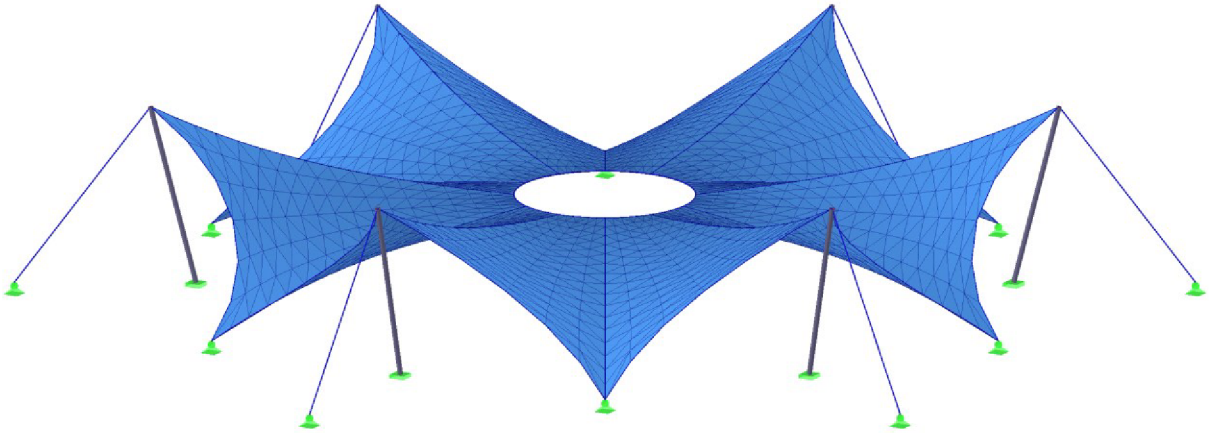

Fig. 132 FE Mesh

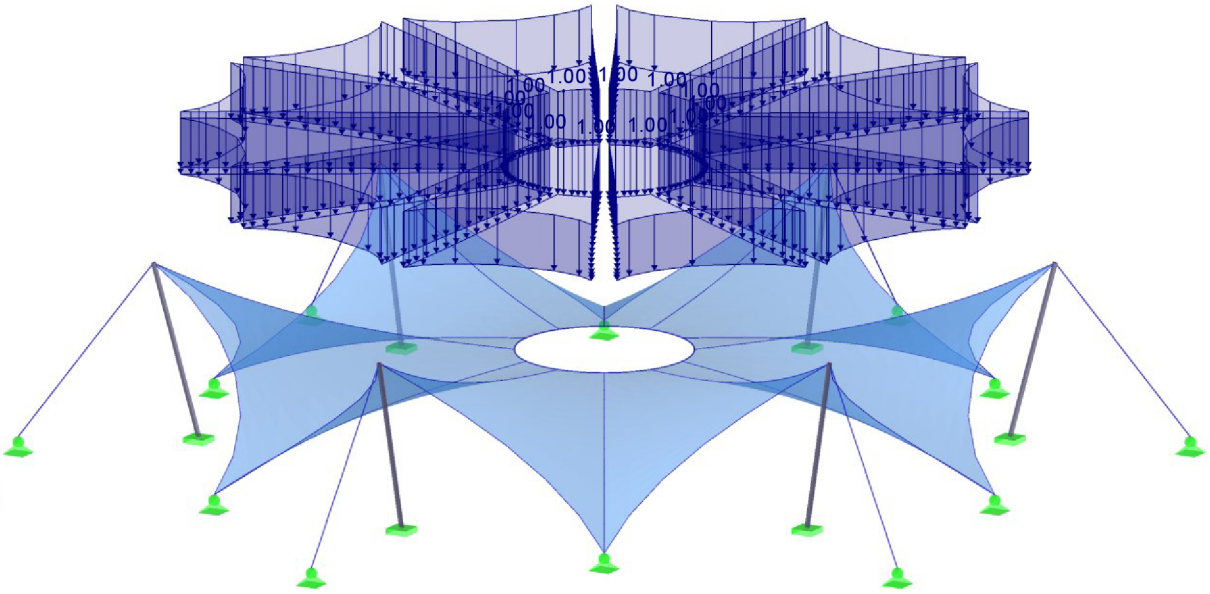

Fig. 133 Snow Load $f_s = 1.00\ \ kN/m^2$

the zero level $h_l = 0.0\ m$, the high points are in the position of $h_h = 4.0\ m$ and the middle ring is situated at the height $h_r = 2.0\ m$ with the diameter $r_r = 2.0\ m$. As can be observed in the following figure, the membrane is reinforced by the cables connecting the inner ring with the outer low and high points (Fig. 131). The definition of the orthotropy directions as well as the FE discretization can be seen in the figure (Fig. 132). Later, the figures of the applied snow and wind loads are presented (Fig. 133, Fig. 134, Fig. 135). The isotropic prestress is defined with the values $n_x = n_y = 1.0\ kN/m$.

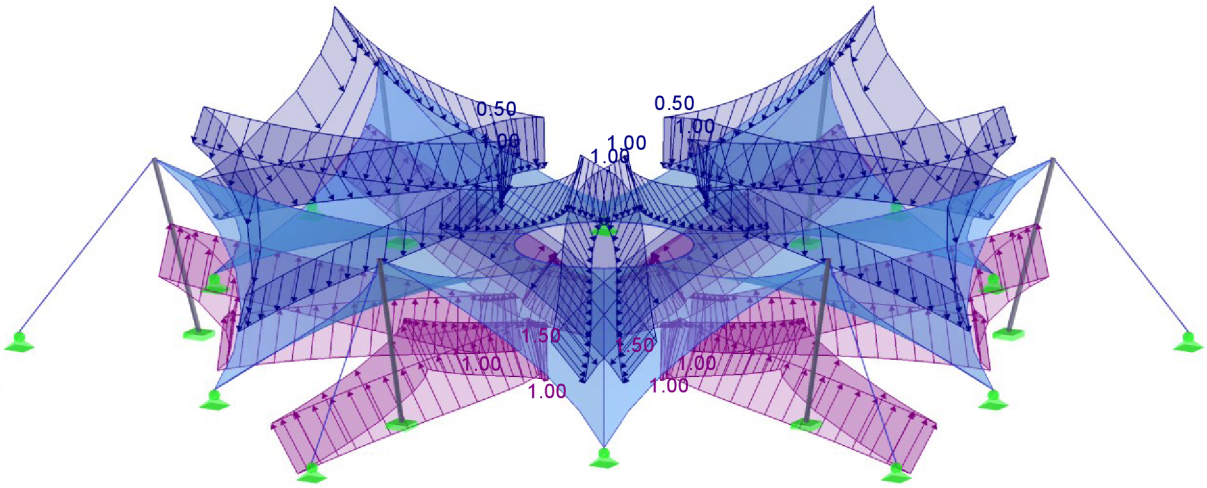

Fig. 134 Wind Load Varying from Pressure Value $f_w = 1.00\ kN/m^2$ until Suction with Value $f_w = -1.50\ kN/m^2$

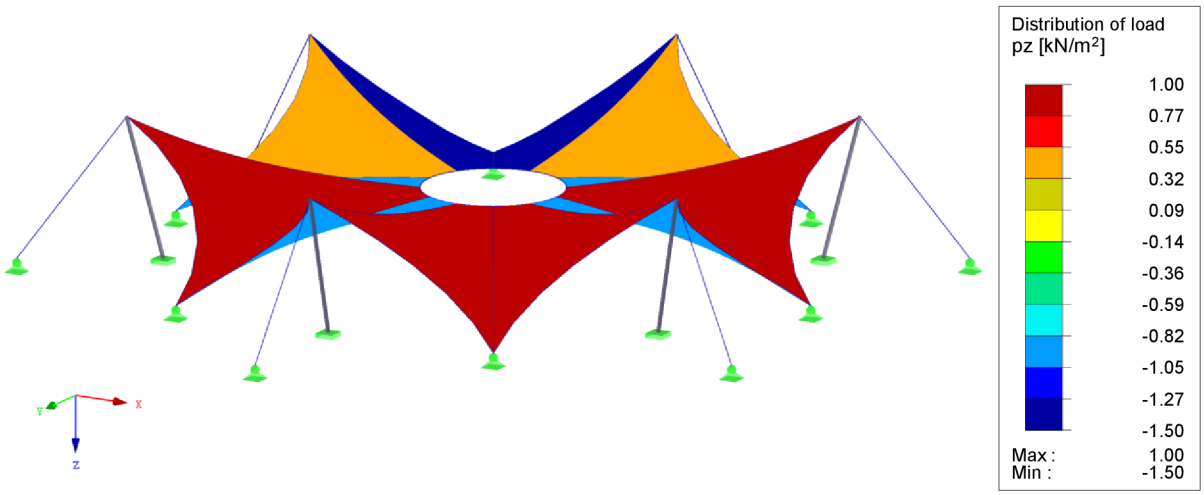

Fig. 135 Wind Load in Coloured Display

A short review of some results is presented below, first the prestress after the form finding process (Fig. 136), then the deformations and the first principal normal forces after the snow (Fig. 137, Fig. 138) and wind (Fig. 139, Fig. 140) load analyses.

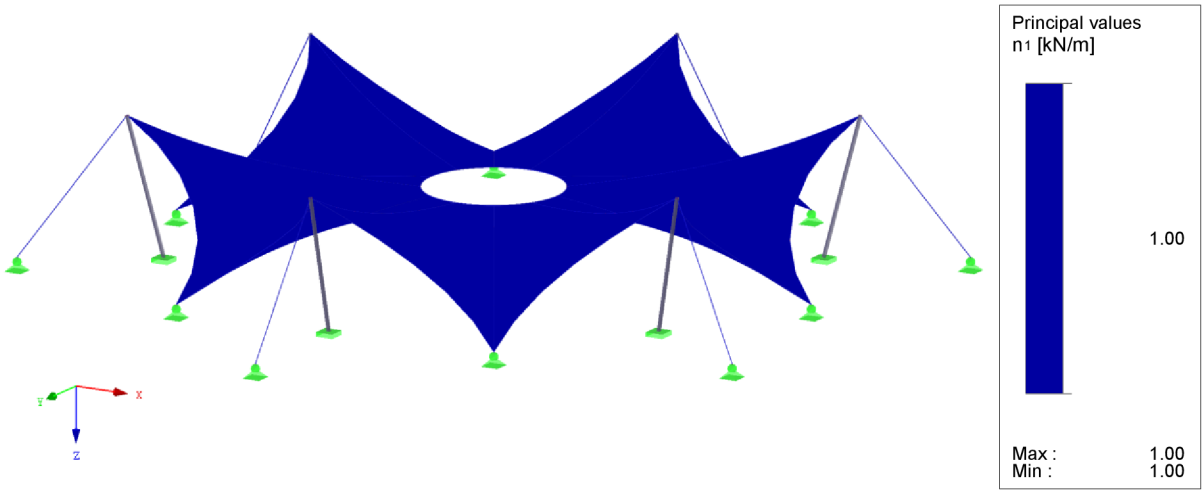

Fig. 136 Prestress in Main Direction n_1 After Form Finding Analysis (Note: $n_2 = n_1$ According to Task Definition)

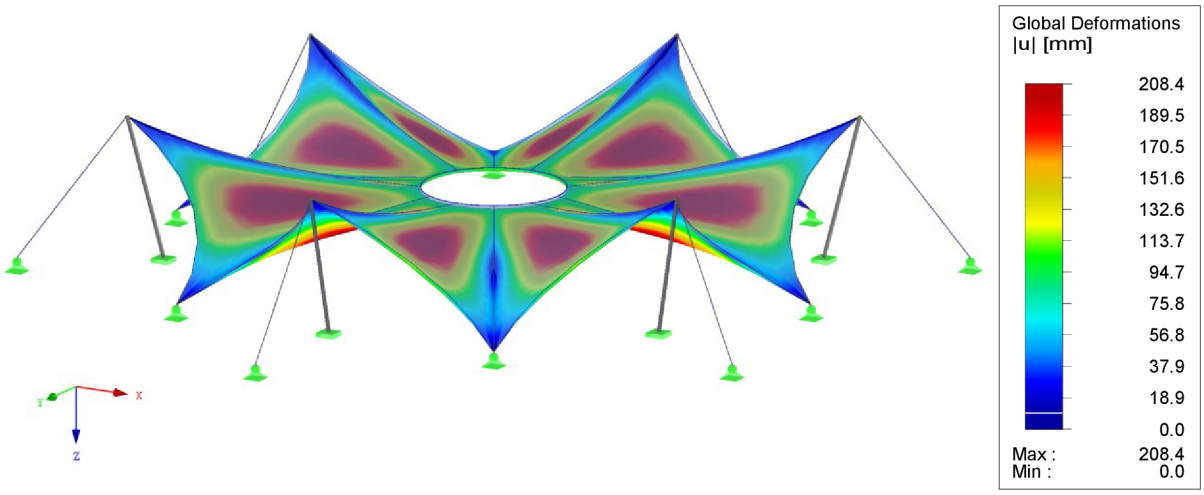

Fig. 137 Snow Load: Global Deformations u

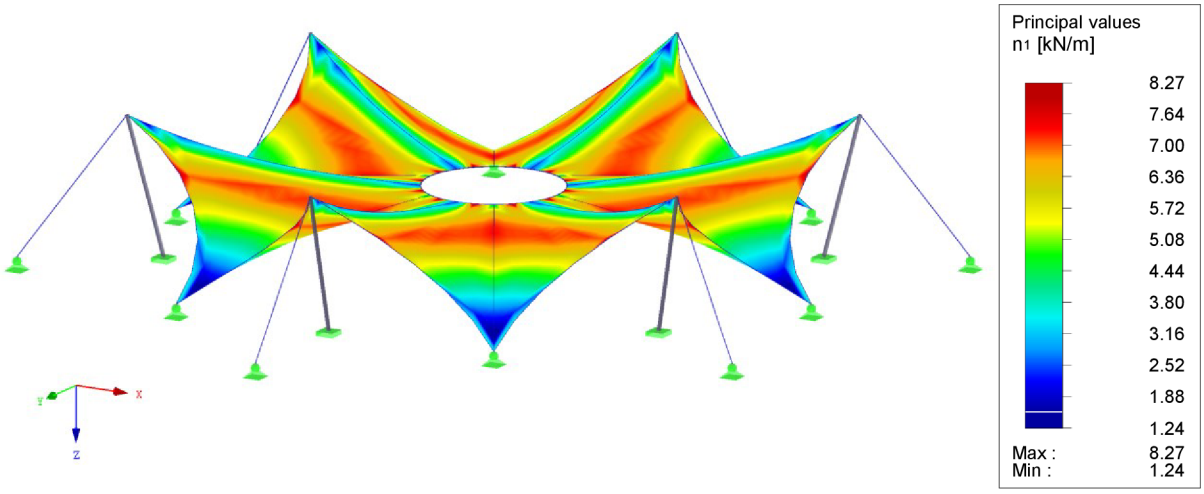

Fig. 138 Snow Load: First Principal Normal Forces n_1

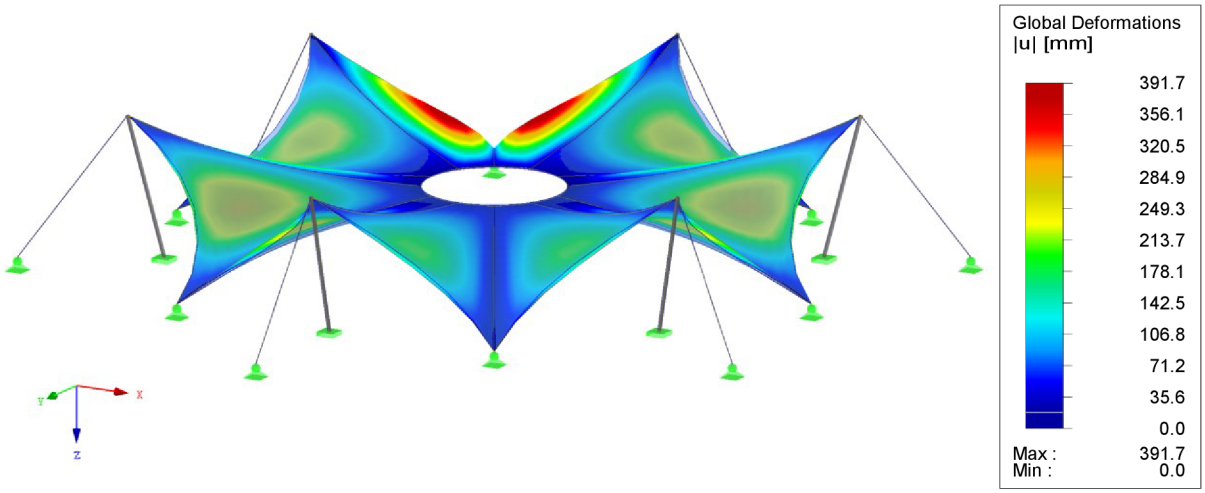

Fig. 139 Wind Load: Global Deformations u

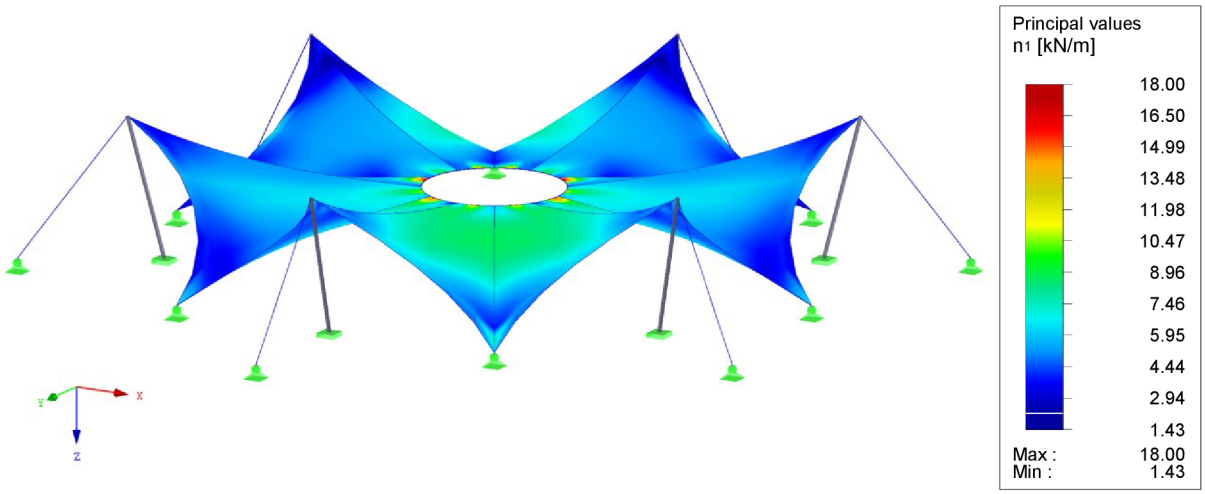

Fig. 140 Wind Load: First Principal Normal Forces n_1

After presenting the results of two load cases of the nonlinear static analysis, the results of the nonlinear time history analyses are presented. In this test case, the periodical changing of the wind load with the angular frequency $\omega = \pi\ rad/s$ is assumed with the load multiplier $\gamma_d = 0.5$. To approximate the damping caused by the surrounding environment, the Rayleigh coefficient $\alpha = 0.5$ is used first, where this quite a high value is assumed because of the low self-weight of the membrane material. Both the implicit Newmark and the explicit central difference methods were used and the results are presented for two selected nodes (Fig. 141) in the form of a graph (Fig. 142) where four results represent the deformations in two discrete nodes for both of the mentioned methods and the time interval of one period $T = 2.0\ s$. A good agreement for both, the implicit and the explicit solutions, can been observed.

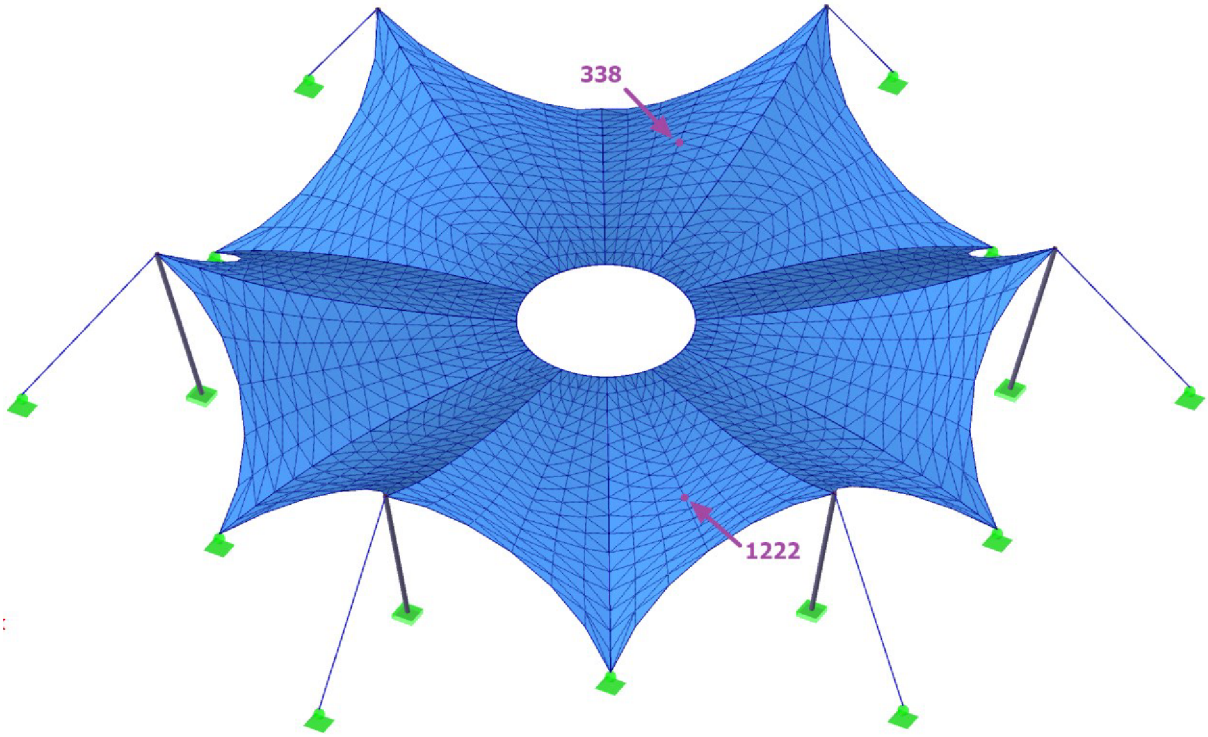

Fig. 141 Investigated Nodes

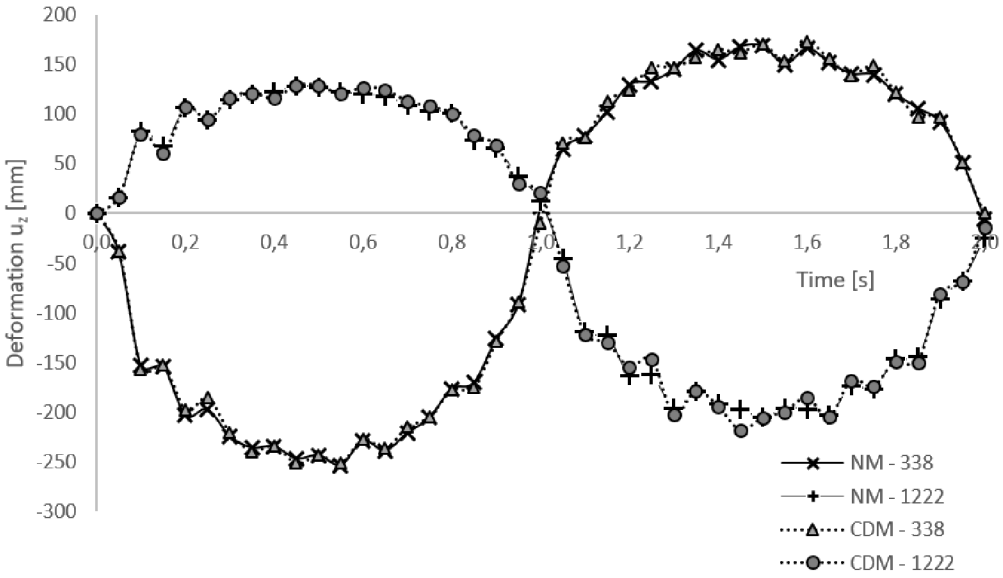

Fig. 142 Deformation u_z of Selected Nodes in Nonlinear Time History Analysis

6 CUTTING PATTERN GENERATION

Due to the discrepancy between the double curvature of membrane structures and the planar pieces of the material they should be made of, the cutting pattern generation is an essential procedure to be performed before the manufacturing process. The quality of the generated patterns strongly affects the quality of the intended prestress approximation, thus this analysis precision is of a high importance.

The whole procedure could be divided into two essential steps. First, it is necessary to cut the spatial shape into appropriately sized pieces, therefore the spatial patterns are obtained. The appropriate width of the patterns is driven by the available material widths, by the curvature of the structure and the aesthetic impression. This step does not bring any approximations as the shape has not been changed yet. However, the manner of the structure division strongly affects the approximation task, which is done in the second step.

The second task to be done is the flattening procedure, thus the planar patterns have to be calculated for their spatial shapes. This is inevitably connected with the necessary distortions, which have to be undertaken. However, it is of the highest interest to come with a procedure, which decrease this discrepancy as much as possible.

In addition to the engineering aspect of this task, the aesthetic importance of cutting patterns has to be considered as well, since the welding lines are a well-visible architectural element (Fig. 143).

Fig. 143 Shopping Centre Chodov in Prague (East Exit from Metro), Czech Republic [X]

In the following, the commonly used cutting lines are described, and the categorization and overview of flattening procedures are further provided. Then, the chosen analysis procedure is presented and finally, the subchapter presenting examples concludes this chapter about the generation of cutting patterns.

6.1 CUTTING LINES

Although the membrane surface could be generally divided into pieces by the arbitrarily chosen lines, there could be practically met two commonly used line types, namely the geodesic lines and the planar sections. The planar sections are created by the intersection of the definition plane with the membrane surface and sometimes, they are preferred. However, the geodesic lines are the most broadly used way when cutting double-curved surfaces, since they have considerable advantages arising from their nature.

It is quite common to meet a definition of the geodesic line, which states that it as a shortest path between the defined nodes. However, a rigorous mathematical definition describes a geodesic line as a line, which does not curve while going through the surface. Therefore, more than one geodesic line can exist for a given surface in general, as could be observed in the following figure (Fig. 144). For sure, the shortest line between the defined nodes is a geodesic line, which is of interest when cutting a membrane.

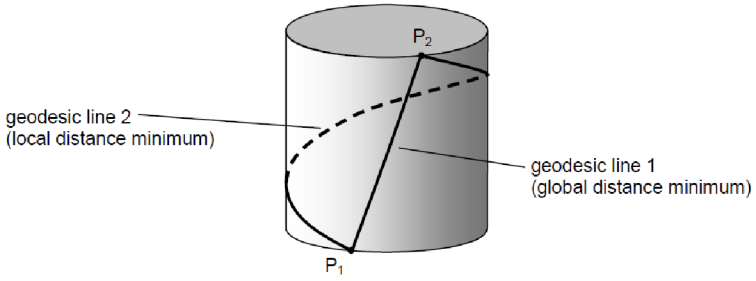

Fig. 144 Possibility of Existence of Different Geodesic Lines [77]

A considerable advantage when using these lines arise from the fact that the geodesic line does not curve when going through the surface as the flattened patterns are relatively straight after flattening when comparing with the patterns defined by different line type. For example, when using planar cuts, the flattened patterns have a curved shape as will be shown in the chapter with examples.

A possible way of a geodesic line calculation on a discretized FE mesh is presented in the figure below (Fig. 145). Considering the point P_{start} as a geodesic line start and P_{end} as its intended end, the line could be searched in the following way. The initial direction in P_{start} is chosen and, when crossing the FE edge, the angle α is preserved. This is based on the geodesic line definition saying that it does not curve in the tangential plane to the surface. Following this algorithm, the line is crossing the FE edges until it reaches the border of the surface. Then, the distance between the current end point position $P_{current}$ and the intended point position P_{end} is a basis for the initial direction adjustment at the point P_{start}. Following this procedure in an iterative way, the current geodesic line end position $P_{current}$ converges to the intended position P_{end}. The left and the middle parts of the figure (Fig. 145) display the spatial FE discretization, the intended geodesic line start and end positions and its final spatial geometry. The right part

of the figure demonstrates the uncurved nature of the geodesic line when transforming the given spatial mesh into a plane.

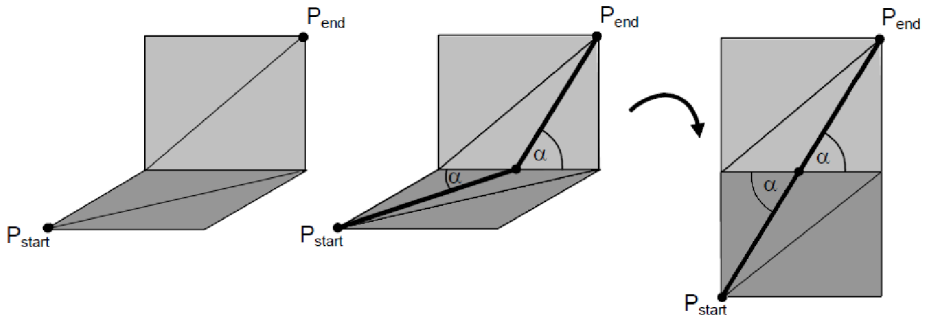

Fig. 145 Geodesic Line on FE Mesh Before and After Flattening ([77] with Modifications)

In the literature, the process presented above can be found in a more detailed description, and other solution procedures are also available [38, 39, 77, 82, 83, 84, 85, 86].

6.2 FLATTENING PROCEDURE

After dividing the surface into a series of spatial patterns, the flattening procedure is to be performed. Essentially, two different classes of this approximative task can be followed: the mathematical solution and the continuum mechanics solution procedures. Further, there will be presented some solution approaches, starting from the earlier simplified methods until the general ones.

6.2.1 Mathematical Flattening

One of the oldest flattening procedures is called the **Simple Triangulation Method**. This approach is based on replacing the initial FE mesh, cut-out by using specified cutting lines, by a special mesh for unfolding. During this process, the mesh for unfolding is created in such a way that the individual elements cross the whole width of the pattern. Thus, the spatial pattern can be further transformed into a plane easily. This process is described in the attached figure (Fig. 146). While replacing the FE mesh by the special one, there is really enormous simplification performed and the methods precision is poor.

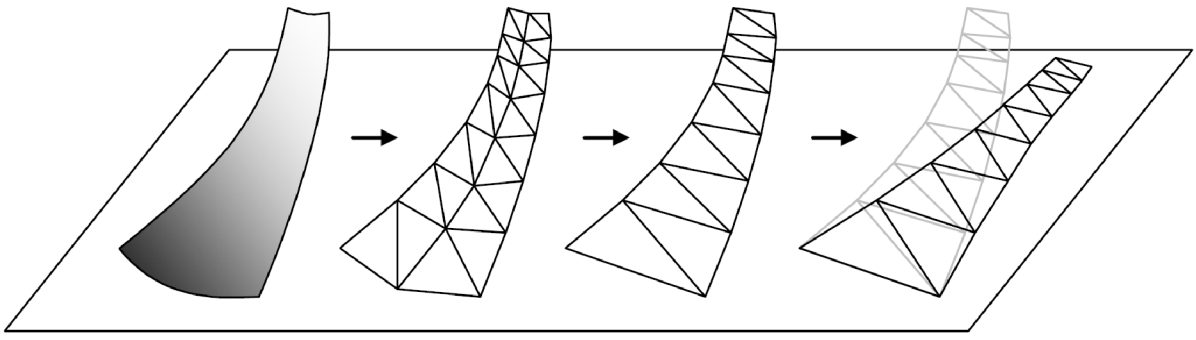

Fig. 146 Basis of Simple Triangulation Method (from left: Spatial Shape, FE Mesh of Spatial Model Used for Form Finding and Structural Analysis Purposes, Modified Mesh for Flattening Purposes, Flattened Pattern) [77]

Far more advanced procedure of this class can be named **Mathematical Squashing**. In this second mathematically based method, the FE mesh of the cut-out membrane pieces is used

during the analysis. Furthermore, the best geometrical approximation of the spatial pattern is searched for by the least square approach, minimizing the prescribed geometrical function.

$$\mathbf{F}(x, y) = \frac{\mathbf{1}}{\mathbf{2}}\mathbf{v}^{\mathbf{T}}\mathbf{P}\,\mathbf{v} \tag{6.1}$$

$$\delta\mathbf{F}(x, y) = 0 \tag{6.2}$$

where **v** represents the vector of residuals, **P** represents the matrix of weights, and **F** is the function to be minimized. More detailed description of this method could be found in the following literature [87, 88].

The **mathematical squashing** is considerably more precise than the **simple triangulation method** described previously. It represents a good compromise between the accuracy and the algorithm performance, as the solution is obtained in a single calculation step. However, this method is still unable to precisely consider the physical properties of the material used for patterns.

6.2.2 Physical Flattening

This class of methods considers the flattening procedure as a physical process, mostly directly derived from the continuum mechanics basis. The pattern shape transformation from the space into the plane causes strains and thus, searching for equilibrium is performed (Fig. 147).

One of the earlier contributions dealing with the comparison of the pattern quality when using different methods was written by E. Moncrieff and B.H.V. Topping. [89]. Further interesting contribution with the proposal of Stress Composition Method (SCM) was presented by the authors B. Maurin and R. Motro [90]. Recently, the authors K.U. Bletzinger and A. Widhammer contributed to this field with the method called Variation of Reference Strategy (VaReS) [91], which inverts the workflow of the Total Lagrangian formulation in principle and searches for the appropriate reference for the prescribed erected (deformed) pattern in the space. In the publications [92, 93, 94, 95], further research works of the author team around K.U. Bletzinger are presented. Another contributions to this area of analyses could be found in [96, 97, 98, 99, 100, 101, 102, 103, 104], where some of the authors replace the continuum by the system of nodes connected with springs.

Considering the methods consistently derived from the continuum mechanics basis, the approaches minimizing the sum of the stress differences as well as the methods minimizing the sum of the energy differences accumulated during the flattening process could be identified. The first one of the mentioned procedures has considerably poorer convergence behaviour than the second one [38, 94]. As presented in the mentioned research works, both procedures lead to quite close resulting pattern shapes.

Using the procedure minimizing the sum of the energy differences accumulated in the patterns during the flattening process, the general principle of the virtual work (2.25), thus also the linearized forms (2.40) and (2.41), is consistently followed. Therefore, the earlier derived equations are appropriate for this analysis

$$\int_{{}^tV} {}_tC_{ijrs}\ {}_t\varepsilon_{rs}\ \delta\ {}_t\varepsilon_{ij}\ {}^tdV + \int_{{}^tV} {}^t\sigma_{ij}\ \delta\ {}_t\eta_{ij}\ {}^tdV = {}^{t+\Delta t}\mathcal{R} - \int_{{}^tV} {}^t\sigma_{ij}\ \delta\ {}_t\varepsilon_{ij}\ {}^tdV \tag{6.3}$$

or in the matrix notation

$$\int_{{}^tV} {}_t\mathbf{C}\ {}_t\boldsymbol{\varepsilon}\ \delta\ {}_t\boldsymbol{\varepsilon}\ {}^t\mathrm{dV} + \int_{{}^tV} {}^t\boldsymbol{\sigma}\ \delta\ {}_t\boldsymbol{\eta}\ {}^t\mathrm{dV} = {}^{t+\Delta t}\boldsymbol{\mathcal{R}} - \int_{{}^tV} {}^t\boldsymbol{\sigma}\ \delta\ {}_t\boldsymbol{\varepsilon}\ {}^t\mathrm{dV} \tag{6.4}$$

By this really natural way, in terms of the FEA, the cutting patterns with a high quality can be calculated under consideration of the given material properties and other possible requirements, as will be presented later.

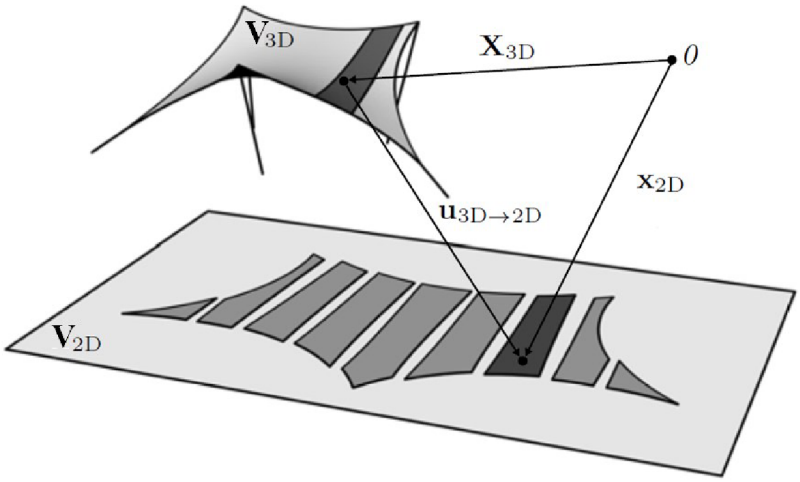

Fig. 147 Flattening Process ([38] with Modifications)

When following this FEA procedure, two strategies can be identified. The **forward flattening process**, squashing down the spatial patterns, or the **backward flattening process**, simulating the erecting process of the patterns into their final position (VaReS) while modifying the reference pattern position.

Whether choosing the first or the second way, the suitable starting shape of planar patterns is of high interest, as gradual deforming from the spatial configuration would exhibit poor calculation performance. This planar shape can be seen as the shape after the first iteration. The pattern projection into the global plane or into the mean tangential plane of the spatial pattern is used quite often, as could be seen in the presented research papers and works. The closer is the initial planar shape to the equilibrium one, the higher is the algorithm performance. Thus, the mathematical squashing could be used as a really good starting position for the subsequent physical analysis.

6.3 SPECIAL REQUIREMENTS FOR FLATTENING PROCEDURE

Even though the physical flattening procedure could be classified as a special case of FEA, there are some peculiarities and differences, which has to be satisfied during this analysis. Specifically, the fact that the orthotropic directions are driven by the planar shape instead of the original spatial one, is of high importance. Furthermore, there is also an important engineering requirement for the compatibility of the seam lines.

6.3.1 Orthotropic Directions

When taking into consideration the material behaviour of the woven fabric during the flattening procedure, the resulting orthotropic directions could not be derived from the standard deformation from the spatial template, thus the spatial pattern, to the plane. This would not lead to the orthogonal orthotropy in the final pattern, which, however, is the physical nature of the woven fabrics. Thus, the local Cartesian axial system of the FE in the pattern has to be driven by its definition in the resulting pattern.

In other words, the orthotropic directions have to be treated carefully while calculating the patterns to avoid violating the flattening process as well as the physical nature of the materials used.

6.3.2 Compatibility of Seam Lines

While the previous requirement was of physical nature, the other one is more the manufacturing restriction. Since the planar patterns are to be connected together in the unstressed state, the seam line compatibility is required. Thus, the same length of the seam lines of the adjacent patterns is a required restriction during the flattening procedure $\Delta L_i = 0$. Therefore, the patterns are not calculated separately, but together to ensure this compatibility for all the patterns (Fig. 148).

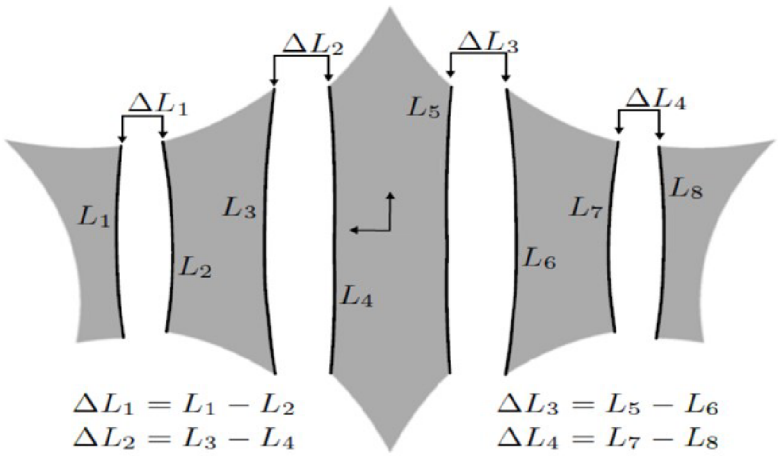

Fig. 148 Ensuring Same Lengths of Boundary Lines of Adjacent Patterns ([38] with Modifications)

6.3.3 Compensation

As the cutting pattern analysis deals with the membrane structures under pretension, the process of stress releasing has to be satisfied. Thus, the final pattern size is adjusted to satisfy the required pretension in the tensioned state.

However, the woven fabric exhibits a nonlinear material response. Therefore, not only the form found shape with the required prestress has to be taken into account, but also the stresses reached in the nonlinear structural analysis. The goal of the applied compensation is to satisfy the approximation of the intended prestress after undergoing the loading cycles. If only the prestress would be compensated, the plastic deformations caused by applying the load would remove the prestress after unloading. Thus, the applied membrane compensation is summing both the expected plastic strains after the loading and unloading cycles and the residual elastic strains for satisfying the prestress in the membrane.

The simulation of the loading and unloading cycles could be seen in the results of a particular biaxial test, where in the first figure, the load history is presented (Fig. 149), and in the second one, the subsequent strain history is monitored (Fig. 150).

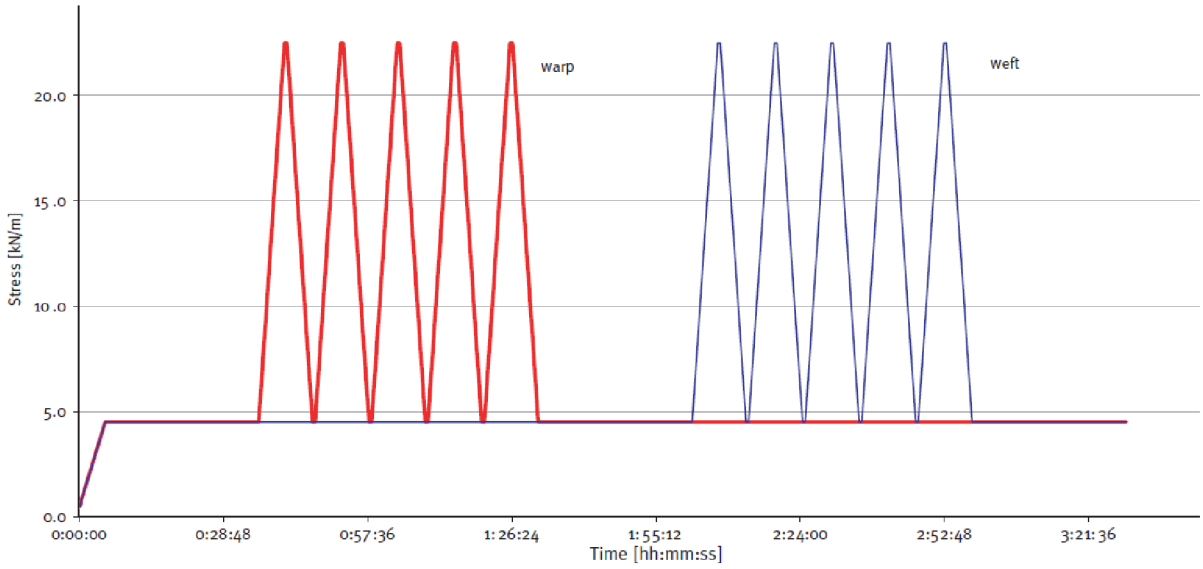

Fig. 149 Biaxial Test: Load History [80]

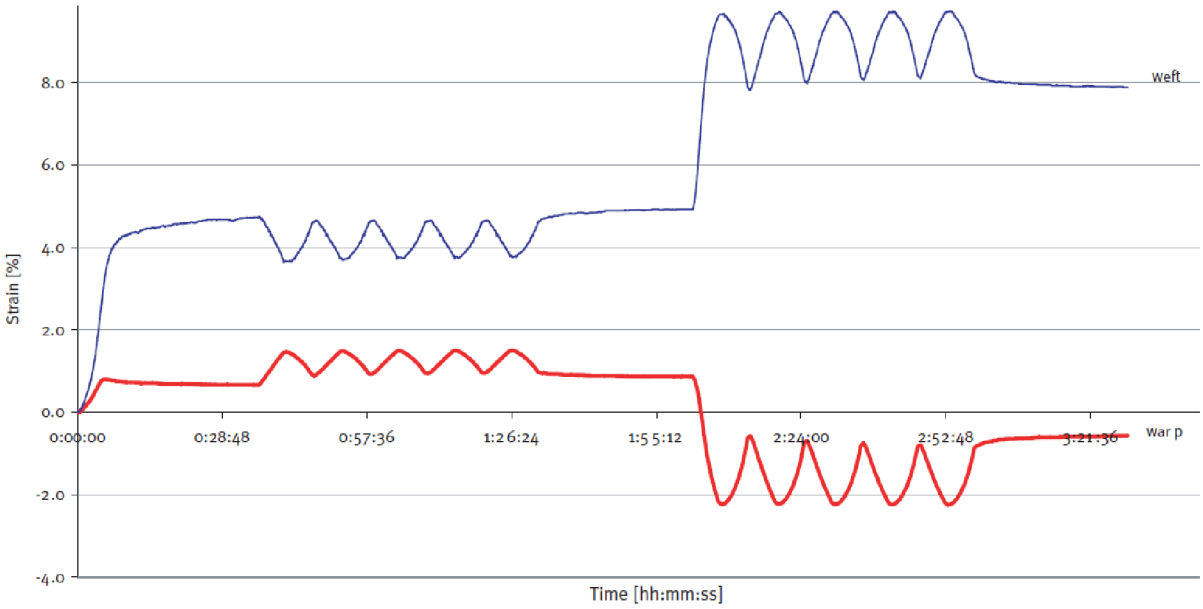

Fig. 150 Biaxial Test: Measured Strains [80]

In the consequence of this complexity, the standard way of the compensation consideration applies the additional strains into the flattening procedure, which contributes to the 'right hand side' of the equilibrium equation (6.3) or (6.4). These strains are obtained by the biaxial testing while applying the prescribed load history, or by using the recommended values when following the simplified way.

There could be observed a research interest in the consideration the compensation automatically by releasing the prestress of the form found membrane with the consideration of the defined material model. However, this way needs further investigation and detailed research as such a procedure is extremely complex. This process would have to deal with the plastic material

model and load history, since both the form finding results and the static analysis results would have to be considered in the process of the automatic compensation estimation. For sure, this is a great field for detailed investigations, research and experimental work.

6.4 SELECTED CALCULATION PROCEDURES

As the examples presented in further chapter were calculated in the software RFEM by the company Dlubal Software [III], using the FEA solver by the FEM consulting company [IV], the selected and consequently implemented procedures are mentioned here.

In the calculation of the geodetic lines, the above-described angular based algorithm was followed.

For the development of the flattening procedure, the combination of the mathematical squashing (for estimation of the shape in the first iteration) and the subsequent minimization of the energy differences sum was followed, as this process provides the optimum combination of the speed and precision with the possibility of applying the selected material definition, structural requirements, etc.

6.5 EXAMPLES

The examples presented below demonstrate some of the facts mentioned above, as for example the consequence of using different cutting lines, the influence of the selected material during the flattening procedure, and the example dealing with the evaluation of the pattern quality [44].

6.5.1 Comparison of Usage of Different Cutting Lines

The first example to be presented is a hypar shaped membrane structure. For splitting this model, different cutting lines are applied to demonstrate their influence on the resulting pattern shape. The prestressed spatial configuration is presented in the first figure (Fig. 151) and the shapes of the resulting patterns are shown in the second figure (Fig. 152).

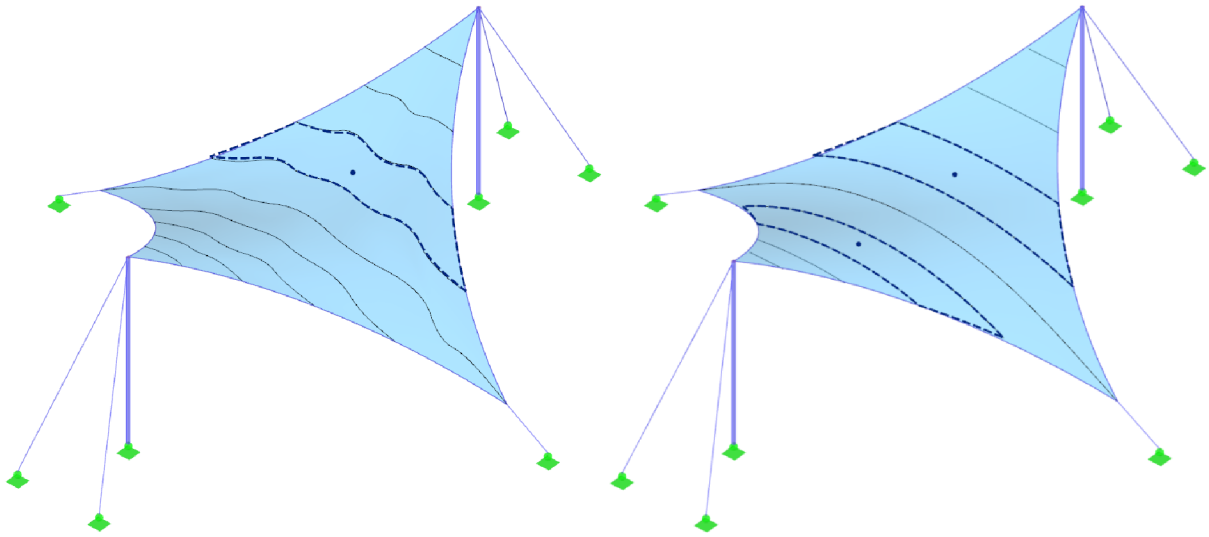

Fig. 151 Different Cutting Lines Used to Split Membrane: Irregular Lines (Left Pattern), Geodesic Lines (Middle Pattern) and Planar Sections (Right Pattern) [44]

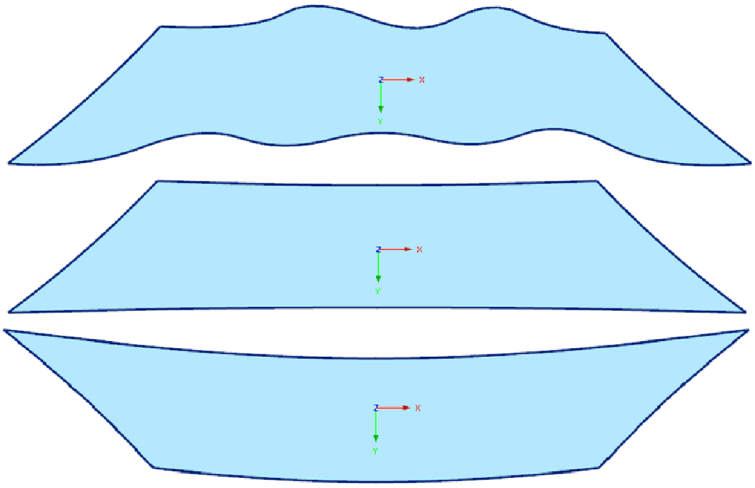

Fig. 152 Planar Patterns: Usage of Irregular Lines (Upper Pattern), Geodesic Lines (Middle Pattern) and Planar Sections (Lower Pattern) [44]

Based on this observation, the reason for preferring the geodesic lines is obvious, as this solution leads to decreasing the material wastage as well as the possibility of a quite close alignment of the warp direction with the seam lines.

6.5.2 Influence of Selected Material Model

The second presented example deals with the influence of the selected material model consideration during the flattening procedure. Here, two different materials are used for the simple structure presented below (Fig. 153). First, the linear response of the ETFE material is assumed with the values $E = 900.0\ MPa, \nu = 0.45$, and further the linear orthotropic response of the coated woven fabric is defined as $E_x = 2000.0\ kN/m, E_y = 1000.0\ kN/m, G = 200.0\ kN/m, \nu_{xy} = 0.20$.

The structure is flattened as one pattern, obviously not appropriate for a real designing case, but for this exemplary demonstration, this choice is suitable, since there can be bigger distortions expected and observed than when the membrane would be cut into small patterns. Furthermore, the resulting strains undergone during the flattening are presented for both cases of the predefined materials (Fig. 154 – Fig. 161).

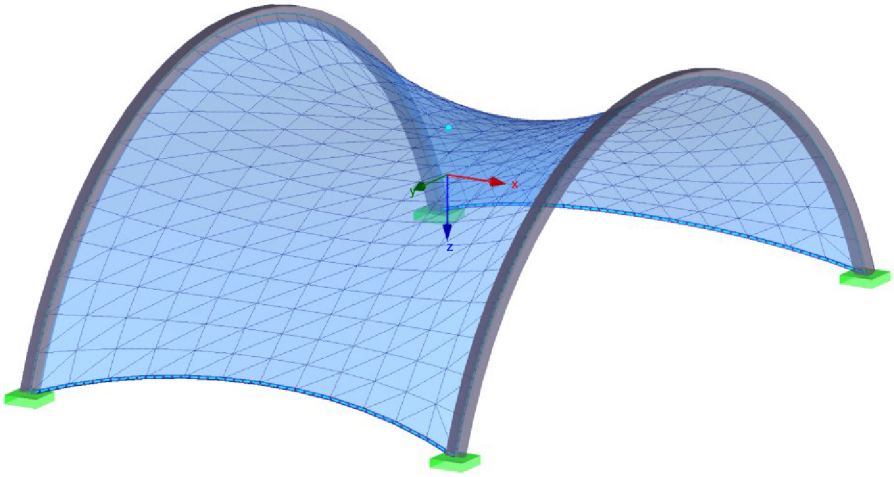

Fig. 153 Membrane Structure to be Flattened

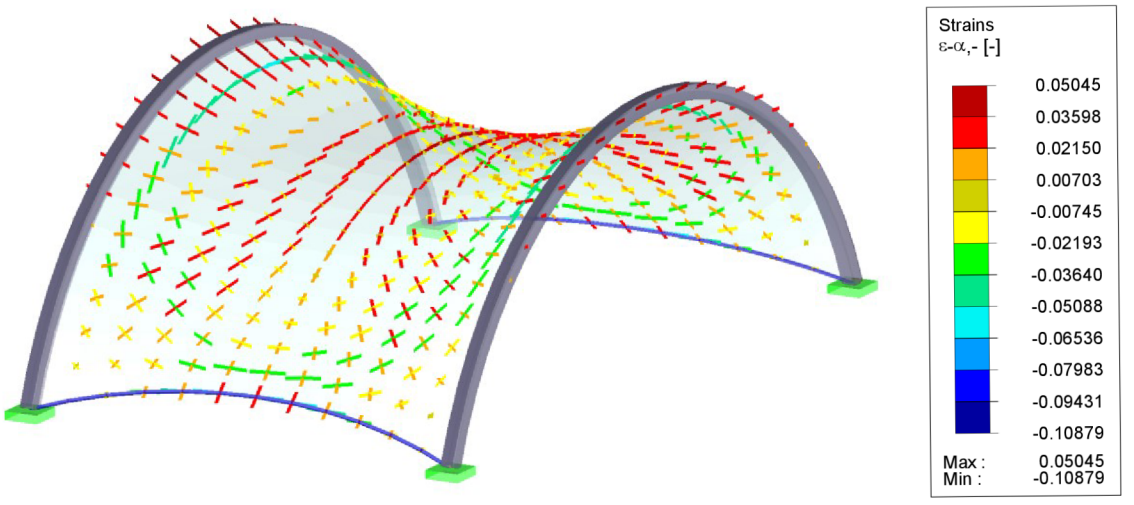

Fig. 154 ETFE: Principal Strains ε_1 and ε_2

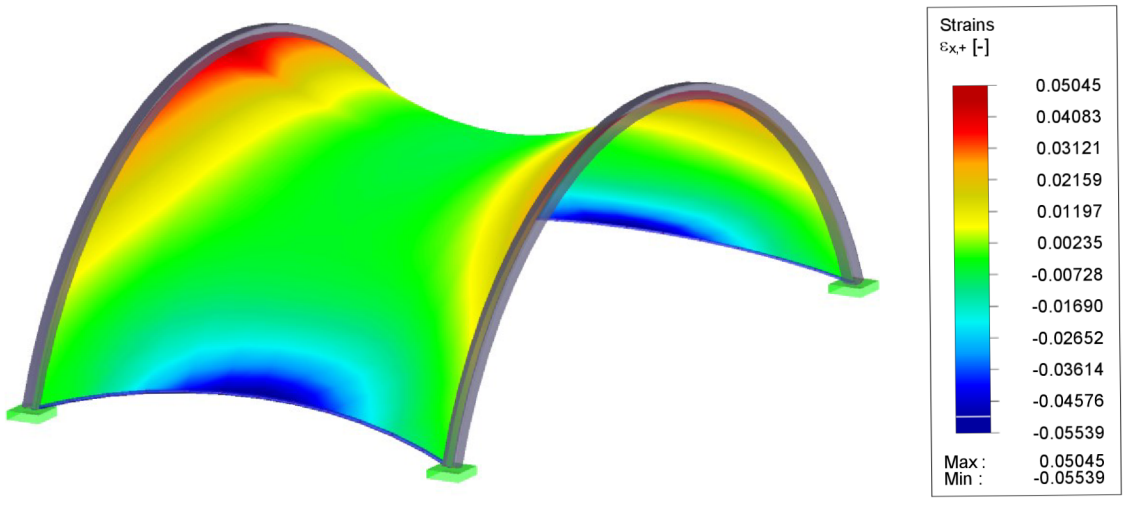

Fig. 155 ETFE: Axial Strains ε_x

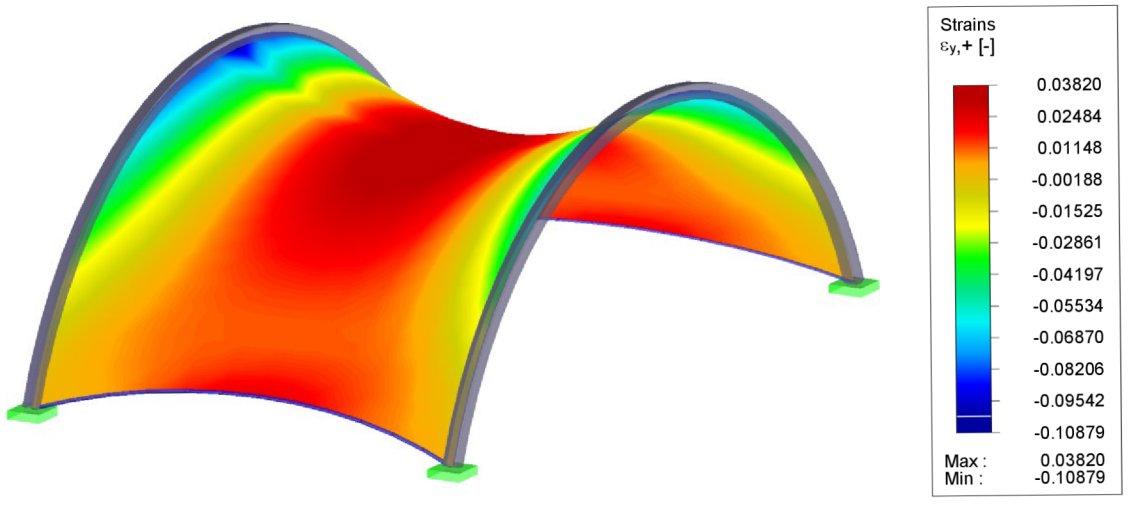

Fig. 156 ETFE: Axial Strains ε_y

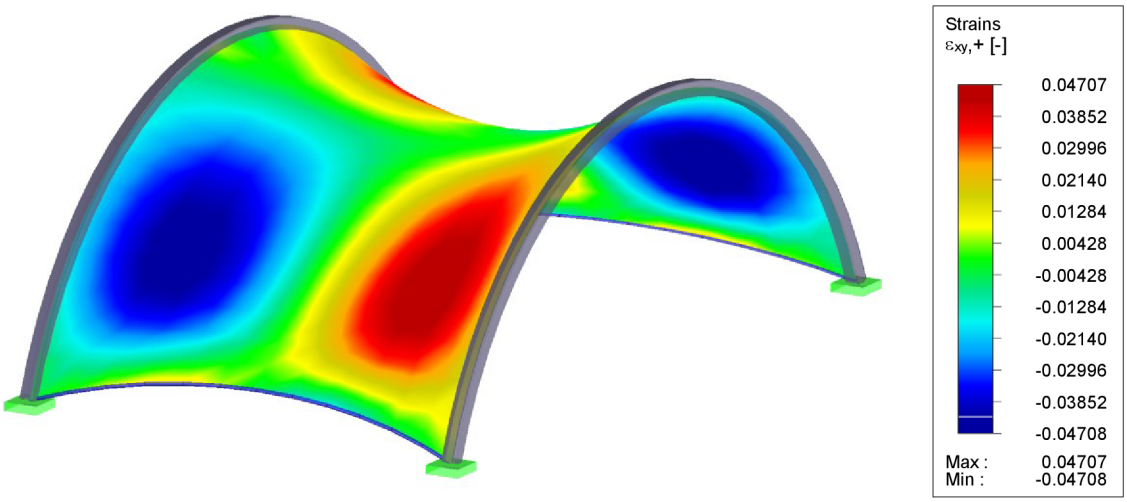

Fig. 157 ETFE: Shear Strains γ_{xy}

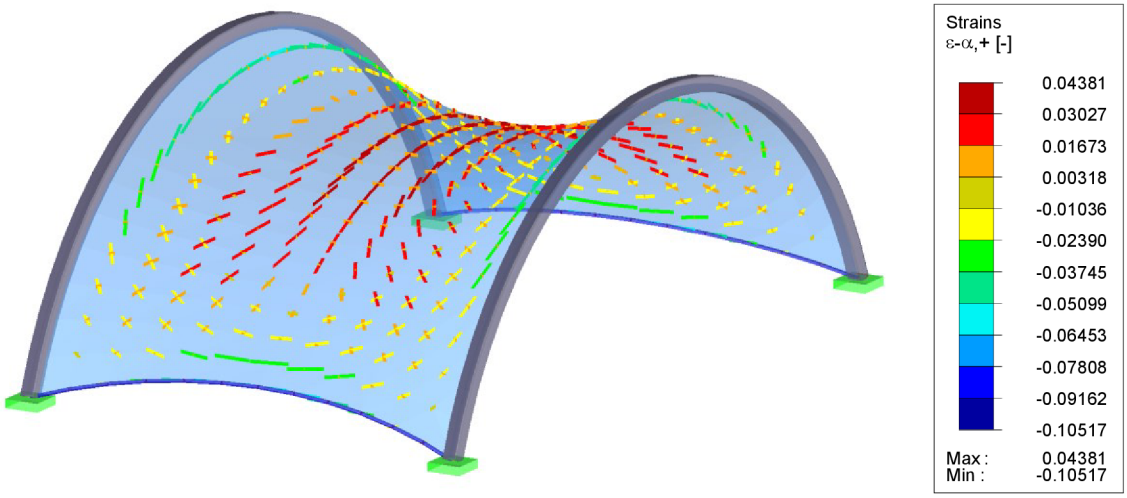

Fig. 158 Woven Fabric: Principal Strains ε_1 and ε_2

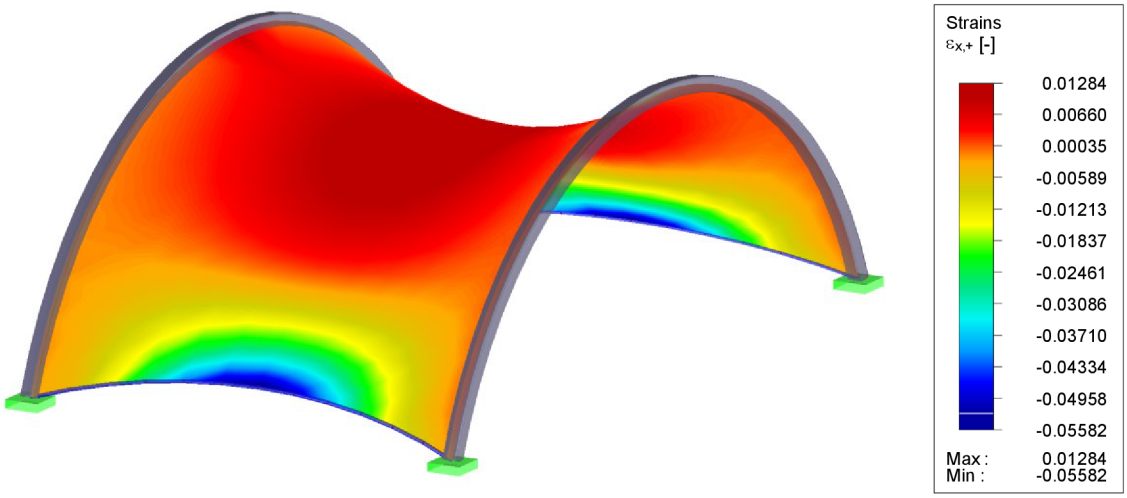

Fig. 159 Woven Fabric: Axial Strains ε_x

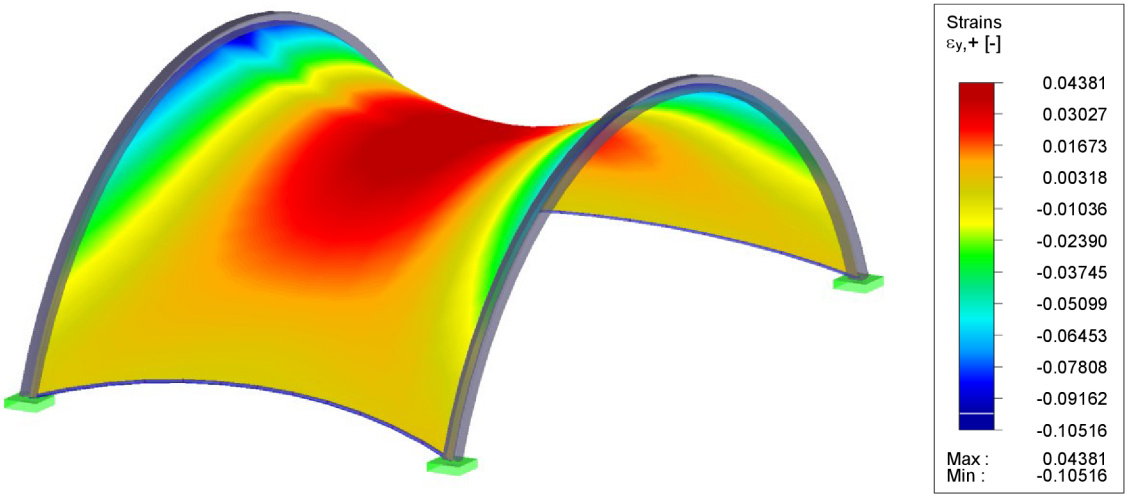

Fig. 160 Woven Fabric: Axial Strains ε_y

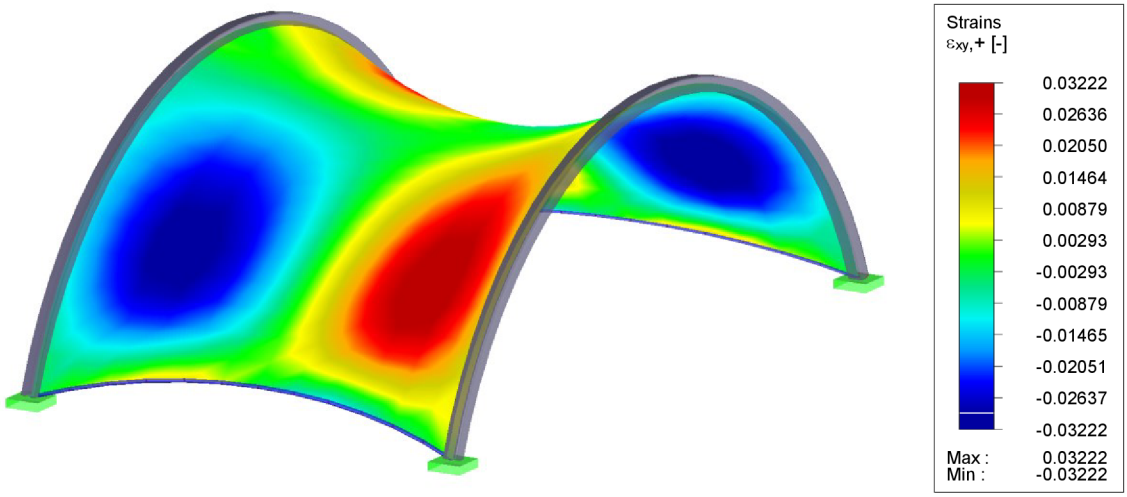

Fig. 161 Woven Fabric: Shear Strains γ_{xy}

6.5.3 Evaluation of Flattened Patterns

The structure presented above is now analyzed by using different cutting pattern layout definitions. Two cases are identified (Fig. 162, Fig. 163), where in the first case, the membrane is divided into three patterns, and in the second case, the membrane is divided into six patterns. The orthotropic material defined above is used.

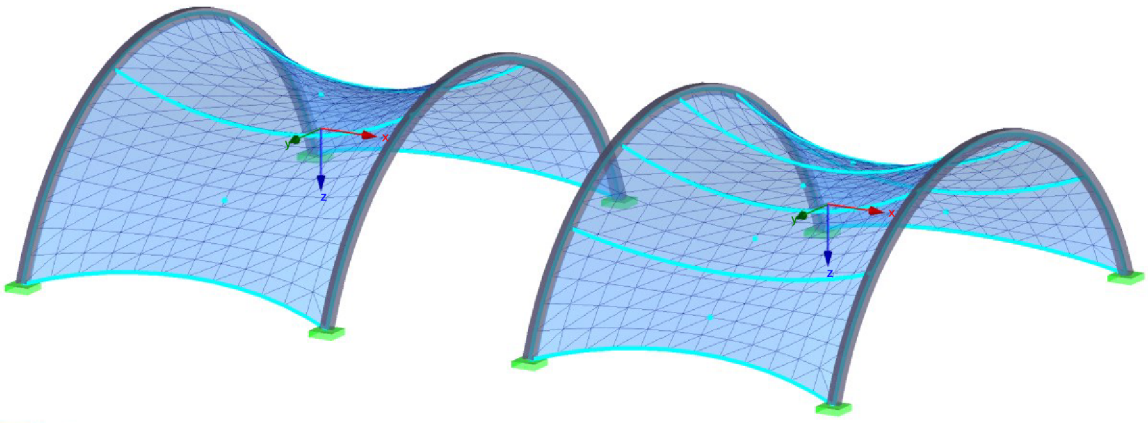

Fig. 162 Different Cutting Pattern Layouts and Orthotropic Directions Definition

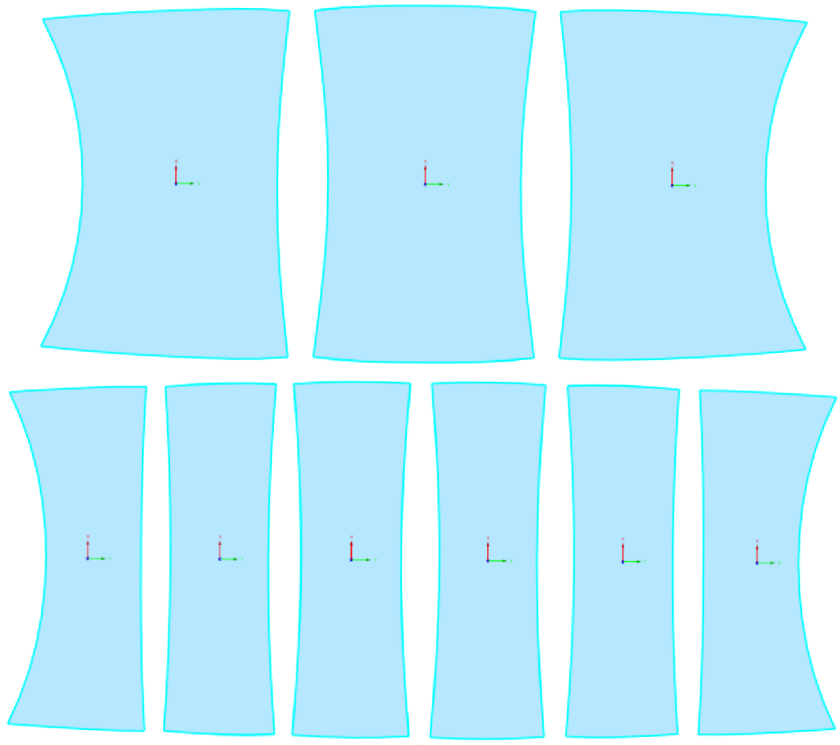

Fig. 163 Different Cutting Patterns Layouts After Flattening

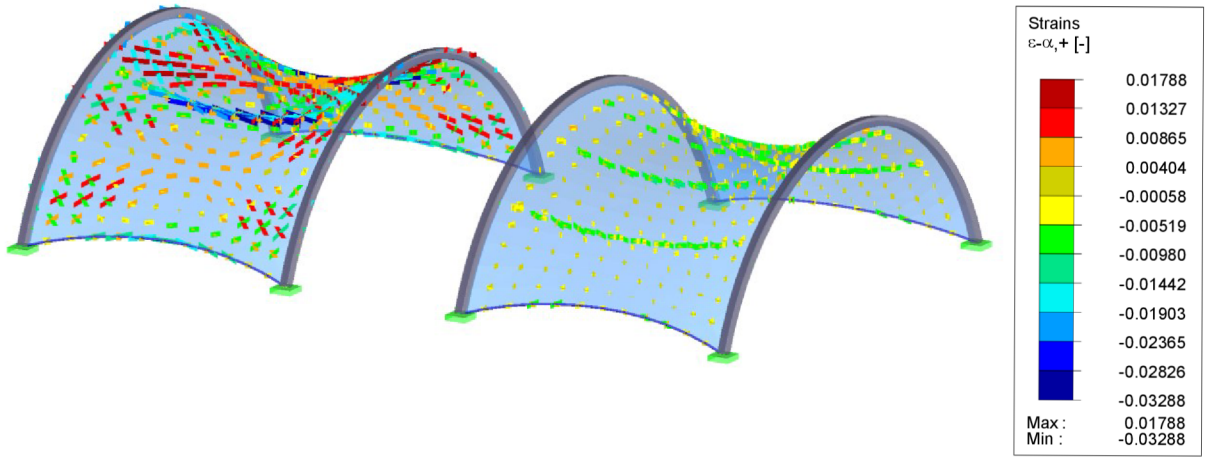

Fig. 164 Principal Strains ε_1 and ε_2

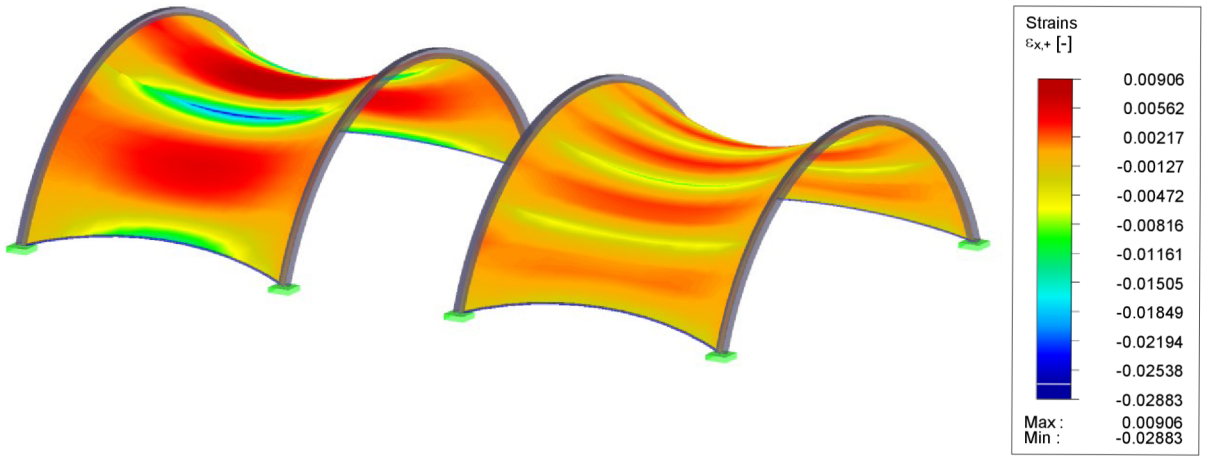

Fig. 165 Axial Strains ε_x

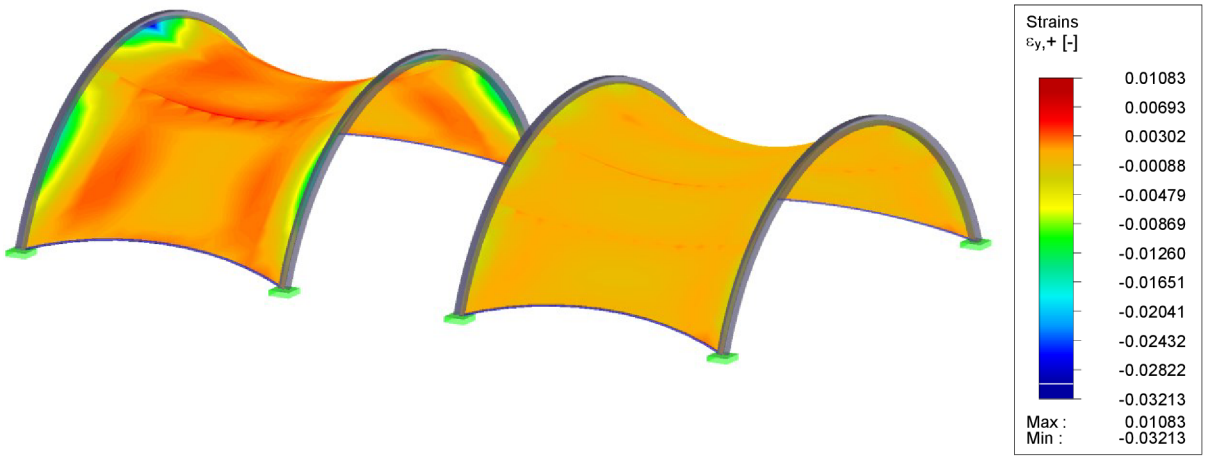

Fig. 166 Axial Strains ε_y

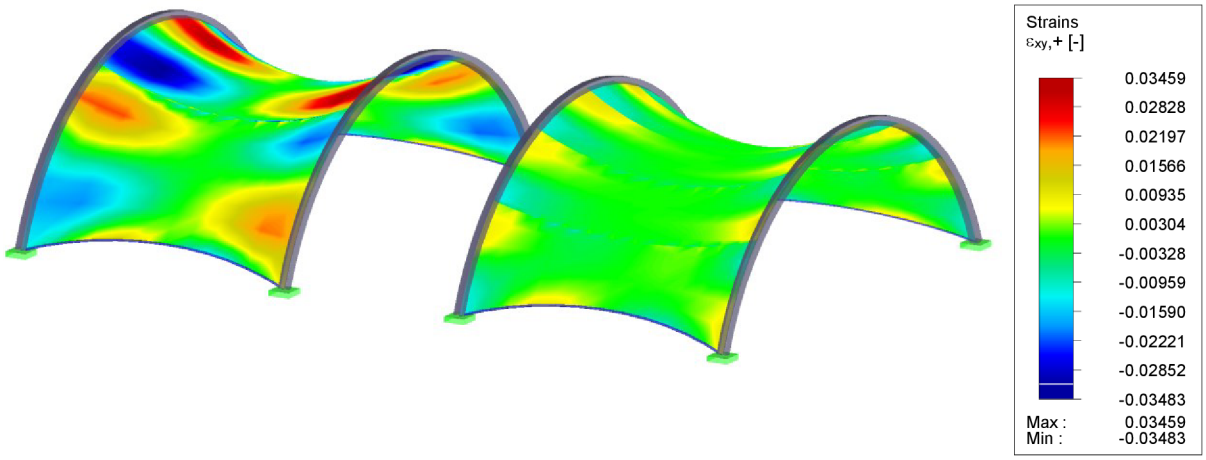

Fig. 167 Shear Strains γ_{xy}

The selected layout has a considerable influence on the strains necessary for reaching the flat configuration (Fig. 164 - Fig. 167). By means of these results, it can be evaluated whether the pattern is suitable or not, when the acceptable distortion is defined. Of course, the smaller are the patterns, the lower are the strains. But the manufacturing process, the aesthetic appearance and the available material widths should be considered as well. The results of the cutting pattern analysis can thus help when deciding the pattern layout and the evaluation of their quality.

6.5.4 Examples of Complex Structure Patterning

The previous structure had quite simple configurations as they were intended to focus on particular tasks. The structure below, on the other hand, has the demonstrative purpose to show the pattern layout for a more complex membrane structure (Fig. 168, Fig. 169).

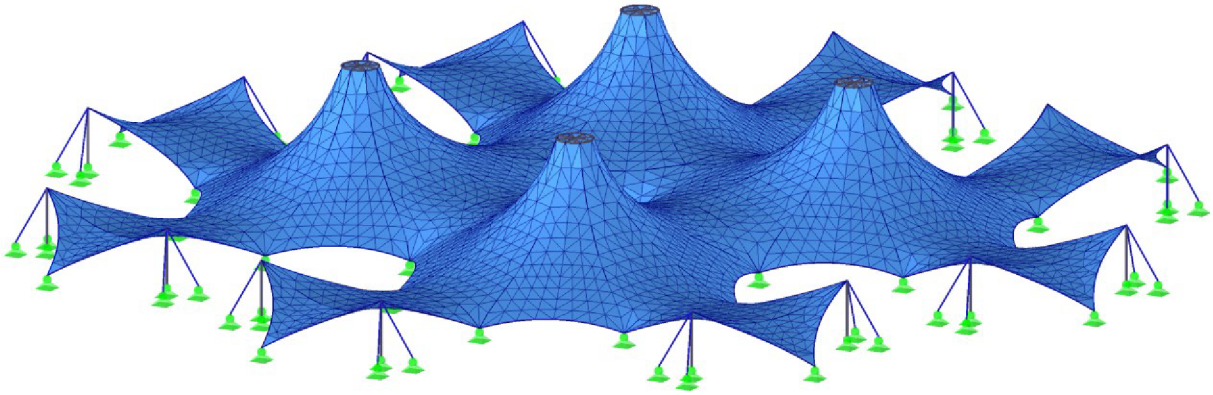

Fig. 168 Composition of Conical and Hypar Membranes

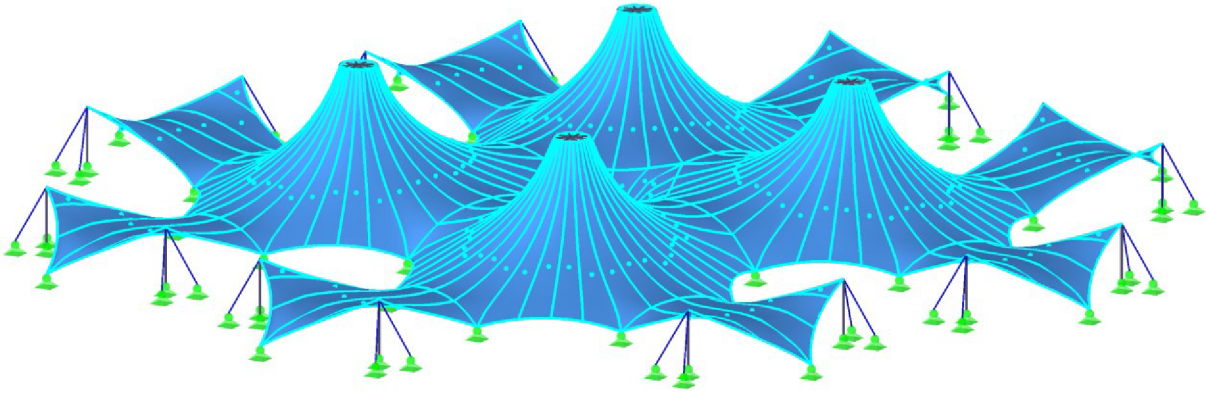

Fig. 169 Pattern Layout

7 USE IN PRACTICE

Due to the possibility of fruitful interconnection of the research work performed at the university environment and the development work performed in the established software companies, the calculation tools for membrane structures were developed in the framework of a teamwork and implemented into the RFEM software [III]. The calculation procedures are implemented as described above.

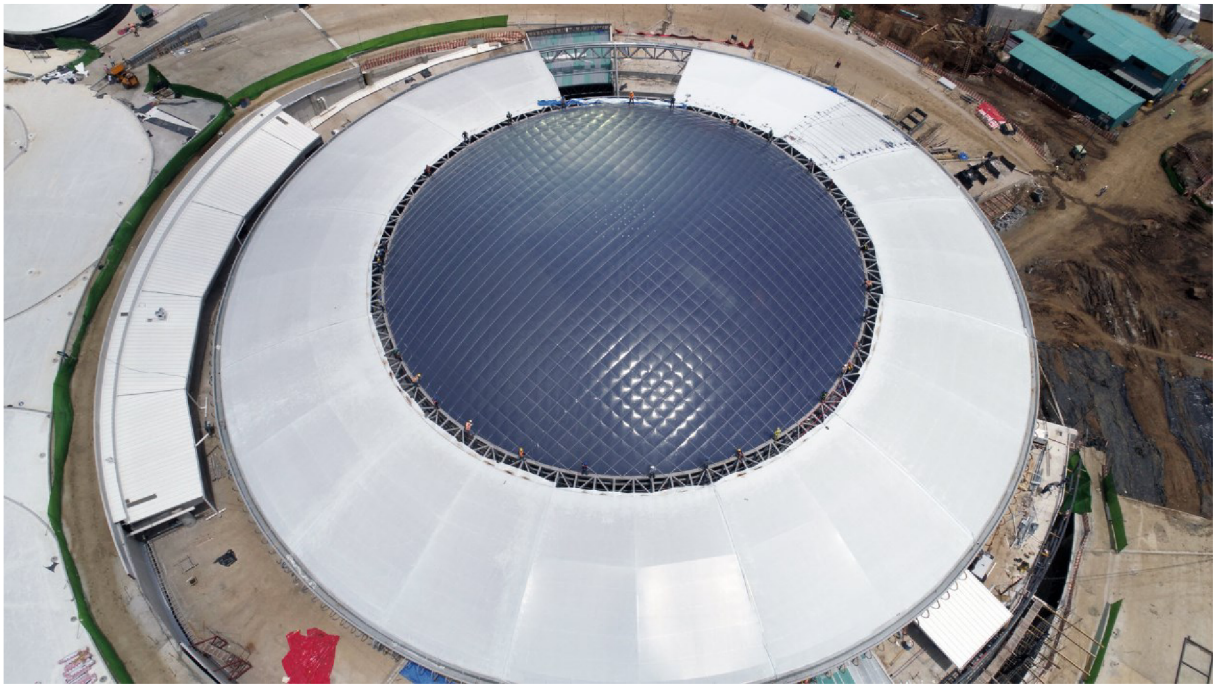

Fig. 170 Oxigeno in San Francisco de Heredia, San José, Costa Rica [XI]

Fig. 171 Interior View of Project Oxigeno, San Francisco de Heredia, San José, Costa Rica [XI]

Here, a really interesting customer project calculated by using the algorithms described above is presented. This project's name is Oxigeno and is located in San José, Costa Rica (Fig. 170, Fig. 171, Fig. 172). The detailed description could be found on this website [XI], where it is also stated: *'The ETFE cushion is the first one in the city of San Francisco de Heredia and at the same time the biggest in the world.'*

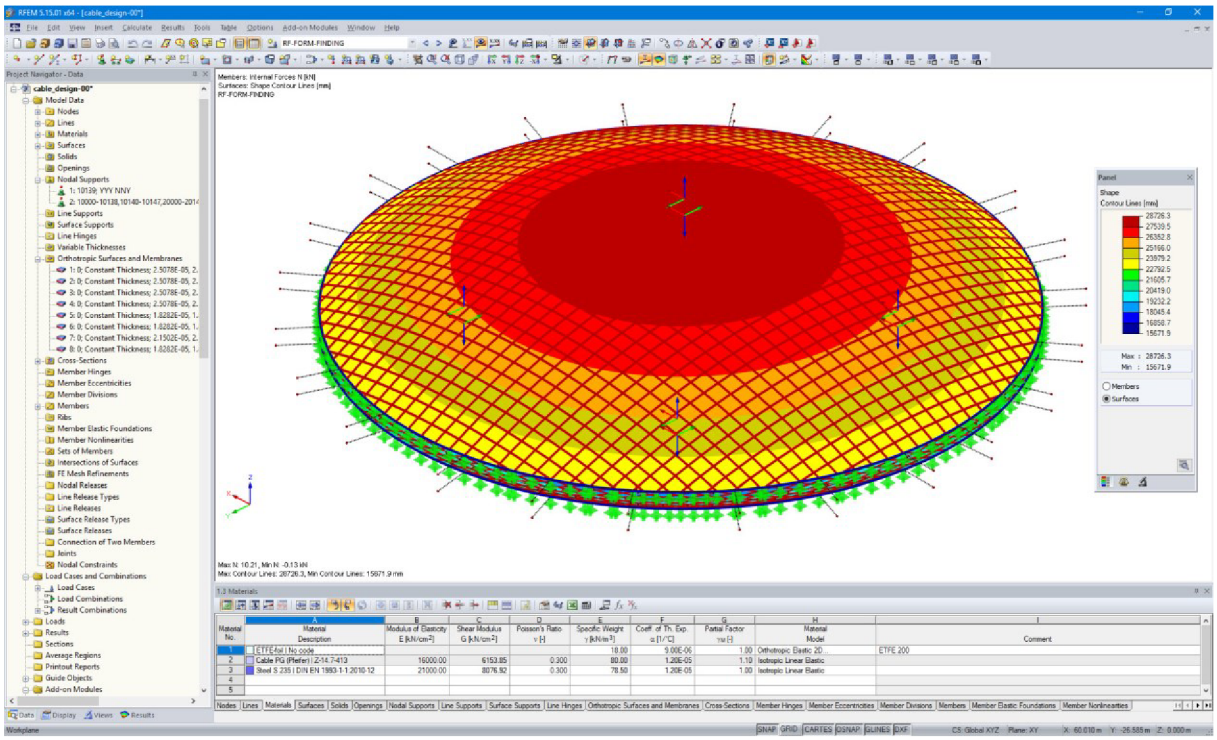

Fig. 172 Numerical Model of Project Oxigeno, San Francisco de Heredia, San José, Costa Rica [XI]

8 CONCLUDING REMARKS

Membrane structures are a really special kind of structures requiring uncommon designing steps in comparison with the conventional structures. The form finding procedure has to be performed at the beginning of their design process and cutting patterns need to be generated for the manufacturing process. For proper structural analysis, it is also necessary to consider the wrinkling phenomenon as the classic membrane theory does not ensure the real stress state estimation.

Each of the stated physical procedures were a part of the presented dissertation, thus the deep investigation of the current state of the art was carried out. Based on these investigations, the theoretical descriptions were written down at the beginnings of the particular chapter. Furthermore, the general and efficient methodologies selected for the numerical analysis were described. Furthermore, the methods and calculation sequences proposed during the research work were presented. Whole work was supported by the beneficial interconnection of the research work at the university environment and the development work for the above-stated software companies. Thus, the theoretical sections, statements and proposals are followed by the results of numerical analyses, that are demonstrating and proving the individual statements.

Based on the investigations performed in the field of the form finding analysis, the selected calculation procedure is derived from the ***geometric stiffness*** and ***hybrid*** platforms. Nevertheless, the crucial point of the form finding analysis consists of the equilibrium searching process itself. The necessity of reaching such a prestress is the cause of many different stabilization techniques. The advanced ***projection method*** was proposed for conical membranes which derives the spatial equilibrium, which would not be possible to define directly, from the equilibrium in the arbitrary oriented projection plane, where it can be defined directly. This strong stabilization technique is quite unique in the principle, as it does not work as an emergency brake of an unrealistic prestress requirement as the stabilization techniques usually work, but it defines the exact equilibrium, although in the implicit manner. During the work focused on the form finding of tensile structures, the attention, in addition to the given scope of the dissertation thesis focus, was paid to the shape optimization procedure of the structures under compression or even of the structures with the mixed form finding requirements. The ***pushing method*** stabilization technique was proposed within the framework of the doctoral thesis to deal with these difficult and complex physical requirements. The above-described calculation procedures and the individual phenomena as well as the crucial implementation necessities were demonstrated on particular examples. Namely, the independence of the equilibrium shape on the chosen initial approximation if the equilibrium of the forces within the given boundary conditions is known, the regeneration of the local axial system, the interaction of the supporting structure with the parts with shape analyzing, presenting the result of the *projection method* and *pushing method* stabilization techniques, or even the extraordinary phenomenon of the multiple equilibrium existence possibility for the structures with the mixed shaping requirements, etc.

Based on the investigations in the field of the wrinkling phenomenon, the new advanced and modular technique was proposed. The process for dealing with the linear elastic materials was

named ***wrinkling separation***, while the procedure for dealing with the nonlinear elastic or plastic materials was named ***elastic prediction modification***, which incorporates the *wrinkling separation* algorithms inside as a modular part. These procedures separate out the unnatural stress which would be considered by the standard membrane theory, but which cannot appear in the membrane in the consequence of its physical nature. Furthermore, the proposed methods were extensively verified and few of the analyzed examples were incorporated to this work to prove their reliability. The first benchmark example disposes with the analytical solution, while the other examples use the well-known equivalency of the wrinkling models with the extensively refined discretization in combination with the shell elements with zero flexural stiffness. Finally, the structural analysis of the whole membrane structure in both the static and dynamic response demonstrated the algorithms capabilities.

In the chapter focused on the generation procedure of cutting patterns, the possible approaches were presented and both their advantages and disadvantages were mentioned. Based on the deep investigations performed in this research area, the ***optimum algorithmic sequence*** was proposed to combine the strengths of the individual methods. As the ***mathematical squashing*** is a really good initial approximation for the planar patterns, the pattern shapes obtained in this way were consequently used for the advanced ***minimization of energy differences*** between the spatial and the planar patterns. This combination thus exhibits increasing of the calculation performance while ensuring the physically optimized patterns. At the end of this section, the numerical examples proved particular statements mentioned in this section as well as demonstrated the possibility of the resulting pattern quality evaluation.

The fascinating field of tensile structures still attracts the attention of many researchers and developers as there is still a huge space for further investigations and improvements. Among others, for example, the automatic compensation of patterns, which has to be derived from intended prestress and inelastic strains undergone during the lifetime. Thus, not only the form finding results, but also the static analysis results have to be the basis of this process. Some authors performed the analyses of the mounting process simulation by tensioning the planar patterns into their final form, as this analysis allow for getting closer to the real stress state of the erected structures. Here, the mutual interaction of all the processes could be observed, as the form finding affects the structural behaviour and the shape to be patterned, the structural analysis influences, the necessary compensation, and the reassembly process leads to a closer approximation of the erected structure, but also affects the structural analysis response itself. Thus, the investigation of proper analysis sequences and impacts is of a great interest and will be a part of a future work in the field of membrane structures.

9 REFERENCES

1 Bathe, K.J. (2016). *Finite Element Procedures.* Watertown: K.J. Bathe.

2 Němec, I., at al. (2010). *Finite element analysis of structures: Principles and Praxis.* (1st ed.). Aachen: Shaker Verlag.

3 Němec, I., Trcala, M., & Rek, V. (2018). *Nelineární mechanika.* Brno: VUTIUM.

4 Newmark, N.M. (1959). A Method of Computation for Structural Dynamics. *Journal of Engineering Mechanics Division*, 85(3), 67-94.

5 Isler, H. (1994). Concrete shells derived from experimental shapes. *Structural Engineering International*, 4(3), 142-147.

6 Otto, F., & Rasch, B. (1995). *Finding Form.* Deutscher Werkbund Bayern: A.Menges.

7 Otto, F., Schleyer, F.K., & Trostel, R. (1973). *Tensile Structures: Design, Structure, and Calculation of Buildings of Cables, Nets, and Membranes.* (1st ed.). Cambridge: The MIT Press.

8 Glaeser, L. (1972). *The Work of Frei Otto.* New York: The Museum of Modern Art.

9 Argyris, J.H., Angelopoulos, T., & Bichat, B. (1974). A general method for the shape finding of lightweight tension structures. *Computer Methods in Applied Mechanics and Engineering*, 3(1), 135-149.

10 Tabarrok, B., & Qin, Z. (1992). Nonlinear analysis of tension structures. *Computers and Structures*, 45(5–6), 973-984.

11 Barnes, M.R. (1988). Form-finding and analysis of prestressed nets and membranes. *Computers and Structures*, 30(3), 685-695.

12 Barnes, M.R. (1999). Form Finding and Analysis of Tension Structures by Dynamic Relaxation. *International Journal of Space Structures*, 14(2), 89-104.

13 Linkwitz, K., & Schek, H.J. (1971). Einige Bemerkungen zur Berechnung von vorgespannten Seilnetzkonstruktionen. *Ingenieur-Archiv*, 40(3), 145-158.

14 Schek, H.J. (1974). The force density method for form finding and computation of general networks. *Computer Methods in Applied Mechanics and Engineering*, 3(1), 115-134.

15 Sánchez, J., Serna, M.Á., & Morer, P. (2007). A multi-step force–density method and surface-fitting approach for the preliminary shape design of tensile structures. *Engineering Structures*, 29(8), 1966-1976.

16 Pauletti, R.M.O., & Pimenta, P.M. (2008). The natural force density method for the shape finding of taut structures. *Computer Methods in Applied Mechanics and Engineering*, 197(49-50), 4419-4428.

17 Maurin, B., & Motro, R. (1998). The surface stress density method as a form-finding tool for tensile membranes. *Engineering Structures*, 20(8), 712-719.

18 Haber, R.B., & Abel, J.F. (1982). Initial equilibrium solution methods for cable reinforced membranes part I—formulations. *Computer Methods in Applied Mechanics and Engineering*, 30(3), 263-284.

19 Haber, R.B., & Abel, J.F. (1982). Initial equilibrium solution methods for cable reinforced membranes part II—implementation. *Computer Methods in Applied Mechanics and Engineering*, 30(3), 285-306.

20 Nouri-Baranger, T. (2002). Form finding method of tensile fabric structures: Revised geometric stiffness method. *Journal of the International Association for Shell and Spatial Structures*, 43(1), 13-21.

21 Bletzinger, K.U., & Ramm, E. (1999). A General Finite Element Approach to the Form Finding of Tensile Structures by the Updated Reference Strategy. *International Journal of Space Structures*, 14(2), 131-145.

22 Linhard, J., & Bletzinger, K.U. (2010). "Tracing" the Equilibrium – Recent Advances in Numerical Form Finding. *International Journal of Space Structures*, 25(2), 107-116.

23 Bletzinger, K.U., Wüchner, R., Daoud, F., & Camprubí, N. (2005). Computational methods for form finding and optimization of shells and membranes. *Computer Methods in Applied Mechanics and Engineering*, 194(30-33), 3438–3452.

24 Bletzinger, K.U., & Ramm, E. (2001). Structural optimization and form finding of light weight structures. *Computers and Structures*, 79(22-25), 2053-2062.

25 Wüchner, R., & Bletzinger, K.U. (2005). Stress-adapted numerical form finding of pre-stressed surfaces by the updated reference strategy. *International Journal for Numerical Methods in Engineering*, 64(2), 143–166.

26 Veenendaal, D., & Block, P. (2012). An overview and comparison of structural form finding methods for general networks. *International Journal of Solids and Structures*, 49(16), 3741–3753.

27 Grüendig, L., Moncrieff, E., Singer, P., & Ströbel, D. (2000). A history of the principal developments and applications of the force density method in Germany 1970–1999. *Fourth International Colloquium on Computation of Shell & Spatial Structures, IASS-IACM 2000*.

28 Argyris, J.H. (1964). Recent Advances in Matrix Methods of Structural Analysis. *Progress in Aeronautical Sciences*, 45(5), 366-367.

29 Fenves, S.J., & Branin, F.H. (1963). Network-Topological Formulation of Structural Analysis. *Journal of the Structural Division*, 89(4), 483-514.

30 Siev, A., & Eidelman, J. (1964). Stress Analysis of Prestressed Suspended Roofs. *Journal of the Structural Division*, 90(4), 103-122.

31 Wood, R.D. (2002). A simple technique for controlling element distortion in dynamic relaxation form-finding of tension membranes. *Computers and Structures*, 80(27-30), 2115–2120.

32 Zhang, J.Y., & Ohsaki, M. (2006). Adaptive force density method for form-finding problem of tensegrity structures. *International Journal of Solids and Structures*, 43(18-19), 5658–5673.

33 Van Mele, T., & Block, P. (2011). A novel form finding method for fabric formwork for concrete shells. *Journal of the International Association of Shell and Spatial Structures*, 52(4), 217–224.

34 Arcaro, K.K., & Klinka, V.F. (2009). Finite element analysis for geometric shape minimization. *Journal of the International Association for Shell and Spatial Structures*, 50, 79–86.

35 Ohyama, H., & Kawamata, S. (1972). A problem of surface design for prestressed cable nets. *Pacific Symposium Part II on Tension Structures and Space Frames, IASS.*

36 Knudson, W.C., & Scordelis, A.C. (1972). Cable forces for desired shapes in cable-net structures. *Pacific Symposium Part II on Tension Structures and Space Frames, IASS.*

37 Boudaoud, A., Patrício, P., & Amar, M.B. (1999). The helicoid versus the catenoid: Geometrically induced bifurcations. *Physical Review Letters*, 83(19), 3836–3839.

38 Dierigner, F.H. (2014). *Numerical Methods for the Design and Analysis of Tensile Structures.* Dissertation, München: Technische Universität München.

39 Novýsedlák, P. (2017). *Tensile Structures – Numerical Design Techniques.* Diploma thesis, Dessau-Roßlau: Anhalt University of Applied Sciences.

40 Widhammer, A.M. (2015). *Variation of Reference Strategy – Generation of Optimized Cutting Patterns for Textile Fabrics.* Dissertation, München: Technische Universität München.

41 Kupzok, A.M. (2009). *Modeling the Interaction of Wind and Membrane Structures by Numerical Simulation.* Dissertation, München: Technische Universität München.

42 Jrusjrungkiat, A. (2009). *Nonlinear Analysis of PneumaticMembranes: "From Subgrid to Interface".* Dissertation, München: Technische Universität München.

43 Lang, R. (2013). *Návrh a výpočet membránové konstrukce zastřešení stationu.* Diploma thesis, Brno: Brno University of Technology.

44 Lang, R. (2017). *Design and Analysis of Membrane Structures in FEM-Based Software.* Diploma thesis, Dessau-Roßlau: Anhalt University of Applied Sciences.

45 Wagner, H. (1931). Flat sheet metal girders with very thin metal web. Part I, General theories and assumptions. *Zeitschrift für Flugtechnik und Motorluftschiffahrt*, 20(8), 200-207.

46 Akita, T., Nakashino, K., Natori, M.C., & Park, K.C. (2007). A simple computer implementation of membrane wrinkle behaviour via a projection technique. *International Journal for Numerical Methods in Engineering*, 71, 1231–1259.

47 Wu, C.H., & Canfield, T.R. (1981). Wrinkling in finite plane-stress theory. *Quarterly of Applied Mathematics*, 39(2), 179–199.

48 Roddeman, D.G., Drukker, J., Oomens, C.W., & Janssen, J.D. (1987). The wrinkling of thin membranes: Part I—theory. *Journal of Applied Mechanics*, 54(4), 884–887.

49 Roddeman, D.G., Drukker, J., Oomens, C.W., & Janssen, J.D. (1987). The wrinkling of thin membranes: Part II—numerical analysis. *Journal of Applied Mechanics*, 54(4), 888–892.

50 Schoop, H., Taenzer, L., & Hornig, J. (2002). Wrinkling of nonlinear membranes. *Computational Mechanics*, 29(1), 68–74.

51 Jarasjarungkiat, A., Wüchner, R., & Bletzinger, K.U. (2009). Efficient sub-grid scale modeling of membrane wrinkling by a projection method. *Computer Methods in Applied Mechanics and Engineering*, 198 (9-12), 1097-1116.

52 Miller, R.K., Hedgepeth, J.M., Weingarten, V.I., Das, P., & Kahyai, S. (1985). Finite element analysis of partly wrinkled membranes. *Computers and Structures*, 20(1-3), 631–639.

53 Ding, H., Yang, B., Lou, M., & Fang, H. (2003). New numerical method for two-dimensional partially wrinkled membranes. *AIAA Journal*, 41(1), 125–132.

54 Ding, H., & Yang, B. (2003). The modeling and numerical analysis of wrinkled membranes. *International Journal for Numerical Methods in Engineering*, 58(12), 1785–1801.

55 Liu, X., Jenkins, C.H., Shur, W.W. (2001). Large deflection analysis of pneumatic envelopes using a penalty parameter modified material model. *Finite Elements in Analysis and Design*, 37(3), 233–251.

56 Fujikake, M., Kojima, O., & Fukushima, S. (1989). Analysis of fabric tension structures. *Computers and Structures*, 32(3-4), 537–547.

57 Contri, P., & Schrefler, B.A. (1988). A geometrically nonlinear finite element analysis of wrinkled membrane surfaces by a no-compression material model. *Communications in Applied Numerical Methods*, 4(1), 5–15.

58 Epstein, M., & Forcinito, M.A. (2001). Anisotropic membrane wrinkling: theory and analysis. *International Journal of Solids and Structures*, 38(30-31), 5253–5272.

59 Lu, K., Accorsi, M., & Leonard, J. (2001). Finite element analysis of membrane wrinkling. *International Journal for Numerical Methods in Engineering*, 50(5), 1017–1038.

60 Miyazaki, Y. (2006). Wrinkle/slack model and finite element dynamics of membrane. *International Journal for Numerical Methods in Engineering*, 66(7), 1179–1209.

61 Raible, T., Tegeler, K., Löhnert, S., & Wriggers, P. (2005). Development of a wrinkling algorithm for orthotropic membrane materials. *Computer Methods in Applied Mechanics and Engineering*, 194(21-24), 2550–2568.

62 Steigmann, D.J., & Pipkin, A.C. (1989). Finite deformations of wrinkled membranes. *The Quarterly Journal of Mechanics and Applied Mathematics*, 42(3), 427–440.

63 Muttin, F. (1996). A finite element for wrinkled curved elastic membranes, and its application to sails. *Communications in Numerical Methods in Engineering*, 12(11), 775–785.

64 Haseganu, E.M., & Steigmann, D.J. (1994). Analysis of partly wrinkled membranes by the method of dynamic relaxation. *Computational Mechanics*, 14(6), 596–614.

65 Kang, S., & Im, S. (1999). Finite element analysis of dynamic response of wrinkling membranes. *Computer Methods in Applied Mechanics and Engineering*, 173(1-2), 227–240.

66 Pargana, J.B., Lloyd-Smith, D., & Izzuddin, B.A. (2007). Advanced material model for coated fabrics used in tensioned fabric structures. *Engineering Structures*, 29(7), 1323–1336.

67 Hornig, J., & Schoop, H. (2005). Wrinkling analysis of membranes with elastic–plastic material behavior. *Computational Mechanics*, 35(2), 153–160.

68 Wang, C.G., Tan, H.F., Du, X.W., & Wan, Z.M. (2007). Wrinkling prediction of rectangular shell-membrane under transverse in-plane displacement. *International Journal of Solids and Structures*, 44(20), 6507–6516.

69 Deng, X., & Pellegrino, S. (2012). Wrinkling of Orthotropic Viscoelastic Membranes. *AIAA Journal*, 50(3), 668-681.

70 Miyamura, T. (2000). Wrinkling on stretched circular membrane under in-plane torsion: Bifurcation analyses and experiments. *Engineering Structures*, 22(11), 1407–1425.

71 Miller, R.K., Hedgepeth, J.M., Weingarten, V.I., Das, P., & Kahyai, S. (1984). *Finite element analysis of wrinkling membranes.* Hampton: NASA-CR-172325 19840015858.

72 Rossi, R., Lazzari, M., Vitaliani, R., & Onate, E. (2005). Simulation of light-weight membrane structures by wrinkling model. *International Journal for Numerical Methods in Engineering*, 62(15), 2127–2153.

73 Pagitz, M.E. (2004). *Computational methods for membrane structures.* Diploma thesis, Cambridge: University of Cambridge.

74 Kang, S., & Im, S. (1997). Finite element analysis of wrinkling membranes. *Journal of Applied Mechanics*, 64(2), 263–269.

75 Roddeman, D.G. (1987). *Force transmission in wrinkled membranes*. Dissertation, Eindhoven: University of Technology.

76 Weis, L. (2014). *Materiálově nelineární řešení konstrukcí z plastů.* Dissertation, Brno: Brno University of Technology.

77 Bletzinger, K.U., Dieringer, F., & Philipp, B. (2013). *Numerical Theory (MM2).* Dessau-Roßlau: Anhalt University of Applied Sciences.

78 Stein, M., & Hedgepeth, J.M. (1961). *Analysis of partly wrinkled membranes.* NASA TN D-813.

79 Gosling, P.D., Bridgens, B.N., Albrecht, A., Alpermann, H., Angeleri, A., Barnes, M., Bartle, N., Canobbio, R., Dieringer, F., Gellin, S., Lewis, W.J., Mageau, N., Mahadevan, R., Marion, J.M., Marsden, P., Milligan, E., Phang, Y.P., Sahlin, K., Stimpfle, B., Suire, O., & Uhlemann, J. (2013). Analysis and design of membrane structures: Results of a round robin exercise. *Engineering Structures*, 48, 313–328.

80 Forster, B., & Mollaert, M. (2004). *European Design Guide for Tensile Surface Structures.* Brussel: Vrije Univ.

81 Balz-Bögner, H., & Blum, R. *Mechanical and Physical Properties and Basic on Structural Engineering (CM03).* Dessau-Roßlau: Anhalt University of Applied Sciences.

82 Gründig, L., Ekert, L., & Moncrieff, E. (1996). Geodesic and Semi-Geodesic Line Algorithms for Cutting Pattern Generation of Architectural Textile Structures. *Asia-Pacific Conference on Shell and Spatial Structures.*

83 Martinez, D., Velho, L., & Carvalho, P.C. (2004). Geodesic paths on triangular meshes. *17th Brazilian Symposium on Computer Graphics and Image Processing.*

84 Surazhsky, V., Surazhsky, T., Kirsanov, D., Gortler, S.J., & Hoppe, H. (2005). Fast Exact and Approximate Geodesics on Meshes. *ACM Transactions on Graphics (TOG)*, 24(3), 553–560

85 Yang, B., & Lu, Y. (2011). Computing Approximate Geodesic on Triangular Mesh. *Journal of Information & Computational Science*, 8(5), 826–832.

86 Martínez, D., Velho, L., & Carvalho, P.C. (2005). Computing geodesics on triangular meshes. *Computers & Graphics*, 29(5), 667–675.

87 Ströbel, D., Gründig, L., & Singer, P. (2013). Selected Examples for the Optimization of Cutting Patterns for Textile Membranes. *VI International Conference on Textile Composites and Inflatable Structures, STRUCTURAL MEMBRANES 2013.*

88 Gründig, L., Moncrieff, E., Singer, P., & Ströbel, D. (2000). High-performance cutting pattern generation of architectural textile structures. *Fourth International Colloquium on Computation of Shell & Spatial Structures.*

89 Moncrieff, E., & Topping, B.H.V. (1990). Computer methods for the generation of membrane cutting patterns. *Computers & Structures*, 37(4), 441–450.

90 Maurin, B., & Motro, R. (1999). Cutting Pattern of Fabric Membranes with the Stress Composition Method. *International Journal of Space Structures*, 14(2), 121–129.

91 Bletzinger, K.U., & Widhammer, A. (2016). Variation of Reference Strategy - A novel approach for generating optimized cutting patterns of membrane structures. *Procedia Engineering*, 155, 131–141.

92 Linhard, J., Wüchner, R., & Bletzinger, K.U. (2008). Introducing Cutting Patterns in Form Finding and Structural Analysis. *Textile Composites and Inflatable Structures II*, 8, 69–84.

93 Goldbach, A.K., Breitenberger, M., Widhammer, A., & Bletzinger, K.U. (2016). Computational Cutting Pattern Generation using Isogeometric B-Rep Analysis. *Procedia Engineering*, 155, 249–255.

94 Bletzinger, K.U., Linhard, J., & Wüchner, R. (2010). Advanced Numerical Methods for the Form Finding and Patterning of Membrane Structures. *New Trends in Thin Structures: Formulation, Optimization and Coupled Problems*, 519, 133–154.

95 Dieringer, F., Wüchner, R., & Bletzinger, K.U. (2011). Advanced cutting pattern generation – Consideration of structural requirements in the optimization process. *International Conference on Textile Composites and Inflatable Structures, STRUCTURAL MEMBRANES 2011.*

96 Azariadis, P.N., & Aspragathos, N.A. (2000). On using planar developments to perform texture mapping on arbitrarily curved surfaces. *Computers & Graphics*, 24(4), 539–554.

97 Gale, S., & Lewis, W.J. (2016). Patterning of tensile fabric structures with a discrete element model using dynamic relaxation. *Computers & Structures*, 169, 112–121.

98 Brew, J.S., & Lewis, W.J. (2013). Spline-based and stress-monitored patterning of fabric structures. *Computers & Structures*, 119, 203–214.

99 Li, J., Zhang, D., Lu, G., Peng, Y., Wen, X., & Sakaguti, Y. (2005). Flattening triangulated surfaces using a mass-spring model. *The International Journal of Advanced Manufacturing Technology*, 25(1-2), 108–117.

100 Ishii, K. (1999). Form Finding Analysis in Consideration of Cutting Patterns of Membrane Structures. *International Journal of Space Structures*, 14(2), 105–119.

101 Zhong, Y., & Xu, B. (2006). A physically based method for triangulated surface flattening. *Computer-Aided Design*, 38(10), 1062–1073.

102 Cai, Z.Y., Li, M.Z., & Zhang, H.M. (2007). A simplified algorithm for planar development of 3D surface and its application in the blank design of sheet metal forming. *Finite Elements in Analysis and Design*, 43(4), 301–310.

103 Kim, J.Y., & Lee, J.B. (2002). A new technique for optimum cutting pattern generation of membrane structures. *Engineering Structures*, 24(6), 745–756.

104 Zhang, Q.L., & Luo, X.Q. (2003). Finite element method for developing arbitrary surfaces to flattened forms. *Finite Elements in Analysis and Design*, 39(10), 977–984.

10 LIST OF PUBLISHED WORKS

105 Lang, R., Němec, I., Hokeš, F., & Trcala, M. (2019). Different Sources of Dynamic Damping and Nonlinear Dynamic Analysis of the Membrane Construction. *First International Nonlinear Dynamics Conference, NODYCON 2019.*

106 Lang, R., & Němec, I. (2017). Form-finding of shell and membrane structures. *International Conference on Textile Composites and Inflatable Structures, STRUCTURAL MEMBRANES 2017.*

107 Hofírek, R., Lang, R., & Zich, M. (2017). Changes in shrinkage after the application of insulation to the concrete surface. *Solid State Phenomena*, 272, 121-126.

108 Hofírek, R., Lang, R., & Zich, M. (2017). Změny průběhu smršťování po aplikování izolace na povrch betonu. *24. Betonářské dny 2017.*

109 Lang, R., Němec, I., & Štekbauer, H. (2017). Navrhování tvarů membránových konstrukcí a výpočet střihových vzorů. *TZB-info*, 2017.

110 Lang, R., Zeiner, M., & Němec, I. (2016). Vytváření střihových vzorů. *Juniorstav 2016.*

111 Lang, R., & Němec, I. (2015). Jak navrhovat membránové konstrukce. *Juniorstav 2015.*

112 Lang, R., Němec, I., & Martinásek, J. (2014). Specifické aspekty ohybově netuhých konstrukcí. *12th International Conference on New Trends in Statics and Dynamics of Buildings.*

113 Lang, R., Němec, I., & Ševčík, I. (2014). Form- finding of membrane structures with regard to its specific necessities. *6th international conference Dynamics of Civil Engineering and Transport Structures and Wind Engineering, DYN-WIND 2014.*

114 Lang, R., Němec, I., & Ševčík, I. (2014). Form-finding of Membrane Structures and Necessary Stabilization of this Process. *Applied Mechanics and Materials*, 617, 130-135.

115 Němec, I., & Lang, R. (2013). Design and analysis of the membrane structure of a stadium roof. *Applied Mechanics 2013.*

116 Lang, R., & Němec, I. (2013). Navrhování membránových konstrukcí. *Modelování v mechanice 2013.*

117 Němec, I., & Lang, R. (2013). Návrh počátečního tvaru pro membránové konstrukce. *Sborník vědeckých prací Vysoké školy báňské – Technické univerzity Ostrava*, 2, 159-162.

11 LINKS

I Wikipedia (2019). Retrieved 7 July 2019, from https://de.wikipedia.org/wiki/Tanzbrunnen

II Tanzbrunnen Köln (2019). Retrieved 7 July 2019, from https://www.koelnkongress.de/en/locations/tanzbrunnen-koeln.html

III Dlubal Software – Structural Engineering Software for Analysis and Desing (2019). Retrieved 7 July 2019, from https://www.dlubal.com/en-US/solutions/industries/analysis-and-design-software-for-tensile-membrane-structures

IV FEM consulting – Research and development of FEM solver (2019). Retrieved 7 July 2019, from http://www.fem.cz/?lang=en

V Architen Landrell (2019). Retrieved 7 July 2019, from http://www.architen.com/articles/basic-theories-of-tensile-membrane-architecture/

VI MIT – MITOPENCOURSEWARE (2019). Retrieved 15 March 2019, from https://ocw.mit.edu/resources/res-2-002-finite-element-procedures-for-solids-and-structures-spring-2010/linear/

VII MIT – MITOPENCOURSEWARE (2019). Retrieved 15 March 2019, from https://ocw.mit.edu/resources/res-2-002-finite-element-procedures-for-solids-and-structures-spring-2010/nonlinear/

VIII Dlubal Software – Structural Engineering Software for Analysis and Desing – Verification examples (2019). Retrieved 19 August 2019, from https://www.dlubal.com/en-US/downloads-and-information/examples-and-tutorials/verification-examples?program=rf-form-finding

IX TZB-info (2019). Retrieved 21 August 2019, from https://stavba.tzb-info.cz/strechy/15513-navrhovani-tvaru-membranovych-konstrukci-a-vypocet-strihovych-vzoru?fbclid=IwAR06Umn8Ct9oveoY1oVSwsFQi7qbKs0au-AQWosVaNvnLMGt0YWlNHrZzSA

X Archtex (2019). Retrieved 7 July 2019, from http://archtex.cz/en/index.html

XI Dlubal Software – Structural Engineering Software for Analysis and Desing – Customer Projects (2019). Retrieved 19 August 2019, from https://www.dlubal.com/en/downloads-and-information/references/customer-projects/001116

12 ABOUT AUTHOR

PERSONAL INFORMATION

Rostislav Lang
Institute of Structural Mechanics
Faculty of Civil Engineering
Brno University of Technology
Veveří 95, 635 00 Brno
Email: lang.r@fce.vutbr.cz

EDUCATION

From 2013 — Student of Doctoral Programme in Civil Engineering — EQF 8
Brno University of Technology, Faculty of Civil Engineering
Brno, Czech Republic
- Degree course: Structures and Traffic Constructions
- Doctorate thesis: Algorithms for design and analysis of membrane structures

2015 - 2017 — Master Programme in Civil Engineering — EQF 7
Anhalt University of Applied Sciences, Institute for Membrane and Shell Technologies e.V.
Dessau-Roßlau, Germany
- Degree course: Membrane Strucutures
- Master thesis: Design and Analysis of Membrane Structures in FEM-Based Software

2011 - 2013 — Master Programme in Civil Engineering — EQF 7
Brno University of Technology, Faculty of Civil Engineering
Brno, Czech Republic
- Degree course: Structures and Traffic Constructions
- Master thesis: Design and Analysis of Membrane Roof of a Stadium

2007-2011 — Bachelor Programme in Civil Engineering — EQF 6
Brno University of Technology, Faculty of Civil Engineering
Brno, Czech Republic
- Degree course: Structures and Traffic Constructions
- Bachelor thesis: The Girder Bridge Analysis

WORK EXPERIENCE

From 10/2016 Tutor

Brno University of Technology, Faculty of Civil Engineering, Institute of Structural Mechanics

Veveří 331/95, 602 00 Brno, Czech Republic

- Courses

  BD003 Structural Analysis 1

  BD004 Structural Analysis 2

  CD002 Nonlinear Mechanics

From 4/2014 Research fellow

FEM consulting s.r.o.

Veveří 331/95, 602 00 Brno, Czech Republic

- Professional and organizational responsibility for algorithmization of calculation tools for the design and analysis of membrane structures within the FEA core by FEM consulting company
- Implementation of form finding algorithms, physical flattening process and wrinkling of membranes into the FEA core
- Responsible for cooperation with the partner company Dlubal Software for development of software packages for membrane structures into RFEM software (RF-FORM-FINDING and RF-CUTTING-PATTERN)

4/2013 – 3/2014 Software development analyst

Dlubal Software s.r.o.

Anglická 28, 120 00 Praha 2, Czech Republic

- Organizational and analytic work for development of calculation modules for membrane structures into RFEM software

2/2013 – 3/2013 Design works and projects

HURYTA s.r.o.

Staňkova 557/18a, 602 00 Brno, Czech Republic

- design and calculation of building structures

6/2012 Diagnostics of constructions / professional experience during study

INSET s.r.o.

Vinohrady 506/40, 639 00 Brno, Czech Republic

- instrumental works during static and dynamic load tests of highway bridges

PARTICIPATION IN RESEARCH PROJECTS

1/2016 – 12/2018	CZ.01.1.02/0.0/0.0/15_019/0004929 Algorithmization of the initial shape design of the membrane structures and their static and dynamic analysis
1/2015 – 12/2015	FAST-J-15-2803 Design of membrane structures
3/2014 – 06/2015	CZ.1.03/2.2.00/23.00705 Development of progressive methods in solid mechanics
1/2014 – 12/2014	FAST-J-14-2351 Design of initial equilibrium shape of membrane structures (form finding)

AWARDS

2015	Award of Josef Hlávka received from the Foundation 'Talent of Josef, Marie and Zdenka Hlavka'
2015	17th International Conference of Postgraduate Students JUNIORSTAV 2015: Diploma for the 1. place in section 2.7 Structural mechanics and diploma for the best paper of the conference
2013	Award for academic achievement received from the dean of the Faculty of Civil Engineering, Brno University of Technology
2013	Award for diploma thesis received from the dean of the Faculty of Civil Engineering, Brno University of Technology
2013	Third place in the theses competition in the degree course Structures and Traffic Constructions. Note: Competition was organized by ČKAIT (Czech chamber of engineers and technicians active in construction) and Brno University of Technology, Faculty of Civil Engineering.